Integrated Experimental and Modeling Studies of Mineral Carbonation as a Mechanism for Permanent Carbon Sequestration in Mafic/Ultramafic Rocks

Type of Report: Final Scientific/Technical Report

Reporting Period State Date: October 1, 2010

Reporting Period End Date: September 30, 2014

PRINCIPAL AUTHORS
Zhengrong Wang†*, Lin Qiu, Shuang Zhang, Edward Bolton†, David Bercovici†,
Jay Ague†, Shun-Ichiro Karato†, Michael Oristaglio†
Yale University, Department of Geology & Geophysics

Wen-lu Zhu†, Harry Lisabeth, University of Maryland, Department of Geology

Kevin Johnson†, University of Hawai'i, Department of Geology & Geophysics

Date: May 2015

DOE Award Number: DE-FE0004375

Submitting Organization:
Yale University, Office of Grant and Contract Administration,
47 College Street, Suite 203, New Haven, CT 06520-8047

Subcontractors:
University of Hawai'i at Mānoa, Honolulu, HI 96822
University of Maryland, College Park, MD 20742

†Principal Investigator

*Now at City College of New York, Department of Earth & Atmospheric Science

DISCLAIMER

NOTE TO READERS

This Final Scientific/Technical Report contains the results of project work carried out under DOE Award Number DE-FE0004375. The main scientific and technical results of the work carried out during the project are being incorporated into manuscripts for submission to peer-reviewed journals. The results and interpretations contained in this report were therefore preliminary at the time of its submission to DOE (May 2015) and may be modified or corrected based on the peer-review process. Interested readers should consult the Bibliography at the end of this report for a list of manuscripts in preparation for publication. If necessary, an updated and corrected version of the report will be filed with DOE after the review process has been completed for the scientific and technical papers resulting from the project.

ABSTRACT

A program of laboratory experiments, modeling and fieldwork was carried out at Yale University, University of Maryland, and University of Hawai‘i, under a DOE Award (DE-FE0004375) to study mineral carbonation as a practical method of geologic carbon sequestration. Mineral carbonation, also called carbon mineralization, is the conversion of (fluid) carbon dioxide into (solid) carbonate minerals in rocks, by way of naturally occurring chemical reactions. Mafic and ultramafic rocks, such as volcanic basalt, are natural candidates for carbonation, because the magnesium and iron silicate minerals in these rocks react with brines of dissolved carbon dioxide to form carbonate minerals. By trapping carbon dioxide (CO_2) underground as a constituent of solid rock, carbonation of natural basalt formations would be a secure method of sequestering CO_2 captured at power plants in efforts to mitigate climate change.

Geochemical laboratory experiments at Yale, carried out in a batch reactor at 200°C and 150 bar (15 MPa), studied carbonation of the olivine mineral forsterite (Mg_2SiO_4) reacting with CO_2 brines in the form of sodium bicarbonate ($NaHCO_3$) solutions. The main carbonation product in these reactions is the carbonate mineral magnesite ($MgCO_3$). A series of 32 runs varied the reaction time, the reactive surface area of olivine grains and powders, the concentration of the reacting fluid, and the starting ratio of fluid to olivine mass. These experiments were the first to study the rate of olivine carbonation under passive conditions approaching equilibrium.

The results show that, in a simple batch reaction, olivine carbonation is fastest during the first 24 hours and then slows significantly and even reverses. A natural measure of the extent of carbonation is a quantity called the carbonation fraction, which compares the amount of carbon removed from solution, during a run, to the maximum amount that could have been removed if the olivine initially present had fully dissolved and the cations released had subsequently precipitated in carbonate minerals.

The carbonation fractions observed in batch experiments with olivine grains and powders varied significantly, from less than 0.01 (1%) to more than 0.5 (50%). Over time, the carbonation fractions reached an upper limit after about 24 to 72 hours of reaction, then stayed constant or decreased. The peak

coincided with the appearance of secondary magnesium-bearing silicate minerals, whose formation competes for magnesium ions in solution and can even promote conditions that dissolve magnesite.

The highest carbonation fractions resulted from experiments with low ratios of concentrated solution to olivine, during which amorphous silica spheres or meshes formed, instead of secondary silicate minerals. The highest carbonation fractions appear to result from competing effects. Precipitation of silica layers on olivine reduces the reactive surface area and, thus, the rate of olivine dissolution (which ultimately limits the carbonation rate), but these same silica layers can also inhibit the formation of secondary silicate minerals that consume magnesite formed in earlier stages of carbonation. Simulation of these experiments with simple geochemical models using the software program EQ3/6 reproduces the general trends observed—especially the results for the carbonation fraction in short-run experiments. Although further experimentation and better models are needed, this study nevertheless provides a framework for understanding the optimal conditions for sequestering carbon dioxide by reacting CO_2-bearing fluids with rocks containing olivine minerals.

A series of experiments at the Rock Physics Laboratory at the University of Maryland studied the carbonation process during deformation of thermally cracked olivine-rich rock samples (dunite) saturated with CO_2 brines of varying compositions. A goal of these geomechanical experiments was to see if flow and deformation processes, which accompany natural carbonation reactions in underground settings, work to enhance or inhibit the reactions. The experiments involved hydrostatic compaction, followed by deformation at a constant rate of strain. Sample permeability was monitored during the reactions. Comparison of the samples' volume changes to their axial strains (shortening) during deformation indicates that samples reacted with CO_2-saturated brines accommodate more axial compaction, before the onset of dilation (a swelling that precedes rock failure), than samples reacted with distilled water.

Analyses of the reacted samples with scanning electron microscope (SEM) images indicate, first, that dissolution of olivine occurring in the initial stages of carbonation can provide pathways to fluid flow that sustain the reaction, and, second, that carbonate minerals precipitated along existing fractures in the rocks may serve as asperities, or roughness on a crack's surface that restricts its closure.

In a related study undertaken by one of the principal investigators as a spin-off of the main project, a simple model of (magnesite) crystal growth in the pore space of basalts undergoing carbonation was developed. The model suggests that, under a carefully controlled program of CO_2 injection, carbonate mineral growth can harden the rock formation against earthquakes that might otherwise be induced by the injection of large fluid volumes (Yarushina and Bercovici, 2013).

The overall conclusion of the research project is that mineral carbonation of underground mafic and ultramafic rock formations is a viable candidate for long-term sequestration of man-made carbon dioxide. No results obtained during the project indicate that the method is inherently intractable in its implementation; moreover, enormous volumes of basalt near Earth's surface are candidate locations for large-scale injection programs. The geochemical experiments do indicate, however, that there will be significant engineering challenges in maintaining high rates of carbonation, by delaying the onset of chemical conditions that promote formation of secondary silicate minerals and, therefore, slow down, or even reverse, the carbonation process. It remains an open question as to whether carbonation processes can be sustained for many years in an engineered system operating on a large scale—a scale capable of accommodating millions of tons of CO_2 annually. The development of realistic theoretical models that can systematically describe the combined effects of reactive flow, precipitation and geomechanical deformation is a major barrier to further understanding of the practical viability of mineral carbonation as large-scale method of carbon sequestration.

TABLE OF CONTENTS

DISCLAIMER 2
NOTE TO READERS 2
ABSTRACT 3
TABLE OF CONTENTS 6
EXECUTIVE SUMMARY 7
INTRODUCTION 13
PART I GEOCHEMICAL EXPERIMENTS 16
PART I References 37
PART I Table 41
PART I Figure Captions 43
PART I Figures 46
PART II GEOMECHANICAL EXPERIMENTS 60
PART II References 66
PARTI II Figure Captions 67
PART II Figures 71
BIBLIOGRAPHY 94
APPENDICES 97
APPENDIX A – SUPPLEMENT TO PART I (GEOCHEMICAL EXPERIMENTS) A-1
APPENDIX B – SYNTHETIC ROCK SAMPLES B-1
APPENDIX C – AUTOCLAVE DESIGN C-1
APPENDIX D – FIELDWORK: SAMPLE COLLECTION AND ANALYSIS D-1
APPENDIX E – MODELING CODES E-1

EXECUTIVE SUMMARY

Scientific and Technical Results

This is the final scientific/technical report for the project "Integrated Experimental and Modeling Studies of Mineral Carbonation as a Mechanism for Permanent Carbon Sequestration in Mafic/Ultramafic Rocks." The original three-year project started in October 2010 with support from Yale Climate & Energy Institute and the National Energy Technology Laboratory (NETL) of the U.S. Department of Energy (DOE). A series of no-cost time extensions from DOE extended the project until September 30, 2014.

The main scientific goal of the project was to develop rigorous methods for estimating the carbon sequestration potential of mafic and ultramafic rock formations subjected to a process called "in situ mineral carbonation." Mineral carbonation, also called carbon mineralization, is the conversion of (fluid) carbon dioxide into (solid) carbonate minerals in rocks, by way of naturally occurring chemical reactions. In the process of in situ mineral carbonation, carbon dioxide in aqueous solution (or in supercritical form) is injected underground into rocks containing magnesium-iron silicate minerals, such as olivine ($(Mg,Fe)_2SiO_4$), under conditions that promote the formation of solid carbonate minerals, such as magnesite ($MgCO_3$). Mineral carbonation mimics the way carbon dioxide cycles naturally over geologic time from the atmosphere and oceans into the solid crust—which is the chief natural mechanism for removing CO_2 from the atmosphere in Earth's long-term carbon cycle.

If artificial mineral carbonation can be engineered to work over short time scales in volcanic basalts—a natural candidate for carbonation because of their abundance near the Earth's surface and their high concentrations of magnesium-iron silicate minerals—this process could become the preferred method of sequestering carbon dioxide captured at power plants, or other point sources, in efforts to mitigate climate change. By trapping CO_2 as a mineral constituent of solid rock, carbonation avoids the issues of long-term leakage that are associated with conventional geologic sequestration methods that inject fluid CO_2 into permeable underground aquifers or petroleum reservoirs (usually, sandstone and

limestone rock formations) and rely mainly on the seal provided by impermeable rock above the reservoir (usually, shale) to hold the fluid.

There were two major scientific tasks of the project. The first was a series of geochemical experiments on minerals and rock assemblages to determine the effective reaction rates of the key mineral carbonation reactions. The second was a set of novel geomechanical experiments to elucidate the processes of reactive fluid flow and deformation that accompany mineral carbonation and may limit the potential to carbonate large volumes of rock by shutting off its available pore space. Part of each task was the development of modeling tools to understand the experimental results. Eight principal investigators (PIs) at 3 institutions carried out or supervised most of the work in the project: 6 PIs at Yale University, 1 at University of Maryland College Park, and 1 at University of Hawai‘i at Mānoa. Also working in the project were a post-doctoral research associate and a graduate student at Yale and a graduate student at Maryland.

The project proceeded largely according to its original statement of work. At Yale, reactions between CO_2-bearing fluids and olivine were systematically investigated in a series of 32 experiments that varied the reaction time, the reactive surface area of olivine grains and powders, the concentration of the reacting fluid, and the ratio of fluid to olivine mass. The results show that, in a simple batch reaction, olivine carbonation is fastest during the first 24 hours and then slows significantly and even reverses. The overall progress of carbonation, as measured by the amount of carbon in solution that is converted to carbonate minerals (called the carbonation fraction), generally reaches an upper limit and then decreases over time, as conditions favorable to the formation of secondary magnesium minerals arise and dissolve magnesite crystals precipitated earlier. An empirical formula for the maximum carbonation fraction that can be achieved by reacting CO_2-bearing fluid and olivine was determined from the experiments and used to estimate the carbon sequestration potential of mafic rocks readily accessible in the crust. The University of Hawai’i participated in sample collection and analysis for this part of the project.

An important outcome of the work at Yale was the design and construction of a new autoclave system that allows monitoring of reaction conditions in laboratory carbonation experiments. The new

system, which has unique features for its relatively low cost, was designed in collaboration with the manufacture AppliTech Corporation and was installed and tested in the geochemical laboratory on Yale West Campus at the end of the project. The system was used to check on the results obtained in the static reaction chamber used for the geochemical experiments.

At the Rock Physics Laboratory at the University of Maryland College Park, a series of geomechanical experiments were performed on thermally cracked dunite samples saturated with CO_2 brines of varying compositions. The experiments involved hydrostatic compaction, followed by (axial) deformation at a constant rate of strain, while reactive brines flowed through the samples. Sample permeability was monitored during the experiments. Comparison of the samples' volume changes to their axial strains (shortening) during deformation suggests that samples reacted with CO_2-saturated brines can accommodate more shortening, before the onset of the dilation (swelling) that accompanies their eventual failure, than samples reacted with distilled water. Possible causes of this behavior are chemical reactions at grain boundaries that convert the original minerals into more compressible reaction products. Analyses of the samples with a scanning electron microprobe indicate, first, that etch pitting via dissolution is the primary mechanism that drives olivine mineralization and, second, that magnesite is the primary reaction product. Magnesite crystals deposited in fractures appear to act as a propping agent to keep the fractures open. Investigation of this phenomenon continued during the extension period with microtomography experiments to monitor, in real time, changes in pore space of olivine undergoing carbonation reactions and deformation. Analysis of the microtomography experiments is continuing and will be reported in a series of papers now in preparation. The microtomography experiments were carried out at the Advanced Photon Source X-ray research facility at Argonne National Laboratory.

In a related study undertaken by one of the principal investigators as a spin-off of the main project, a simple model of (magnesite) crystal growth in the pore space of basalts undergoing carbonation was developed. The model suggests that, under a carefully controlled program of CO_2 injection, carbonate

mineral growth can harden the rock formation against earthquakes that might otherwise be induced by the injection of large fluid volumes (Yarushina and Bercovici, 2013).

The overall conclusion of the study is that mineral carbonation of underground mafic and ultramafic rock formations is a viable candidate for long-term sequestration of man-made carbon dioxide. No results obtained during the project indicate that the method is inherently intractable in its implementation; moreover, there are enormous volumes of basalt near the Earth' surface that could serve as candidate locations for large-scale injection programs. The geochemical experiments do indicate, however, that there will be significant engineering challenges in maintaining high carbonation rates by delaying the onset of chemical conditions that promote formation of secondary silicate minerals and, therefore, slow down, or even reverse, the carbonation process.

Our current understanding of mineral carbonation of basalts suggest that an engineered process of mineral carbonation would require availability of rock formations with significant reactive surface area in the form of a connected network of natural, or artificially induced, fractures. The geomechanical experiments indicate, first, that the dissolution of olivine occurring during the initial stages of carbonation can provide pathways for fluid flow to help sustain the reaction, and, second, that carbonate minerals precipitated along existing fractures may serve as asperities—roughness on the surface of a crack that restricts its closure under deformation. It remains an open question as to whether these processes can be sustained for many years in an engineered system operating on a large scale—one capable of accommodating millions of tons of CO_2 annually in natural basalt formations near the Earth's surface.

Development of realistic theoretical models that can systematically describe the combined effects of reactive flow, precipitation and geomechanical deformation is a major barrier to further understanding of the practical viability of mineral carbonation as large-scale method of carbon sequestration.

Project Accomplishments

The major accomplishments of the project included the following:

- Compilation of a table of products and carbonation fractions for reaction-rate experiments on olivine powders and grains.
- Completion of geomechanical experiments involving thermally cracked dunite samples saturated with carbon dioxide brines of varying composition, with sample permeability monitored in situ.
- Development of a new method for producing synthetic olivine rock samples with controlled porosity by sintering of olivine powders.
- Design, development and installation of a new autoclave system to allow better control and monitoring of mineral carbonation reactions in the laboratory.

Publications

Four manuscripts containing the key results of the project work described in this final report are in preparation for submission to peer-reviewed journals:

[1] Liu, Q., Wang, Z., Zhang, S., Karato, S-I., Ague, J.J., Oristaglio, M.L., Johnson, K.T.M., Bolton, E., and Bercovici, D., 2015. The mineral carbonation potential of olivine for carbon sequestration. To be submitted to *American Journal of Science*.

[2] Lisabeth, H., Zhu, W., and Crispin, K., 2015. Reaction textures in actively carbonating olivine aggregates.

[3] Lisabeth, H., Zhu, W., and Kelemen, P., 2015. Reaction enhanced compaction in rapidly carbonating dunites.

[4] Zhu, W., Fusseis, F., Lisabeth, H., Xing, T., Xiao, X., and Karato, S., 2015. Cracking via mineral carbonation in olivine: Insights from in-situ microtomography.

In addition, six papers covering related research undertaken by the principal investigators as spin-offs of the project, partially supported by project funds, have been published in refereed journals:

[R1] Cai, Z., and Bercovici, D., 2013. Two-phase damage models of magma-fracturing, *Earth and Planetary Science Letters* **368**: 1–8.

[R2] Cai, Z., and Bercovici, D., 2014. Two-phase visco-elastic damage theory, with applications to subsurface fluid injection, *Geophys. J. Int.* **199**: 1481-1496, http://dx.doi.org/10.1093/gji/ggu344.

[R3] Tian, M., and Ague, J., 2014. The Impact of Porosity Waves on Crustal Reaction Progress and CO_2 Mass Transfer. *Earth and Planetary Science Letters* **390**: 80–92.

[R4] Fusseis, F., Steeb, H., Xiao, X., Zhu, W., Butler, I., Elphick, S., and Mäder, U., 2014. A low-cost X-ray transparent experimental cell for Synchrotron-based X-ray microtomography studies at geological reservoir conditions, *Journal of Synchrotron Radiation* **21**, 251-253, doi:10.1107/S1600577513026969.

[R5] Yarushina, V., and Bercovici, D., 2013. Mineral carbon sequestration and induced seismicity, *Geophysical Research Letters* **40**: 814-818, doi:10.1002/grl.50196.

[R6] Yarushina, V., Bercovici, D. and Oristaglio, M., 2013. Rock deformation models and fluid leak-off in hydraulic fracturing, *Geophys. J. Int.* **194** (3): 1514-1526.

Numerous talks and posters have been presented at conferences.

Integrated Experimental and Modeling Studies of Mineral Carbonation as a Mechanism for Permanent Carbon Sequestration in Mafic/Ultramafic Rocks

Final Scientific/Technical Report

INTRODUCTION

Mineral carbonation is the conversion of (fluid) carbon dioxide into (solid) carbonate minerals in rocks, by way of naturally occurring chemical reactions. This process, also called carbon mineralization, has been proposed as a highly secure method of sequestering man-made carbon dioxide (CO_2) from the atmosphere in attempts to mitigate climate change (Seifritz, 1990; Lackner et al., 1995). The rapid conversion of carbon dioxide into solid minerals underground, by an engineered carbonation process, would be more likely to avoid problems of fluid leakage than conventional methods of carbon sequestration that inject CO_2 in solution (or in supercritical form) into porous, permeable underground reservoirs, and rely mainly on the seal provided by impermeable rock above the reservoir ("caprock") to trap the fluid underground for long periods of time (IPCC, 2005).

The recent review by Power et al. (2013) describes a number of different methods of mineral carbonation that have been proposed and studied in the recent Earth science and engineering literature. The focus of the project described in this report is a form of sequestration called "in situ mineral carbonation," in which carbon dioxide in solution is injected underground to react with silicate minerals in mafic and ultramafic rocks. The terms "mafic" and "ultramafic" refer to rocks composed of silicate minerals with a high concentration of magnesium (Mg) and iron (Fe) atoms. An important example is the volcanic rock called basalt, which is among the most abundant rocks in the Earth's shallow crust.

The goal of the project covered by this report was to develop rigorous scientific methods for estimating the practical carbon sequestration potential of mafic and ultramafic rock formations readily accessible near the surface. There were two major scientific tasks of the project. The first was a series of laboratory geochemical experiments on minerals and rock assemblages to determine the reaction rates of

the key mineral carbonation reactions involving the mineral olivine. This work was done at Yale University, the main contractor for the project, in a laboratory at Yale West Campus that was specially outfitted for long-duration high-pressure and high-temperature experiments.

The second major scientific task of the project was a set of novel laboratory geomechanical experiments to elucidate the flow and deformation processes that accompany mineral carbonation and may limit the potential to carbonate large volumes of rock underground. This work was carried out in a laboratory at the University of Maryland College Park, under a subcontract to Yale University.

Part of each task was the development of modeling tools to understand the experimental results. Finally, a program of fieldwork and laboratory analysis was carried out in Hawai'i to collect samples of natural Hawaiian rocks, and to analyze their constituent silicate mineral phases. The results of this fieldwork, carried out by the University of Hawai'i under subcontract to Yale University, were intended to provide a basis for the design of field tests of mineral carbonation in a possible continuation of the project into a demonstration phase. (The proposal for a demonstration phase was not funded because of budget constraints.)

Although mineral carbonation reactions have been studied before in the laboratory (see the Introduction to Part I of this report), the work done here was (to our knowledge) the first systematic attempt to study these rates over long periods of time under conditions that are likely to apply in a system engineered on a large-enough scale for significant carbon sequestration. For example, the largest conventional carbon sequestration projects that are currently active, such as the one at Sleipner oil field in Norway (Boait et al., 2012; Global CCS Institute, 2015), inject about one million tons of CO_2 underground every year. Global CO_2 emissions into the atmosphere from human activity are estimated today to be about 38 billion tons per year, while the atmospheric concentration of CO_2 is increasing by about 2 parts per million (ppm) every year (Power et al. 2013). These figures highlight the scale of the challenge of carbon sequestration as a practical method of mitigating man-made climate change.

Report Organization

The organization of this report is as follows. There are two main parts devoted to the two major scientific tasks: Part I is a comprehensive report on the laboratory geochemical experiments designed to study reaction rates of carbonation experiments with olivine samples. Part II covers the full set of geomechanical experiments. Tables, Figure Captions, Figures, and References are provided separately for Parts I and II. Five Appendices cover complementary work carried out during the project:

- Appendix A describes the modeling and calibration studies performed to validate the results of the geochemical experiments. This modeling of the experiments described in Part I of the report was carried out with the public-domain geochemical modeling code EQ3/6 (Wolery, 2002).
- Appendix B describes a new method of creating synthetic rock samples with controlled porosity that was developed during the project.
- Appendix C describes the design of a new autoclave system developed at Yale University as part of the project.
- Appendix D describes the field samples collected in and their geochemical analyses.
- Appendix E provides a description and mathematical overview of several simulation codes developed during the project by combining reactive transport and deformation models for porous media.

Integrated Experimental and Modeling Studies of Mineral Carbonation as a Mechanism for Permanent Carbon Sequestration in Mafic/Ultramafic Rocks

Final Scientific/Technical Report

PART I GEOCHEMICAL EXPERIMENTS

1 Introduction

Mafic and ultramafic silicate rocks are promising candidates for mineral carbonation because of their abundance and accessibility near Earth's surface, and because of the energetic favorability of converting magnesium-iron silicates into magnesium-iron carbonates (Kelemen and Matter, 2008; Matter and Kelemen, 2009). For example, the simple net reaction for carbonation of the olivine mineral forsterite (Mg_2SiO_4),

$$Mg_2SiO_{4(s)} + 2CO_{2(aq)} \rightarrow 2MgCO_{3(s)} + 2SiO_{2(s)}, \quad (1)$$

is exothermic (releases heat), with a enthalpy change of about 89 J/mol under standard conditions (IPCC, 2005). In this reaction, forsterite reacts with carbon dioxide in aqueous solution to produce the minerals magnesite ($MgCO_3$) and quartz (SiO_2). The net reaction, as written above, leaves out many intermediate steps, including the key ones involving dissolution of olivine, releasing Mg^{2+} and Fe^{2+} ions into solution to combine with carbonate ions CO_3^{2-} and precipitate magnesite and siderite ($FeCO_3$). Natural carbonation of ultramafic rocks has been observed both at the surface and in the shallow subsurface in many different settings (Wilson et al., 2009; Kelemen et al., 2011). Moreover, the weathering of silicates by acidic rainwater and the eventual precipitation of carbonates in seawater is a key process in the long-term geochemical cycles that remove carbon dioxide from the atmosphere (Berner et al., 1983).

As a major constituent of mafic and ultramafic rocks, olivine dissolves rapidly at near-surface pressures and temperatures because the divalent ions (Mg^{2+} and Fe^{2+}) that connect silica tetrahedra (SiO_4^{4-}) in its mineral structure are easily replaced by hydrogen ions (H^+). The cations released into

solution can then readily combine with carbonate ions to form minerals such as magnesite and siderite. Previous studies have shown that carbonate solutions react significantly faster with olivine than with other magnesium-iron silicates such as clinopyroxene, plagioclase or serpentine (O'Connor et al., 2002; Giammar et al., 2005; Bearat et al., 2006; Dufaud et al., 2009; Garcia et al., 2010; King et al., 2010). High rates of carbonation were reported by Kelemen et al. (2011) in concentrated bicarbonate solutions at approximately 185°C and 150 bar (pCO_2).

These previous studies, however, have essentially simulated ex-situ olivine carbonation and sometimes used stirrers and sonicators to accelerate dissolution of olivine (Wolff-Boenisch et al., 2011; Bearat et al., 2006). Moreover, the dissolution and precipitation rates obtained from experiments to date apply for conditions far from chemical equilibrium that may not be sustained for long periods.

Hovelmann et al. (2012) and van Noort et al. (2013) conducted experiments to investigate the carbonation reaction of natural peridotite and to simulate in situ mineral carbonation processes. This work focused on the dissolution rate and on the evolution of microstructure and porosity during carbonation of a natural peridotite, but did not investigate systematically the variation of carbonation rate with solution chemistry or the possible formation of secondary minerals.

This report describes on a series of experiments reacting olivine grains and powders with CO_2-bearing fluid in a batch reactor in runs lasting between 1 to 14 days. We start in section 2 with a brief discussion of potential reaction pathways for the carbonation of olivine and define a quantity called the carbonation fraction to measure the overall efficiency of a reaction that proceeds for a specified time. In section 3, we describe the samples and conditions for the laboratory experiments, and the methods used to analyze the results, including methods used to determine the carbonation fraction in each run. Section 4 summarizes the results of 32 experiments varying the form of olivine (grains or powders of different sizes), the concentration of carbonate in solution, and the reaction time. In section 5 we return to the question of reaction pathways and describe our attempts to model the observations using the standard software package for geochemical modeling EQ3/6 (Wolery, 2002). The results highlight the need for more sophisticated geochemical models of mineral carbonation. We conclude in section 6 with a

discussion of the implications of our experiments and models for optimizing conditions that can lead to high carbonation fractions, an obvious requirement for the use of mineral carbonation as a practical method of carbon sequestration.

2 Mineral carbonation reactions

The olivine samples used in our experiments were nearly pure forsterite, with compositions $(Mg_{1-X}Fe_X)_2SiO_4$, where *X* is in the range (0.090, 0.095). For simplicity, this initial discussion focuses on the carbonation of pure forsterite, with the net equation (1) above. A simple pathway for carbonation involves the dissolution of olivine by hydrogen ions in solution, followed by precipitation of magnesite in reactions between magnesium and carbonate ions in solution:

(Forsterite dissolution) $$Mg_2SiO_4 + 4H^+ \rightarrow 2Mg^{2+} + SiO_{2(aq)} + 2H_2O \quad (2)$$

(Magnesite precipitation) $$Mg^{2+} + {CO_3}^{2-} \rightarrow MgCO_3. \quad (3)$$

With silica and magnesium ions in solution, however, other precipitation reactions are available, including pathways forming magnesium-bearing silicate minerals other than forsterite. Examples are the following reactions:

(Brucite) $$Mg^{2+} + 2H_2O \rightarrow Mg(OH)_2 + 2H^+ \quad (4)$$

(Talc) $$3Mg^{2+} + 4SiO_{2(aq)} + 4H_2O \rightarrow Mg_3Si_4O_{10}(OH)_2 + 6H^+ \quad (5)$$

(Chrysotile) $$3Mg^{2+} + 2SiO_{2(aq)} + 5H_2O \rightarrow Mg_3Si_2O_5(OH)_4 + 6H^+ \quad (6)$$

(Antigorite) $$48Mg^{2+} + 34SiO_{2(aq)} + 79H_2O \rightarrow Mg_{48}Si_{34}O_{85}(OH)_{62} + 96H^+ \quad (7)$$

These latter reactions can be combined in ways that consume magnesite. For example, a net equation involving magnesite, talc, silicic acid and dissolved carbon dioxide is

$$3MgCO_3 + 4H_4SiO_{4(aq)} + 4H_2O = Mg_3Si_4O_{10}(OH)_2 + 3CO_{2(aq)} + 7H_2O. \quad (8)$$

Similar net equations can be written for brucite, chrysotile and antigorite.

Results from our long-duration batch experiments with forsterite show evidence for the formation of secondary silicate minerals that have consumed magnesite after its initial precipitation in the carbonation reactions (2–3). Because of the small quantities involved, however, we have not been able to identify the specific secondary minerals produced. We return to this discussion in section 5.

2.1 Carbonation fraction

We use a quantity called the carbonation fraction to measure the overall extent of olivine carbonation in the experiments. The carbonation fraction is defined as the net change during the experiment in the amount of dissolved inorganic carbon (DIC) in the reacting solution, normalized by the amount of divalent cations that would have been available for carbonation if all of the olivine present had fully dissolved. For convenience, the fraction can be expressed in terms of molar concentrations. For example, in a reaction with pure forsterite, the carbonation fraction at time T is given by

$$\text{Carbonation Fraction} = \frac{\Delta_T[\text{DIC}]}{[\text{Mg}^{2+}]_c} = \frac{\Delta_T[\text{CO}_2] + \Delta_T[\text{HCO}_3{}^-] + \Delta_T[\text{CO}_3{}^{2-}]}{[\text{Mg}^{2+}]_c}. \quad (9)$$

Here, $\Delta_T[\,\cdot\,] = [\,\cdot\,]_T - [\,\cdot\,]_0$ indicates the measured change at time T from the initial concentration and $[\,\cdot\,]_c$ indicates a calculated concentration—in this case the concentration of magnesium ions in solution that would result from full dissolution of pure forsterite starting material of a given weight. The carbonation fraction defined in this way is a net quantity that is not sensitive to intermediate steps in the reaction and can range from 0 (no net removal of carbon from solution) to 1 (full dissolution of olivine and conversion of all of its cations to carbonates). The next section describes the full experimental procedure, along with the methods used to determine the carbonation fraction accurately.

3 Experimental Methods and Samples

3.1 Samples

We used gem quality olivine grains (Figure 1a) from Brazil and powders crushed from San Carlos olivine samples in our experiments. The grains, which each weighted between 0.17 and 0.22 g, had the composition of $Fo_{90.5}$—that is, $(Mg_{0.905}Fe_{0.095})_2SiO_4$—as determined by Hyperprobe (JEOL JXA-8530 F) at Yale University; there was little inter- or intra-granular variation in their major element compositions. These values are consistent with previous studies (Pokrovsky and Schott, 2000). The geometric surface area of the grains was estimated to be about 4.5 cm^2/g, varying by up to 10% among samples. The San Carlos olivines had the composition of $Fo_{91.0}$. Powders were made by first crushing the samples, followed by handpicking, cleaning, and grinding in an agate Planetary Mono Mill (Fritsch Pulverisette 6). Two batches of the olivine powders were used for this study: Batch-A olivine powder with grain sizes less than 30 μm and a bimodal size distribution peaking at about 1.8 μm and 13.5 μm (measured by Mastersizer 2000 at Yale University), and Batch-B olivine powders with a roughly Gaussian grain-size distribution that peaks at about 50 μm (Figure 1c) and has a standard deviation of about 20 μm. Geometric surface areas estimated by assuming spheres in the measured size distributions were approximately 3970 cm^2/g and 594 cm^2/g for Batch-A and Batch-B olivine powders, respectively.

The reactive surface areas of all samples were also measured using a Quantachrome Autosorb-iQ at Yale University using the seven-point BET krypton method (Brunauer et al., 1938). Batch A and B powders yielded BET surface areas of approximately 707,000 cm^2/g and 4,300 cm^2/g, respectively, whereas the olivine grains yielded BET surface areas of about 42.3 cm^2/g. The typical uncertainty of the BET measurement is less than 10% (2σ). There are clearly large differences between the geometric surface area calculated for the powders by assuming spherical grains and the measured BET surface areas.

3.2 Experimental setup and analysis of reaction products

In an experiment, either one large olivine grain (0.17 to 0.22 g) or approximately 40 mg of olivine powder was sealed in a gold capsule with 0.5 to 1.0 ml of $NaHCO_3$ solution. The solutions ranged in

concentration from about 0.25 to 3 molal (*m*, mol/kg H_2O). Dissolved inorganic carbon in the starting solution was measured by titration using a Thermo DL15 titrator. The gold capsules (Figure 1b), approximately 1.2 ml in size for grain experiments and 0.7 ml for powder experiments, were sealed using a Lampert® precision welder and were weighed accurately. At the start of each run, several gold capsules were placed in an autoclave pressurized by argon gas and heated externally. All of the experiments were carried out at 200 (± 3)°C and 150 (± 2) bar.

The experiments lasted between 1 to 14 days. At the end of each run, capsules were quenched in water, reaching room temperature within less than two minutes, and were weighed to check for leakage. Fluids and solids in capsules without any leakage were collected (only a handful of samples had to be rejected because of obvious leaks). The fluids were centrifuged and separated from solids; the solids were washed with Milli-Q water and ethanol, to eliminate solid $NaHCO_3$ possibly deposited during quenching, and were dried in a clean room.

Solutions with $NaHCO_3$ concentrations higher than 1 *m* required special treatment. To achieve these high concentrations, enough solid $NaHCO_3$ was added to the capsule to make a solution of the desired concentration at 200°C. The solubility of $NaHCO_3$ is about 2.8 mol/L at 100°C (Lide, 2003), and our modeling results indicate that up to 4.5 mol of dissolved inorganic carbon can be present in 1 kg of water at 200°C (see Figure A4 in Appendix). After opening the gold capsules from these high-concentration experiments, a specific quantity of Milli-Q water was added to dilute the solution to approximately 1 *m* to prevent precipitation of $NaHCO_3$ at room temperature. As controls for each batch of experiment, we placed gold capsules containing only $NaHCO_3$ solutions into the autoclave along with the capsules containing olivine. These standards were treated as normal samples and used to monitor systematic errors in handling (see Appendix).

The reaction products were analyzed as follows. For the solution, dissolved inorganic carbon was measured by titration using a Thermo DL15 titrator, and elemental concentrations were determined by inductively coupled plasma mass spectrometry (ICP-MS), using an Element-XR™ instrument at Yale.

Repeated measurements of standard solutions (BHVO-2 samples from USGS) with this instrument gave a better than 5% uncertainty (2σ).

To analyze solid products, selected samples from the experiments with olivine grains were mounted in epoxy, cut open and polished by aluminum oxide in mineral oil, and cleaned with soap water and ethanol. Polished cross sections were imaged by scanning electron microscopy (SEM) and energy-dispersive X-ray spectroscopy. Elemental maps of cross sections were created with a JEOL JXA-8530F HyperProbe Electron Probe Microanalyzer at Yale. The solid products in experiments with olivine powders were analyzed using the powder X-ray diffraction method with a Bruker D8-Focus P-XRD at Yale. In most samples, XRD analysis could detect the presence of the mineral magnesite, but signals were too week to identify specific secondary silicate minerals, probably because of the small quantity of reaction products generated during each experiment. SEM images do, however, provide conclusive evidence of secondary reaction products in addition to magnesite (Section 4.2).

3.3 Determination of the carbonation fraction

For most runs, the carbonation fraction was determined from equation (9) and measurements of the change in dissolved inorganic carbon in the reacting solution. The concentrations before and after an experiment (the numerator) were obtained by titration, with the equivalence volume determined by a Gran plot. The moles of divalent cations available for carbonation (the denominator) were determined from the weight and composition of the olivine sample. Gold capsules containing only reacting solution were used as standards in all experimental runs. Titration of these standards showed that some dissolved carbon was lost during handling, probably during welding and opening of capsules and during titration. Measurements showed that this loss of carbon from handling was about 0.047 ± 0.015 mol/kg (of solution) and did not correlate with the length of experiments or the concentration of the reacting solution at experimental conditions. Thus, the measured value of carbon lost from the standard in each run was used to correct the numerator in equation (9). For 40 mg of olivine in 1 ml of reacting solution, an uncertainty of ±0.015 mol/kg in carbon accounting translates to an uncertainty of ±0.026 in the calculated

carbonation fraction. Appendix A.2 contains a full discussion of methods used to control different sources of error in determining the carbonation fraction by titration.

To check on the accuracy of determining the carbonation fraction by titration, the amounts of carbonate produced in runs with some olivine powder samples were determined by combustion. In this method, a 1 mg aliquot of olivine powder after reaction is thermally decomposed in a resistance furnace at about 800ºC, and an elemental analyzer measures the amount of CO_2 released. Repeated measurements of a standard showed that the precision of the combustion method leads to an uncertainty in the carbonation fraction of about ±0.005 (2σ) for a 40 mg sample. Figure 2 shows that carbonation fractions determined by titration generally agree with those determined by combustion within the uncertainty. Since the combustion method requires crushed powder samples and involves their destruction, we used the titration method for consistency between experiments with olivine powders and olivine grains, with one exception.

Runs lasting 1 and 3 days with olivine grains and 1 *m* $NaHCO_3$ solution had before-to-after differences in dissolved inorganic carbon that could not be measured by titration. We therefore used an indirect method to estimate the change in dissolved carbon for these experiments. For pure forsterite starting material, if no secondary silicate minerals or SiO_2 precipitates during reaction, then the silica in solution is a proxy for the amount of olivine dissolved and the Mg^{2+} ions in solution represent the net result of olivine dissolution and magnesite precipitation. Thus, the carbonation fraction can be estimated with the following equation:

$$\text{Carbonation Fraction} = \frac{\left(2m_{\text{Si}} - m_{\text{Mg}^{2+}}\right) \cdot W_{\text{solution}}}{2\ \text{mol(olivine)}}, \tag{10}$$

where m_{Si} and $m_{\text{Mg}^{2+}}$ are the molalities of total Si and Mg^{2+} in solution, respectively; W_{solution} is the weight of the solution; and mol(olivine) is the number of moles of olivine in the original sample. This indirect method was used to estimate the low carbonation fractions (less than 0.003) resulting from experiments reacting 1 *m* $NaHCO_3$ solution with olivine grains, which are the least likely to precipitate secondary silicates. For high carbonation fractions, the values calculated by this method also matched

those obtained by titration, provided that no minerals other than magnesite were produced in significant quantities (Table 2).

4 Experimental results

This section summarizes the experimental results, which are compiled in Table 1. Figure 3 shows the carbonation fractions in 4 series of runs in which olivine grains or olivine powders (Batch A) were reacted with 1 *m* or 3 *m* sodium bicarbonate solution. Each experimental series—for example, an olivine grain reacting with 1 *m* solution—has runs lasting 1, 3, 5 and 14 days. The general observation is that the carbonation fraction does not increase monotonically with time in these (unassisted) batch reactions. In fact, in 3 of the 4 series the carbonation fraction was stable within the analytical uncertainty after only 1 day of reaction. Even in the exceptional case—olivine powder reacting with 3 *m* solution—the carbonation fraction rises from 0.42 after 1 day to 0.52 after 3 days, is essentially stable at 0.50 at 5 days, and falls back to 0.42 at 14 days. Nevertheless, rates of carbonation at 40% or higher in these unassisted batch reactions with olivine powders are impressive.

In the series reacting an olivine grain with 3 *m* solution, the carbonation fraction rises from 0.0047 at 1 and 3 days to 0.020 at 5 days, but then falls back to zero at 14 days. Although these low values determined by titration are all within the 2σ uncertainty of zero net carbonation, there is strong visual evidence in the SEM images that carbonation did increase initially in these runs. For example, the SEM images in Figure 7 (right panels) show magnesite crystals growing on an olivine grain exposed to 3 *m* solution after 1 day of reaction, and the coverage clearly increases from day 1 to day 5. By day 14, however, the entire grain surface appears covered with secondary minerals. For a grain exposed to 1 *m* solution (left panels), the SEM images indicate that the amount of magnesite increases only marginally from day 1 to day 14. (See Section 4.2 for a further discussion of the SEM images.)

The bottom panel of Figure 4 shows that the variation of the carbonation fraction with the initial concentration of the reacting solution is essentially linear for Batch-A powders reaching with $NaHCO_3$ with initial concentrations in the range from 0.25 to 3 *m*. Such a linear variation is expected from kinetic

arguments (see Appendix A.3). Figure 5 shows that this linear variation also holds for Batch-B powders reacted with either obtained with either $NaHCO_3$ or $KHCO_3$ solutions under similar conditions. Straight-line fits to these plots have R^2 values greater than or equal to 0.98.

The effect of grain size, or reactive surface area, is obvious in the data. Under equivalent conditions, the carbonation fractions obtained with Batch-A powders, with an average grain size of about 30 μm and BET surface area of $7 \cdot 10^5$ cm^2/g, are about 2 to 3 times higher than the fractions obtained with Batch-B powders, with an average grain size of about 50 μm and BET surface area of 4300 cm^2/g, and at least 10 times higher than the fractions obtained with a single large olivine grains with BET surface area of 42.3 cm^2/g.

4.1 Dissolved elemental concentrations

Figure 6 shows that the concentrations of Mg, Fe and Si in solution generally vary by less than order of magnitude after 1 day of reaction. (All of these concentrations must of course increase significantly during the first day of reaction, from zero concentration in the starting solution.). For example, in the series reacting an olivine grain with 3 *m* $NaHCO_3$, the Mg concentration went from 152 ppm (day 1) to 174 ppm (day 3), 108 ppm (day 5), and 347 ppm (day 14). The Si concentration in this same series varied between 50 ppm (day 1) to 94 ppm (day 5). The Fe concentration showed the largest variation, from 3.5 ppm (day 1) to 11.6 ppm (day 5). Elemental concentrations measured in final solutions were within a few ppm in repeated experiments.

As with the carbonation fraction, elemental concentrations measured in solution after experiments of a fixed duration varied in a relatively simple way with the initial concentration of the reacting fluid. In the collection of 3-day experiments shown in the top panel of Figure 4, for example, Si and Fe concentrations increased monotonically as the concentration of the starting solution increased, whereas the Mg concentration initially decreased as the concentration increased from 0.25 to 1 *m*, then increased by nearly an order of magnitude as the starting solution went from 1 to 3 *m* $NaHCO_3$.

4.2 SEM images

The SEM images of olivine grains after reaction (Figure 7) show the following conspicuous features. First, as the carbonation reaction proceeded, the number and size of magnesite crystals increased until the olivine grain was covered by magnesite. In experiments with 3 *m* bicarbonate solutions, magnesite covered a single olivine crystal after 3 days of reaction, whereas with 1 *m* solutions, magnesite crystals appeared only sporadically on the surface of a single grain even after 14 days of reaction. Second, large amounts of secondary magnesium-silicate minerals covered the surface of olivine grains exposed to 3 *m* bicarbonate solutions for 14 days.

Elemental maps generated from electron microprobe scans of cross-sections of single olivine grains offer more insights into the reactions. Figure 8 shows that, after 1 day of exposure to 3 *m* bicarbonate solution, the surface of an olivine grain becomes serrated by dissolution and magnesite crystals (with trace amounts of Fe) appear in the gaps. After exposure for 3 days, the serrations become longer and sharper, and larger magnesite crystals appears in the gaps. This observation indicates that fluid access to the olivine surface was still present, and the apparent armoring did not stop olivine dissolution. Some teeth in the serrations lose connection to the original olivine grain surface between 3 and 5 days, leaving needle-shaped olivine domains within the growing magnesite layer. By day 14, most of the angular magnesite crystals have decomposed into less regularly shaped ("fluffy") minerals (Figures 7). Although it was not possible to identify these fluffy minerals precisely, elemental maps indicate silicates, possibly talc or antigorite (see Section 5).

The elemental maps are consistent with chemical compositions of the final solutions. For example, in experiments with olivine grains and 3 *m* bicarbonate solutions, the increase in Mg, Si and Fe concentrations in solution after 1-day and 3-day experiments suggests that dissolution of olivine and precipitation of magnesite were the major reactions. During this period, the ratio of Mg to Si remains below 1.8—the stoichiometric ratio in olivine—which is consistent with the formation of magnesite and the increase in the carbonation fraction. Between 3 and 5 days, however, there is a significant decrease in the elemental concentration of Mg, the Mg/Si ratio and the carbonation fraction; in addition, the elemental

concentrations of Si and Fe increase as a slower rate. These trends are consistent with a reduction in the rates of dissolution of olivine and precipitation of magnesite, as indicated by the measured carbonation fractions in Figure 3. Finally, between 5 and 14 days, there is a significant increase in the concentration of Mg in solution and in the Mg/Si ratio, accompanied by decreases in the concentration of Si and Fe. These last trends are consistent with the formation of secondary magnesium silicates such as talc (Mg/Si ratio of 0.75), chrysotile (1.50) and antigorite (1.41).

These results for olivine grains can be contrasted with results for olivine powders with much larger reactive surface area. Experiments with 3 *m* bicarbonate solutions and olivine powders show only small changes in concentrations of Mg, Si and Fe, and in the Mg/Si ratio and the carbonation fraction between experiments lasting 1 day and 3 days (Figure 6). This suggests that the carbonation reactions occurred largely within the first day of exposure to the reacting solution. In these runs, the Mg/Si molar ratio is 3.6, much higher than the stoichiometric olivine ratio—indicating substantial secondary mineral precipitation. In the period between 3 and 5 days for powder experiments, there is a slight decrease in the concentration of Mg and in the Mg/Si ratio, accompanied by an increase in the concentration of Si—indicating that precipitation of magnesite continued. In the period between 5 and 14 days, when the measured carbonation fraction drops (Figure 3), there is a decrease in the concentration of Si, which is accompanied by an increase in the concentration of Mg and Fe and in the Mg/Si ratio. As in the experiments with olivine grains, these last trends suggest the formation of secondary magnesium silicates at the expense of magnesite.

4.3 Effect of the fluid/mineral ratio

We conducted two experiments—L1 and L2 in Table 1—to test if the amount of fluid in the reaction vessel is a factor independent of its dissolved carbon. In these experiments, an amount of $NaHCO_3$ that mixed with 1 ml of water would give 3 *m* solution was mixed with only 0.17 ml of water, and was reacted with olivine grains weighing 0.19 and 0.18 in runs lasting 1 and 7 days, respectively. The amount of $NaHCO_3$ in each capsule is thus identical to the amount present using 1 ml of 3 *m* $NaHCO_3$. (If all of the

$NaHCO_3$ had dissolved in the water, the resulting solution would be approximately 17 *m* $NaHCO_3$. Calculation using EQ3/6 suggest, however, that the actual concentration of $NaHCO_3$ under the reaction conditions of 200°C and 150 bar is probably closer to 3.8 *m* based on dissolved Na^+, and the concentration of dissolved inorganic carbon is about 4.5 *m.* See Appendix for a more detailed discussion.) SEM observations suggest that the carbonation rates were much faster in these experiments than in the ones with larger fluid-to-rock ratios. For example, the olivine grain is already fully covered with magnesite in the 1-day experiment (Figure 9), similar to five-day olivine-grain experiments with high fluid-to-solid ratios. This result is consistent with the expectation from kinetic arguments that the initial carbonation rate should increase linearly with the initial concentration of carbonate in solution. Nevertheless, when there is only olivine and $NaHCO_3$ powder in the vessel, no magnesite is formed in a 14-day experiment.

5 Modeling carbonations reactions

We used the geochemical modeling program EQ3/6 (Wolery, 2002) to simulate carbonation reactions comparable to our experiments. The SEM images suggest that at least the following reactions should be relevant to the batch experiments:

$$(\mathrm{Mg}_{1-X}\mathrm{Fe}_X)_2\mathrm{SiO}_4 + 4\mathrm{H}^+ \rightleftharpoons 2(1-X)\mathrm{Mg}^{2+} + (2X)\mathrm{Fe}^{2+} + \mathrm{H}_4\mathrm{SiO}_4, \quad (11)$$

$$\mathrm{Mg}^{2+} + \mathrm{CO}^{3-} \rightleftharpoons \mathrm{MgCO}_3, \quad (12)$$

$$3\mathrm{MgCO}_3 + 4\mathrm{H}_4\mathrm{SiO}_4 \rightleftharpoons \mathrm{Mg}_3\mathrm{Si}_4\mathrm{O}_{10}(\mathrm{OH})_2\ (talc) + \ 3\mathrm{CO}_{2(aq)} + \ 7\mathrm{H}_2\mathrm{O}, \quad (13)$$

$$3\mathrm{MgCO}_3 + 2\mathrm{H}_4\mathrm{SiO}_4 \rightleftharpoons \mathrm{Mg}_3\mathrm{Si}_2\mathrm{O}_5(\mathrm{OH})_4\ (chrysotile) + \ 3\mathrm{CO}_{2(aq)} + \ 2\mathrm{H}_2\mathrm{O}, \quad (14)$$

$$48\mathrm{MgCO}_3 + 34\mathrm{H}_4\mathrm{SiO}_4 \rightleftharpoons \mathrm{Mg}_{48}\mathrm{Si}_{34}\mathrm{O}_{85}(\mathrm{OH})_{62}\ (antigorite) + \ 48\mathrm{CO}_{2(aq)} + \ 37\mathrm{H}_2\mathrm{O}, \quad (15)$$

where $X = \{0.095, 0.090\}$ for olivine grains and powders, respectively. The first two reactions represent the basic olivine carbonation mechanism. Equations (13) through (15) are net reactions to form talc, chrysotile and antigorite from magnesite precipitated by the first two reactions. The standard thermodynamic databases available for use with EQ3/6 do not easily allow modeling of reactions (13–15)

directly. Instead the following two net reactions are available for producing magnesite and secondary magnesium silicates directly from forsterite,

$$4Mg_2SiO_4 + 5HCO_3^- + H_2O \rightarrow Mg_3Si_4O_{10}(OH)_2(talc) + 5MgCO_3 + 5OH^-, \quad (13a)$$

$$34Mg_2SiO_4 + 20HCO_3^- + 31H_2O \rightarrow Mg_{48}Si_{34}O_{85}(OH)_{62}(antigorite) + 20MgCO_3 + 20OH^-, \quad (14a)$$

along with the following reaction for conversion of talc to antigorite,

$$16Mg_3Si_4O_{10}(OH)_2(talc) + 15H_2O \rightarrow Mg_{48}Si_{34}O_{85}(OH)_{62}(antigorite) + 30SiO_{2(aq)}. \quad (15a)$$

We carried out a series of simulations within EQ3/6 for these reactions, to understand better possible reaction pathways under different conditions. The Appendix contains a full description of these simulations. In this section, we focus on the simulation for the reaction of 3 *m* $NaHCO_3$ solution with olivine grains and powder and compare the results to the experimental runs for these cases, which showed the most variation over time in the carbonation fraction. To simulate an olivine grain, the reactive surface area was set at a low value 2.3 cm^2/g; for olivine powder, at a high value, 1340 cm^2/g. The actual masses of starting olivine mineral and solution were used in the simulations. Reactions were run at 200°C and 15.5 bar, because EQ3/6 is limited to simulations along the water boiling curve. The thermodynamic parameters do not change dramatically with pressure, so these conditions should be comparable with those of the experiments.

The bottom panel of Figure 10 shows the reaction path predicted by EQ3/6 for the reactions (11, 12, 13a, 14a, 15a) when 3 *m* bicarbonate solution is reacted with an olivine grain. The results are presented in activity coordinates, $a_{Mg^{2+}}$, a_{H^+}, and $a_{SiO_2(aq)}$, with the activity ratio $\log(a_{Mg^{2+}}/a_{H^+}^2)$ plotted versus $\log a_{SiO_2(aq)}$. These coordinates are commonly used to describe carbonation reactions (Marini, 2007). As explained in the Appendix, the labeled lines on this plot represent mineral-solution equilibrium boundaries for the different minerals in the two-dimensional space spanned by the coordinates, with all other activities held fixed. Modeling calculations indicate that there is little variation of water activity, but some reduction of the bicarbonate ion activity, from changes in pH and dissolved

inorganic carbon over the course of the simulated reaction. Because of this, the position of the magnesite equilibrium line—which is fixed by the pH and carbonate activity—changes as the simulation evolves, whereas the other lines stay fixed.

According to the simulations, olivine dissolves along the marked line until Mg^{2+} and CO_3^{2-} in solution reach the equilibrium saturation line for magnesite, where the mineral starts to precipitate. As magnesite precipitates, the ratio $\left(a_{\mathrm{Mg^{2+}}}/a_{\mathrm{H^{+}}}^2\right)$ stays nearly constant], but $a_{\mathrm{SiO_2}(aq)}$ continues to increase because olivine is still dissolving. When the reaction path reaches the saturation line for talc, it proceeds to the left up talc-solution equilibrium line, precipitating talc and magnesite simultaneously (13a). Along this line $a_{\mathrm{SiO_2}(aq)}$ decreases (silica precipitates as talc), but the $a_{\mathrm{Mg^{2+}}}/a_{\mathrm{H^{+}}}^2$ increases. By day 3, the simulated reaction reaches the antigorite-solution equilibrium line and forms both antigorite and magnesite, from dissolving forsterite (reaction 14a), and from conversion of talc to antigorite (reaction 15a) until the simulation ends on day 14.

The top panel of Figure 10 shows the distribution of Mg in different minerals produced along the reaction path in the top panel. Aside from its prediction of specific secondary silicate minerals—initially talc, with only antigorite remaining by day 14—the simulation indicates that magnesite continues to form for the duration of the run. Figure 11 shows the evolution of the carbonation fraction and pH for the simulations and for the comparable experiments. The two sets agree up to day 5, but diverge for day 14, where the experiments show nearly a complete reversal of the carbonation fraction, accompanied by a drop in pH. From the SEM images, we interpret this reversal as caused by precipitation of secondary silicate minerals, replacing magnesite on the olivine grain surface. As mentioned, such reactions cannot be included in the EQ3/6 model in its current form.

There is a similar discrepancy between the experiments and simulations for 3 *m* bicarbonate solution reacting with olivine powder. In these simulations, powder is modeled by increasing the reactive surface area of the sample significantly, while keeping its mass low. In this case, shown by the gray circle in the reaction path diagram (bottom panel of Figure 10), EQ3/6 predicts that the reactants quickly reach

an equilibrium point, with all forsterite dissolved and the solution in equilibrium with precipitated magnesite, antigorite and talc (top panel). This happens by day 1, with no further changes through day 14. The simulated carbonation fraction saturates at 0.475: all olivine has been dissolved, but less than half of the Mg^{2+} released has precipitated as magnesite that removes carbonate ions CO_3^{2-} from solution. The rest of the magnesium has precipitated in secondary silicate minerals. In contrast, the experiments with 3 m solution and Batch-A olivine powder show that magnesite continues to precipitate only through day 3, with the carbonation fraction reaching about 0.52. The carbonation fraction then reverses gently to about 0.43 by day 14, indicating that some magnesite has dissolved. Note that this decrease of the carbonation fraction by 14 is well outside the estimated experimental error.

6 Discussion: Optimizing olivine carbonation

In our sealed batch experiments, the carbonation fraction reached a maximum value after a certain period of time, then remained essentially constant or decreased—that is, carbonation eventually either ceased, or reversed with magnesite dissolving to release carbon back into solution. The time required to reach a maximum carbonation fraction for a given reaction series was shorter for experiments using olivine powders than for olivine grains, with other factors held constant, and shorter for solutions with higher molar concentrations of sodium bicarbonate for solutions with lower concentrations, with other factors held constant. Figure 12 summarizes these basic observations from the experimental runs.

As discussed in earlier sections, we believe that the formation of secondary silicate minerals consuming magnesite limits the progress of carbonation seen in these batch experiments. The reasons are as follows: First, most of the reacting solutions contained enough carbonate ions to transform all of the olivine present into magnesite. For example, the number of divalent ions $\{Mg^{2+}, Fe^{2+}\}$ available for carbonation was 0.40 to 0.58 mmol (10^{-3} mol) in the experiments with olivine powders, which would have required only 0.13 to 0.19 ml of 3 *m* sodium bicarbonate solution, or 0.4 to 0.58 ml of 1 *m* solution, to achieve full carbonation (carbonation fraction of 1). There was 0.5 ml of solution present for all of these experiments, but the maximum carbonation fraction observed was only 0.519 (for 3 *m* solution

reacting with olivine powder). Second, the SEM images and elemental maps of olivine grains, superficially coated with magnesite, still show empty spaces between magnesite and olivine, indicating that reactive surface area for olivine dissolution and further carbonation, though significantly reduced, was still present. Finally, attainment of the maximum carbonation fraction in each experimental series coincides with the maximum elemental Si concentration in solution, suggesting that maximum carbonation is correlated with the start of precipitation of secondary silicate minerals that remove silicon from solution.

If this model is correct, then it is possible to estimate the upper limit of carbonation in any experiment as follows: Assume that all elemental Si from full dissolution of olivine is eventually consumed in formation of secondary silicate minerals. These secondary silicates in turn consume a fixed amount of Mg cations from the amount released by olivine, and the remaining cations form magnesite. For example, if no siderite ($FeCO_3$) is formed, and if the valance charge of Fe is dominantly 3+, this model predicts that the maximum carbonation fraction would be approximately as follows: 0.525 for formation of pure talc from all elemental silicon released by dissolution of olivine, 0.150 for the formation of pure chrysotile, 0.194 for the formation of pure antigorite, and 0.304 for formation of a mixture of talc and antigorite with molar ratio of 1:2 (Figure 13). This is a conservative estimate of the maximum carbonation fraction, because it ignores residual dissolved SiO_2 in the final solution (which in any case appears to be relatively low in these experiments). The limits on the maximum carbonation fraction increase by up to 10% if Fe is predominantly 2+ and occupies the same site as Mg in the carbonate and secondary silicates formed. Moreover, the carbonation fraction can increase significantly if SiO_2 precipitates out of solution and removes the starting material for secondary silicates.

The maximum carbonation fraction in all our experiments was 0.519 (experiments 156, 161 with Batch-A olivine powders), and no SiO_2 was present in the solid-phase products of these runs. The model described above then implies that talc should be the primary secondary silicate mineral present in experiments 156 and 161. The formation of small amounts of serpentine, chrysotile or antigorite,

however, cannot be ruled out in other experiments, particularly experiment 165 (14 day and 3 *m* $NaHCO_3$), which has a lower carbonation fraction.

6.1 Raising the carbonation fraction by suppressing secondary silicate minerals

Silicon, either as aqueous SiO_2 or H_4SiO_4 in solution, is essential to the formation of secondary silicates that can limit carbonation. Precipitation of SiO_2 from the reacting solution should therefore raise the carbonation fraction of olivine. This holds even if reactions (13a) and (14a) proceed and the secondary silicates do not consume magnesite. Consider the phase diagram in activity coordinates shown in Figure 10, if the reaction path along the magnesite-solution equilibrium curve first meets the quartz-solution equilibrium line, then only amorphous silica and magnesite precipitate and the carbonation fraction will continue to increase. One way to test this model experimentally is to (artificially) increase the amount of Si precipitated as SiO_2. This can be achieved by several methods. For example, as shown in the Appendix, a reduction of reaction temperature would raise the equilibrium lines for the secondary silicates (antigorite and talc in the bottom panel of Figure 10), compared to the magnesite equilibrium line. Another way to raise the equilibrium lines for secondary silicate minerals, compared to the magnesite line, is to reduce water activity. A third way is to maintain a high concentration of HCO_3^- and relatively low pH: when pH is low, the dissolution rate of olivine will be high and the magnesite-solution equilibrium curve moves downward in the activity diagram. Conversely, as the HCO_3^- concentration falls (magnetic precipitates), the pH value is hard to maintain and the magnesite equilibrium line moves upward and eventually hits an equilibrium line where secondary silicates start to precipitate.

Reducing reaction temperature may suppress the formation of secondary silicates during carbonation, but it also reduces the carbonation reaction rate. By contrast, reducing the ratio of fluid to solid increases the concentration of the silicon ions in solution (for a given amount of olivine dissolved) and reduces the activity of water (Figure A4 in Appendix A). These conditions promote early precipitation of SiO_2, instead of secondary silicates, through the reaction:

$$H_2SiO_4 \rightarrow 2H_2O + SiO_{2(am)}.$$

These observations are consistent qualitatively with our experiments L1 and L2, exposing olivine grains to a small amount of fluid. The (mass) ratio of fluid to rock was approximately 1:1 in these experiments compared to 7:1 for all other experiments. SEM images of the experimental results show nearly complete coverage of the olivine grain by magnesite crystals after just one day (Figures 9a through c). Moreover, the interface between magnesite and olivine is smoother than in the experiments with larger amounts of solution (compare Figures 7 and 9): there are no residual olivine teeth at the interface, and the magnesite crystals are much larger—about 100 μm wide compared to 30 to 50 μm in other experiments. Unfortunately, the carbonation fractions could not be measured accurately by titration after these experiments because of the small volumes of the remaining solutions. Nevertheless, the reaction products from these experiments visually indicate a much faster carbonation reaction. In addition, only magnesite and amorphous silica spheres are visible on the surface of olivine or in the interior of magnesite crystals (Figures 9c); no talc or serpentine appears to be present; and after 7 days, a silica mesh-layer is visible (Figure 9d).

These observations suggest the following model for the carbonation process in experiments with low fluid-to-olivine ratios: First, a small amount of olivine dissolves, releasing magnesium ions that react with carbonate ions in solution to form magnesite. Because of the low water activity, the solution quickly becomes supersaturated with respect to H_2SiO_4 created by olivine dissolution (see Figure A4 in the Appendix). A silica gel in the form of spherical amorphous silica grains precipitates (equation 17), increasing the water activity and allowing more $NaHCO_3$ to dissolve. The solution continues to dissolve olivine, and quickly forms more magnesite crystals. In this model, equations (10) through (12) are effectively replaced by the simplest net carbonation reaction for olivine because of the fast precipitation of amorphous silica in the intermediate step:

$$Mg_2SiO_4(olivine) + 2CO_{2(aq)} \rightarrow 2MgCO_3(magnesite) + SiO_{2(am)}.$$

This is not an elementary reaction because the presence of water is essential: when only $NaHCO_3$ powder and olivine grain are present, there is no evidence of magnesite formation even after 14 days at high temperature and pressure.

The experiments with low volumes of solution are consistent with previous studies reported in the literature. For example, the highest carbonation efficiencies reported by Garcia et al. (2010) occurred a fluid-to-solid ratio approximately equal to 1. Andreani et al. (2009) suggested that carbonate formation in natural peridotite is favored in domains with reduced water flow. Klein and Garrido (2011) indicated that the complete carbonation of a serpentine occurred at small fluid-to-rock ratios, and that prolonged fluid influx resulted in de-carbonation and solidification.

Precipitation of SiO_2 during carbonation reactions has been observed in previous studies, but its role in mineral carbonation reactions is still debated. Some studies have suggested that precipitation of a layer of silica coating the olivine surface will reduce the olivine dissolution rate and inhibit carbonation (Bearat et al., 2006; Daval et al., 2011). Others have seen little passivation effect of silica precipitation on overall carbonation rates (e.g., Daval et al., 2009). Our SEM images and the model described above suggest that these two views do not necessarily conflict: SiO_2 precipitation that reduces the reactive surface area of olivine will obviously slow the carbonation reaction. But it can also increase the maximum achievable carbonation fraction by preventing the formation of secondary silicate minerals that either limit the carbonation fraction, by removing magnesium ions otherwise available for carbonation, or reverse carbonation, by promoting conditions that consume magnesite (as observed in our experiments). In our experiments with low volumes of solution, the SiO_2 mesh layer that formed still had voids and channels to facilitate olivine dissolution underneath the layer and magnesite precipitation above the layer (Figures 8d and 8e). Of course, as more SiO_2 precipitates to form a dense layer coating the olivine grain, dissolution and carbonation will likely slow down or even stop.

6.2 Conclusions and implications for geological storage of CO_2

This study once again demonstrates the feasibility of storing CO_2 in rocks abundant in olivine. It shows that the carbonation fraction in general is proportional to the concentration of $NaHCO_3$, implying that higher concentration of $NaHCO_3$ could help accelerate carbonation reaction rate and increase the final carbonation yields. It also shows that the precipitation of secondary magnesium-bearing silicate minerals will limit the maximum amount of carbonation. Experimental and theoretical analyses demonstrate reducing water activity by decreasing solution/olivine ratios could postpone the appearance of secondary silicate minerals and increase the overall carbonation fraction. Our study identified limitations of simulations using EQ3/6 program, and called upon new models to describe dissolution and precipitation kinetics. This work provides experimental information for technological developments regarding carbonation of ultramafic rocks using $NaHCO_3$-bearing solutions in any engineered process, either in situ and ex situ.

Acknowledgements

We thank Zhenting Jiang and Jim Eckert for their assistance in the SEM, ICP-MS and Microprobe labs.

PART I References

Aagaard, P., and Helgesen, H.C., 1982. Thermodynamic and kinetic constraints on reaction rates among minerals and aqueous solutions; I, Theoretical considerations. *American Journal of Science* **282**(3): 237-285.

Andreani, M. et al., 2009. Experimental study of carbon sequestration reactions controlled by the percolation of CO_2-rich brine through peridotites. *Environmental Science & Technology* **43**(4): 1226-1231.

Bearat, H. et al., 2006. Carbon sequestration via aqueous olivine mineral carbonation: Role of passivating layer formation. *Environmental Science & Technology* **40**(15): 4802-4808.

Boait, F.C., White, N.J., Bickle, M.J., Chadwick, R.A., Neufeld, J.A., and Huppert, H.E., 2012. Spatial and temporal evolution of injected CO2 at the Sleipner Field, North Sea. *J. Geophysical Res.* **117**, B03309, doi:10.1029/2011JB008603.

Brunauer, S., Emmett, P.H., and Teller, E., 1938. Adsorption of gases in multimolecular layers. *Journal of the American Chemical Society* **60**: 309-319.

Daval, D. et al., 2009. Mechanism of wollastonite carbonation deduced from micro- to nanometer length scale observations. *American Mineralogist* **94**(11-12): 1707-1726.

Daval, D. et al., 2011. Influence of amorphous silica layer formation on the dissolution rate of olivine at 90 ^{o}C and elevated pCO_2. *Chemical Geology* **284**(1-2): 193-209.

Dufaud, F., Martinez, I., and Shilobreeva, S., 2009. Experimental study of Mg-rich silicates carbonation at 400 and 500 ^{o}C and 1 kbar. *Chemical Geology* **265**(1-2): 79-87.

Garcia, B. et al., 2010. Experiments and geochemical modelling of CO_2 sequestration by olivine: Potential, quantification. *Applied Geochemistry* **25**(9): 1383-1396.

Giammar, D.E., Bruant, R.G., and Peters, C.A., 2005. Forsterite dissolution and magnesite precipitation at conditions relevant for deep saline aquifer storage and sequestration of carbon dioxide. *Chemical Geology* **217**(3-4): 257-276.

Global CCS Institute, Sleipner CO_2 Storage Project, accessed May 26, 2015, www.globalccsinstitute.com/project/sleipner%C2%A0co2-injection.

Helgesen, H.C., 1969. Thermodynamics of hydrothermal systems at elevated temperatures and pressures. *American Journal of Science* **267**(7): 729-804.

Hovelmann, J., Austrheim, H., and Jamtveit, B., 2012. Microstructure and porosity evolution during experimental carbonation of a natural peridotite. *Chemical Geology* **334**: 254-265.

IPCC, 2005, IPCC Special Report on Carbon Dioxide Capture and Storage, Prepared by Working Group III of the Intergovernmental Panel on Climate Change, Metz, B., O. Davidson, H. C. de Coninck, M. Loos, and L. A. Meyer (eds.), Cambridge University Press.

Kelemen, P.B., and Matter, J., 2008. In situ carbonation of peridotite for CO_2 storage. *Proceedings of the National Academy of Sciences of the United States of America* **105**(45): 17295-17300.

Kelemen, P.B. et al., 2011. Rates and mechanisms of mineral carbonation in peridotite: Natural processes and recipes for enhanced, in situ CO_2 capture and storage. *Annual Review of Earth and Planetary Sciences* **39**: 545-576.

King, H.E., Plumper, O., and Putnis, A., 2010. Effect of secondary phase formation on the carbonation of olivine. *Environmental Science & Technology* **44**(16): 6503-6509.

Klein, F., and Garrido, C.J., 2011. Thermodynamic constraints on mineral carbonation of serpentinized peridotite. *Lithos* **126**(3-4): 147-160.

Lackner, K.S., Wendt, C.H., Butt, D.P., Joyce, E.L., and Sharp, D.H., 1995. Carbon-dioxide disposal in carbonate minerals. *Energy* **20**(11): 1153-1170.

Lasaga, A.C., 1981. Transition state theory. *Reviews in Mineralogy and Geochemistr*y **8**(1): 135-168.

Lide, D.R., 2003. Aqueous solubility of inorganic compounds at various temperatures. *CRC Handbook of Chemistry and Physics*, 84th Edition, CRC Press: 8-116.

Marini, L., 2007. Geological sequestration of carbon dioxide, thermodynamics, kinetics, and reaction path modeling, *Developments in Geochemistry*, Elsevier.

Matter, J.M., and Kelemen, P.B., 2009. Permanent storage of carbon dioxide in geological reservoirs by mineral carbonation. *Nature Geoscience* **2**(12): 837-841.

McKelvy, M.J., Chizmeshya, A.V.G., Squires, K., Carpenter, R.W., and Béarat, H., 2006. A novel approach to mineral carbonation: enhancing carbonation while avoiding mineral pretreatment process cost. Annual Report to Department of Energy.

O'Connor, W.K., Dahlin, D.C., Rush, G.E., Dahlin, C.L., and Collins, W.K., 2002. Carbon dioxide sequestration by direct mineral carbonation: process mineralogy of feed and products. *Minerals & Metallurgical Processing* **19**(2): 95-101.

Oh, K.D., Morikawa, H., Iwai, S.-i., and Aoki, H., 1973. Hydrothermal growth of magnesite single crystals. *American Mineralogist* **58**: 339-340.

Palandri, J., and Kharaka, Y.K., 2004. A compilation of rate parameters of water-mineral interaction kinetics for application to geochemical modeling. USGS Open File Report 2004-1068.

Pokrovsky, O.S., and Schott, J., 2000. Kinetics and mechanism of forsterite dissolution at 25ºC and pH from 1 to 12. *Geochimica et Cosmochimica Acta* **64**(19): 3313-3325.

Schott, J., Pokrovsky, O.S., and Oelkers, E., 2009. The link between mineral dissolution/precipitation kinetics and solution chemistry. *Review in Mineralogy & Geochemistry* **70**: 207-258.

Seifritz, W., 1990. CO_2 disposal by means of silicates. *Nature* **345**(6275): 486-486.

Shannon, R.D., 1976. Revised effective ionic radii and systematic studies of interatomic distances in halides and chalcogenides. *Acta Crystallographica Section A* **32**(5): 751-767.

van Noort, R., Spiers, C.J., Drury, M.R., and Kandianis, M.T., 2013. Peridotite dissolution and carbonation rates at fracture surfaces under conditions relevant for *in situ* mineralization of CO_2. *Geochimica Cosmochimica Acta* (special ed.) **106**: 1-24.

Wilson, S.A. et al., 2009. Carbon dioxide fixation within mine wastes of ultramafic-hosted ore deposits: examples from the Clinton Creek and Cassiar Chrysotile Deposits, Canada. *Economic Geology* **104**(1): 95-112.

Wolery, T.J., 2002. EQ3/6—Software for Geochemical Modeling, Version 8.0, UCRL-CODE-2003-009. Lawrence Livermore National Laboratory, Livermore, California.

Wolff-Boenisch, D., Wenau, S., Gislason, S.R., and Oelkers, E.H., 2011. Dissolution of basalts and peridotite in seawater, in the presence of ligands, and CO_2: Implications for mineral sequestration of carbon dioxide. *Geochimica Cosmochimica Acta* **75**(19): 5510-5525.

PART I Table

Table 1. Comprehensive table of mineral carbonation experiments. All olivine grain and powder samples used in the experiments are listed, with the sample number, a description of the type of sample and weight, the fluid volume and initial concentration of sodium bicarbonate ($NaHCO_3$) reacting fluid, the duration of the experiment, the initial pH, and the initial concentration of dissolved inorganic carbon (DIC). The remaining columns show the results of the analysis of the samples and reaction products after each experiment.

Number	Samples	Weight (g)	fluid volume (ml)	NaHCO3 concentration (mol/L)	Duration (Day)	Initial pH	Initial DIC	pH (after reaction)	DIC (after reaction)	NaHCO3 consumed (mol)	mol of Mg+Fe	Carbonation fraction[a]	CF[b]	Mg	Si	Fe	Mg/Si	$SI_{magnesite}$	SI_{talc}	$SI_{chrysotile}$
151	olivine grain	0.1931	1	1	1	9.28	0.865	9.24	0.867	-2.21E-06	0.00132	0.0%	0.38%	1.6	70.8	2.18	0.03	-1.1	3.4	-0.3
158	olivine grain	0.2133	1	1	3	9.27	0.867	9.17	0.877	-1.00E-05	0.00145	0.0%	0.34%	1.3	70.3	0.38	0.02	-1.2	3.1	-0.5
154	olivine grain	0.2038	1	1	5	9.15	0.884	9.16	0.878	6.44E-06	0.00139	0.2%	0.31%	1.3	61.9	0.24	0.02	-1.2	2.8	-0.7
162	olivine grain	0.2133	1	1	14	9.18	0.870	9.23	0.866	1.25E-05	0.00145	0.4%	0.39%	1.3	80.1	0.61	0.02	-1.2	3.3	-0.4
152	olivine grain	0.1854	1	3	1	9.00	0.899	8.94	0.895	-4.47E-05	0.00126	0.0%	N/A	86.6	129.1	22.37	0.78	-0.6	1.3	-3.2
159	olivine grain	0.1977	1	3	3	9.00	0.899	8.93	0.901	-7.39E-05	0.00135	0.0%	N/A	183.6	225.0	36.85	0.94	-0.3	3.2	-1.8
196	olivine grain	0.1716	1	3	5	8.79	0.898	8.99	0.884	4.72E-05	0.00117	2.0%	N/A	86.7	270.0	45.40	0.37	-0.6	2.6	-2.6
169	olivine grain	0.2181	1	3	5	8.99	0.906	9.07	0.888	5.78E-05	0.00149	1.9%	N/A	90.8	253.4	40.97	0.41	-0.6	2.6	-2.6
163	olivine grain	0.1671	1	3	14	9.00	0.899	8.98	0.914	-9.12E-05	0.00114	0.0%	N/A	206.0	229.6	31.87	1.04	-0.2	3.4	-1.7
L1	olivine grain	0.1896	0.17	17	1	N/A	N/A	N/A	N/A	N/A	N/A	N/A	N/A	N/A	N/A	N/A	N/A	N/A	N/A	N/A
L2	olivine grain	0.1796	0.17	17	7	N/A	N/A	N/A	N/A	N/A	N/A	N/A	N/A	N/A	N/A	N/A	N/A	N/A	N/A	N/A
153	Olivine (0-30mm) Batch A	0.0396	0.5	1	1	9.28	0.865	10.04	0.694	8.99E-05	0.00027	16.6%	N/A	21.1	7.2	0.33	3.37	0.0	2.7	1.1
160	Olivine (0-30mm) Batch A	0.0401	0.5	1	3	9.27	0.867	10.04	0.693	9.17E-05	0.00027	16.8%	N/A	20.6	4.9	0.24	4.87	0.0	2.0	0.8
157	Olivine (0-30mm) Batch A	0.0415	0.5	1	5	9.15	0.884	10	0.707	9.25E-05	0.00028	16.4%	N/A	19.7	12.0	0.38	1.89	0.0	3.5	1.5
166	Olivine (0-30mm) Batch A	0.042	0.5	1	14	9.18	0.870	10.04	0.699	9.35E-05	0.00029	16.3%	N/A	24.1	4.6	0.33	6.09	0.1	2.1	0.9
172	Olivine (0-30mm) Batch A	0.0411	0.5	0.25	3	9.03	0.223	9.76	0.215	1.65E-05	0.00028	2.9%	N/A	39.5	0.6	0.02	75.51	0.4	2.5	3.0
173	Olivine (0-30mm) Batch A	0.0396	0.5	0.5	3	9.03	0.445	9.94	0.379	4.08E-05	0.00027	7.6%	N/A	31.0	2.3	0.10	15.72	0.4	3.8	3.2
174	Olivine (0-30mm) Batch A	0.0394	0.5	2	3	9.17	0.892	9.85	0.743	1.59E-04	0.00027	29.6%	N/A	33.5	44.7	0.40	0.86	-0.8	-0.3	-3.6
161B	Olivine (0-30mm) Batch A	0.0398	0.5	3	1	9.00	0.899	9.56	0.736	2.39E-04	0.00027	44.0%	N/A	152.8	49.7	3.53	3.55	-0.3	0.4	-3.4
161	Olivine (0-30mm) Batch A	0.0412	0.5	3	3	9.00	0.899	9.57	0.730	2.44E-04	0.00028	43.4%	N/A	174.0	55.8	3.82	3.60	-0.3	0.8	-3.1
156	Olivine (0-30mm) Batch A	0.039	0.5	3	5	9.00	0.899	9.5	0.736	2.50E-04	0.00027	46.9%	N/A	108.3	93.9	3.77	1.33	-0.5	1.1	-3.2
165	Olivine (0-30mm) Batch A	0.0414	0.5	3	14	9.00	0.899	9.61	0.767	1.91E-04	0.00028	33.9%	N/A	347.3	69.1	11.56	5.81	0.0	2.0	-2.1
181	Olivine (0-30mm) Batch A	0.03	0.5	0.5	5	9.04	0.467	9.93	0.386	4.16E-05	0.00020	10.2%	N/A	24.7	3.7	0.07	7.64	0.3	4.4	3.3
183	Olivine (0-30mm) Batch A	0.0308	0.5	2	5	9.21	0.907	9.74	0.718	1.82E-04	0.00021	43.3%	N/A	16.9	45.8	0.48	0.43	-1.1	-1.1	-4.5
				KHCO3																
191	Olivine (<50) Batch B	0.0393	0.5	1	3	8.91	0.879	9.4	0.815	3.36E-05	0.00027	6.3%	N/A	4.6	55.0	0.14	0.10	-0.7	4.3	0.9
192	Olivine (<50) Batch B	0.0414	0.5	0.5	3	8.82	0.460	9.3	0.433	1.39E-05	0.00028	2.5%	N/A	3.1	20.1	0.02	0.18	-0.6	4.6	2.1
193	Olivine (<50) Batch B	0.0415	0.5	0.25	3	8.46	0.242	8.86	0.248	0.00E+00	0.00028	0.0%	N/A	3.6	13.8	0.01	0.30	-0.6	4.9	2.7
				NaHCO3																
213	Olivine (<50) Batch B	0.0395	0.5	1	3	9.27	0.867	9.56	0.8013	3.89E-05	0.00027	7.2%	N/A	3.2	3.5	0.03	1.05	-0.8	-1.0	-2.0
214	Olivine (<50) Batch B	0.0392	0.5	0.5	3	9.22	0.425	9.64	0.418	2.09E-05	0.00027	3.9%	N/A	3.0	15.0	0.01	0.23	-0.6	4.1	1.9
215	Olivine (<50) Batch B	0.04	0.5	0.25	3	9.15	0.216	9.22	0.238	5.12E-06	0.00027	0.9%	N/A	3.7	6.2	0.01	0.69	-0.6	3.5	2.0

a: the carbonation fraction measured based on titration method

b: the carbonation fraction calculated based on the chemistry of the final solutions, see text 4.1 for details

TABLE 1

PART I Figure Captions

Figure 1. (TOP) Photos of a gem-quality olivine grain (a) and a gold capsule (b) used in our experiments. (BOTTOM) Particle size distribution for Batch-A and Batch-B powders.

Figure 2. Comparison of carbonation fraction determined by combustion and by titration. The uncertainties for both methods are less than 0.005 (2σ). The vertical axis on the right is the value of carbon storage for a given carbonation fraction. The carbon storage in mg-carbon/g-olivine is given by the formula: $S_C = F_C \cdot 12/W_{\text{olivine}} \cdot 2 \cdot 1000$, where W_{olivine} is the (gram) molecular weight of olivine, and F_C is the carbonation fraction.

Figure 3. Carbonation fraction in long-run experiments. Top panel shows the carbonation fraction in experiments lasting 1, 3, 5 and 14 days with batch-A olivine powders reacted with 1 *m* and 3 *m* $NaHCO_3$. The bottom panel shows the carbonation fractions for olivine grains under similar conditions. The carbonation fractions for olivine grains reacted with 1 m solution were determined by combustion; all other results were determined by titration. Note the large difference in vertical scales between the top and bottom plots.

Figure 4. Effect of the reacting solution. The bottom panel shows the near linear variation of the carbonation fraction with the concentration of the reacting sodium bicarbonate solution for Batch-A olivine powders reacted for 3 days. The quantities in parentheses are the slope, intercept and R^2 value of the regression line. The top panel shows the elemental concentrations Mg, Si and Fe and the Mg/Si ratio in solution, also as a function of the sodium bicarbonate concentration in the starting solution.

Figure 5. Variation of the carbonation fraction with concentration of the reacting solution for Batch-B powders reacted for 3 days with sodium and potassium bicarbonate solutions. Quantities in parentheses are the slopes, intercepts, and R^2 values of the regression lines.

Figure 6. Variation of the elemental concentrations Mg, Si and Fe and the Mg/Si ratio in solution as a function of length of the reaction.

Figure 7. SEM images on the surface of a carbonated olivine grain. The left column shows the surface evolution in 1 *m* $NaHCO_3$ solutions for 1 to 14 days, and the right column shows the surface evolution in 3 *m* $NaHCO_3$ solutions for 1 to 14 days. The smaller insert on the upper right illustrates the crystallographic habit of the magnesite or secondary Mg-bearing silicate minerals (SMBSMs) found on the olivine surface.

Figure 8. SEM images and elemental maps. Figures in the middle two rows are the BSE (backscattered electron) images of the cross section of a carbonated olivine in a reaction using 3 *m* $NaHCO_3$ solution. The figures at the top and bottom rows are the elemental maps of the particular part circumscribed by the red rectangle in the BSE images. The brightness of the color indicates the relative concentration of the same element in the element map.

Figure 9. Experiments with low fluid-to-mineral ratios. The top two rows show SEM images of the olivine surface (a, c and d) and BSE images of cross-sections of carbonated olivine minerals in one-day (b) and seven-day (d) experiments. The red line in panel (d) indicates where the cross-sections (e) were cut; (e) presents the BSE image and elemental maps of particular cross-sections. The brightness of the color indicates the relative concentration of the same element in all maps.

Figure 10. Modeling reaction pathways for olivine carbonation. The bottom panel shows mineral-solution phase boundaries in activity coordinates. The solid and dashed lines are the mineral-solution equilibrium lines for forsterite, talc and antigorite (see Appendix). The blue and pink rectangular areas are equilibrium zones for magnesite and quartz, which span a range of values in these coordinates. The thick line marked Model Pathway is the reaction path predicted by EQ3/6 for olivine reacted with 3 *m* sodium bicarbonate solution. Solid squares of different gray level show the progress of the simulation for an olivine grain after 1, 3, 5 and 14 days. The small light gray circle shows the progress for olivine powder, which is essentially fully carbonated after 1 day. The plot in the top panel shows how the distribution of magnesium among the different minerals evolves during the simulation with an olivine grain. In the simulation with olivine powder, the reaction is static after 1 day at the levels indicated to the right of the plot. See text for further details on the simulations. The pale to dark red squares in the upper right of the lower panel show where the experimental results plot in these coordinates.

Figure 11. Comparison of simulations with experiments. Simulations with EQ3/6 for the model described in the text match the general trends pH values (top) and carbonation fractions (bottom) observed in the experiments.

Figure 12. Relationship between the carbonation fractions and concentration of $NaHCO_3$ in initial solutions. The carbonations fraction in experiments (of the same duration) with increasing concentrations of $NaHCO_3$ tend to lie on the same increasing line, until the carbonation fraction reaches a limit; the inset (b) compares carbonation fractions between experiments using $NaHCO_3$ and $KHCO_3$ solutions with batch-B olivine powders for three days. The uncertainties in determining the carbonation fractions are better than 0.005 (2σ). The vertical axis on the right is the value of carbon storage (see Figure 2).

Figure 13. Limits on olivine carbonation. Lines show the upper limit on the carbonation fraction as a function of the partitioning of silicon (liberated by dissolving olivine) into different secondary minerals. For example if 20% of the Si in solution precipitates as quartz (SiO_2) and the rest as talc, the maximum carbonation fraction is about 0.6. The calculation makes the following assumptions: no siderite is formed, the valance charge of Fe is mainly 3+, and any remaining Mg and Si atoms in solution can be ignored. Thus, Si and Mg from olivine dissolution end up either in magnesite or in secondary silicate minerals (such as talc). These estimates could increase by up to 10% if Fe is dominantly 2+, and it occupies the same site as Mg in the carbonate and secondary silicates. The upper limit is set by the starting olivine composition, $Fo_{0.90}$.

PART I Figures

FIGURE 1

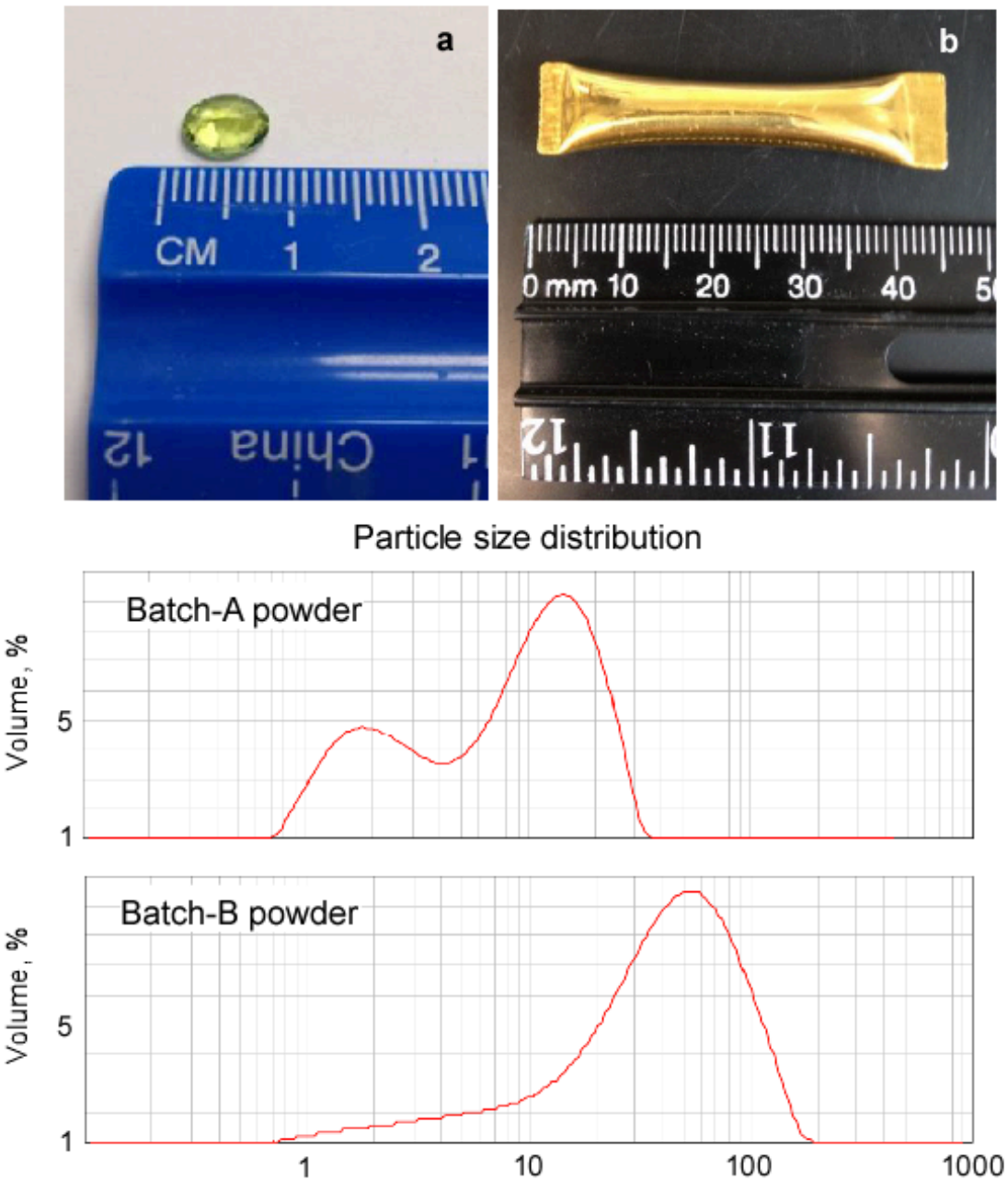
a
b
CM 1 2
China
0 mm 10 20 30 40
Particle size distribution
Batch-A powder
Volume, %
5
1
Batch-B powder
Volume, %
5
1
1
10
100
1000

FIGURE 2

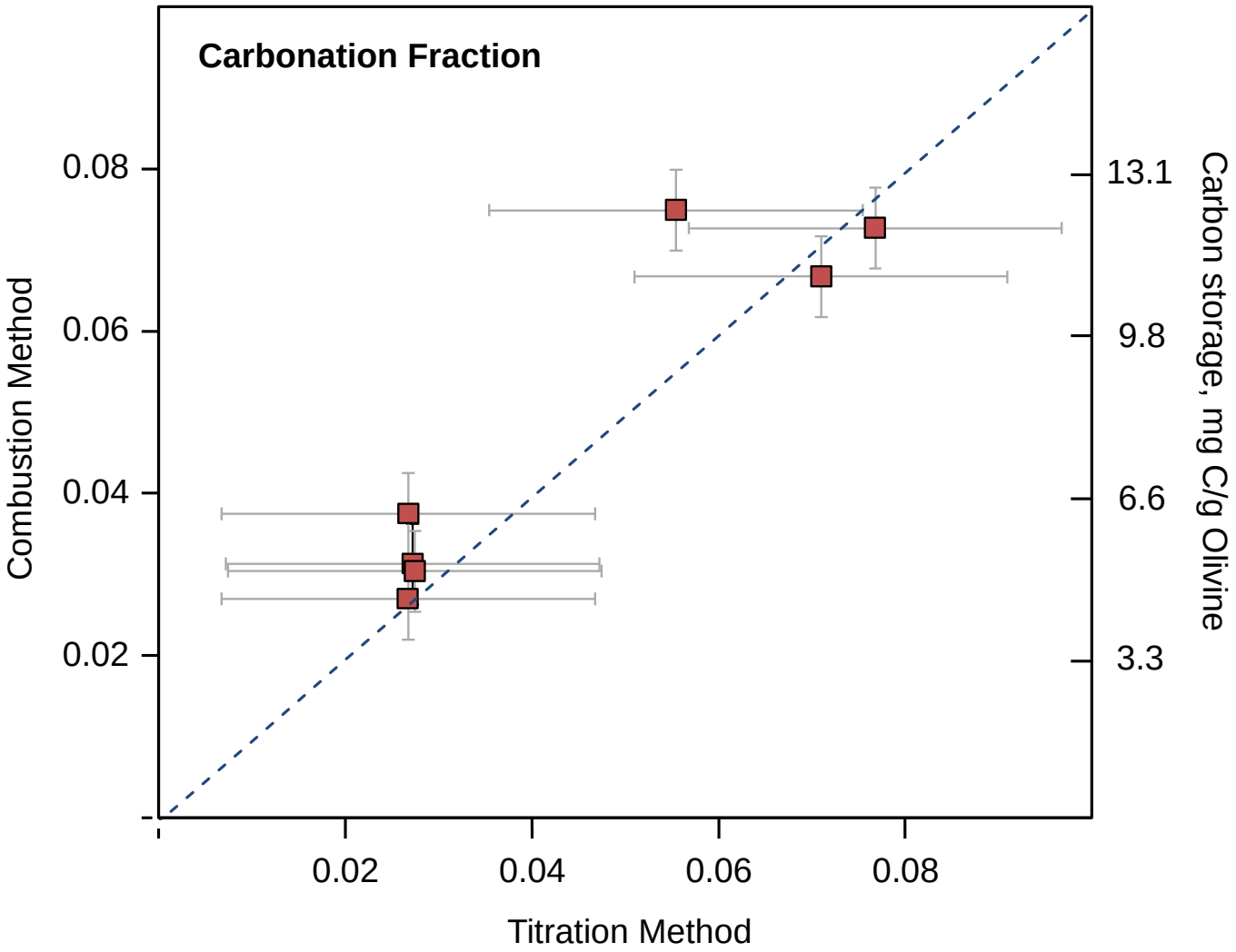
Carbonation Fraction
Combustion Method
0.08
0.06
0.04
0.02
13.1
9.8
6.6
3.3
Carbon storage, mg C/g Olivine
0.02
0.04
0.06
0.08
Titration Method

FIGURE 3

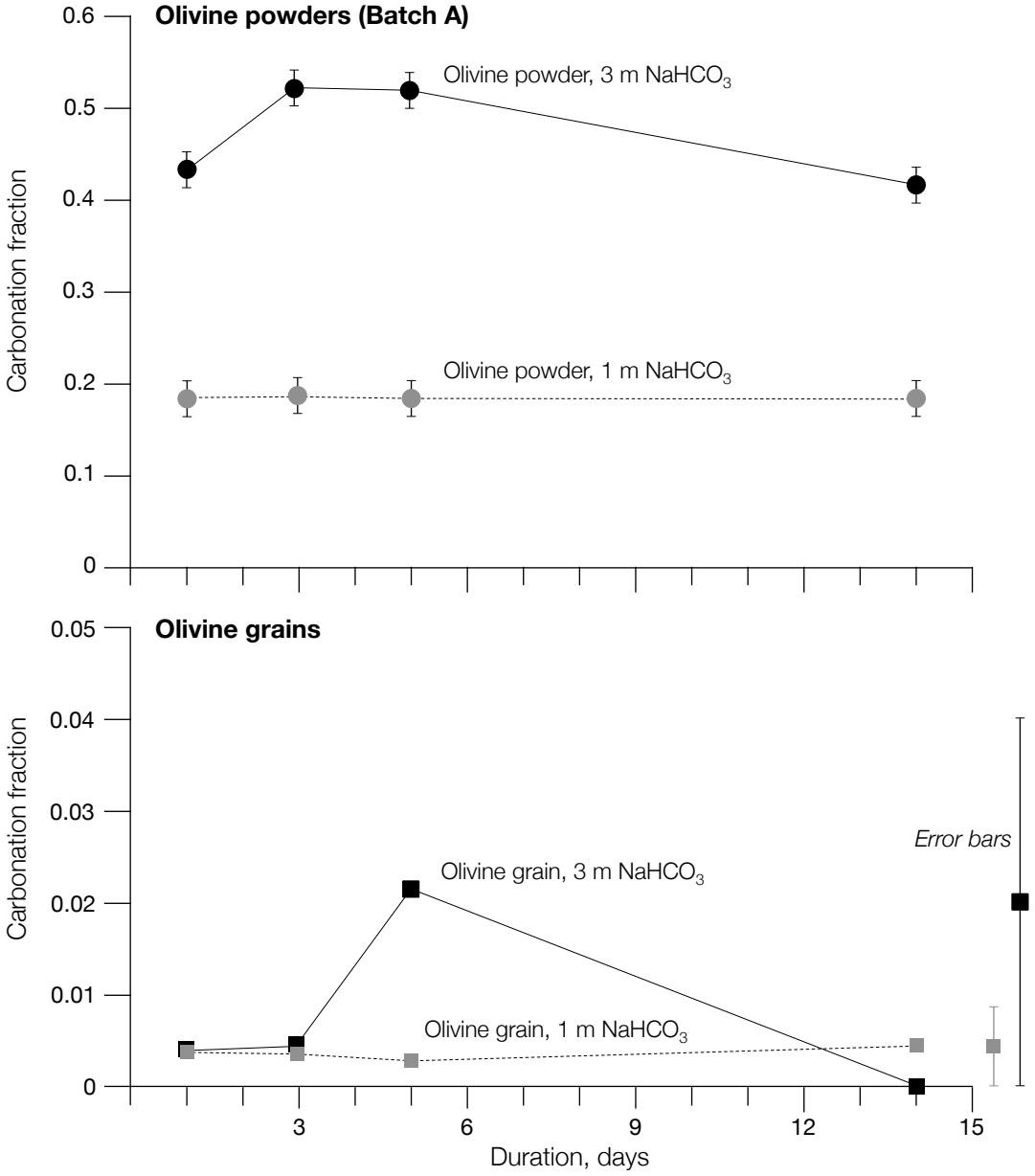
Olivine powders (Batch A)
Olivine powder, 3 m NaHCO3
Olivine powder, 1 m NaHCO3
Carbonation fraction
0.6
0.5
0.4
0.3
0.2
0.1
0
Olivine grains
Olivine grain, 3 m NaHCO3
Olivine grain, 1 m NaHCO3
Error bars
Carbonation fraction
0.05
0.04
0.03
0.02
0.01
0
3
6
9
12
15
Duration, days

FIGURE 4

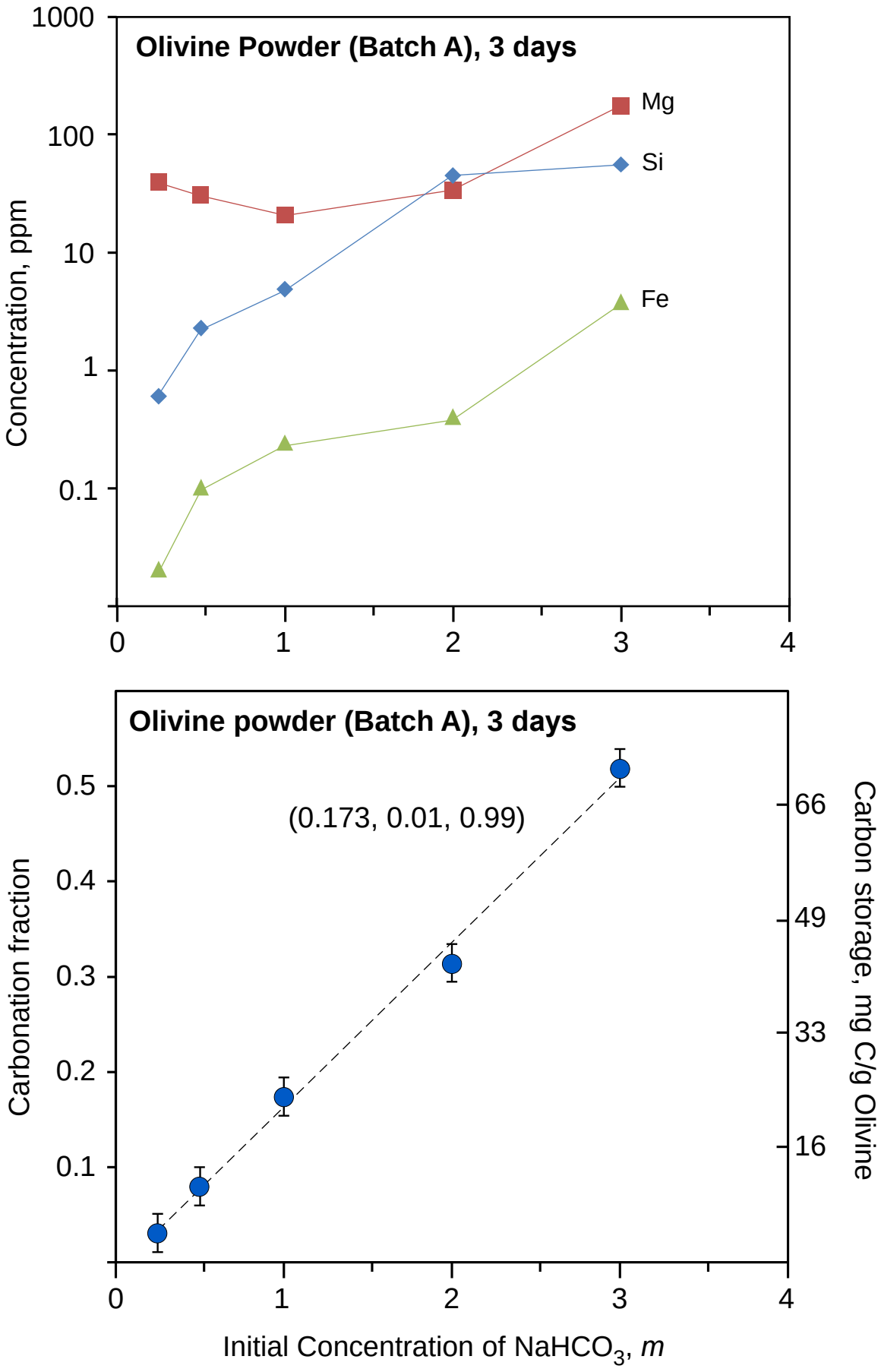
Olivine Powder (Batch A), 3 days
Concentration, ppm
1000
100
10
1
0.1
Mg
Si
Fe
0
1
2
3
4
Olivine powder (Batch A), 3 days
(0.173, 0.01, 0.99)
Carbonation fraction
0.5
0.4
0.3
0.2
0.1
66
49
33
16
Carbon storage, mg C/g Olivine
Initial Concentration of NaHCO3, m

FIGURE 5

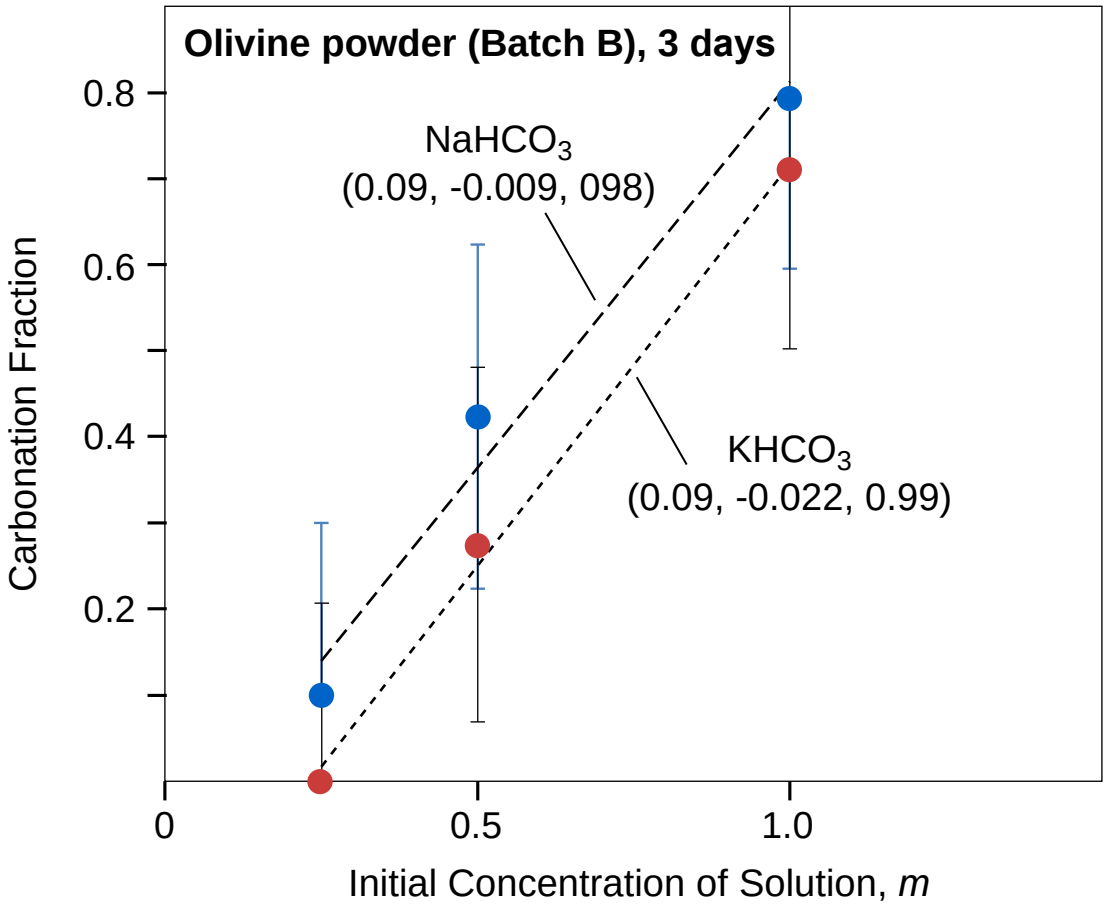
Olivine powder (Batch B), 3 days
NaHCO3
(0.09, -0.009, 098)
KHCO3
(0.09, -0.022, 0.99)
Carbonation Fraction
0.8
0.6
0.4
0.2
0
0.5
1.0
Initial Concentration of Solution, m

FIGURE 6

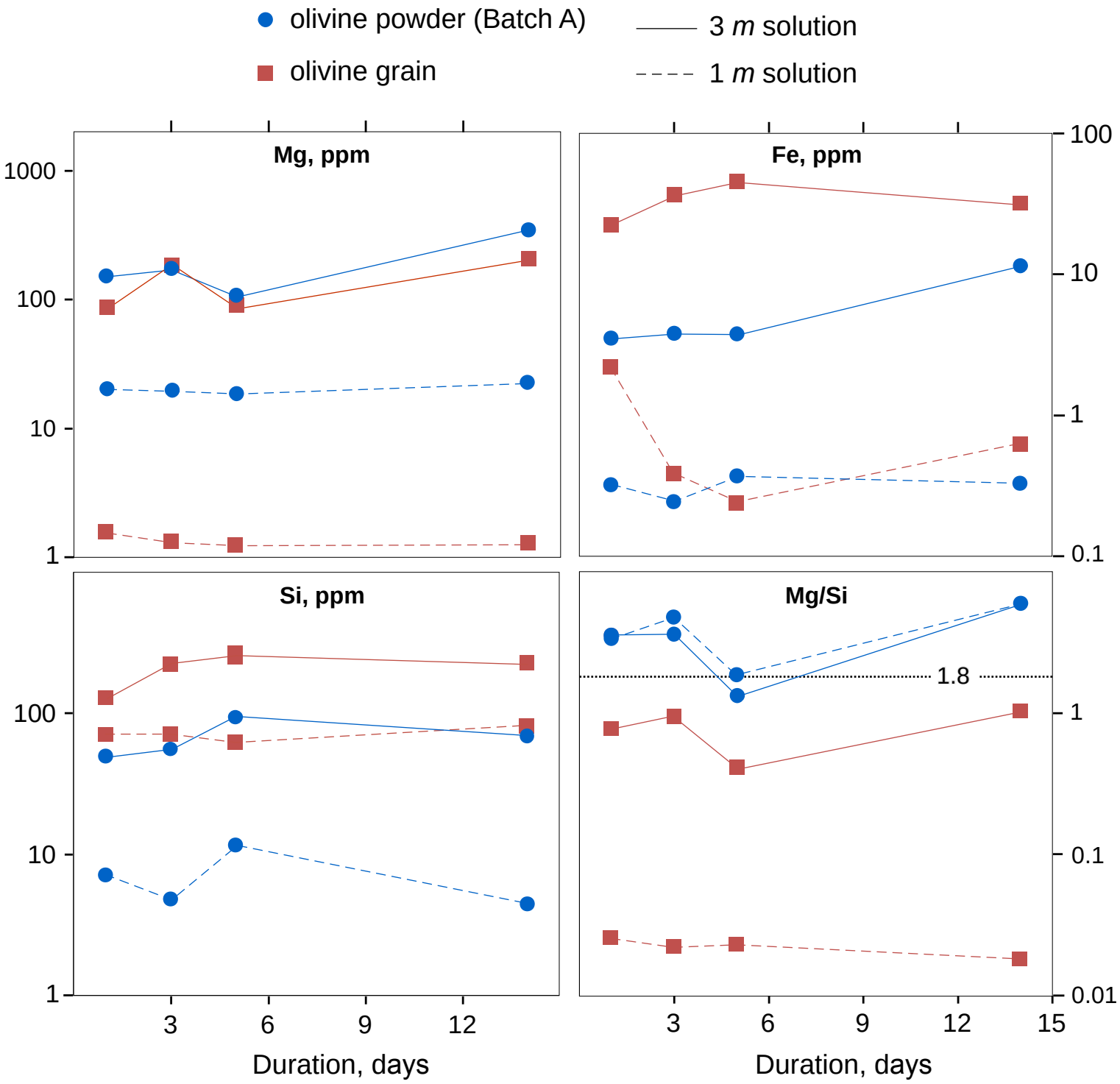
olivine powder (Batch A)
olivine grain
3 m solution
1 m solution
Mg, ppm
Fe, ppm
Si, ppm
Mg/Si
1.8
1000
100
10
1
100
10
1
0.1
100
10
1
1
0.1
0.01
3
6
9
12
3
6
9
12
15
Duration, days
Duration, days

FIGURE 7

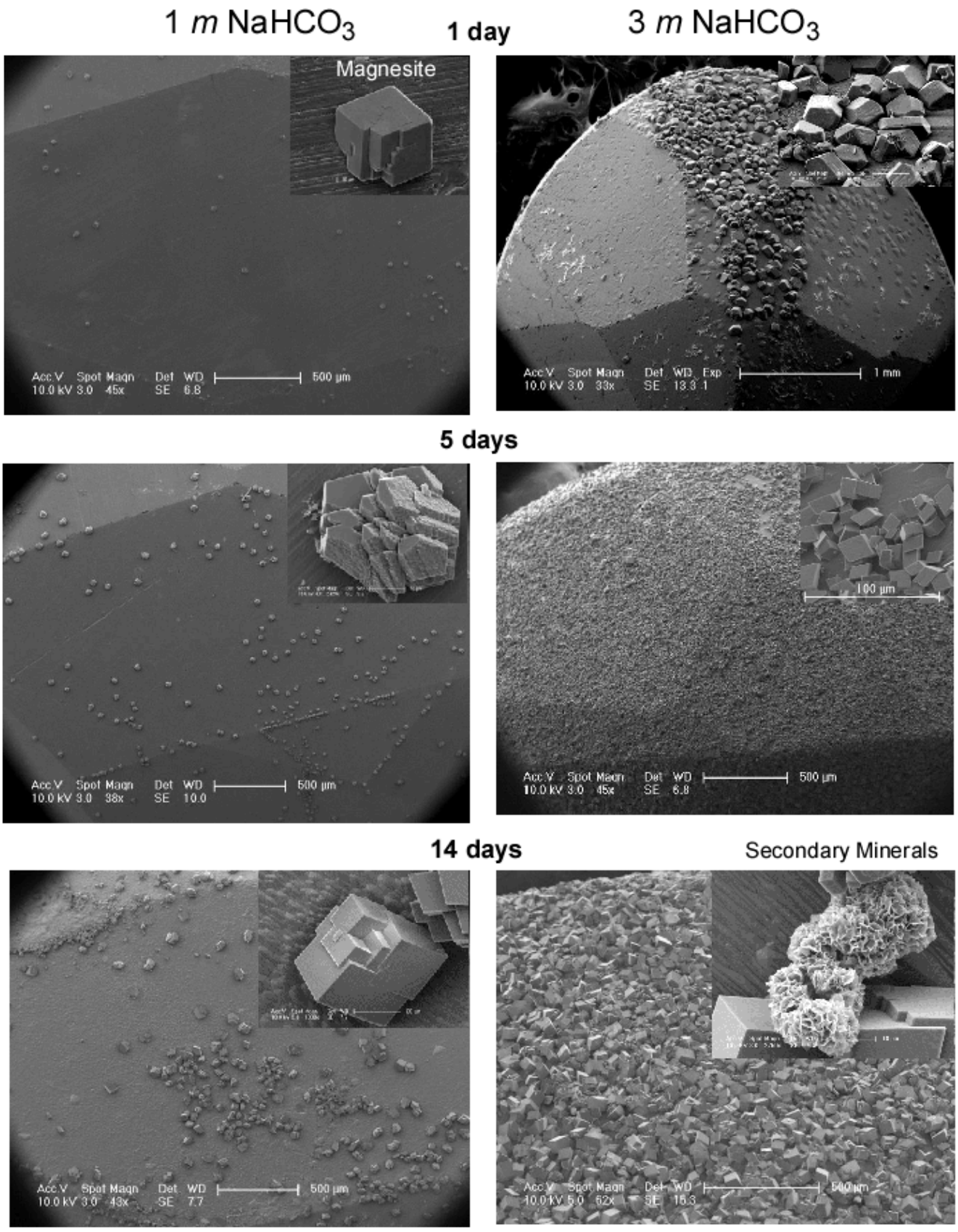
1 *m* $NaHCO_3$
1 day
3 *m* $NaHCO_3$
Magnesite
Acc.V Spot Magn Det WD
10.0 kV 3.0 45x SE 6.8
500 µm
Acc.V Spot Magn Det WD Exp
10.0 kV 3.0 33x SE 13.3 1
1 mm
5 days
Acc.V Spot Magn Det WD
10.0 kV 3.0 38x SE 10.0
500 µm
100 µm
Acc.V Spot Magn Det WD
10.0 kV 3.0 45x SE 6.8
500 µm
14 days
Secondary Minerals
Acc.V Spot Magn Det WD
10.0 kV 3.0 43x SE 7.7
500 µm
Acc.V Spot Magn Det WD
10.0 kV 5.0 62x SE 15.3
500 nm

FIGURE 8

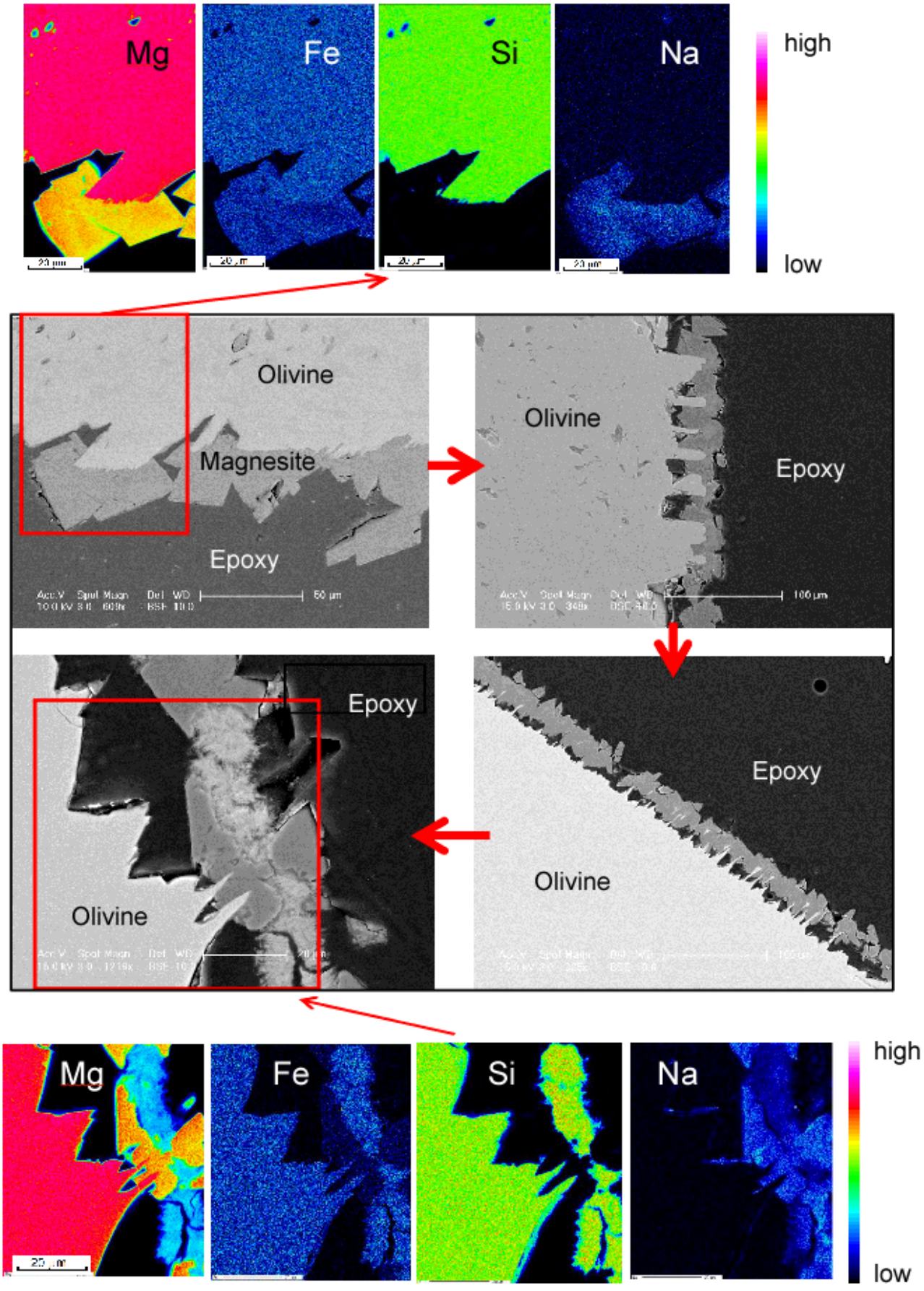
Mg
Fe
Si
Na
high
low
Olivine
Magnesite
Epoxy
Olivine
Epoxy
Epoxy
Olivine
Epoxy
Olivine
Mg
Fe
Si
Na
high
low

FIGURE 9

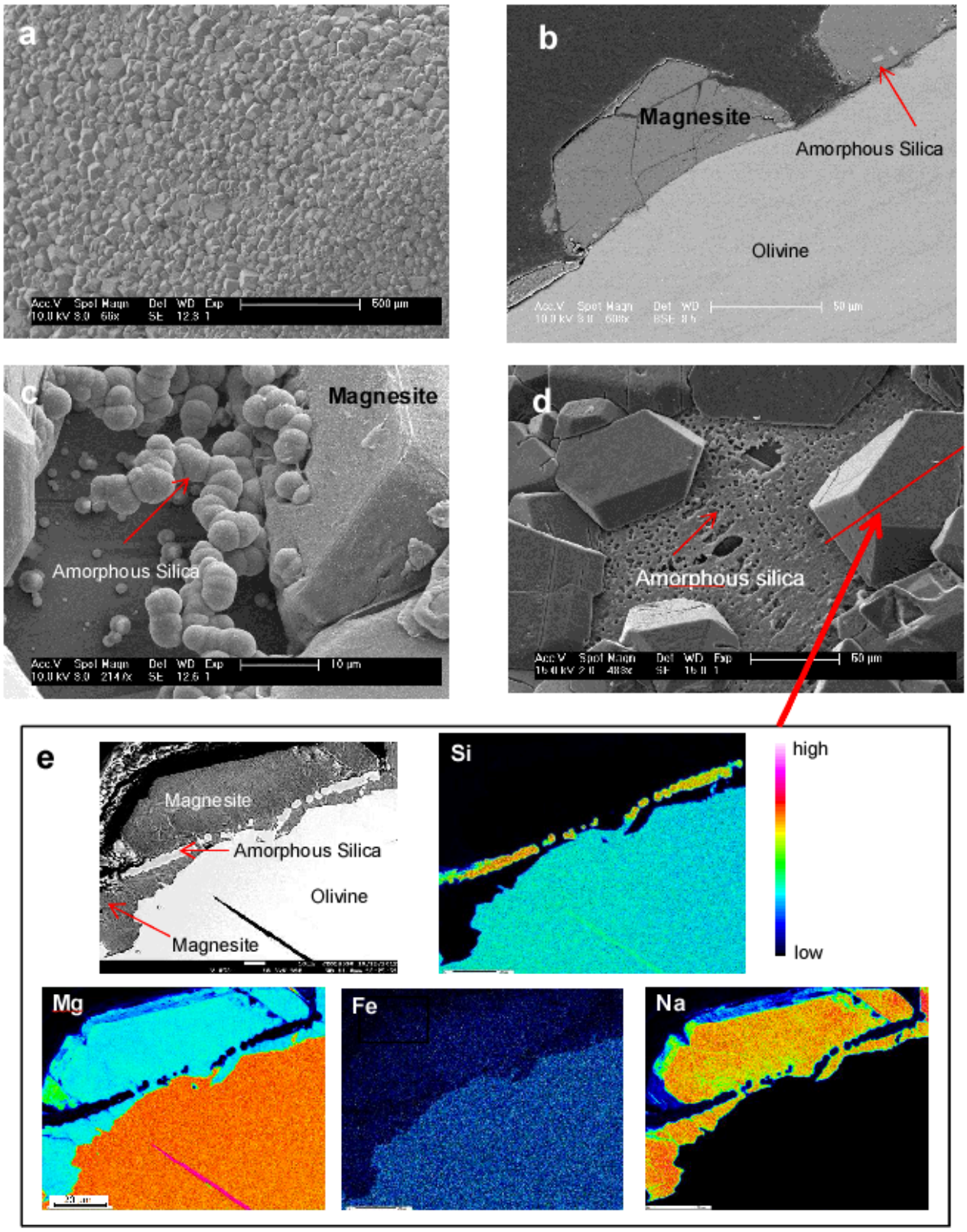
a
b
Magnesite
Amorphous Silica
Olivine
c
Magnesite
Amorphous Silica
d
Amorphous silica
e
Magnesite
Amorphous Silica
Olivine
Magnesite
Si
high
low
Mg
Fe
Na

FIGURE 10

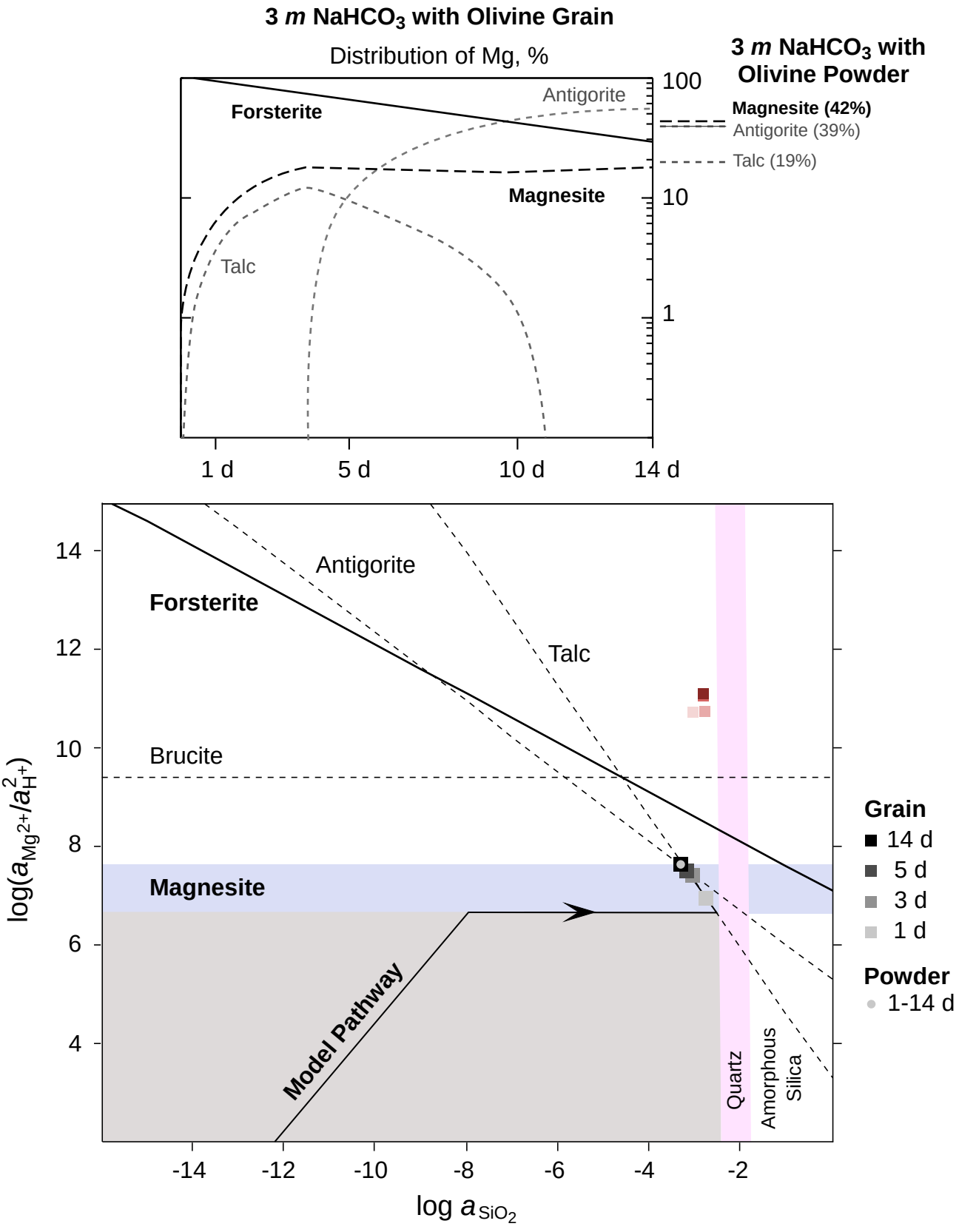
3 m NaHCO3 with Olivine Grain
Distribution of Mg, %
Forsterite
Antigorite
Magnesite
Talc
100
10
1
1 d
5 d
10 d
14 d
3 m NaHCO3 with Olivine Powder
Magnesite (42%)
Antigorite (39%)
Talc (19%)
Forsterite
Antigorite
Talc
Brucite
Magnesite
Model Pathway
Quartz
Amorphous Silica
log(aMg2+/aH+2)
log aSiO2
14
12
10
8
6
4
-14
-12
-10
-8
-6
-4
-2
Grain
14 d
5 d
3 d
1 d
Powder
1-14 d

FIGURE 11

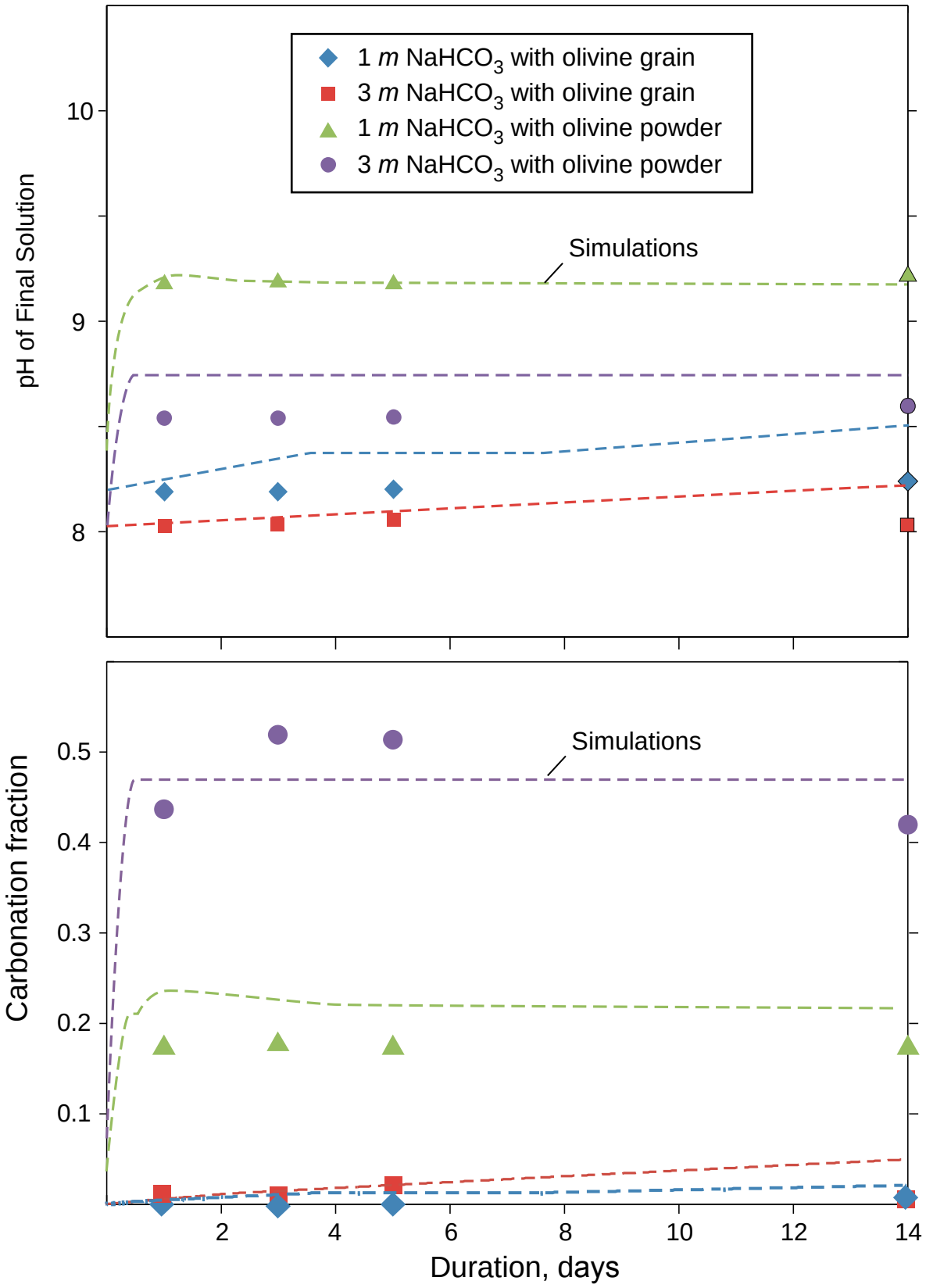
1 m NaHCO3 with olivine grain
3 m NaHCO3 with olivine grain
1 m NaHCO3 with olivine powder
3 m NaHCO3 with olivine powder
Simulations
pH of Final Solution
10
9
8
Simulations
Carbonation fraction
0.5
0.4
0.3
0.2
0.1
2
4
6
8
10
12
14
Duration, days

FIGURE 12

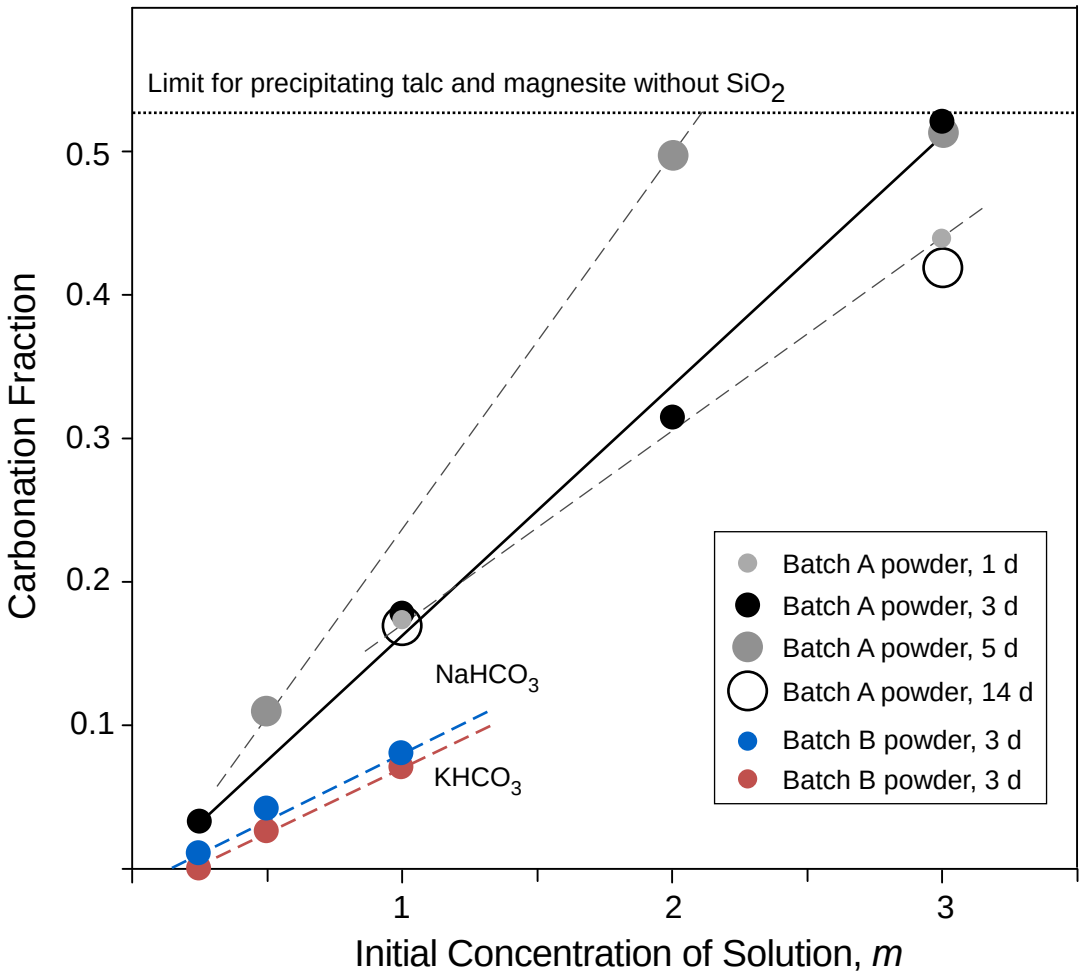
Limit for precipitating talc and magnesite without SiO_2
Carbonation Fraction
0.5
0.4
0.3
0.2
0.1
1
2
3
Initial Concentration of Solution, *m*
$NaHCO_3$
$KHCO_3$
Batch A powder, 1 d
Batch A powder, 3 d
Batch A powder, 5 d
Batch A powder, 14 d
Batch B powder, 3 d
Batch B powder, 3 d

FIGURE 13

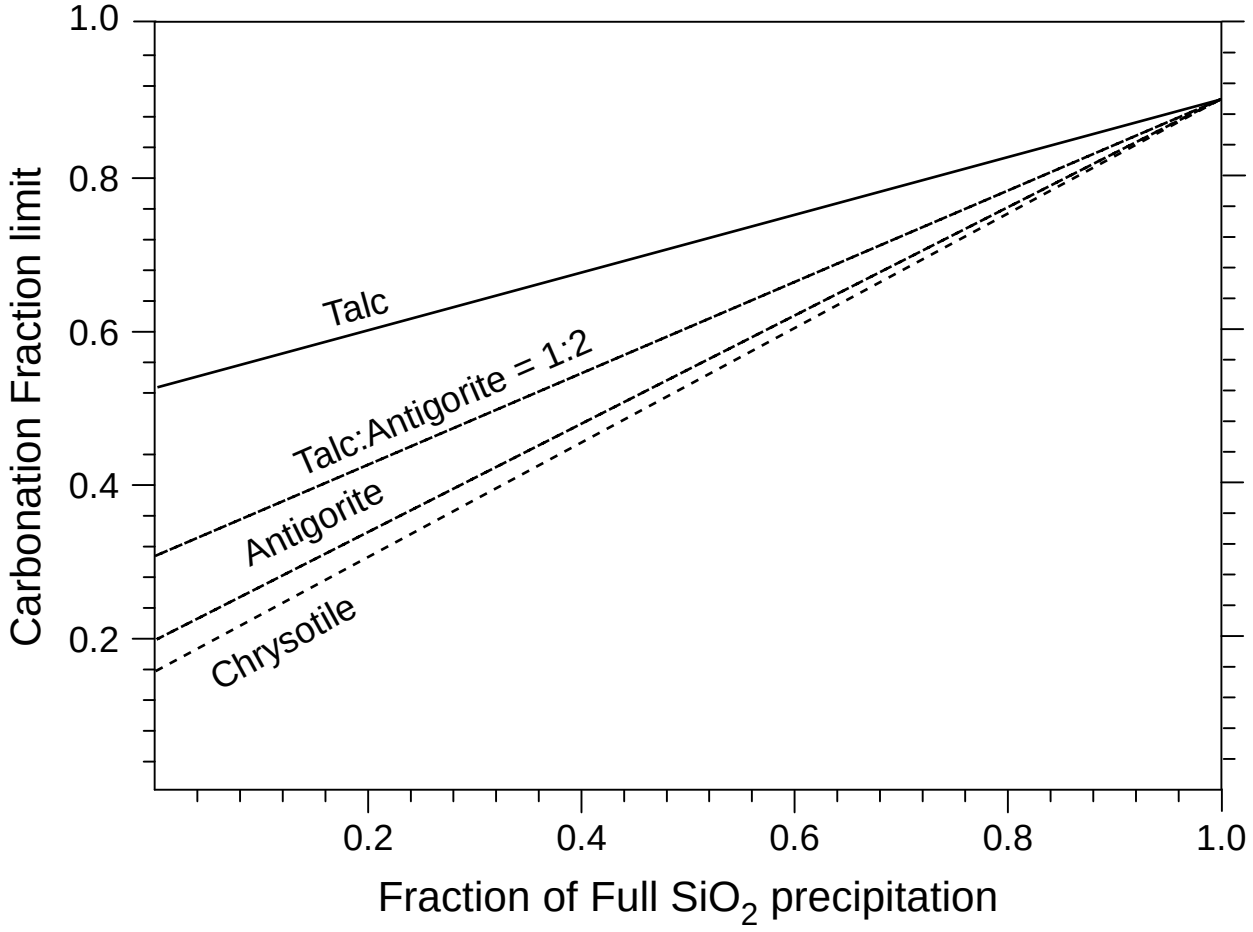
1.0
0.8
0.6
0.4
0.2
Carbonation Fraction limit
Talc
Talc:Antigorite = 1:2
Antigorite
Chrysotile
0.2
0.4
0.6
0.8
1.0
Fraction of Full SiO2 precipitation

Integrated Experimental and Modeling Studies of Mineral Carbonation as a Mechanism for Permanent Carbon Sequestration in Mafic/Ultramafic Rocks

Final Scientific/Technical Report

PART II GEOMECHANICAL EXPERIMENTS

In addition to the static geochemical experiments, the project conducted a series of dynamic geomechanical experiments in the Rock Physics Laboratory at the University of Maryland. These experiments studied olivine mineralization in natural dunite samples that were subjected to permeable fluid flow simultaneously with deformation at high pressure and temperature. The goal was to understand the mechanisms of olivine carbonation under different stress regimes and to elucidate the deformation processes that may accompany in situ mineral carbonation deep underground. The results provide important constraints on the pore structure evolution, which is essential for realistic assessments of the extent and rate of olivine mineralization in ultramafic rocks.

1 Experimental methods and samples

The geomechanical experiments involved the flow of CO_2-saturated brine through thermally cracked dunite samples under different stress conditions. The basic experiment consisted of hydrostatic compaction, followed by deformation at constant strain rate. Both short (48 hour) and long duration (200 hour) experiments were performed. The setup allowed monitoring of sample permeability throughout the experiments. The reacted samples were analyzed with a focused ion beam scanning electron microscope (FIB-SEM). We also designed and constructed a pressure cell transparent to X-rays. This development allowed in-situ X-ray microtomography to obtain, for the first time, high-resolution images of the pore structure of rocks that were deforming under high pressures and temperatures in the presence of reactive

pore fluids. The samples used in the experiments were thermally cracked dunite rocks (nearly pure olivine) with a natural porosity of 2 to 4%.

Figure 1 shows a schematic of the apparatus built for the experiments. It consists of a conventional triaxial deformation apparatus retrofitted with a pore fluid mixing system to prepare and introduce CO_2-saturated brine into sample pore space.

1.1 Short-run Tests

Figure 2 shows results of a typical short hydrostatic creep test, during which samples were allowed to react with pore fluids of different compositions for several days at a confining pressure of 15 MPa and a pore pressure of 10 MPa. The cyan curve records data from an experiment at room temperature with distilled water as the pore fluid, whereas the blue curves record data from experiments at 150°C with distilled pore water. The red curve records data from 150°C experiments with a pore fluid consisting CO_2-satured brine (0.6M $NaHCO_3$); the green curves record data from 150°C experiments with a more concentrated brine (1.5M $NaHCO_3$). Little compaction is observed at room temperature. Samples with CO_2-saturated pore fluid show less initial compaction than samples with distilled water, but exhibit accelerated compaction later on. The reduction in compaction during the early stage appears to be related to secondary mineralization along crack surfaces. Figure 3 shows in detail the volumetric strain versus time for one of the samples (DUN-24, the red curve in Figure 2). The complex behavior of the data can be fit using a hybrid model (Main 2000) that incorporates two competing processes: an initial process with negative feedback caused by local hardening (self-limiting) and a later process with positive feedback caused by crack interactions. The mathematical model describing volumetric strain as a function of time t has the form,

$$F = A(1 + t/T)^m + B\left(1 - t/t_f\right)^{-v},$$

where T and t_f are independent time scales, m and v are rate exponents and A and B are constants. The blue symbols in Figure 2a show a fit of this model to the data; the parameters determined by the fit are $A = 3.6 \cdot 10^{-6}$; $T = 0.7$; $m = 0.7$; $B = 0.044$; $t_f = 2.6 \cdot 10^5$; $v = 0.1$.

Figures 4 and 5 show the evolution of permeability in the samples for these short-run tests. There does not appear to be a systematic change in permeability evolution with different pore fluid concentrations, despite the differing mechanical behavior.

Figure 6 shows the results of the deformation experiments to test the mechanical response of samples after a period of reaction. Following the runs shown in the previous figures, in which the samples were reacted with pore fluid under hydrostatic pressure, the rocks were subjected to deformation at a nominal constant (axial) strain rate of about 10^{-5} s^{-1}. Among the samples that were run at elevated temperature, those reacted with CO_2-saturated pore fluids underwent less volumetric compaction than samples reacted with distilled water. In addition, samples reacted with CO_2-saturated pore fluid accommodated more axial strain before beginning to dilate (a characteristic swelling of rock samples before failure).

The difference in mechanical response between the two classes of samples appears to arise from the precipitation of secondary minerals along fracture surfaces, as illustrated in Figures 7 through 11. Figure 7 shows SEM images from unreacted sample material, which shows only olivine and angular fracture surfaces. Figure 8 shows FIB-SEM images of different dunite samples after three days reaction. In the sample reacted with distilled water at room temperature (DUN-19), shown in Figure 8a, the crack walls are largely unaltered. In the sample reacted with distilled water at 150°C (DUN-18), shown in Figure 8b, the crack walls show incipient dissolution features. In the sample reacted at 150°C with high-concentration bicarbonate brine (1.5M $NaHCO_3$), large magnesite and flaky hydromagnesite crystals covering crack walls are visible in Figures 8c-d. Finally, the sample reacted at 150°C, with low-concentration brine (0.6M $NaHCO_3$) exhibits extensive dissolution of olivine and precipitation of magnesite along crack walls visible in Figures 8e-f. Figure 9 shows images of the precipitated carbonates.

1.2 Detailed Analysis of Sample DUN-24

Figures 10 and 11 provide further detail, through FIB serial sectioning, of the sample reacted with low-concentration brine (DUN-24). An area where a pore intersects the fracture surface (Figure 10a) was

polished using the ion beam (10b), then imaged at an angle for serial sectioning: a protective layer of platinum was deposited on the polished surface, trenches were dug (10c), and a serial section was milled into the fracture face in order to image the 3D structure of the reaction interface into the bulk of the sample (10d). Layers of focused porosity are apparent.

Figure 11 shows SEM images of polished thin sections of the sample DUN-24. Evident in this figure are walls of pre-existing cracks heavily altered by dissolution-induced porosity and by precipitation of secondary minerals such as amorphous serpentine. Dissolution channels form a roughly planar interconnected network normal to the crack wall, joining with a second planar network of channels parallel to the crack surface, and approximately 10 mm into the surface. Figure 12 shows the average porosity within the serial FIB section. Two bands of high porosity are apparent near the crack surface (front left) and about 10 microns down (rear right). At some points the average porosity is as high as 60%.

A numerical permeability model was constructed for this sample by digitizing the 3D FIB section data using ImageJ (imagej.nih.gov) and Avizo (www.fei.com) software packages. Figure 14 shows relative fluid velocity in the pore space, simulated by the numerical model, with warmer colors representing higher flow. These results indicate that the sample pore space, after reaction, is organized into interconnected channels, with flow focused in the direction parallel to the cracks. These images are consistent with the 1D model of porosity-band formation developed by Merino et al. (1983), which shows that a slight porosity anomaly (a fracture in the case of our experiments) can grow and induce satellite porosity bands at some distance from the initial anomaly (Figure 14).

1.2 Long-run Tests

Two long-run hydrostatic creep tests allowed samples to react with distilled water and low-concentration brine for several days at 15 MPa confining pressure and 10 MPa pore fluid pressure. Permeability was measured every half hour during the experiment, and fluid samples were taken periodically to assess pore fluid chemistry. Figures 15 through 20 show results from these long-run experiments. Figure 15 shows the volumetric strain versus time; Figures 16 and 17 show permeability (on linear and logarithmic scales)

versus time. As in the short-run tests, samples filled with CO_2-saturated pore fluid show less compaction than samples filled with distilled water. The reduced compaction appears to be related to secondary mineralization along crack surfaces.

Figure 18 shows concentrations of different elements (Mg, Si, Ca, Fe) in the fluid samples over time. The data suggest fast initial dissolution of olivine, followed by precipitation of magnesite: in the sample filled with CO_2-saturated pore fluid, the concentration of magnesium rises immediately, and then falls quickly. In both samples, the concentration of silicon increases for about 50 hours, and then begins to fall (very slowly in the sample exposed to distilled water), indicating precipitation of a Si-rich phase, such as amorphous silica or serpentine. Figure 19 shows results of modeling a possible reaction path for these experiments using the software package PHREEQC (USGS, 2015). After the dissolution of olivine, magnesite is the first phase to precipitate in abundance, followed quickly by amorphous silica. Serpentine ($Mg_3Si_2O_5(OH)_4$) precipitates slowly (consuming amorphous silica), and brucite ($Mg(OH)_2$) appears near the end of the simulation. The results of the model agree with chemical data from the experiments, as well as with the SEM images (Figure 20) and with ex-situ microstructural analysis.

1.3 X-ray Images of Reactive Flow Experiments

A final part of the geomechanical project at University of Maryland was the development of new modular X-ray-transparent cell suitable for imaging of fluid-rock interactions at conditions of high temperature and high pressure (Fusseis et al., 2014). Figure 21 shows a schematic of the cell, with its peripheral hardware, along with a photo of the assembled device.

The cell was used in a pilot experiment to characterize pore structure evolution in real time during mineral carbonation of porous olivine aggregates. The sample was a cylindrical porous olivine cup with an outer diameter of 2 mm and an inner diameter of 1 mm, filled with coarse olivine sand with grain sizes in the range 100–500 micron. The cup itself was made of porous olivine aggregates with grain sizes in the range 0–20 microns, hot pressed at 1400°C for 4 hours under reducing conditions. During the experiment, the sample assembly, saturated with high-concentration brine ($NaHCO_3$ at 1.5 M) at a pore pressure of 10

MPa, was held at a confining pressure of 13 MPa and was heated to 473 K (200°C). Constant pressure and temperature conditions were then maintained during the experiments lasting up to 128 hours. Using a polychromatic beam at the Advanced Photon Source at Argonne National Lab, 3D microtomography data were collected every 30 minutes and used to construct tomographic images with a voxel size of about 1.5 µm. Preliminary results show substantial increase in surface roughness, as well as the development of reaction-driven cracks (Figure 22).

2 Conclusions of Geomechanical Experiments

The purposes of the geomechanical experiments were, first, to understand how the chemical alteration of olivine by mineral carbonation affects its mechanical behavior and, second, to gain insight into the evolution of porosity and permeability of samples undergoing carbonation in conditions where the sample volume is not constant.

The results of the initial experiments—combining reactive flow under hydrostatic conditions, followed by compaction of natural, thermally cracked dunite samples—suggest the following:

- Reactive brine can enhance hydrostatic compaction in dunite accommodated by extensive dissolution of crack walls produced a highly porous layer with enhanced compressibility.
- Permeability is reduced during compaction, but enhanced compaction is not correlated with enhanced permeability reduction. Carbonate precipitates may serve as asperities along crack surfaces, restricting crack closure and permeability sealing. Dissolution networks may provide additional pathways to fluid flow.
- The production of pore space during carbonation may facilitate larger extents of carbonation than would otherwise be possible.

PART II References

Fusseis, F., Steeb, H., Xiao, X., Zhu, W., Butler, I., Elphick, S., and Mäder, U., 2014. A low-cost X-ray transparent experimental cell for Synchrotron-based X-ray microtomography studies at geological reservoir conditions, *Journal of Synchrotron Radiation* **21**: 251-253, doi:10.1107/S1600577513026969.

Power, I.M., Harrison, A.L., Dipple, G.M., Wilson, S.A., Kelemen, P.B., Hitch, M., and Southam, G., 2013. Carbon Mineralization: From Natural Analogues to Engineered Systems, *Reviews in Mineralogy & Geochemistry* **77**: 305-360.

Main, I.G., 2000. A damage mechanics model for power-law creep and earthquake aftershock and foreshock sequences. *Geophysical Journal International* **142**(1): 151–161. doi:10.1046/j.1365-246x.2000.00136.x.

USGS, PHREEQC (Version 3)—A Computer Program for Speciation, Batch-Reaction, One-Dimensional Transport, and Inverse Geochemical Calculations, accessed May 2015, http://wwwbrr.cr.usgs.gov/projects/GWC_coupled/phreeqc/.

PARTI II Figure Captions

Figure 1. Schematic of reactive flow and deformation experiments. A conventional triaxial deformation apparatus was retrofitted with a pore fluid mixing system to prepare and introduce CO_2-saturated brine into sample pore space while maintaining independent control of pore pressure to prevent degassing.

Figure 2. Volumetric strain versus time for short-run hydrostatic creep tests. Positive volumetric strain represents compaction (shortening of the sample). Samples were allowed to react with pore fluid of different compositions for several days, at a confining pressure of 15 MPa and a pore fluid pressure of 10 MPa. The cyan curve (bottom curve) is data from an experiment at room temperature with distilled water as the pore fluid. The blue curves (top) are data from 150°C experiments with distilled pore water. The red curve is data from 150°C experiments with CO_2-satured brine with 0.6 M NaHCO3. The green curves are data from 150°C experiments with CO_2-satured brine with 1.5 M NaHCO3. Little compaction is observed at room temperature. Samples with CO_2-saturated pore fluid show less initial compaction than samples with distilled water, but exhibit accelerated compaction later on. Examination of the samples suggests that the reduction in compaction during the early stage appears to be related to secondary mineralization along crack surfaces

Figure 3. Volumetric strain versus time for sample DUN-24. The complex behavior of the data can be fit using a model incorporating two competing processes, one self-limiting and one self-intensifying. Blue symbols are an initial fit for the hybrid model of Main (2000) with the following parameters: $A = 3.6 \cdot 10^{-6}$; $T = 0.7$; $m = 0.7$; $B = 0.044$; $t_f = 2.6 \cdot 10^5$; $v = 0.1$.

Figure 4. Normalized permeability versus time for short-run hydrostatic creep tests. Coloring of curves is the same as in Figure 2. All samples show a reduction in permeability with compaction. There does not appear to be a systematic change in permeability evolution with different pore fluid concentrations, despite the differing mechanical behavior.

Figure 5. Permeability versus time for short hydrostatic creep tests. Coloring is the same as in Figures 2 and 3. All samples show a reduction in permeability with compaction. There does not appear to be a systematic change in permeability evolution with different pore fluid concentrations, despite the differing mechanical behavior.

Figure 6. Volumetric strain as a function of axial strain for deformation experiments on samples after short hydrostatic creep tests. Coloring of curves is the same as in previous figures. After samples were allowed to react with pore fluid during hydrostatic creep tests, constant strain rate deformation tests were

run at a nominal strain rate of 10^{-5} s^{-1} to test the mechanical response of samples after a period of reaction. Among samples run at elevated temperature, samples with CO_2-saturated pore fluids display less volumetric compaction (for a given axial strain) than samples with distilled water as the pore fluid. In addition, samples with CO_2-saturated pore fluids accommodate more axial strain before beginning to dilate (a characteristic swelling of rocks before the onset of failure). This change in mechanical response is attributed to the precipitation of secondary minerals along fracture surfaces.

Figure 7. SEM images from unreacted sample material. (a) Overview of fracture surface in unreacted material. (b) Fracture surface shows only olivine and angular fracture surfaces.

Figure 8. Focused ion beam scanning electron microscope (FIB-SEM) images of dunite samples after three days of reaction. (a) DUN-19, with distilled water at room temperature: crack walls are largely unaltered. (b) DUN-18, with distilled water at 150°C: crack walls show incipient dissolution features. (c,d) DUN-23, with high concentration bicarbonate brine at 150°C: large (2-20 mm) magnesite (mgs) crystals and flaky hydromagnesite (hmg) cover crack walls. (e,f) DUN-24, with low concentration brine at 150°C: extensive dissolution of olivine and precipitation of magnesite along crack walls.

Figure 9. SEM images of precipitated carbonates. (a) DUN-23, with high concentration bicarbonate brine: crystals of hydromagnesite precipitated along crack wall. (b) DUN-23: compound magnesite crystal visible with complex structure. (c) DUN- 24, low concentration bicarbonate brine: extensive etching of a crack wall. (d) DUN-24: well-terminated magnesite crystal visible.

Figure 10. Focused ion beam serial sections of sample DUN-24. This sample was reacted with 0.6M $NaHCO_3$. (a) The area of interest is a pore intersecting the fracture surface we are imaging. (b) The surface is polished using the ion beam. (c) The polished area is imaged at an angle for purposed of serial sectioning. (c) A protective layer of platinum is deposited on the polished surface, trenches are dug, and a serial section is milled into the fracture face in order to image the 3D structure of the reaction interface into the bulk of the sample. (d) Layers of focused porosity are apparent.

Figure 11. Scanning electron micrographs of sample DUN-24. (TOP) Polished thin section of sample after three-days reaction. The walls of pre-existing cracks in olivine (ol) are heavily altered by dissolution induced porosity and precipitation of secondary minerals such as amorphous serpentine (serp). (BOTTOM) Focused ion beam serial section of a cross-section into the wall of a crack. Dissolution channels form a roughly planar interconnected network normal to the crack wall, joining with a second planar network of channels parallel to the crack surface approximately 10 mm into the surface.

Figure 12. Average porosity within the serial FIB section. Two bands of high porosity are apparent near the crack surface (front left) and about 10 microns down (rear right). At some points the average porosity is a high as 60%.

Figure 13. Results of a numerical permeability model of the pore space in sample DUN-24. Colors represent relative fluid velocity, with warmer colors representing higher flow. 3D FIB section data is reconstructed into a digital geometry using the ImageJ and Aviso software packages and a model of the resulting permeability structure can be run. The data show that pore space is organized into interconnected channels, with flow focused in the crack-parallel direction.

Figure 14. Porosity anomaly versus position for a one-dimensional model of porosity band formation based on a model from Merino et al. (1983). Different colored lines represent iterations of the model. This model shows how a slight porosity anomaly (a fracture in the case of our experiments) can grow and induce satellite porosity bands at some distance from the initial anomaly.

Figure 15. Volumetric strain versus time for long hydrostatic creep tests. Positive volumetric strain represents compaction. Samples were allowed to react with pore fluid of different compositions for several days at 15 MPa confining pressure and 10 MPa pore-fluid pressure. Permeability was measured every half hour during the experiment and fluid samples were taken periodically to assess pore fluid chemistry evolution. Coloring is the same as previous figures. Samples with CO_2-saturated pore fluid show less compaction than samples with distilled water. The reduced compaction appears to be related to secondary mineralization along crack surfaces.

Figure 16. Permeability versus time for long hydrostatic compaction experiments. Coloring is the same as in previous figures. Permeability is reduced throughout compaction. It is difficult to assess the systematic difference between samples with different pore fluids due to variation in initial permeability

Figure 17. Permeability versus time for long hydrostatic compaction experiments (logarithmic scale). Coloring is the same as in Figure 16. Permeability is reduced throughout compaction. It is difficult to assess the systematic difference between samples with different pore fluids due to variation in initial permeability.

Figure 18. Chemistry data for long hydrostatic compaction experiments as a function of time: (a) magnesium, (b) silicon, (c) calcium, and (d) iron. Data show fast initial dissolution followed by precipitation. In the sample with CO_2-saturated pore fluid, magnesium rises quickly then immediately begins to reduce, indicating the precipitation of a Mg phase, in this case magnesite. For both samples,

silicon increases for about 50 hours, then begins to reduce, indicating the precipitation of a Si-rich phase, in this case serpentine and amorphous silica.

Figure 19. Results of a reaction path model from the software package PHREEQC. The plot shows moles of reaction products in assemblage versus reaction step. Each reaction step represents the dissolution of forsterite in a hydrothermal system at the same conditions as our experiments with CO_2-saturated brine. Magnesite is the first phase to precipitate in abundance, followed quickly by amorphous silica. Serpentine precipitates slowly throughout the reaction, and brucite comes into the assemblage near the end of the simulation. The results of the model agree with chemical data from experiments as well as ex-situ microstructural analysis.

Figure 20. SEM images from long hydrostatic compaction experiments. (a) Overview of a crack surface from sample DUN-7, saturated with distilled water. Crack surface is mostly olivine, with initial serpentine mineralization. (b) Crack intersecting the crack surface of DUN-7 being imaged shows signs of incipient etch pitting. (c) Serpentine flakes growing on the fracture surface of DUN-7. (d) Overview of fracture surface from sample DUN-8, reacted with 0.6M $NaHCO_3$ brine. Sheets of magnesite coat the olivine crack surface. (e) Magnesite is precipitated in layers on the fracture surface, and these layers appear porous and cracked. (f) Close up on magnesite co-precipitated with serpentine. Secondary mineral coating show pores and cracks.

Figure 21. Schematic diagram of an X-ray transparent pressure cell with flow through capability (from Fusseis et al., 2014).

Figure 22. (TOP) Comparison of the surface roughness of a single olivine grain at 8 hours (left) and 128 hours (right) after the onset of carbonation. (BOTTOM) 3D image of porous olivine aggregates, showing a reaction-driven crack 128 hours after the onset of carbonation.

PART II Figures

FIGURE 1

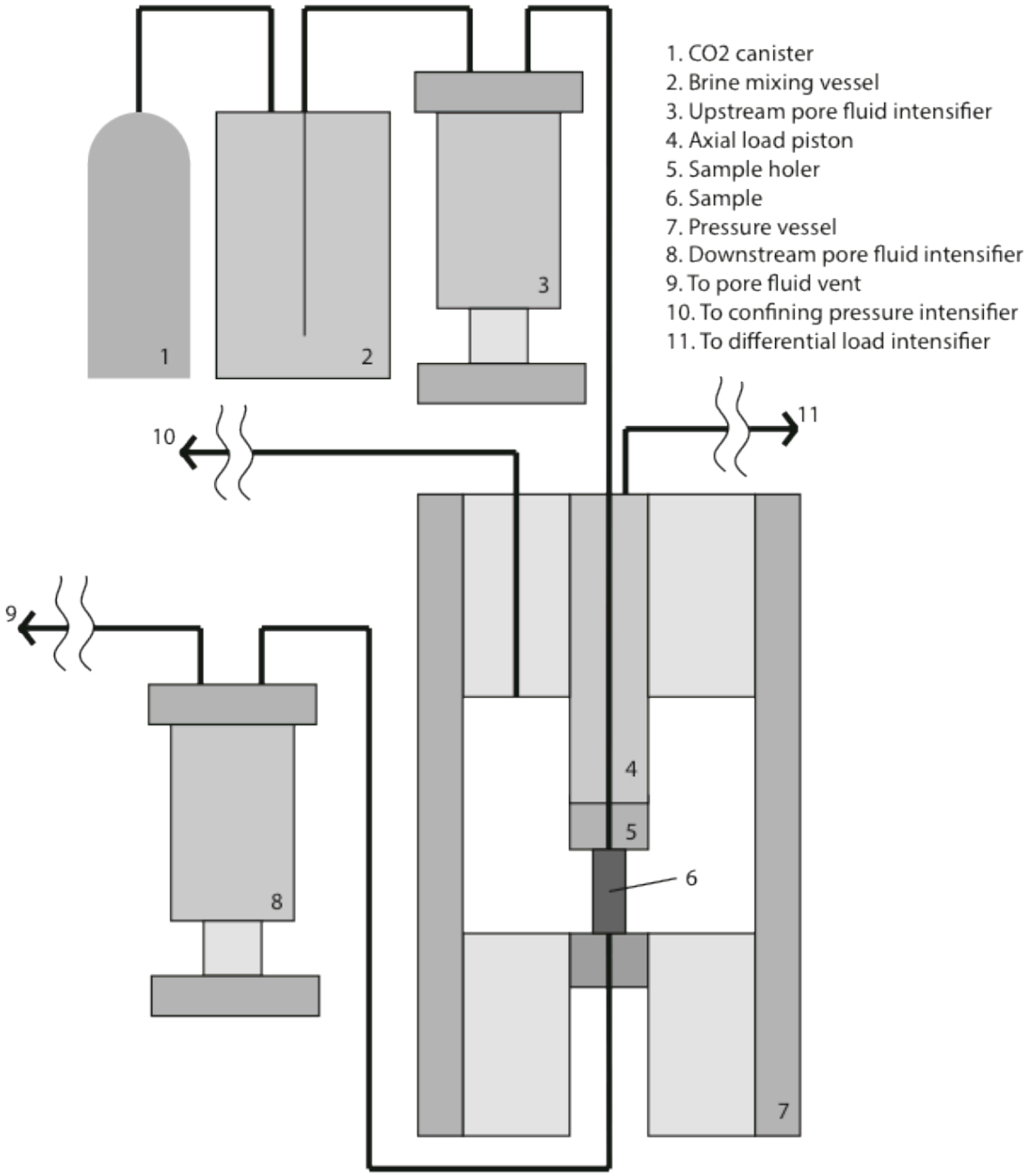
1. CO2 canister
2. Brine mixing vessel
3. Upstream pore fluid intensifier
4. Axial load piston
5. Sample holer
6. Sample
7. Pressure vessel
8. Downstream pore fluid intensifier
9. To pore fluid vent
10. To confining pressure intensifier
11. To differential load intensifier
1
2
3
4
5
6
7
8
9
10
11

FIGURE 2

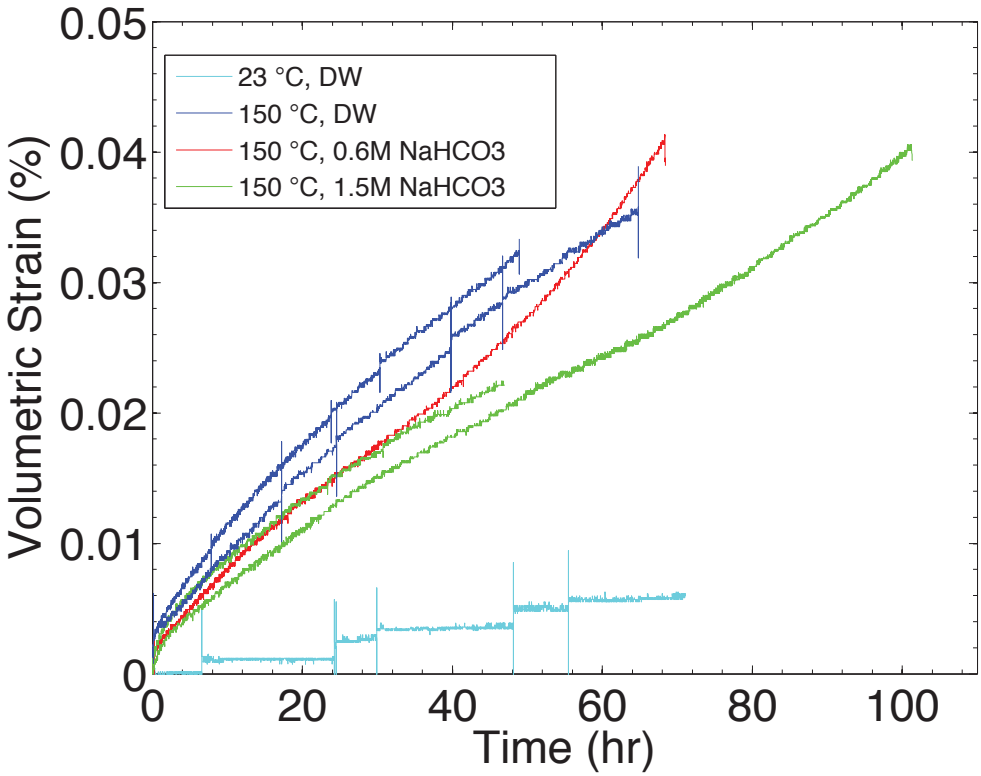
0.05
0.04
0.03
0.02
0.01
0
Volumetric Strain (%)
0
20
40
60
80
100
Time (hr)
23 °C, DW
150 °C, DW
150 °C, 0.6M NaHCO3
150 °C, 1.5M NaHCO3

FIGURE 3

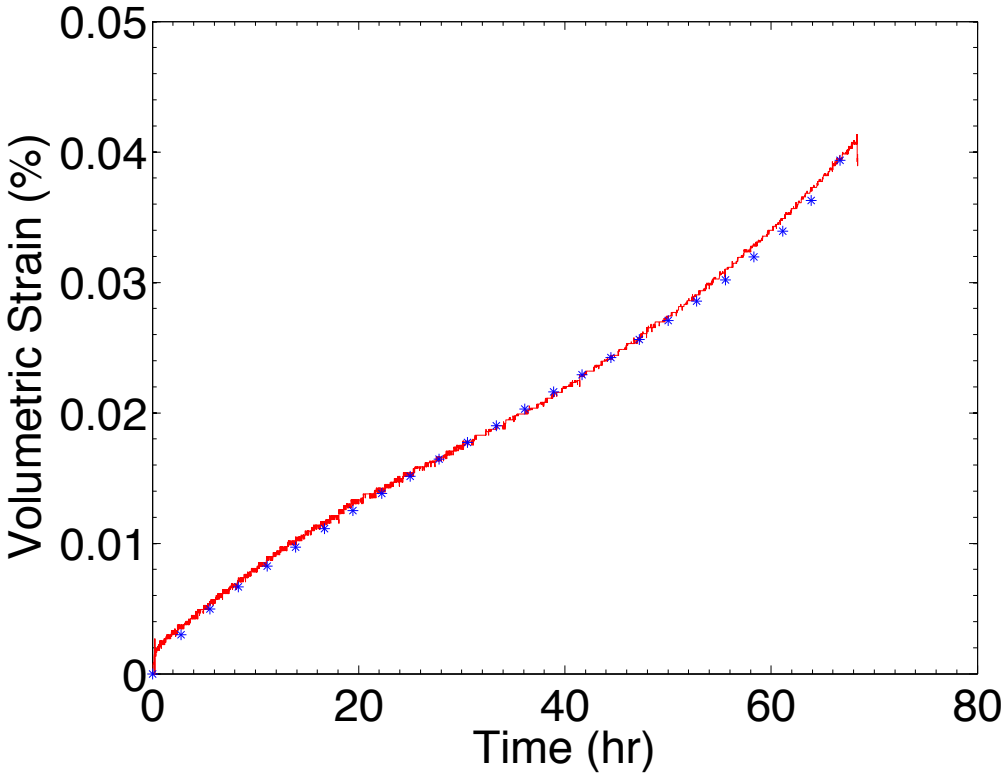

FIGURE 4

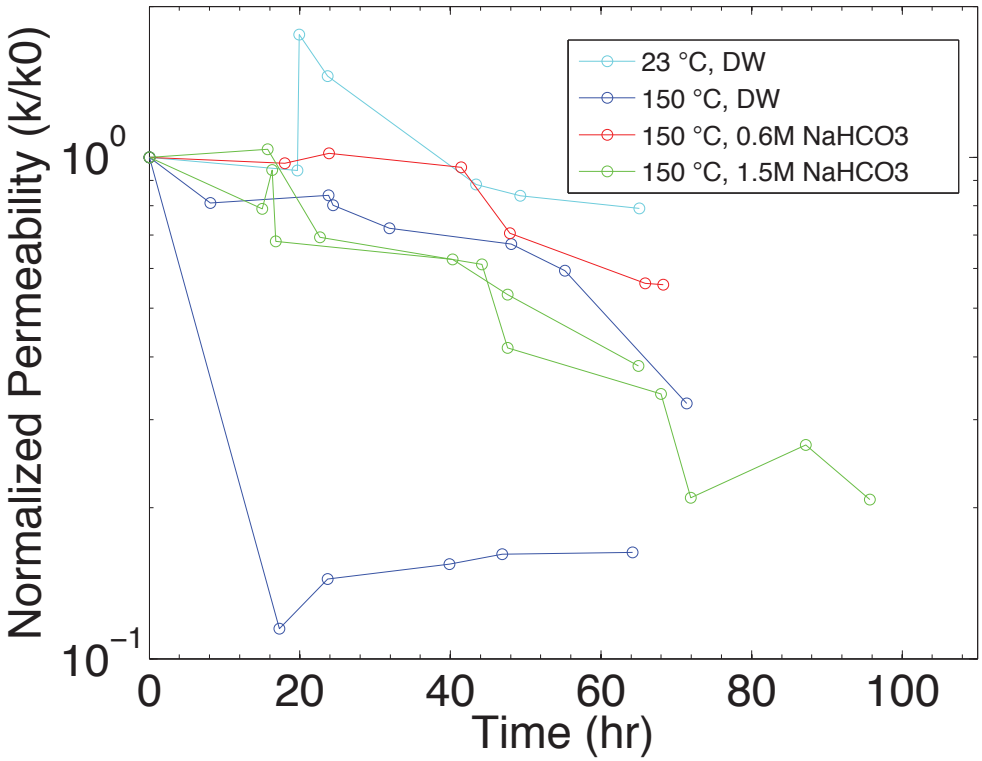
Normalized Permeability (k/k0)
10^0
10^{-1}
0
20
40
60
80
100
Time (hr)
23 °C, DW
150 °C, DW
150 °C, 0.6M NaHCO3
150 °C, 1.5M NaHCO3

FIGURE 5

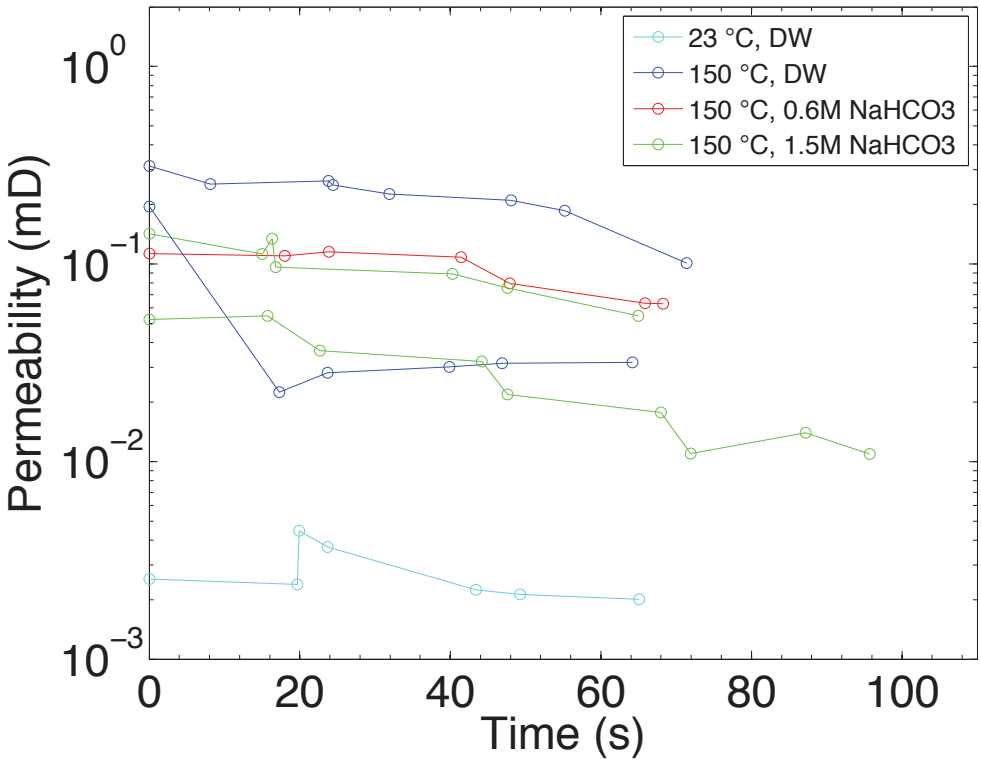
23 °C, DW
150 °C, DW
150 °C, 0.6M NaHCO3
150 °C, 1.5M NaHCO3
Permeability (mD)
10^{0}
10^{-1}
10^{-2}
10^{-3}
0
20
40
60
80
100
Time (s)

FIGURE 6

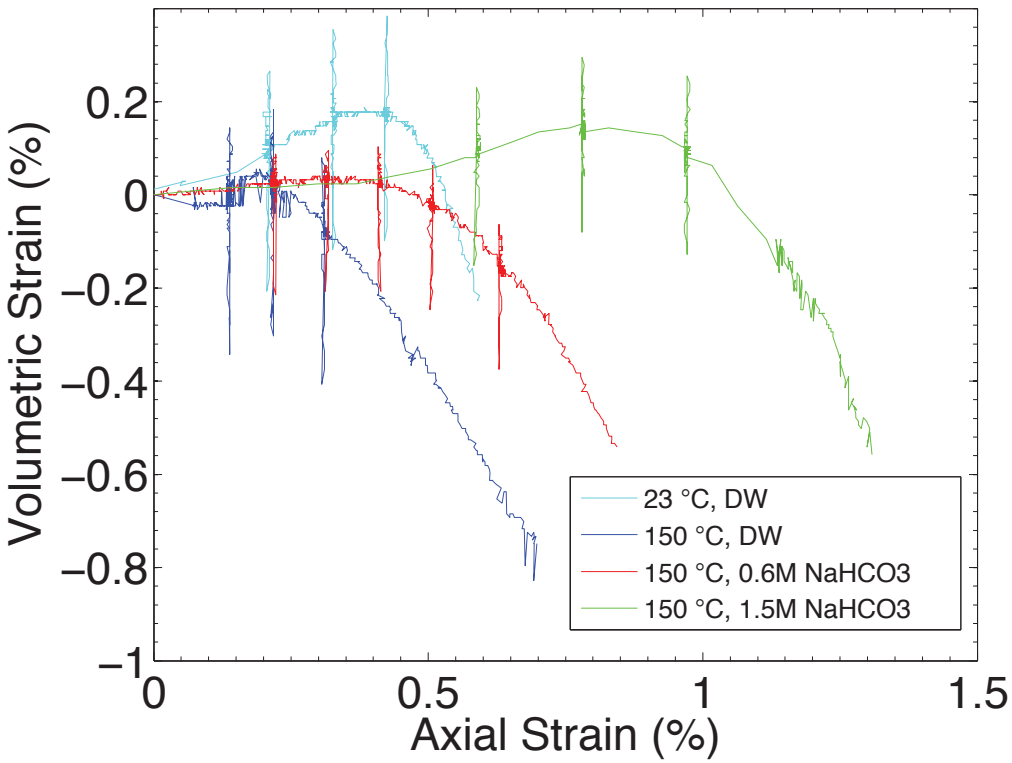
Volumetric Strain (%)
Axial Strain (%)
0.2
0
−0.2
−0.4
−0.6
−0.8
−1
0
0.5
1
1.5
23 °C, DW
150 °C, DW
150 °C, 0.6M NaHCO3
150 °C, 1.5M NaHCO3

FIGURE 7

a.

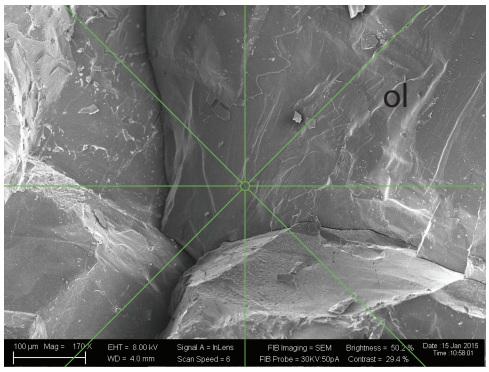

b.

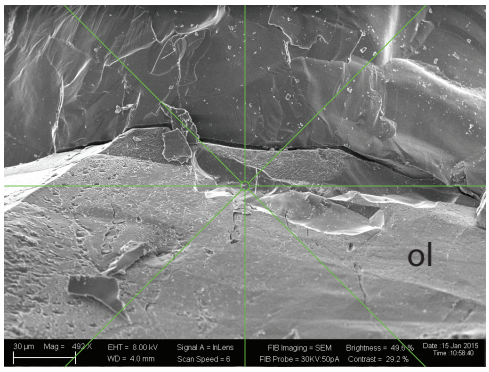

FIGURE 8

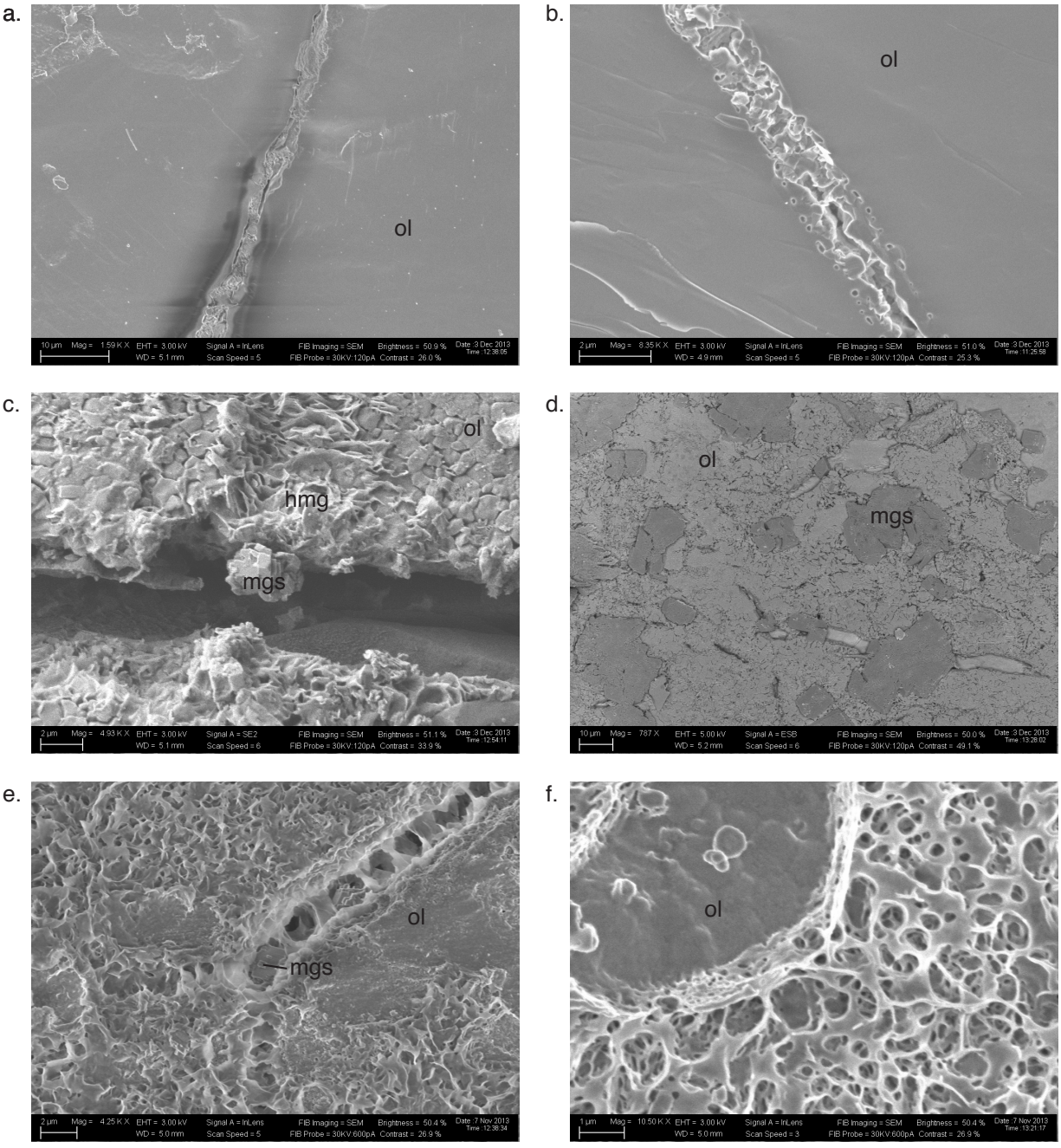

FIGURE 9

a.

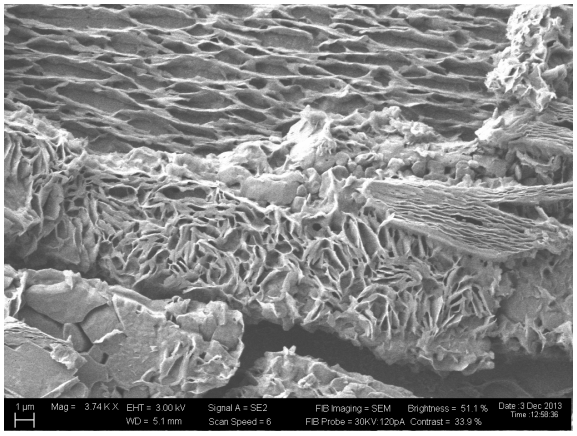

b.

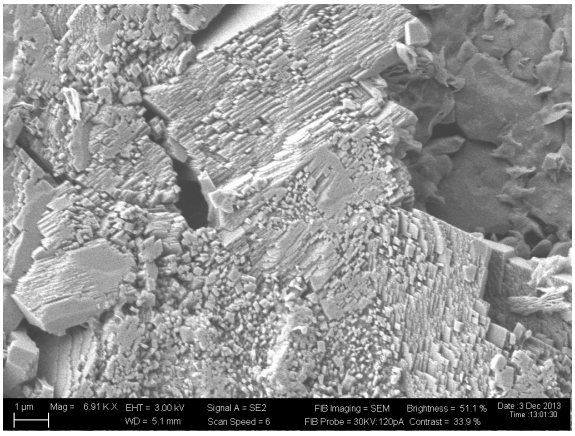

c.

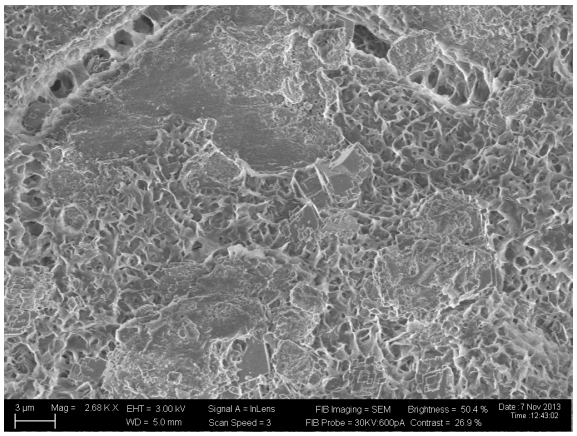

d.

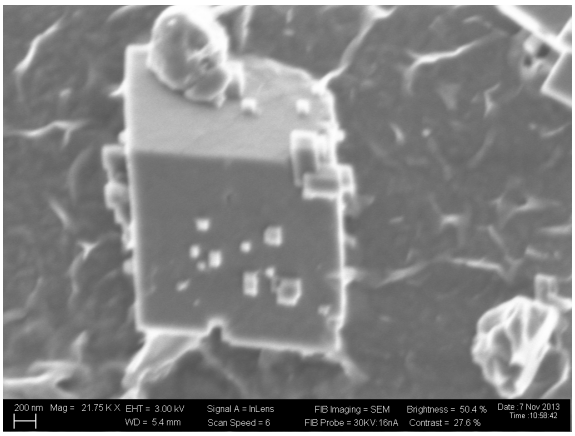

FIGURE 10

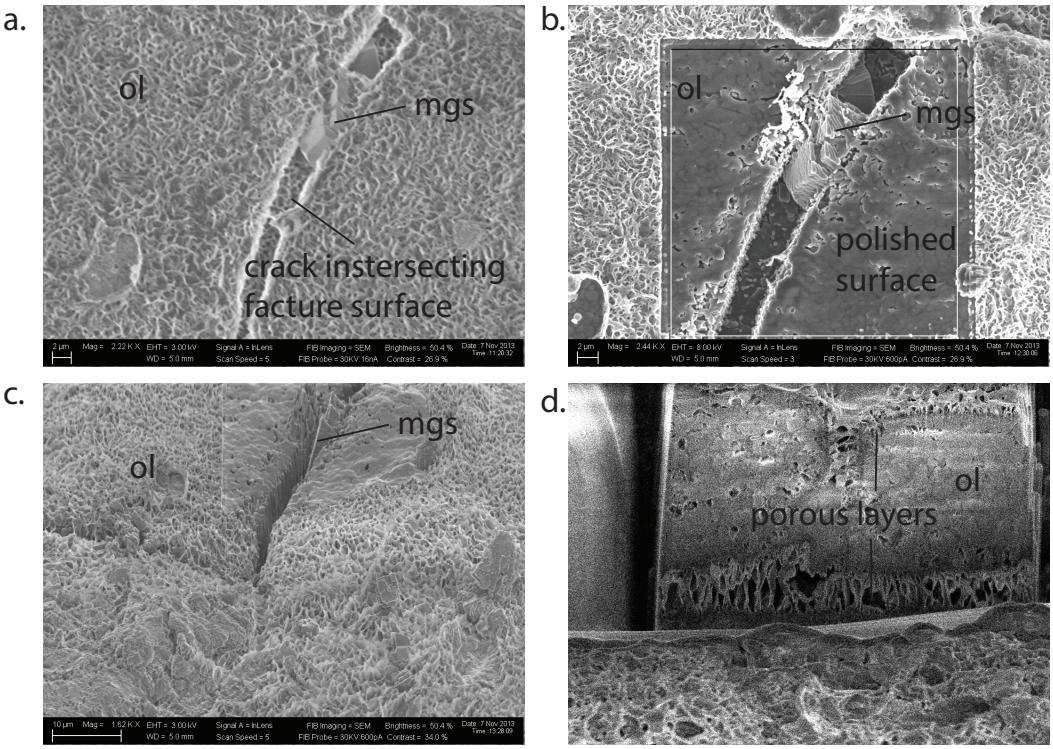
a.
ol
mgs
crack instersecting facture surface
b.
ol
mgs
polished surface
c.
mgs
ol
d.
ol
porous layers

FIGURE 11

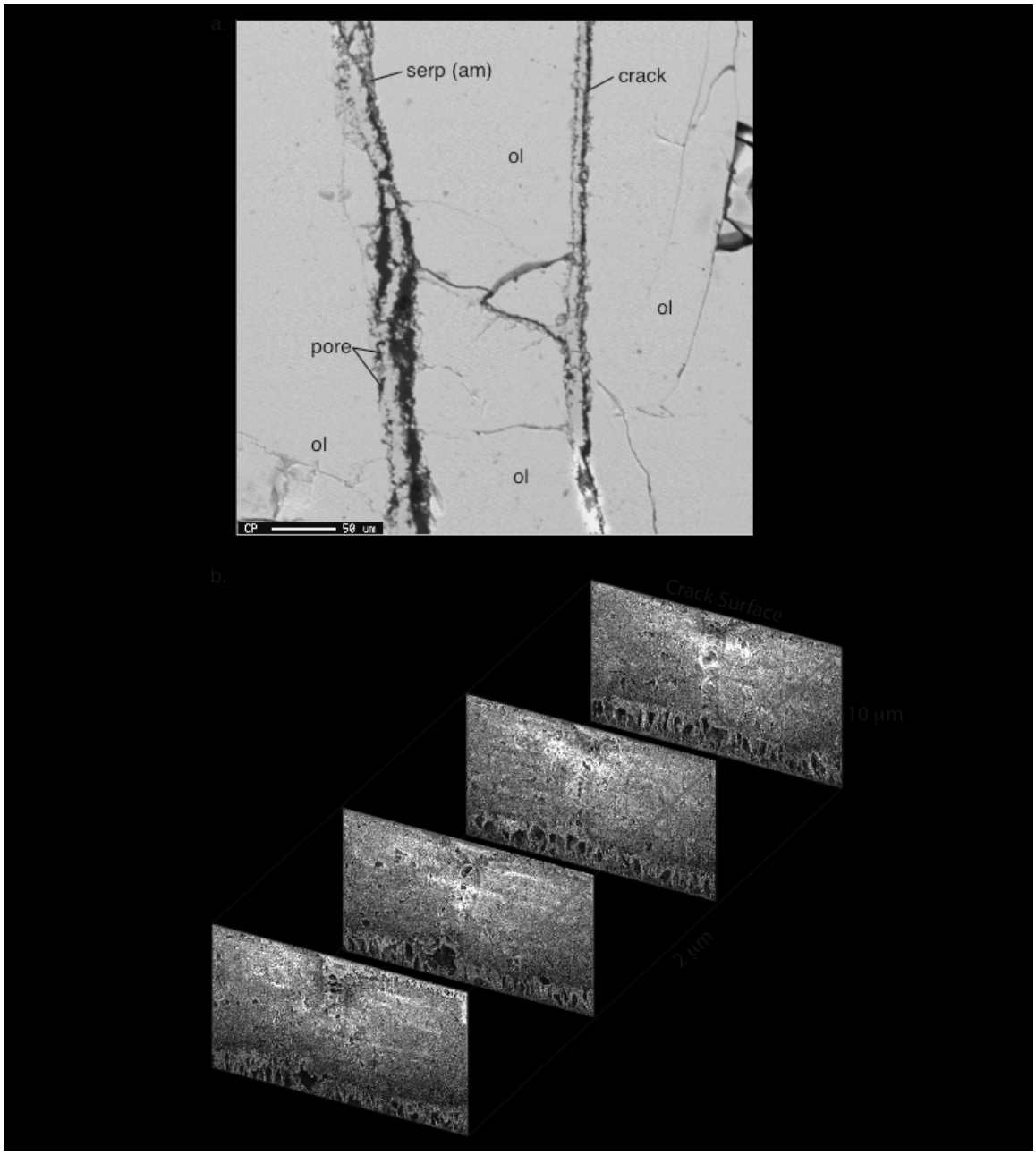
a.
serp (am)
crack
ol
ol
pore
ol
ol
CP
50 um
b.
Crack Surface
10 µm
2 µm

FIGURE 12

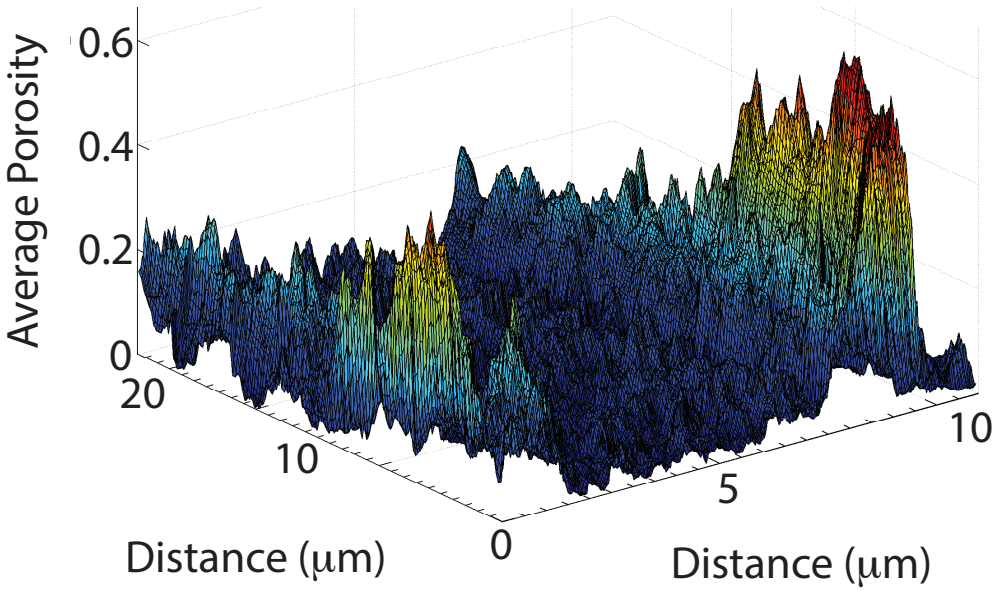
Average Porosity
0.6
0.4
0.2
0
20
10
0
Distance (μm)
10
5
Distance (μm)

FIGURE 13

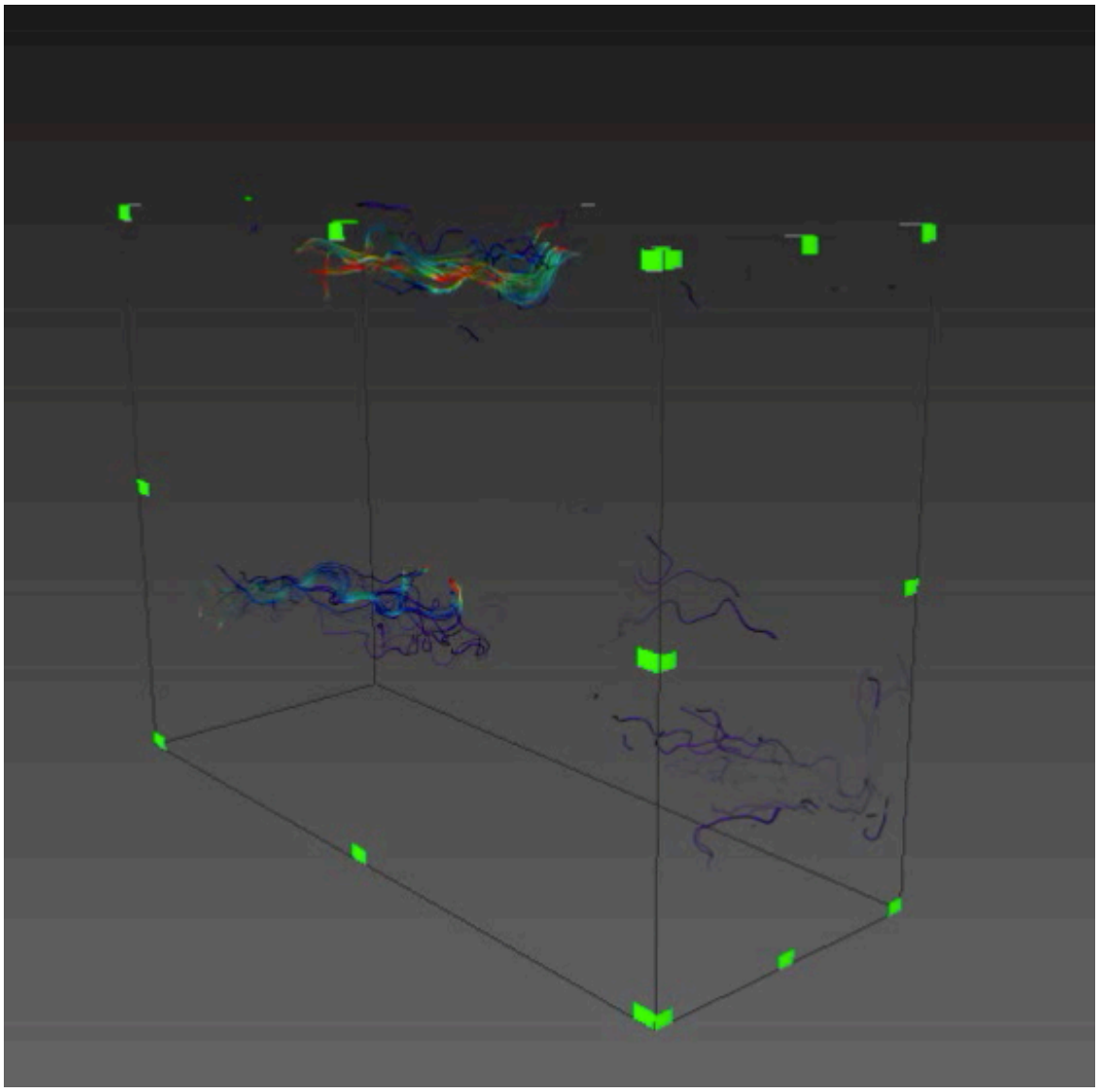

FIGURE 14

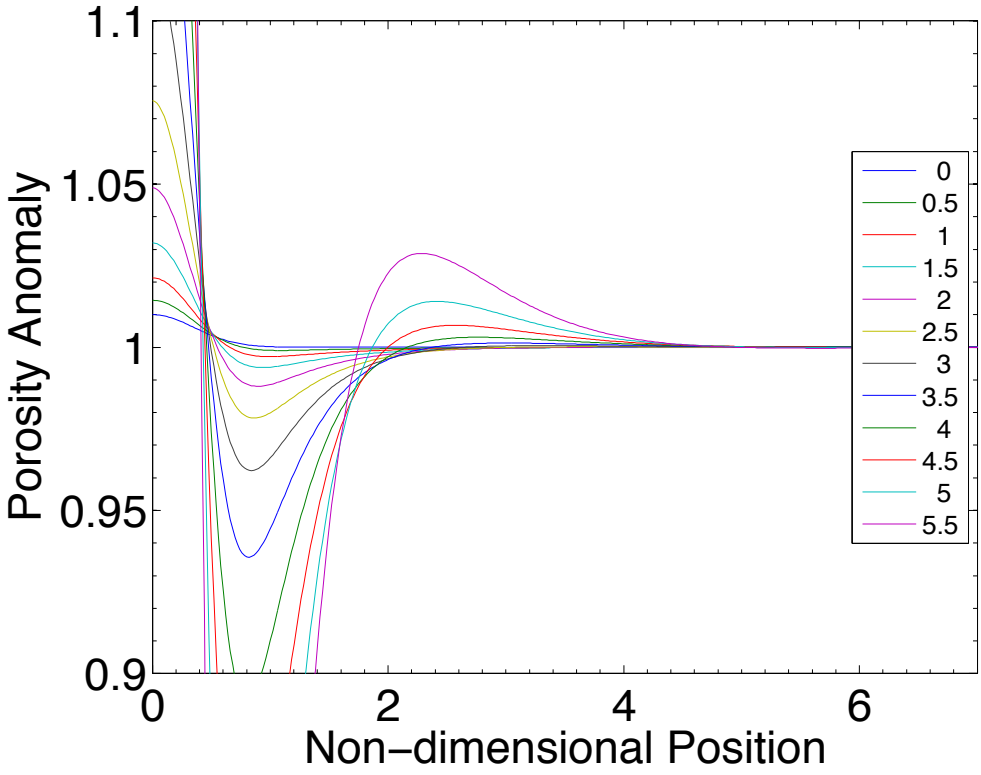
1.1
1.05
1
0.95
0.9
Porosity Anomaly
0
2
4
6
Non−dimensional Position
0
0.5
1
1.5
2
2.5
3
3.5
4
4.5
5
5.5

FIGURE 15

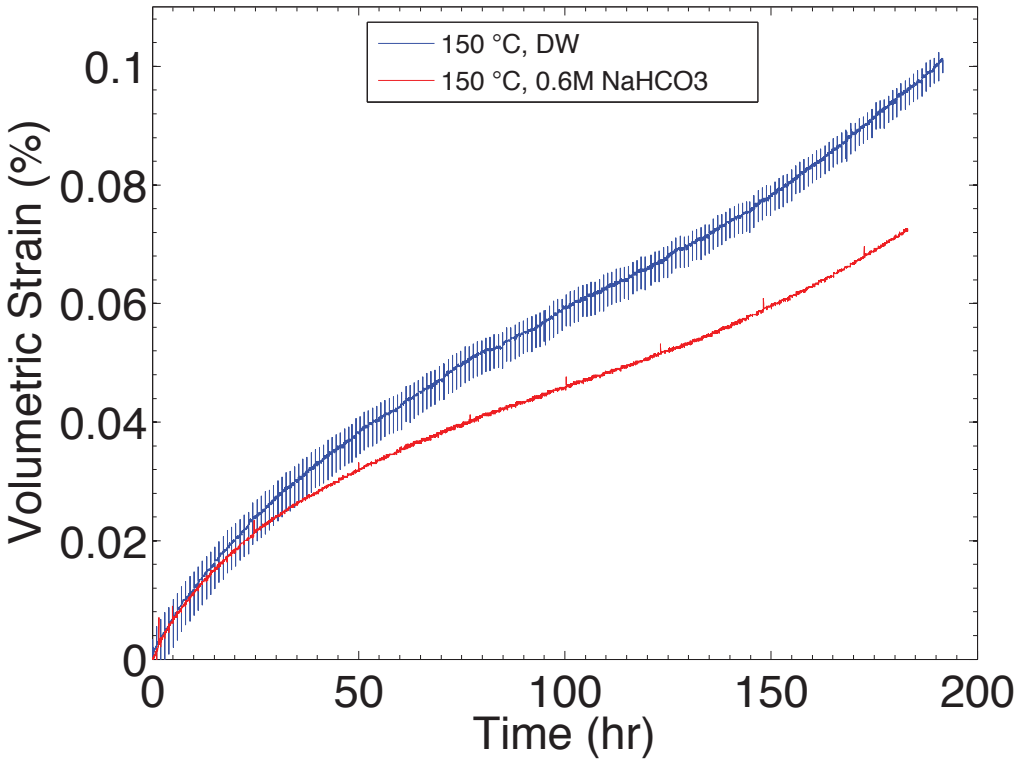
150 °C, DW
150 °C, 0.6M NaHCO3
Volumetric Strain (%)
0
0.02
0.04
0.06
0.08
0.1
0
50
100
150
200
Time (hr)

FIGURE 16

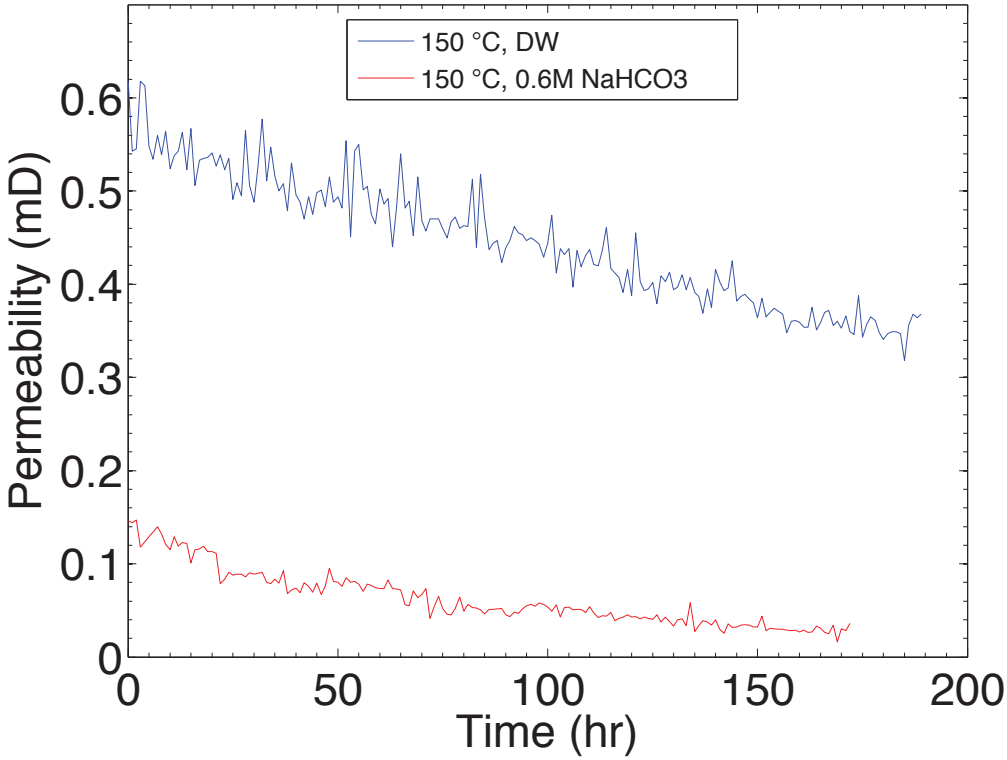
150 °C, DW
150 °C, 0.6M NaHCO3
Permeability (mD)
0
0.1
0.2
0.3
0.4
0.5
0.6
0
50
100
150
200
Time (hr)

FIGURE 17

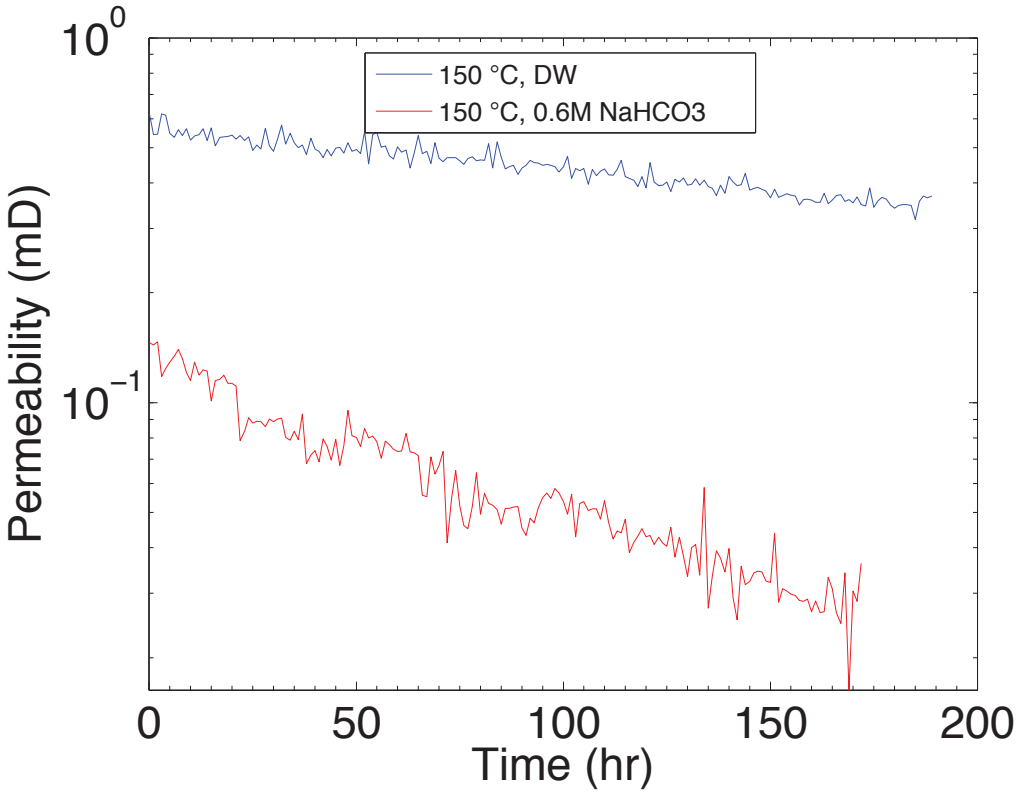
150 °C, DW
150 °C, 0.6M NaHCO3
Permeability (mD)
10^0
10^{-1}
0
50
100
150
200
Time (hr)

FIGURE 18

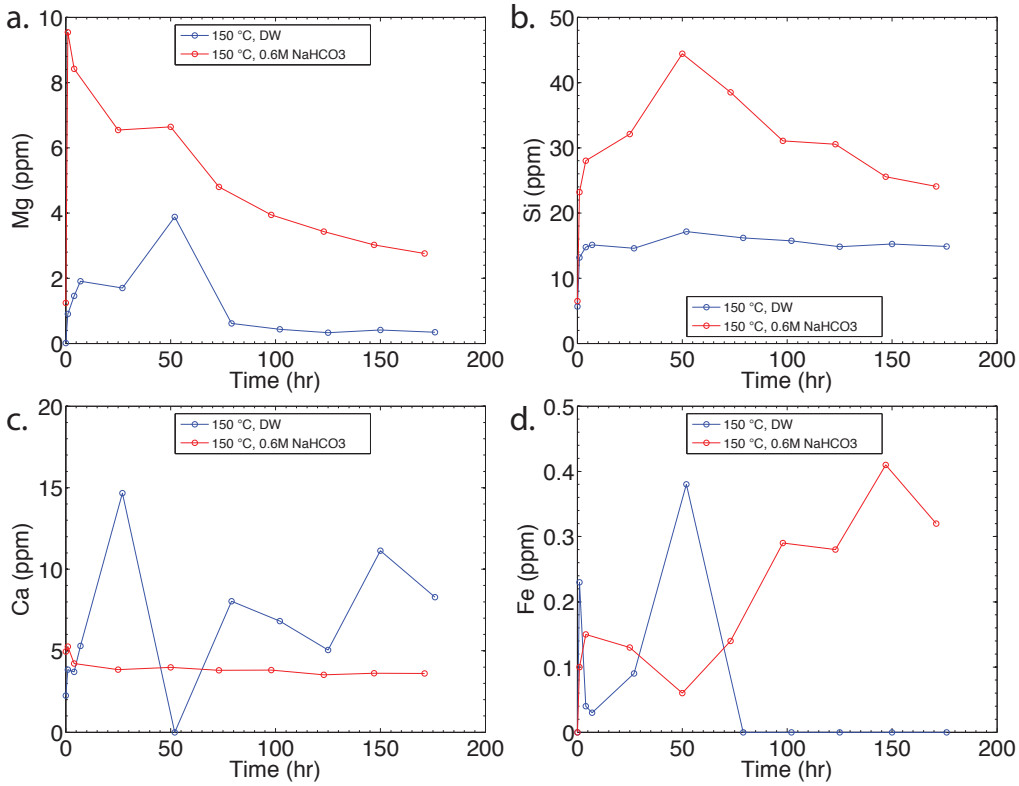
a.
Mg (ppm)
Time (hr)
150 °C, DW
150 °C, 0.6M NaHCO3
b.
Si (ppm)
Time (hr)
150 °C, DW
150 °C, 0.6M NaHCO3
c.
Ca (ppm)
Time (hr)
150 °C, DW
150 °C, 0.6M NaHCO3
d.
Fe (ppm)
Time (hr)
150 °C, DW
150 °C, 0.6M NaHCO3

FIGURE 19

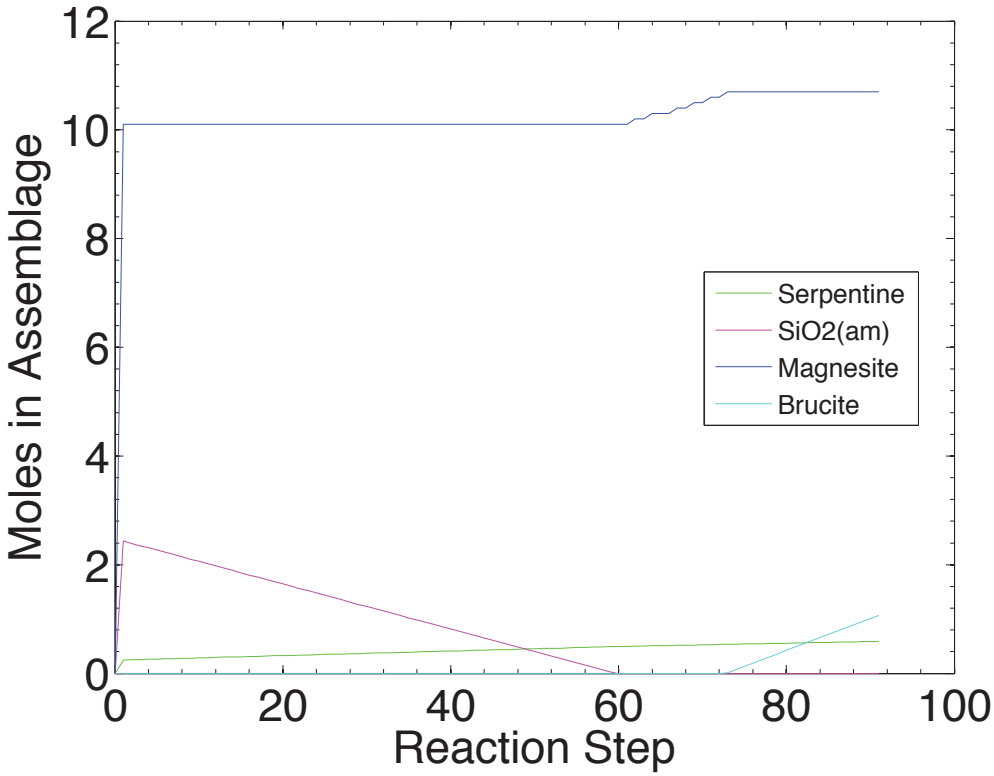
Moles in Assemblage
Reaction Step
0
2
4
6
8
10
12
0
20
40
60
80
100
Serpentine
SiO2(am)
Magnesite
Brucite

FIGURE 20

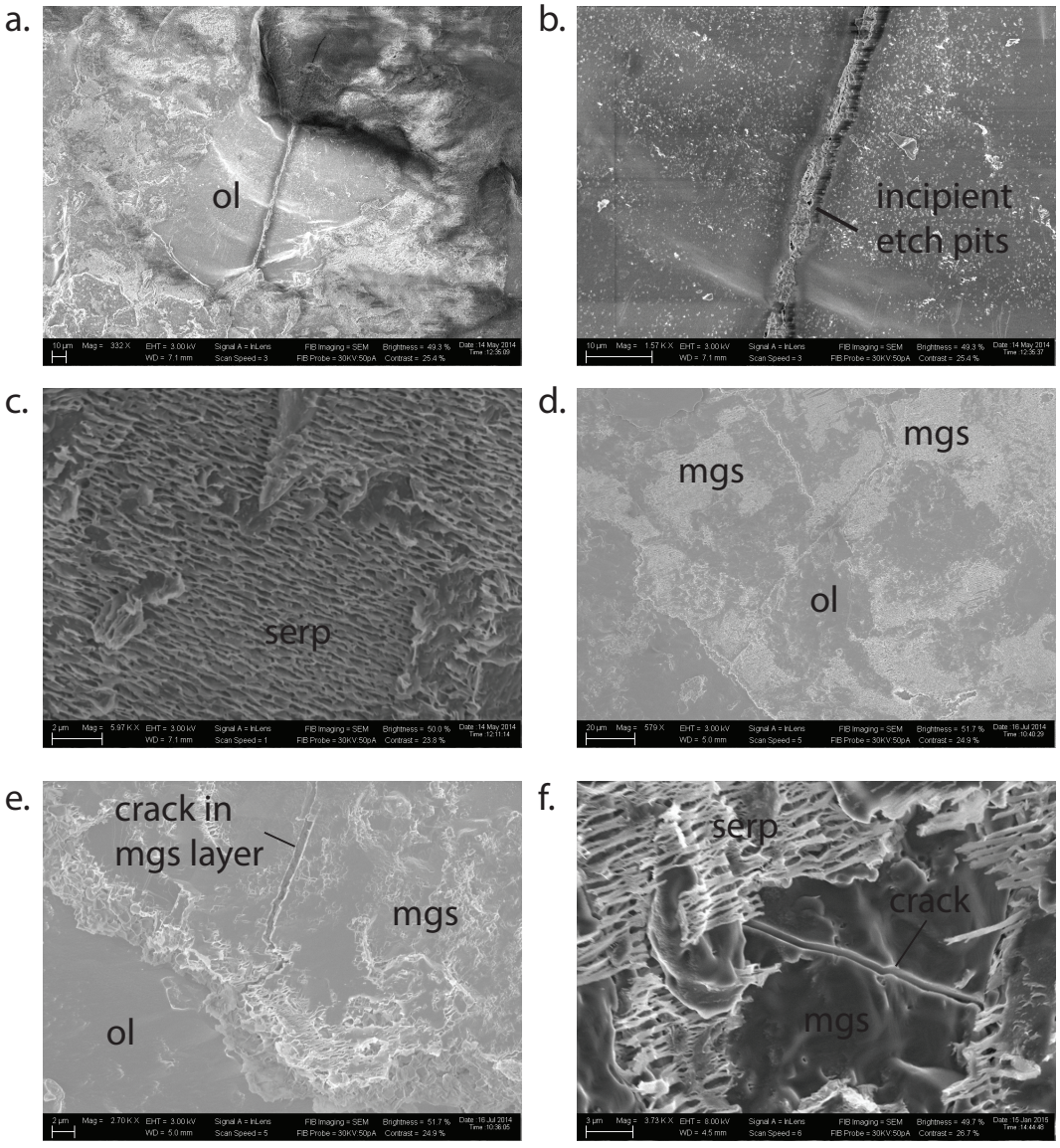
a.
ol
b.
incipient
etch pits
c.
serp
d.
mgs
mgs
ol
e.
crack in
mgs layer
mgs
ol
f.
serp
crack
mgs

FIGURE 21

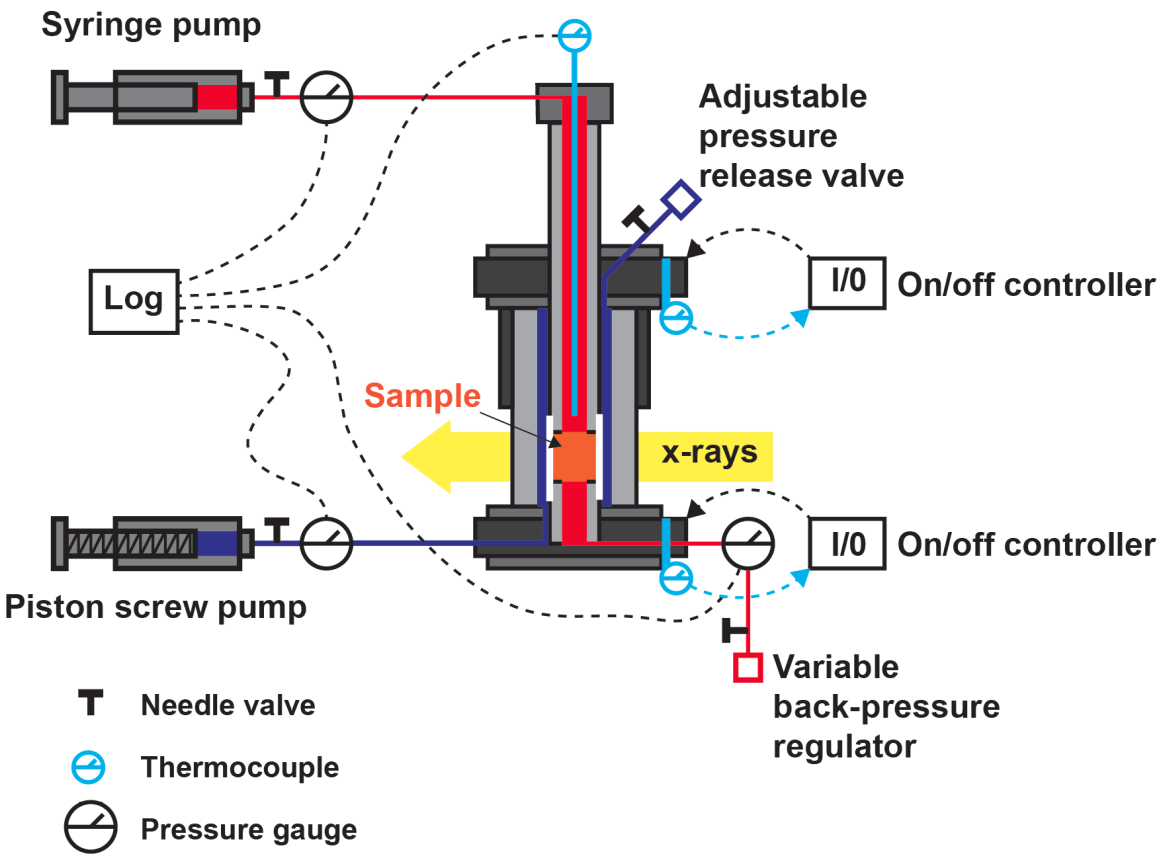
Syringe pump
Adjustable pressure release valve
Log
I/0
On/off controller
Sample
x-rays
I/0
On/off controller
Piston screw pump
Variable back-pressure regulator
Needle valve
Thermocouple
Pressure gauge

FIGURE 22

BIBLIOGRAPHY

The following **manuscripts in preparation** for submission to peer-reviewed journals will cover the key scientific and technical results of the project.

Liu, Q., Wang, Z., Zhang, S., Karato, S-I., Ague, J.J., Oristaglio, M.L., Johnson, K.T.M., Bolton, E., and Bercovici, D., 2015. The mineral carbonation potential of olivine for carbon sequestration. To be submitted to *American Journal of Science*.

Lisabeth, H., Zhu, W., and Crispin, K., 2015. Reaction textures in actively carbonating olivine aggregates.

Lisabeth, H., Zhu, W., and Kelemen, P., 2015. Reaction enhanced compaction in rapidly carbonating dunites.

Zhu, W., Fusseis, F., Lisabeth, H., Xing, T., Xiao, X., and Karato, S., 2015. Cracking via mineral carbonation in olivine: Insights from in-situ microtomography.

The following **published papers** covering related research undertaken by the principal investigators as spin-offs of the project, partially supported by project funds, have appeared in refereed journals.

Cai, Z., and Bercovici, D., 2013. Two-phase damage models of magma-fracturing, *Earth and Planetary Science Letters* **368**: 1–8.

Cai, Z., and Bercovici, D., 2014. Two-phase visco-elastic damage theory, with applications to subsurface fluid injection, *Geophys. J. Int.* **199**: 1481-1496, http://dx.doi.org/10.1093/gji/ggu344.

Tian, M., and Ague, J., 2014. The Impact of Porosity Waves on Crustal Reaction Progress and CO_2 Mass Transfer. *Earth and Planetary Science Letters* **390**: 80–92.

Fusseis, F., Steeb, H., Xiao, X., Zhu, W., Butler, I., Elphick, S., and Mäder, U., 2014. A low-cost X-ray transparent experimental cell for synchrotron-based X-ray microtomography studies at geological reservoir conditions, *Journal of Synchrotron Radiation* **21**: 251-253, doi:10.1107/S1600577513026969.

Yarushina, V., and Bercovici, D., 2013. Mineral Carbon Sequestration and Induced Seismicity, *Geophysical Research Letters* **40**, 814-818, doi: 10.1002/grl.50196.

Yarushina, V., Bercovici, D. and Oristaglio, M., 2013. Rock deformation models and fluid leak-off in hydraulic fracturing, *Geophys. J. Int.* **194** (3): 1514-1526.

The following chronological list is a **partial list of abstracts, poster papers and presentations** made at conferences covering research carried out in the project.

Wang et al., 2011. Integrated experimental and modeling studies of mineral carbonation, Workshop on Geological Carbon Capture & Storage in Mafic and Ultramafic Rocks, January 8–10, 2011, Oman.

Wang et al., 2011. An experimental study of mineral sequestration of CO_2 by mafic/ultramafic rocks, AGU Fall Meeting 2011, 5–9 December 2011.

Qiu et al., 2012. Integrated experimental and modeling studies of mineral carbonation, USGS Workshop on Carbon Sequestration in Unconventional Reservoirs, March 28–29, 2012.

Qiu et al., 2012. Experimental study of the kinetics of CO_2-sequestration by olivines and Hawaiian picrites, 22nd V.M. Goldschmidt Conference, June 24–29, 2012, Montréal, Canada

Qiu et al., 2013. Experimental study of the reaction kinetics between CO_2-bearing solution and olivine, 23rd V.M. Goldschmidt Conference, August 25–30, 2013, Florence, Italy.

Zhang et al., 2012, Experimental Study of the Kinetics of CO2-Sequestration by Hawaiian Picrites, AGU Fall Meeting, 3-7 December 2012, San Francisco.

Zhang et al., 2013. Experimental study of the reaction kinetics between CO2-bearing solution and picrite cubes, AGU Fall Meeting, 9-13 December 2013, San Francisco.

Zhu, W., Fusseis, F., Lisabeth, H., and Xiao, X., 2013. In-situ X-ray Synchrotron Microtomography: Real Time Pore Structure Evolution during Olivine Carbonation. Abstract MR31A-2293, 2013 Fall Meeting, AGU Fall Meeting, 9-13 December 2013, San Francisco.

Lisabeth, H., Zhu, W., Kelemen, P.B., 2013. Effect of CO_2-saturated brine on the mechanical and hydraulic behavior of dunite. Abstract MR33B-08, AGU Fall Meeting, 9-13 December 2013, San Francisco.

Lisabeth, H., Zhu, W., Kelemen, P.B., 2014. A grain scale mechanism for olivine carbonation in rapidly carbonating dunites. Poster presentation at the Gordon Research Conference on Rock Deformation, Tilden, NH, August 2014.

Zhu, W., Fusseis, F., Lisabeth, H., and Xiao, X., 2014. Real time pore structure evolution during olivine mineral carbonation. Abstract V52A-2328, 2014 Fall Meeting, AGU, San Francisco, CA.

APPENDICES

APPENDIX A – SUPPLEMENT TO PART I (GEOCHEMICAL EXPERIMENTS)

APPENDIX B – SYNTHETIC ROCK SAMPLES

APPENDIX C – AUTOCLAVE DESIGN

APPENDIX D – FIELDWORK: SAMPLE COLLECTION AND ANALYSIS

APPENDIX E – MODELING CODES

APPENDIX A – SUPPLEMENT TO PART I (GEOCHEMICAL EXPERIMENTS)

A.1 Modeling carbonation reactions with EQ3/6

We used the general-purpose geochemical modeling program EQ3/6 to simulate carbonation reactions comparable to our experiments (Wolery, 2002; works referenced in this Appendix can be found in the References for Part I). As described in Part I, the reactions described by the set of equations (11, 12, 13a, 14a, 15a) are available to model olivine carbonation in the standard databases of thermodynamic parameters available with EQ3/6. For most runs, we chose the database file SHV, based on the program SUPCRT92 (Johnson et al. 1992), because of its internal consistency and range of chemical elements and species of interest in fluid-rock interactions. In models involving the solid phase of sodium bicarbonate (nahcolite), we used the composite data file CMP that comes with EQ3/6, because nahcolite parameters are not available in SHV.

We calculated activity coefficients using three standard methods: B-dot (Helgesen, 1969), Davies (1962), and Pitzer (1991). The three methods agree reasonably well for concentrations below 1 *m*, but diverge at higher concentrations. We used the B-dot equation for its self-consistency and for the larger number of species included. Because the concentrations of all species except N^+ and HCO_3^- are low, their calculated activities can be used in other solutions having the same concentration of $NaHCO_3$. Also, since our sealed experimental apparatus did not allow direct measurement of the solution pH during reactions at 200°C and 150 bar, we used EQ3/6 to calculate initial and final pH values of the solution from its elemental concentrations by assuming negligible variation in the sodium ion (Na^+) concentration during experiments (see Section A.5).

We assumed for the model an ideal mixing of forsterite (Mg_2SiO_4) and fayalite (Fe_2SiO_4) end members to calculate the thermodynamic properties of olivine samples used in the experiments. We also assumed that the overall dissolution rate of samples is controlled by dissolution of the abundant forsterite end member, and then partitioned it according to the proportions of the forsterite and fayalite end-

members, so that samples in the model dissolve congruently—that is, the Mg/Fe ratio going into solution at any moment is the same as the ratio in the olivine mineral structure. The EQ3/6 software treats olivine dissolution using classical transition state theory taking into account proton-, water- and hydroxyl-promoted mechanisms (Lasaga, 1981; Aagaard and Helgeson, 1982; Schott et al., 2009), which are represented as follows:

$$r = S \cdot k_{\mathrm{H}}^{298.15K} \cdot \exp\left[-\frac{E_{\mathrm{H}}}{R}\left(\frac{1}{T}-\frac{1}{298.15}\right)\right] \cdot a_{\mathrm{H}}^{n_1} \cdot \left[1-\ \exp\left(\frac{A}{RT}\right)\right]$$

$$+ S \cdot k_{\mathrm{H_2O}}^{298.15K} \cdot \exp\left[-\frac{E_{\mathrm{H_2O}}}{R}\left(\frac{1}{T}-\frac{1}{298.15}\right)\right] \cdot a_{\mathrm{H_2O}}^{n_2} \cdot \left[1-\ \exp\left(\frac{A}{RT}\right)\right]$$

$$+ S \cdot k_{\mathrm{OH}}^{298.15K} \cdot \exp\left[-\frac{E_{\mathrm{OH}}}{R}\left(\frac{1}{T}-\frac{1}{298.15}\right)\right] \cdot a_{\mathrm{OH}}^{n_1} \cdot \left[1-\ \exp\left(\frac{A}{RT}\right)\right],$$

where *S* is the surface area, *k* is the rate constant, *E* is the activation energy, *n* is the reaction order, and *A* is the chemical affinity. For reaction-rate parameters, we used the compilation by Palandri and Kharaka (2004). This treatment of the kinetics applies only to the dissolution of olivine in the simulations; for the rest, EQ3/6 calculates the formation of minerals such as magnesite and magnesium silicates by rules governing instantaneous partial equilibrium (to avoid super-saturation).

A.2 Tracking reaction paths

To follow the reaction paths for the experiments lasting 1, 3, 5, and 14 days, intermediate results were projected onto the space spanned by the activity coordinates, $\log\left(a_{\mathrm{Mg^{2+}}}/a_{\mathrm{H^{+}}}^2\right)$ and $\log a_{\mathrm{SiO_2}(aq)}$. In this space, phase boundaries are based on the following equations for mineral-solution equilibrium (Marini, 2007):

Forsterite: $$\mathrm{Mg_2SiO_4 + 4H^+ \leftrightharpoons 2Mg^{2+} + SiO_{2(aq)} + 2H_2O} \quad \text{(A1)}$$

Magnesite $$\mathrm{MgCO_3 + H^+ \leftrightharpoons Mg^{2+} + HCO_3^-} \quad \text{(A2)}$$

Silica (amorphous, "*am*") $$\mathrm{SiO_{2(am)} \leftrightharpoons SiO_{2(aq)}} \quad \text{(A3)}$$

Quartz $$\mathrm{SiO_2}(quartz) \leftrightharpoons \mathrm{SiO_{2(aq)}} \quad \text{(A4)}$$

Brucite $$\mathrm{Mg(OH)_2 + 2H^+ \leftrightharpoons Mg^{2+} + 2H_2O} \quad \text{(A5)}$$

Talc $$\mathrm{Mg_3Si_4O_{10}(OH)_2 + 6H^+ \leftrightharpoons 3Mg^{2+} + 4SiO_{2(aq)} + 4H_2O} \quad \text{(A6)}$$

Chrysotile $$\mathrm{Mg_3Si_2O_5(OH)_4 + 6H^+ \leftrightharpoons 3Mg^{2+} + 2SiO_{2(aq)} + 5H_2O} \quad \text{(A7)}$$

Antigorite $$\mathrm{Mg_{48}Si_{34}O_{85}(OH)_{62} + 96H^+ \leftrightharpoons 48Mg^{2+} + 34SiO_{2(aq)} + 79H_2O} \quad \text{(A8)}$$

with corresponding equilibrium constants:

$$\log K_{\text{forsterite}} = 2\log\left(a_{\mathrm{Mg^{2+}}}/a_{\mathrm{H^+}}^2\right) + \log a_{\mathrm{SiO_2(aq)}} + 2\log a_{\mathrm{H_2O}} \quad \text{(A1a)}$$

$$\log K_{\text{magnesite}} = 2\log\left(a_{\mathrm{Mg^{2+}}}/a_{\mathrm{H^+}}^2\right) + \log a_{\mathrm{HCO_3^-}} + 2\log a_{\mathrm{H^+}} \quad \text{(A2a)}$$

$$\log K_{\text{silica}} = \log a_{\mathrm{SiO_2(aq)}} \quad \text{(A3a)}$$

$$\log K_{\text{quartz}} = \log a_{\mathrm{SiO_2(aq)}} \quad \text{(A4a)}$$

$$\log K_{\text{brucite}} = \log\left(a_{\mathrm{Mg^{2+}}}/a_{\mathrm{H^+}}^2\right) + 2\log a_{\mathrm{H_2O}} \quad \text{(A5a)}$$

$$\log K_{\text{talc}} = 3\log\left(a_{\mathrm{Mg^{2+}}}/a_{\mathrm{H^+}}^2\right) + 4\log a_{\mathrm{SiO_2(aq)}} + 4\log a_{\mathrm{H_2O}} \quad \text{(A6a)}$$

$$\log K_{\text{chrysotile}} = 3\log\left(a_{\mathrm{Mg^{2+}}}/a_{\mathrm{H^+}}^2\right) + 2\log a_{\mathrm{SiO_2(aq)}} + 5\log a_{\mathrm{H_2O}} \quad \text{(A7a)}$$

$$\log K_{\text{antigorite}} = 48\log\left(a_{\mathrm{Mg^{2+}}}/a_{\mathrm{H^+}}^2\right) + 34\log a_{\mathrm{SiO_2(aq)}} + 79\log a_{\mathrm{H_2O}}. \quad \text{(A8a)}$$

The equilibrium constants are given by thermodynamic databases. If the activities of water and bicarbonate ions are held constant, each of these equations for mineral-solution equilibrium projects to a straight line with $\log\left(a_{\mathrm{Mg^{2+}}}/a_{\mathrm{H^+}}^2\right)$ plotted versus $\log a_{\mathrm{SiO_2(aq)}}$. For example,

$$\log\left(a_{\mathrm{Mg^{2+}}}/a_{\mathrm{H^+}}^2\right) = -\frac{4}{3}\log a_{\mathrm{SiO_2(aq)}} + \frac{1}{3}\left(\log K_{\text{talc}} - 4\log a_{\mathrm{H_2O}}\right).$$

Trial calculations indicated that there is little variation of water activity during simulated runs, but there was obviously some variation of bicarbonate ion activity ($a_{\mathrm{HCO_3^-}}$), from carbonate ions being removed

from solution and from changes in pH brought about by the carbonation reaction. Thus, the intercept of the horizontal magnesite equilibrium line (A2a)—which is fixed by the pH and carbonate activity—changes as the simulation evolves (generally the vertical position of this line rises on the plot). All other lines stay fixed.

In addition to the activity plot, several other plots are useful to track the progress of the simulated reactions for comparison to the experimental results: variation of the carbonation fraction, the pH and the elemental concentrations in solution, and the partitioning of Mg ions among the different mineral present.

A.3 Simulations

Simulations were run for 1 *m* and 3 *m* concentrations of $NaHCO_3$ solution with the actual masses of fluid, olivine powders and olivine grains used in specific experiments. In a first set of model runs, we used the surface areas of samples as measured by BET: 707,000 cm^2/g for Batch-A olivine powders and 42.3 cm^2/g for olivine grains (section 3.1). As shown in Figure A1, the simulations with these parameters yielded carbonation fractions and pH values (of the final solution) that were generally much higher than those observed in the experiments, especially for the models designed to simulate carbonation of olivine grains. There can be many explanations for these differences, including mismatches between the any of measured properties of the samples and compiled thermodynamic parameters in the databases. But reactive surface area is probably the least understood and most uncertain parameter. So, for comparison, we ran a second set of simulations in which surface areas were reduced to 2.3 cm^2/g for the olivine grain simulations and to 1340 cm^2/g for the olivine powder simulations. Note that these new values are comparable to (but still smaller than) the geometric surface areas estimated from the sizes of the samples (see Section 3.1).

As shown in Figure 11 of Part I, evolution of the solution pH and the carbonation fraction in the simulations with reduced reactive surface areas follows more closely the experimental values. Results for the elemental concentration of Si in solution also matched the experimental values reasonably well, but the results for Mg and Fe still fall well below the measured concentrations of these elements. A feature of

reactions (11, 12, 13a, 14a, 15a) in Part I is that magnesite can continue to precipitate even as secondary silicates compete for magnesium ions in solution. In this model, competition for magnesium ions limits, but does not reverse, the carbonation fraction as the reaction proceeds through 14 days (Figure 10, Part I).

A.3 Modeling the effect of solution chemistry on olivine carbonation

Most of the results observed in the experiments and simulations can be understood through classical transition state theory. Consider, for example, the results showing a strong linear correlation of the carbonation fraction with the concentration of sodium bicarbonate in the starting solution (Figures 4 and 5, Part I), which can be written

$$F_C = B \times m_{\mathrm{NaHCO_3}} + A, \tag{A9}$$

where A and B are constants determined by the fit to experimental results.

The basic carbonation reaction (equations 11 and 12 in Part 1) can be combined into the following elementary reaction:

$$0.5\ \mathrm{Mg_2SiO_{4(s)}} + \mathrm{HCO3^-} \longrightarrow \mathrm{MgCO_3} + 0.5\ \mathrm{SiO_{2(aq)}} + \mathrm{OH^-}. \tag{A9}$$

The overall rate for this reaction may be expressed as follows:

$$r = r_+\left(1 - e^{\Delta G/RT}\right), \tag{A10}$$

where r_+ is the forward reaction rate, ΔG is the Gibbs energy difference between products and reactants, R is gas constant, and T is the absolute temperature.

Although the mineral phase in the transitional state is unknown—it could be the complex of water-Mg-SiO_2-HCO_3^-, or metastable nesquehonite, or hydrous magnesite)—transition state theory suggests that the forward reaction rate may nevertheless be written as follows:

$$r_+ = k[\mathrm{HCO_3^-}][\mathrm{Mg_2SiO_4}]^{0.5}, \tag{A11}$$

where k is reaction constant that can be expressed as follows:

$$k = f(T)e^{-\Delta G^*/RT}, \quad \text{(A12)}$$

where ΔG^* is the energy difference between the transition state phase and the reactants, and $f(T)$ is a function of temperature.

Equation (A11) indicates that the reaction rate r_+ should be proportional to the concentration of bicarbonate ions. The reaction rate multiplied by the reaction time gives the total amount of carbonate produced. Since the concentration of the starting solution is the only parameter that varies in Figure 7 (Part 1), the reaction constant k (equation A11) will map to the slope b (equation A9) divided by the reaction time. Equation (A12) also predicts that the slope B will be a function of the experimental temperature and the Gibbs free energies of reactants and products. An increase in the surface area of olivine will raise its total Gibbs energy, but reduce ΔG^*, so it is to be expected that Batch-A olivine powders, with high surface areas, have bigger k (or B) values than Batch-B olivine powders and olivine grains. The experimental results are all consistent with these observations.

This correlation between the slope B (controlling the carbonation reaction) and the surface area of olivine (controlling the dissolution rate of olivine) suggests a coupling between dissolution and carbonation rates—that is, a larger surface area of olivine should give a higher dissolution rate, leading to a higher concentration of divalent ions in solution, resulting in a higher carbonation rate. This coupling could, however, be compromised by the formation of secondary silicates and the length of the experiment. For example, slope B increases with reaction time in experiments using Batch-A olivine powders until conditions promoting the formation of secondary silicates prevail, as discussed in section 5.3. The slope B thus decreases with reaction time after 5 days (Figure 12, Part 1).

Equation (A11) predicts of course that reaction rate should go to zero with the concentration of the sodium bicarbonate solution. The straight line fit to the experimental results for sodium bicarbonate solutions gives effectively zero intercept. But the intercept calculated reactions between $KHCO_3$ solutions and Batch-B olivine powders is finite within the estimated error, $A = -0.022 \pm 0.004$. This result indicates that some cations in the reacting solution could have subtle second-order effects on carbonation,

as suggested by McKelvy et al. (2006), who determined that $NaHCO_3$ was most effective for olivine carbonation among bicarbonate solutions containing alkali-group metals (including Li, K, and Na) at a similar concentration. The difference could be explained by the possible involvement of cations in the formation of the transition state phase: for example, sodium (Na) may not pose an energy barrier for the formation of transition state phase, whereas potassium (K) or lithium (Li) does. This difference could also be understood by the affinities of these alkali-group metals to the carbonate structure. For example, the ionic radius of $^{VI}Na^{+}$ with a coordination number of 6 at 102 pm (picometer) is smaller than that of $^{VI}K^{+}$ (138 pm) and closer to that of $^{VI}Mg^{2+}$ (72 pm) (Shannon, 1976). Thus, Na^{+} might be more suitable in the structure of magnesite than K^{+}. The elemental maps of carbonated olivine cross-sections from our experimental runs that a small, but significant, amount of Na is present not only on the magnesite surface as proposed previously (Oh et al., 1973), but also in the magnesite interior (Figures 8 and 9, Part I).

A.4 Determining the carbonation fraction

As described in the text, we calculated the net carbonation fraction for most of our experiments by comparing the dissolved inorganic carbon (DIC) before and after reactions, as determined by titration of the starting and final solutions. The accuracy of this calculation depends on the handling of samples and on the precision of DIC and pH measurements. Errors can arise during sample preparations, carbonation experiments, and post-experiment handling and processing (Figure A2). Sources of systematic error include the following: (1) temperature fluctuation: pH values of all experiments were measured at room temperature, whereas experiments were carried out at 200°C; (2) loss of carbon in handling: carbon could be lost as CO_2 when welding gold capsules and when opening the sealed capsules; (3) inaccurate dilution: all solutions were diluted after experiments for pH measurements and titration to determine DIC; (4) ambient interference: atmospheric CO_2 could interfere with pH measurements when the concentration of the solution is low.

We performed a series of tests with standards to quantify the net effect of these sources of systematic error. Figure A3 shows total DIC measured for standard $NaHCO_3$ solutions reduced to 1 *m*

concentration—that is, before titration, all solutions containing Na^+ ions at concentrations higher than 1 *m* were first diluted to 1 *m*, then diluted further by 400 times for DIC measurement by titration. No olivine was added to these solutions, so that in theory the carbon content in the gold capsule should not have changed after experimental handling, including cooking in the reaction vessel.

Figure A3 show, however, that DIC in these standards measured after experimental handling are generally lower than the starting values. This loss of carbon represents a systematic error. For example, the average DIC value determined for samples of standard 1-*m* $NaHCO_3$ solution was 0.929±0.0101 mol/kg (7 samples). (All precisions quoted in this section are at one standard deviation.) After experimental handling and different lengths of time in the reaction vessel, samples of the same 1-*m* $NaHCO_3$ solution were analyzed to have the following DIC concentrations:

0.870±0.006 after 1 day (4 samples),

0.875±0.012 after 3 days (7 samples),

0.884±0.011 after 5 days (18 samples),

0.906±0.005 after 10 days (2 samples), and

0.877±0.010 after 14 days (2 samples).

Similarly, the DIC concentrations of standard 3-*m* pure NaHCO3 solutions after experimental handling were determined to be:

0.899±0.002 after 1 day (2 samples),

0.858±0.029 after 3 days (4 samples)

0.899±0.010 after 5 days (5 samples), and

0.920 after 10 days (1 sample).

The loss of carbon reflected in these values has little correlation with the length of time in the reaction chamber. The loss was therefore treated as a correction factor, applicable both to the standards and to the samples undergoing carbonation reactions. In computing the carbonation fraction by equation (9), the changes in DIC concentrations of solutions undergoing reactions were based on comparison to the concentrations of standards undergoing the same experimental handling. That is,

$$\Delta_T[\cdot] \equiv [\cdot]_T - [\cdot]_0 \approx [\cdot]_T - [\cdot]_T^{\text{standard}}.$$

The standard deviation of the concentrations of DIC for the standards after experimental handling is thus a measure of the systematic error.

A.5 Determining the pH

The pH value of the reacting solutions under the actual experimental conditions (200°C and 150 bar) is needed for the simulations, and to understand the thermodynamics and kinetics of carbonation. Since our experimental apparatus did not allow measurement of the pH, we used the following method to estimate it under the experimental conditions from measurements made before and after the experiments (note that all pH measurements refer to samples appropriately diluted to allow an accurate measurements):

1. For each run, a gold capsule containing only standard $NaHCO_3$ solution was carried through the same experimental procedure as the capsule with olivine. The molality of the standard solution gives the its DIC concentration at the start of the experiment (M_1, step 0 in Figure A2). As described previously, external processes during experimental handling can cause loss of CO_2 from samples, independent of carbonation reactions. We estimated this external loss by measuring the pH of the standard solution after the experiment and cooling to 25°C (pH_5 in Figure A2). Then, assuming a constant Na concentration during the experiment (no loss of sodium), we used EQ3/6 to calculate the final DIC concentration (M_1'). The fraction M_1/M_1' is a correction factor for reacted samples.
2. The DIC concentration in the solution reacted with an olivine sample in the same run is estimated. To do this, the pH of the reacted solution and its elemental concentrations (Mg, Fe, Si) are measured, after cooling to 25°C. From these values and the Na concentration (assumed constant), we use EQ3/6 to estimate the actual concentration of DIC in the reacted solution (M_2'). Assuming that the standard and reacted solutions have suffered the same fractional external losses of CO_2, we correct the DIC concentration in the reacted solution (at 25°C) by

$$M_2 = \frac{M_1}{M_1'} \cdot M_2'.$$

Note that if the solution has been diluted to allow more accurate concentration measurements, then the concentration of DIC in the capsule is $M_2 \cdot N$, where N is the dilution factor.

3. Finally, we use EQ3/6 to calculate the pH under experimental conditions using the (undiluted) DIC concentration obtained in step 2 ($M_2 \cdot N$), the measured elemental concentrations of the final solution and the starting Na concentration.

A.6 Variation of water activity during dissolution of sodium bicarbonate

To simulate the experiments with low fluid-to-mineral ratios (experiments L1 and L2), we used EQ3/6 model the dissolution of approximately 17 mol of mineral sodium bicarbonate (nahcolite) in approximately 1 kg of water at 200°C (Figure A4). For these simulations, the CMP data file was used for all parameters because only this database contains equations for nahcolite. These simulations showed that water activity decreases as nahcolite dissolves. After 2.30 mol of nahcolite dissolves in water, Na_2CO_3 begins to precipitate from solution, as nahcolite continues to dissolve. The concentrations of DIC and Na^+ ion in the solution increase continuously. After 5.32 mol of nahcolite dissolves, about 0.8 mol of Na_2CO_3 has precipitated and the concentration of DIC reaches about 4.5 *m*. At this point, the solution is saturated with respect to nahcolite and Na_2CO_3. No further dissolution occurs and the water activity drops to 0.861.

For comparison, these simulations were repeated using the SHV database. The results for the water activity and concentrations of DIC (Figure A3) start to deviate from those calculated using CMP database only when Na_2CO_3 start to dissolve. In simulating the experiments L1 and L2, we assumed that the solution was saturated with respect to Na_2CO_3 and $NaHCO_3$ from the beginning of the simulation.

A.7 Thermogravimetric analysis of run-product

A possible source of uncertainty in the analysis leading to the carbonation fraction is incomplete washing of the samples, leaving residual sodium bicarbonate ($NaHCO_3$) from the original solution. Thermogravimetric method was used to characterize the reaction products, to verify if the $NaHCO_3$ has

been completely washed out of final solids, and to explore if this can be used as an independent approach to determine the amount of $MgCO_3$ in solid run products. Analyses were carried out using a TGA/DSC 1 instrument (Mettler Toledo) in the Key Laboratory of Surficial Geochemistry, Ministry of Education, Nanjing University. Solid run products were dried overnight in an oven at approximately 40°C, and 10.0 ± 0.1 mg of solids were then weighed and loaded to 70 µl alumina oxide crucibles. Blanks were tested three times before each batch of sample measurements, the average of which was subtracted from the results. The typical drift for blank test is smaller than 1‰ of mass. The temperature ramping rates for both samples and blanks were 5°C/min between 30 and 100°C, 10°C/min between 100-300°C, 5°C/min between 300-700°C and 10°C/min between 700-1100°C.

Pure $CaCO_3$, $NaHCO_3$ and $MgCO_3$, hydrous magnesite powders were used as calibration standards. Results are shown in Figure A4, which demonstrates that each carbonate has its distinct extrapolated onset temperature (or decomposing temperature), with $Na_2CO_3 > CaCO_3 > MgCO_3 \approx MgCO_3 \cdot nH_2O > NaHCO_3$. The two steps of $NaHCO_3$ decomposition of can be expressed in the following equations:

$$2NaHCO_3 \xrightarrow{\text{about } 120^\circ C} Na_2CO_3 + H_2O + CO_2 ,$$

$$Na_2CO_3 \xrightarrow{\text{about } 935^\circ C} Na_2O + CO_2 .$$

The calibrations also show that when system contains H_2O, the degassing pattern becomes complex. $MgCO_3$ has a very small decrease of weight when temperature is higher than 800°C

Results of mixture of $NaHCO_3$ and $MgCO_3$ have also been investigated (Figure A5). When $NaHCO_3/MgCO_3$ ratio is low (< 0.5), the weight loss curve doesn't have clear plateau, but the weight ratio can be calculated with reasonable precision from the weight loss curve.

Results of thermogravimetric analysis on our samples are shown in Figure A6. It has several features different from our carbonate standards or their mixtures: (1) the first significant weight loss started at less than 100°C, presumably originated from the degassing of hydrous minerals; (2) the second significant weight loss started at around 400°C, which indicates the decomposition of $MgCO_3$. However, this weight loss continued to about 500°C, in contrast to the sharp drop in the standard $MgCO_3$ curve.

This difference could be caused by the bigger grain size in our samples compared with $MgCO_3$ standards (<10 μm); (3) after the weight loss due to decomposition of $MgCO_3$, there is continued weight loss. This could be due to continued water loss from hydrous minerals. All our samples, stopped weight loss before 900°C, where Na_2CO_3 started to decompose, indicating that our cleaning technique is efficient to remove $NaHCO_3$, and our estimation of carbonation fraction based on DIC differences is reliable.

APPENDIX A FIGURE CAPTIONS

Figure A1. Comparing carbonation experiments with simulations. Simulations with EQ3/6, for the model described in the text using the reactive surface areas determined by BET, generally overestimates the pH values (top) and carbonation fractions (bottom) observed in the experiments. Compare with Figure 11 (Part I) showing the same plots for simulations with reduced reactive surface area.

Figure A2. Steps in the experimental process that can introduce systematic variations in pH and dissolved inorganic carbon.

Figure A3. Quantifying systematic error. Normalized dissolved inorganic carbon (DIC) measured in standards before and after experiments as a function of experiment duration. These standards with no olivine present show small losses of carbon uncorrelated with the starting concentration or length of time in the reaction vessel. Note that solutions prepared for higher than 1 m concentration at high temperature are diluted to 1 m before measurement at room temperature.

Figure A4. Simulation of nahcolite dissolution using CMP and SHV thermodynamic data. Top panel shows water activity (top) and bottom panel shows concentrations of various different species as a function of dissolved nahcolite (the mineral form of sodium bicarbonate).

Figure A5. Results of thermogravimetric analysis on $CaCO_3$, $MgCO_3$, $NaHCO_3$, $MgCO_3 \cdot nH_2O$ standards.

Figure A6. Results of thermogravimetric analysis on the mixture of $MgCO_3$ and $NaHCO_3$ standards.

Figure A7. Results of thermogravimetric analysis on our run-products in the powered experiments.

APPENDIX A Figures

FIGURE A1

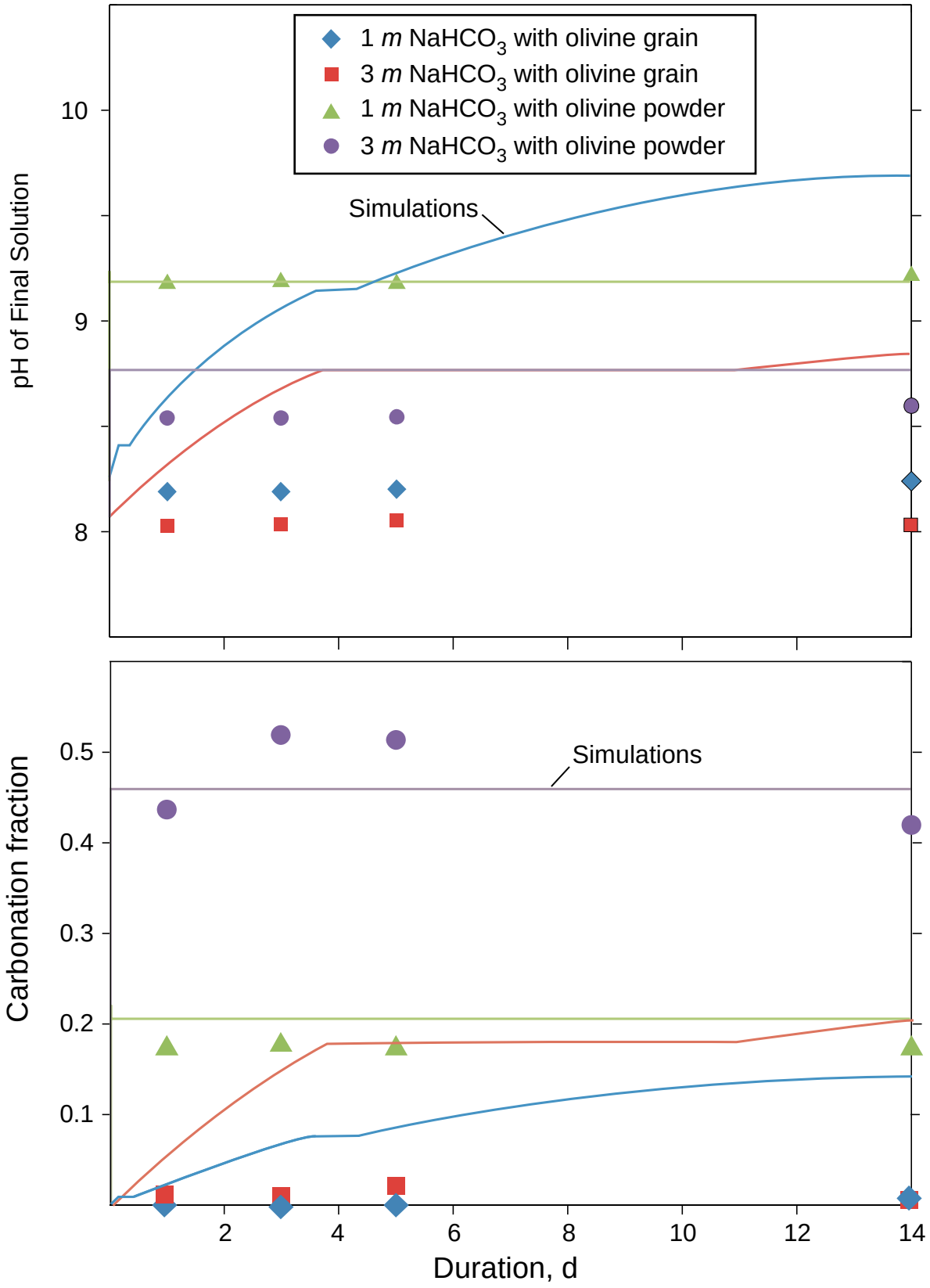
1 m NaHCO3 with olivine grain
3 m NaHCO3 with olivine grain
1 m NaHCO3 with olivine powder
3 m NaHCO3 with olivine powder
Simulations
pH of Final Solution
10
9
8
Simulations
Carbonation fraction
0.5
0.4
0.3
0.2
0.1
2
4
6
8
10
12
14
Duration, d

FIGURE A2

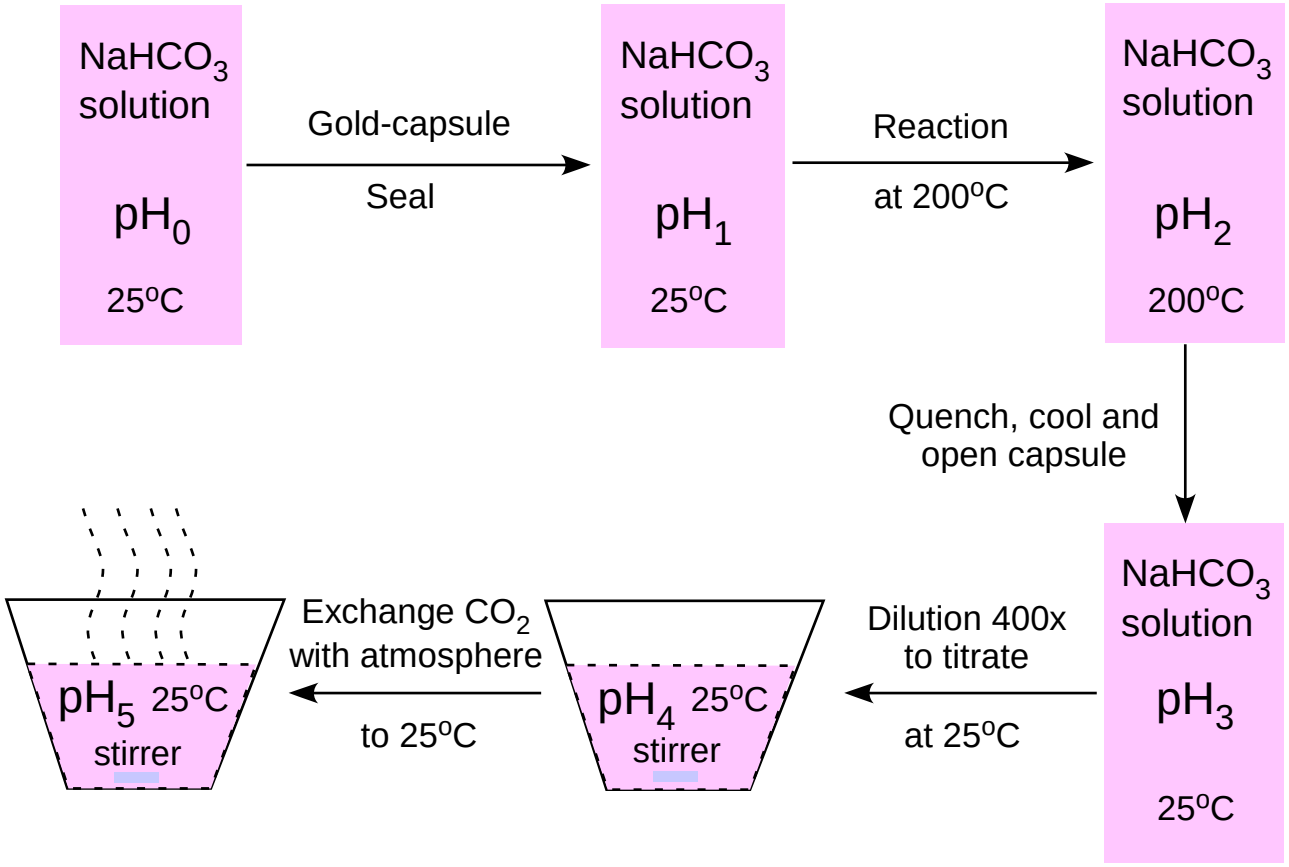
NaHCO3 solution
pH0
25°C
Gold-capsule
Seal
NaHCO3 solution
pH1
25°C
Reaction
at 200°C
NaHCO3 solution
pH2
200°C
Quench, cool and open capsule
NaHCO3 solution
pH3
25°C
Dilution 400x to titrate
at 25°C
pH4 25°C stirrer
Exchange CO2 with atmosphere
to 25°C
pH5 25°C stirrer

FIGURE A3

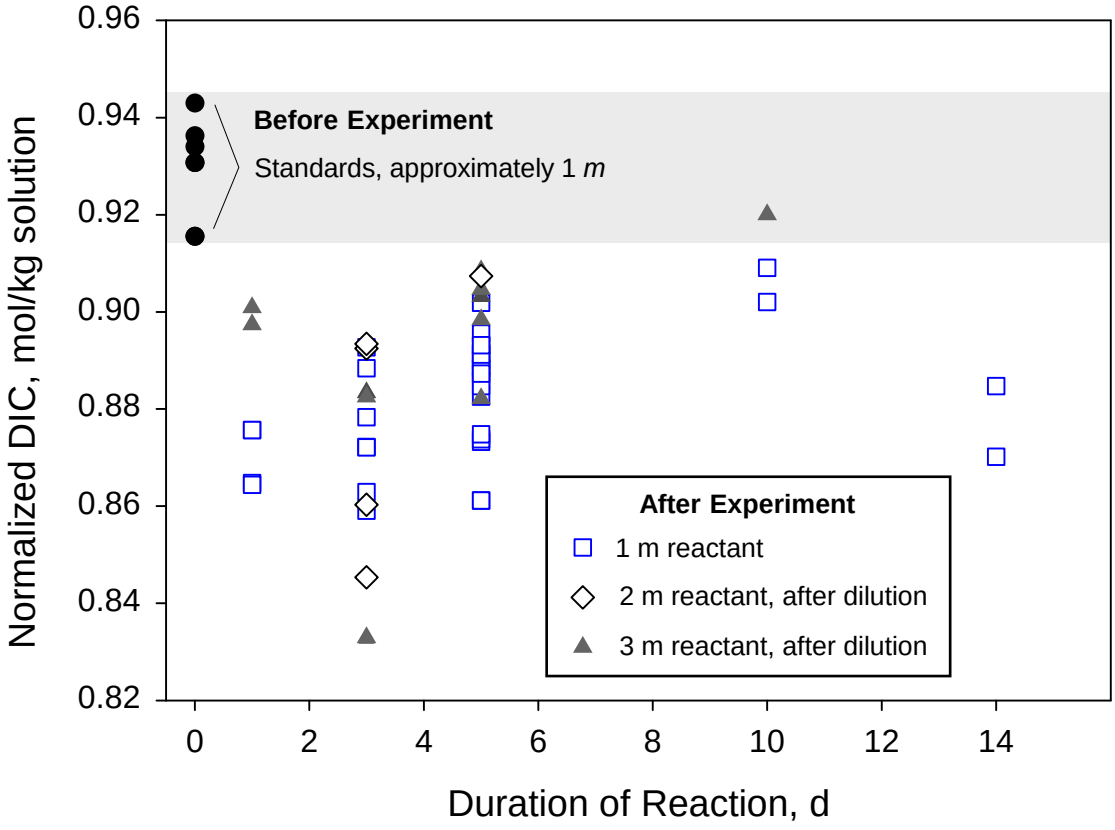
Normalized DIC, mol/kg solution
0.96
0.94
0.92
0.90
0.88
0.86
0.84
0.82
0
2
4
6
8
10
12
14
Duration of Reaction, d
Before Experiment
Standards, approximately 1 m
After Experiment
1 m reactant
2 m reactant, after dilution
3 m reactant, after dilution

FIGURE A4

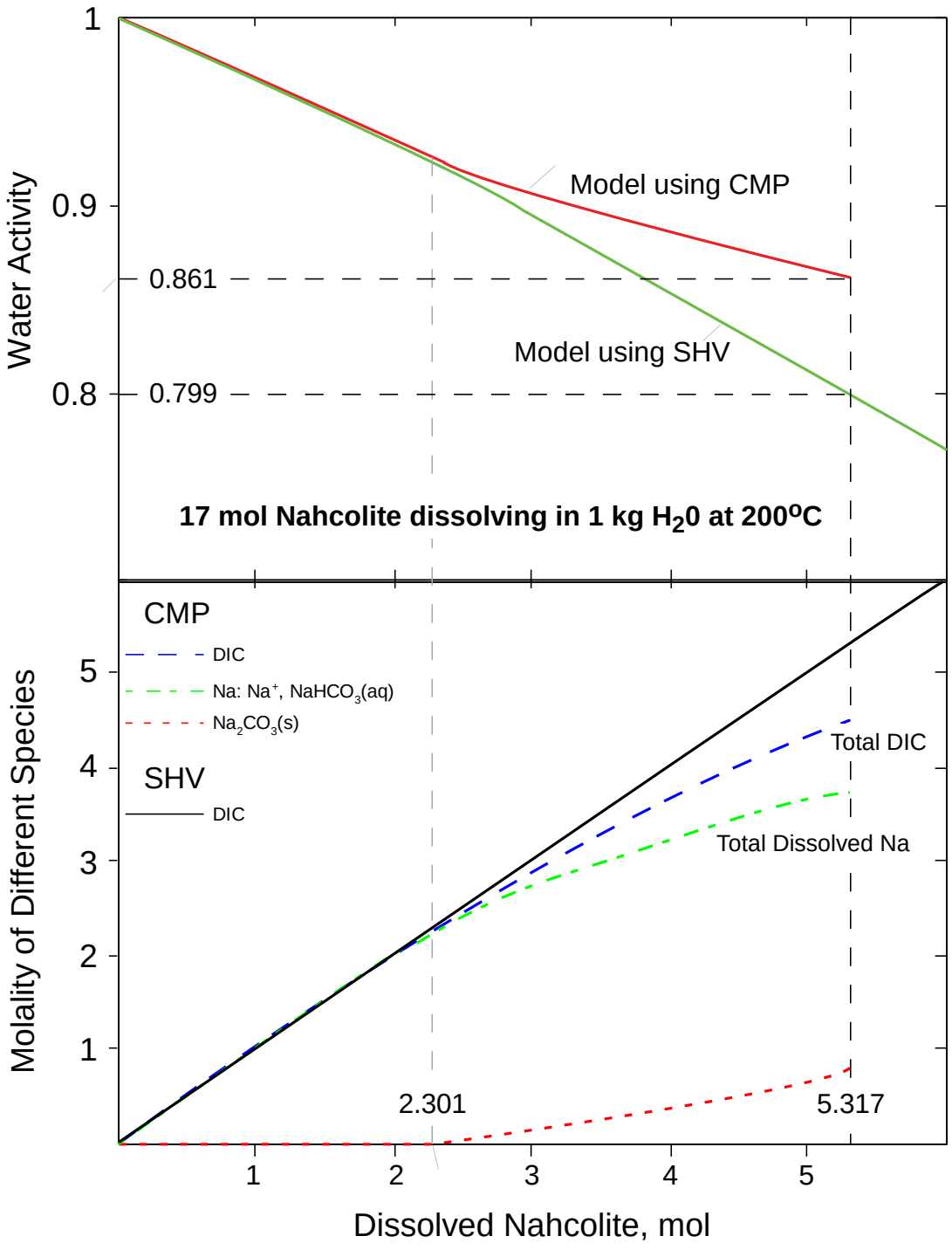
Water Activity
1
0.9
0.8
0.861
0.799
Model using CMP
Model using SHV
17 mol Nahcolite dissolving in 1 kg H20 at 200°C
Molality of Different Species
CMP
DIC
Na: Na+, NaHCO3(aq)
Na2CO3(s)
SHV
DIC
Total DIC
Total Dissolved Na
2.301
5.317
1
2
3
4
5
Dissolved Nahcolite, mol

FIGURE A5

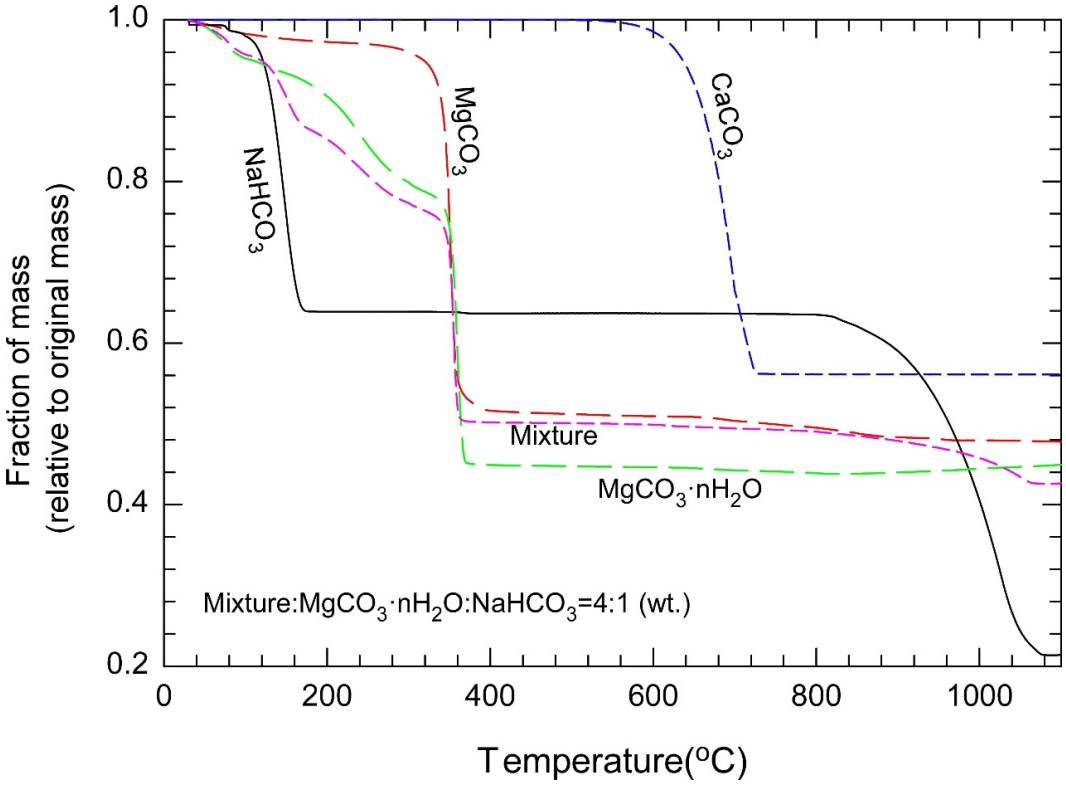
1.0
0.8
0.6
0.4
0.2
0
200
400
600
800
1000
Fraction of mass
(relative to original mass)
Temperature(°C)
NaHCO3
MgCO3
CaCO3
Mixture
MgCO3·nH2O
Mixture:MgCO3·nH2O:NaHCO3=4:1 (wt.)

FIGURE A6

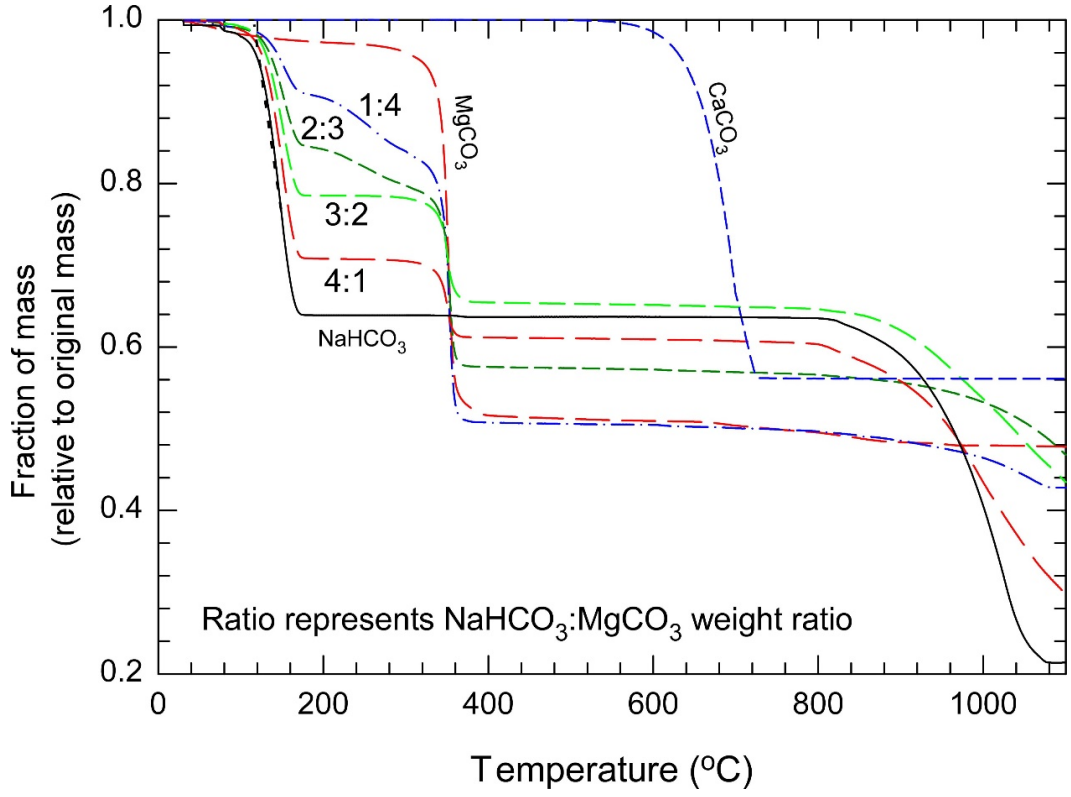
1.0
0.8
0.6
0.4
0.2
0
200
400
600
800
1000
Fraction of mass
(relative to original mass)
Temperature (°C)
1:4
2:3
3:2
4:1
NaHCO3
MgCO3
CaCO3
Ratio represents NaHCO3:MgCO3 weight ratio

FIGURE A7

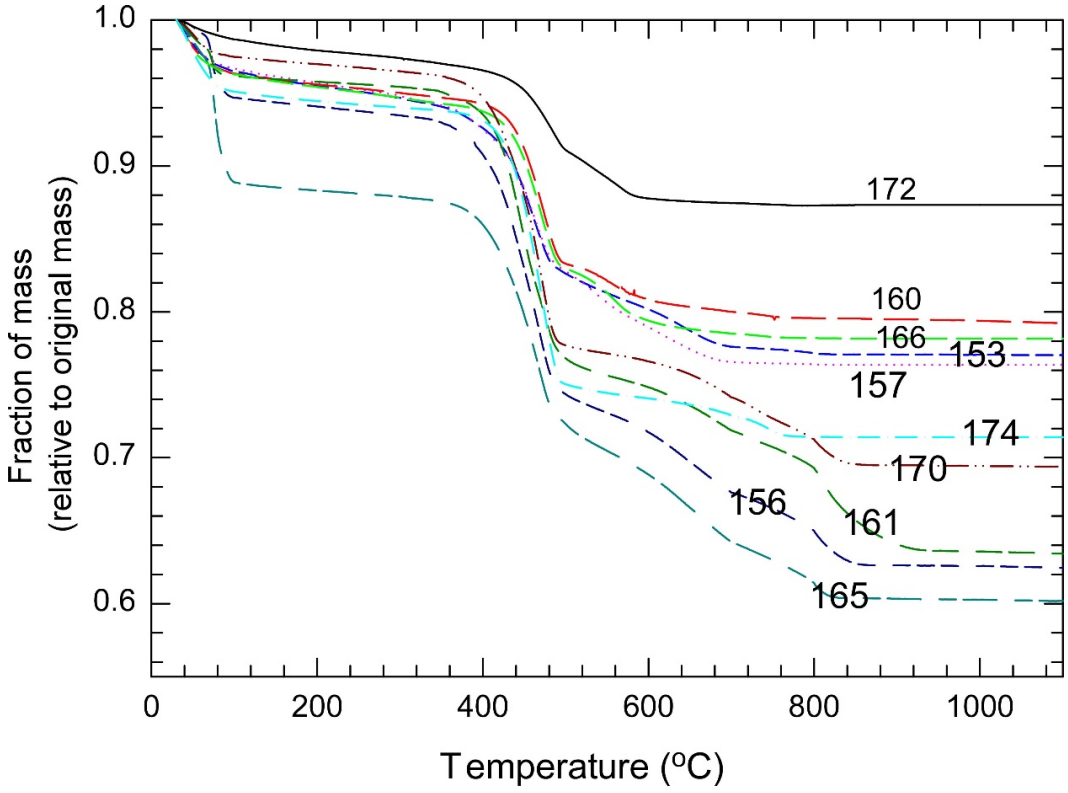
1.0
0.9
0.8
0.7
0.6
Fraction of mass
(relative to original mass)
0
200
400
600
800
1000
Temperature (°C)
172
160
166
153
157
174
170
156
161
165

APPENDIX B – SYNTHETIC ROCK SAMPLES

One of the subtasks of the project involved the development of new ways to preparing synthetic rock samples with controlled grain size and porosity, for eventual use in flow through and deformation experiments. This Appendix describes the methods developed for this task by using sieving, followed by controlled sedimentation and sintering under different conditions.

Sorting powders with different grain sizes

Powders with grain sizes in different ranges from 0 to 100 µm were prepared in the following bins: 0–20 µm, 20–40 µm, 40–60 µm, 80–100 µm. SEM images of the 5 and 50 µm grain-size powders are shown in Figures D1 and D2 below.

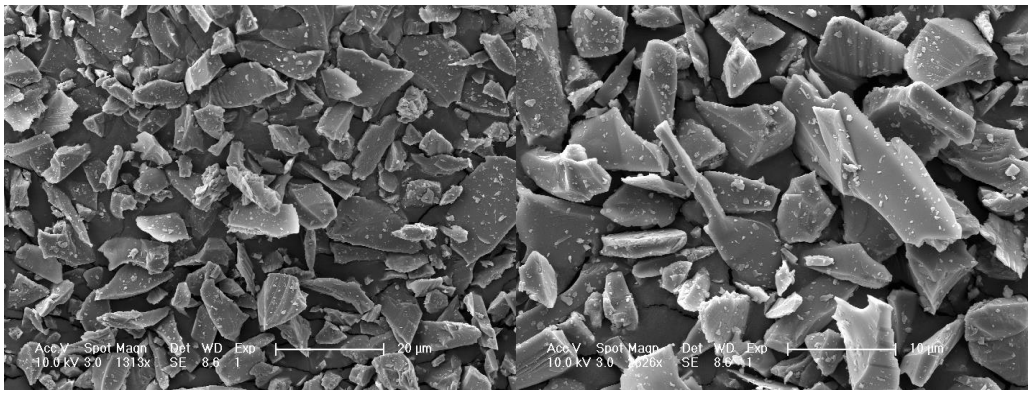

FIGURE B1 | 5 µm grain size powder (close up, right). Sample was sorted with 5 µm wire mesh sieve, followed by sedimentation.

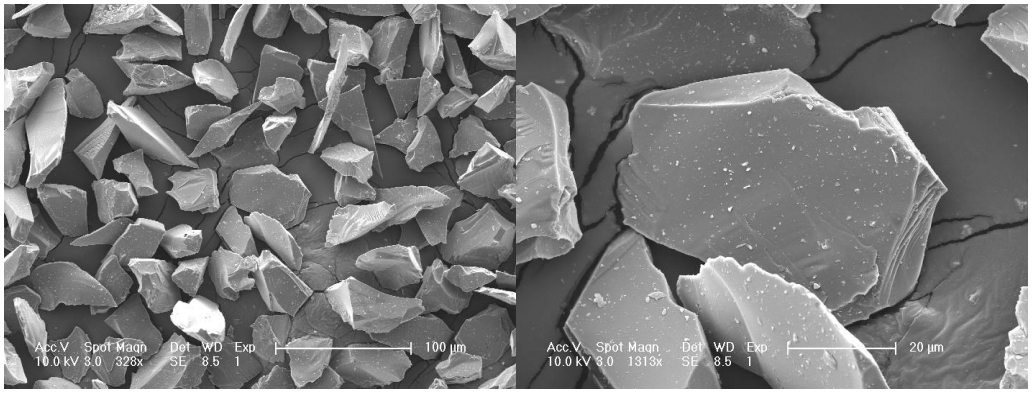

FIGURE B2 | 50 µm grain size powder (close up, right). Sample was sorted with 20 and 40 µm wire mesh sieves, followed by sedimentation.

Preparation of samples for deformation experiments

Starting with different grain size powders, pellets were prepared by cold pressing using a piston cylinder. Different sizes of pellets were prepared:

Diameter	Thickness
12 mm	5 mm
4 mm	5 mm
4 mm	10 mm

To prepare large solid samples with defined porosity, several of the prepared pellets were sintered for 3 to 12 hours in a furnace at a vacuum pressure of approximately $5 \cdot 10^{-3}$ Torr (0.666 Pa) and a sintering temperature between 1300°C and 1400°C. Stacked pellets were sintered together to produce longer samples (Figure D3). Up to 5 pellets, each about 5 mm thick, were stacked, enclosed in a 5 μm thick nickel-foil capsule and annealed under a load of about 600 grams.

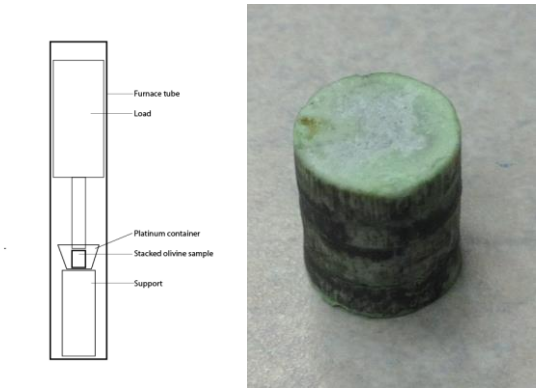

FIGURE B3 | Sample prepared by stacking and sintering under vacuum.

Sintering under vacuum and controlled atmospheric conditions

Figure D4 (below) shows the sample after controlled vacuum sintering. The border between the pellets shows very good continuity, but very little porosity was observed in these vacuum sintered samples. In an effort to further increase the porosity, pellets composed of grain powders of different starting sizes were sintered in a controlled atmosphere of CO/CO_2 gas (1:1 ratio), at temperatures from 1300°C to 1400°C, followed by an Argon/Hydrogen gas mixture (Ar + 1% H_2) at 800°C during the cool down period.

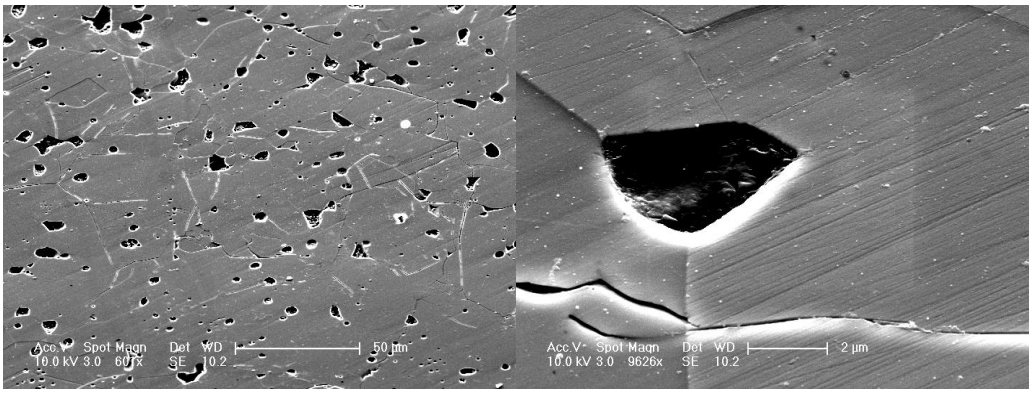

FIGURE B4 | Vacuum sintered sample. Sample is FO269 after vacuum sintering a powder of average grain size of 10µm for 12 hours at 1300°C. Close-up on the left shows the geometry of a single pore near equilibrium.

Samples and conditions are summarized in the table below.

Table B1 | Conditions for sample preparation

Experiment #	Grain size	Conditions	Size of pellet
FO294	0–20 µm	1300°C, 4hrs	5mm thick, 12mm diameter 5mm thick, 4mm diameter
FO295	0–20 µm	1400°C, 4hrs	5mm thick, 12mm diameter 5mm thick, 4mm diameter
FO297	20–40 µm	1400°C, 4hrs	5mm thick, 12mm diameter 5mm thick, 4mm diameter
FO298	80–100 µm	1400°C, 4hrs	5mm thick, 12mm diameter 5mm thick, 4mm diameter
*FO316a, b	5 µm, 50 µm	1400°C, 8hrs	5mm thick, 4mm diameter
*FO325a, b	5 µm, 50 µm	1400°C, 4hrs	5mm thick, 4mm diameter

*Sedimentation of the powder was carried out in order to collect a narrower distribution of the grain size. Ethanol was used as the sedimentation media. The powder used for sedimentation was collected from the sieving process.

Figure D5 (below) shows samples FO316a and FO316b after preparation.

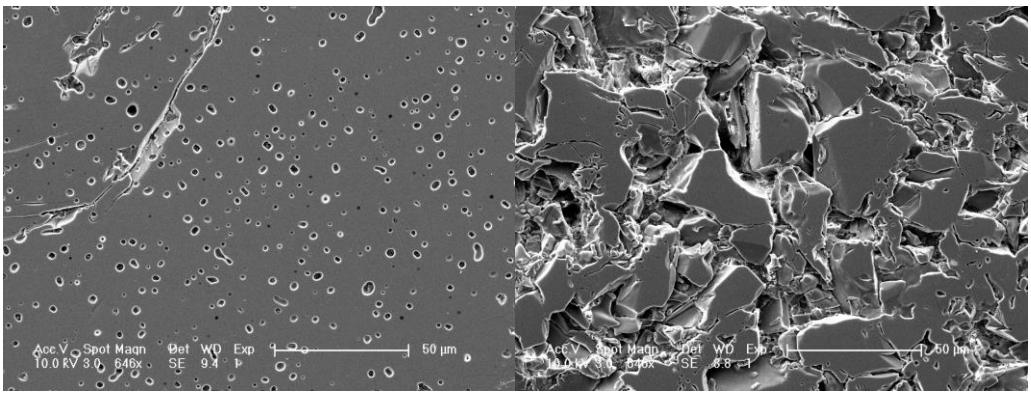

FIGURE B5 | Sintered samples in controlled atmosphere. (LEFT) Polished sample FO316a, obtained from grain powder with 5-µm average size after sintering for 8 hours at 1400°C. Pores are closed. (RIGHT) Polished sample FO316b, obtained from grain powder with 50-µm average size after sintering for 8 hours at 1400°C.

Finally, a large sample, approximately 2 cm long was sintered under controlled atmosphere without stacking (Figure D6). Powder was first loaded in a nickel foil capsule, and then cold pressed and sintered at high temperature in a controlled atmosphere. The nickel foil was peeled off after completion of the process. The initial grain sizes of the cold pressed aggregate were in the range 0–20 μm; the sample length was 20mm; its diameter was 12 mm. The sample was sintered for 4 hours at 1400°C in CO/CO_2 atmosphere, followed by the Argon/Hydrogen gas mixture at 800°C during cool down.

FIGURE B6 | Sample 2 cm long, sintered under controlled atmosphere.

APPENDIX C – AUTOCLAVE DESIGN

Results of the static geochemical experiments described in Part I revealed the need for a new autoclave system to allow better control and monitoring of mineral carbonation experiments in the laboratory. The Yale team designed a new system in collaboration with the manufacturer AppliTech Corporation and, in one of the last tasks of the project, finished installed the system in the summer of 2014 in the project's high-pressure bunker facility on Yale West Campus. Figure E1 shows a photo of the apparatus during installation and testing. For its price, the new apparatus has some unique features for laboratory geochemical experiments (Figure E2). The system contains two 300 ml Hastelloy-C reaction vessels, magnetic stirrer, pH probes, and fluid-pumping systems. The pumping systems allow sampling and injecting of fluid for real-time control and monitoring of fluids during a reaction run. A bridge between the two vessels allows flow-through experiments. A computer controls both reaction vessels and all auxiliary systems.

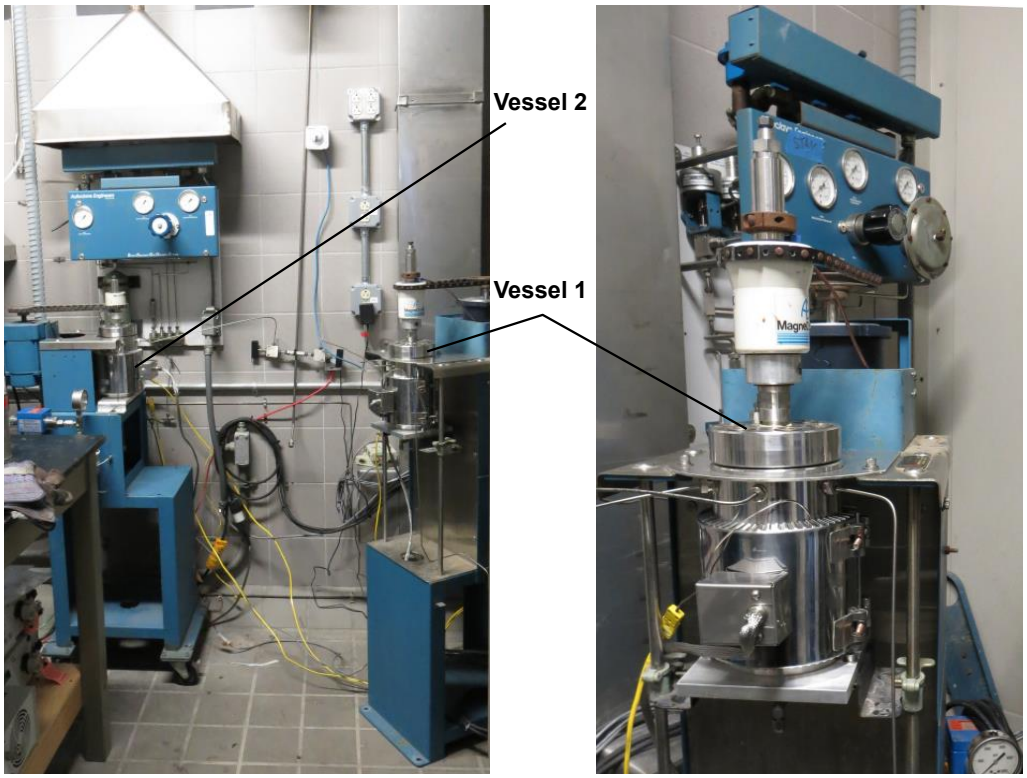

FIGURE C1 | Photos of the new autoclave system in the project laboratory on Yale West Campus. Photo at right is a close-up of the main reaction chamber (vessel 1).

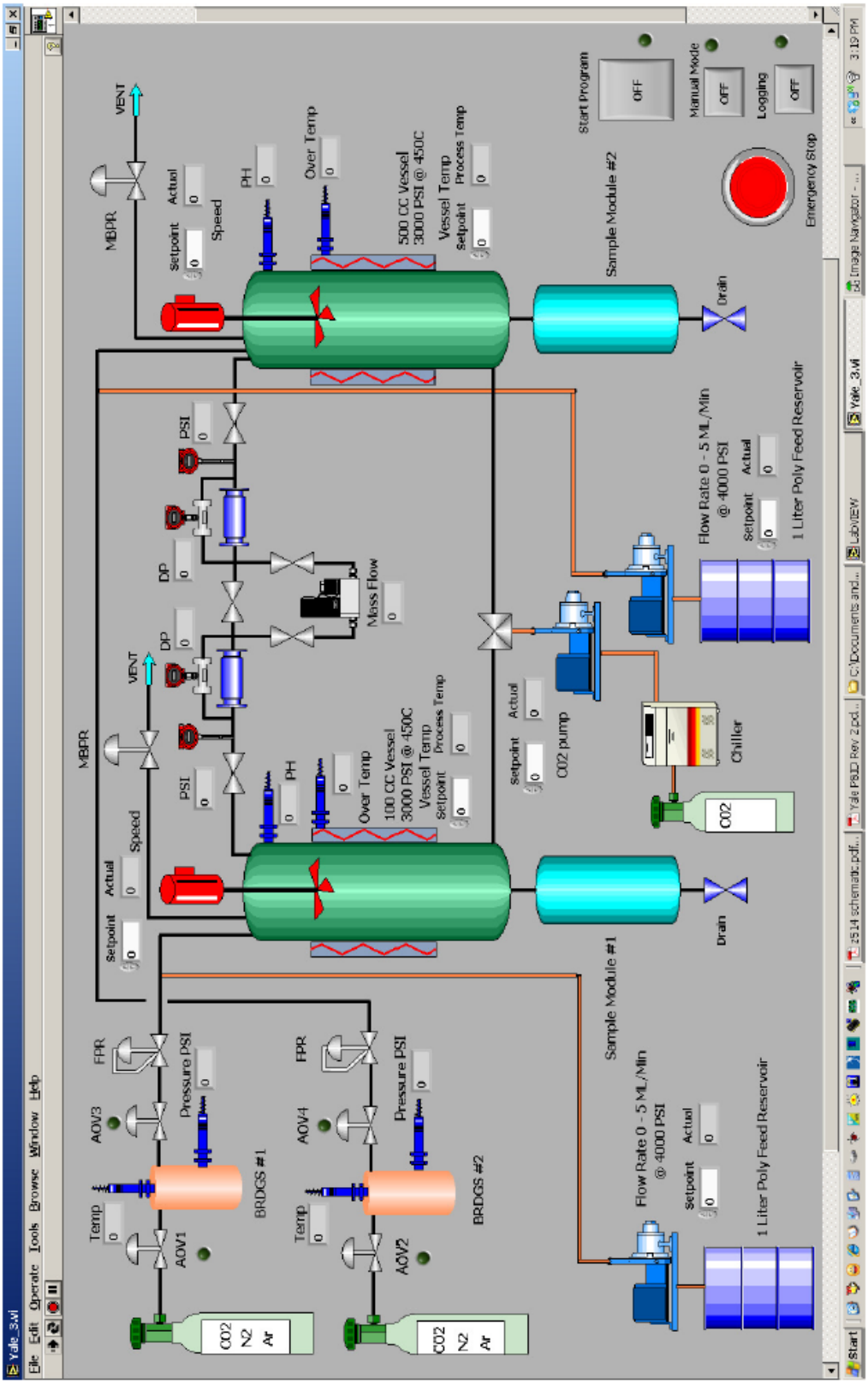

FIGURE C2 | Schematic of the new autoclave system, designed in collaboration with AppliTech Corporation. The system has two reaction chambers (green) with stirrers and flow-through ports.

APPENDIX D – FIELDWORK: SAMPLE COLLECTION AND ANALYSIS

As described in the Introduction to this report, one of the project tasks was a program to collect samples of natural Hawaiian rocks, and to analyze their constituent silicate mineral phases. The University of Hawai'i at Mānoa carried out the fieldwork and sample analyses under subcontract to Yale University. The samples were chosen to represent rock types containing suitable mineral phases for evaluating carbonation potential of common silicates in Hawaiian lavas; the results were intended to provide a basis for the design of field tests of mineral carbonation in a possible continuation of the project into a demonstration phase at a suitable site on the island. The proposal for a demonstration phase was not funded because of budget constraints.

The following report, submitted as the Final Report on the subcontract by the principal investigator (Kevin T. M. Johnson), covers the fieldwork and sample analyses performed at the University of Hawai‘i for this task of the project.

Integrated Experimental and Modeling Studies of Mineral Carbonation as a Mechanism for Permanent Carbon Sequestration in Mafic/Ultramafic Rocks

FINAL REPORT (Award Period 1 October 2010 – 30 September 2013)

University of Hawai‘i sub-award from Yale University, DOE Award No. DE-FE0004375

PI: Kevin T.M. Johnson, PhD, Department of Geology and Geophysics, University of Hawai‘i at Mānoa, Honolulu, HI 96822 USA

Submitted November 30, 2014

Abstract

This project studied basic questions about the carbonation of basalts and their constituent minerals. Experiments on olivine and several basaltic rock assemblages collected in Hawai‘i were performed under variable run durations, pressure, temperature, fluid composition, and grain size conditions to define carbonation reaction kinetics. Basalts used for the experiments were collected by the University of Hawai‘i from 15 sites on the island of Hawai‘i. The samples were chosen to represent rocktypes containing suitable mineral phases for evaluating carbonation potential of common silicates in Hawaiian lavas. The lavas were fully characterized by petrographic and geochemical analysis and were used as starting materials for experiments on basalt carbonation potential at 50 – 250°C and 50 – 200 bars in the presence of $NaHCO_3$. The common igneous mineral, olivine, was found to be highly reactive in the presence of CO_2 in various fluid forms. Based on results from this work and other studies, we show that basalts comprising the bulk of the main Hawaiian Ridge have the capacity to sequester most of the anthropogenic CO_2 currently produced globally, even at less than optimum carbonation efficiency.

Project Objectives

The overall project objective is to understand factors controlling chemical reactions between basalts and H_2O-CO_2 fluids and to define optimum conditions for carbonation of basalts to be practical on a large scale. University of Hawai‘i was responsible for field sample collection, description and chemical analysis and was also involved with design and interpretation of geochemical experiments on natural Hawaiian rocks and their constituent silicate mineral phases. The results of this project provide a basis for scaling up to field tests of mineral carbonation in basaltic terrains. The experiments and physical properties of rock samples collected in Hawai‘i are also used to constrain numerical models of carbonation reactions in fluid-rock systems.

The project examined the carbonation capacity of several important basaltic rock types in Hawai‘i – vesicular olivine basalt, olivine-rich basalts (picrites), and clinopyroxene-olivine-rich basalts (ankaramites) – and the carbonation rates of major silicate□forming minerals in those rocks – olivine, clinopyroxene, orthopyroxene, and plagioclase – as a function of temperature, PCO_2, fluid/mineral ratios, surface area, extent of reaction, fluid salinity, gas species composition, and amount of additives (e.g., pH buffers, halogen content). The overall project involved related, interdisciplinary efforts at Yale University, University of Hawai‘i, University of Maryland and Pacific Northwest National Lab (PNNL). A significant portion of the work focused on establishing an experimental and theoretical framework to quantitatively describe the geochemical and geomechanical consequences of carbonation reactions applicable to a broad range of geological settings.

Sample Collection

Kevin Johnson, the University of Hawai‘i principal investigator, directed sample collection fieldwork in May, 2012 and August, 2013. Locations and samples were selected based on large

phenocryst size and abundance and to ensure adequate starting material for all experimental work. Basalt samples were collected from the following locations:

Table 1. Sample Locations and Rocktypes

Sample	Latitude (°N)	Longitude (°W)	Sample type
HAP-1	19.99633	155.82714	Ankaramite, Mauna Kea volcano
HAP-2	19.99549	155.82640	Ankaramite, Mauna Kea volcano
HAP-3	19.99490	155.82578	Ankaramite, Mauna Kea volcano
HAP-4	19.99640	155.82710	Ankaramite, Mauna Kea volcano
KIL1960-1	19.51594	154.81106	Olivine basalt, Kilauea volcano
KIL1960-2	19.50918	154.82825	Olivine basalt, Kilauea volcano
ML494-2	19.05922	155.69500	Picrite basalt, 1868 flow, Mauna Loa volcano
ML499	19.08008	155.81067	Picrite basalt, 1750 flow, Mauna Loa volcano
ML647-1	19.04842	155.60908	Picrite basalt, Mauna Loa volcano
ML647-2	19.05131	155.61031	Picrite basalt, Mauna Loa volcano
ML647-3	19.04883	155.60895	Picrite basalt, Kahili Pali, Mauna Loa volcano
ML811-1	19.6354	155.4868	Olivine basalt, Mauna Loa
WAI-1	20.11932	155.58972	Plagioclase megacryst-bearing basalt, Waipio Valley, Kohala volcano
WAI-2	20.11898	155.58805	Plagioclase megacryst-bearing basalt, Waipio Valley, Kohala volcano
WAI-3	20.12263	155.59842	Plagioclase megacryst-bearing basalt, Waipio Valley, Kohala volcano

Sample Location Maps

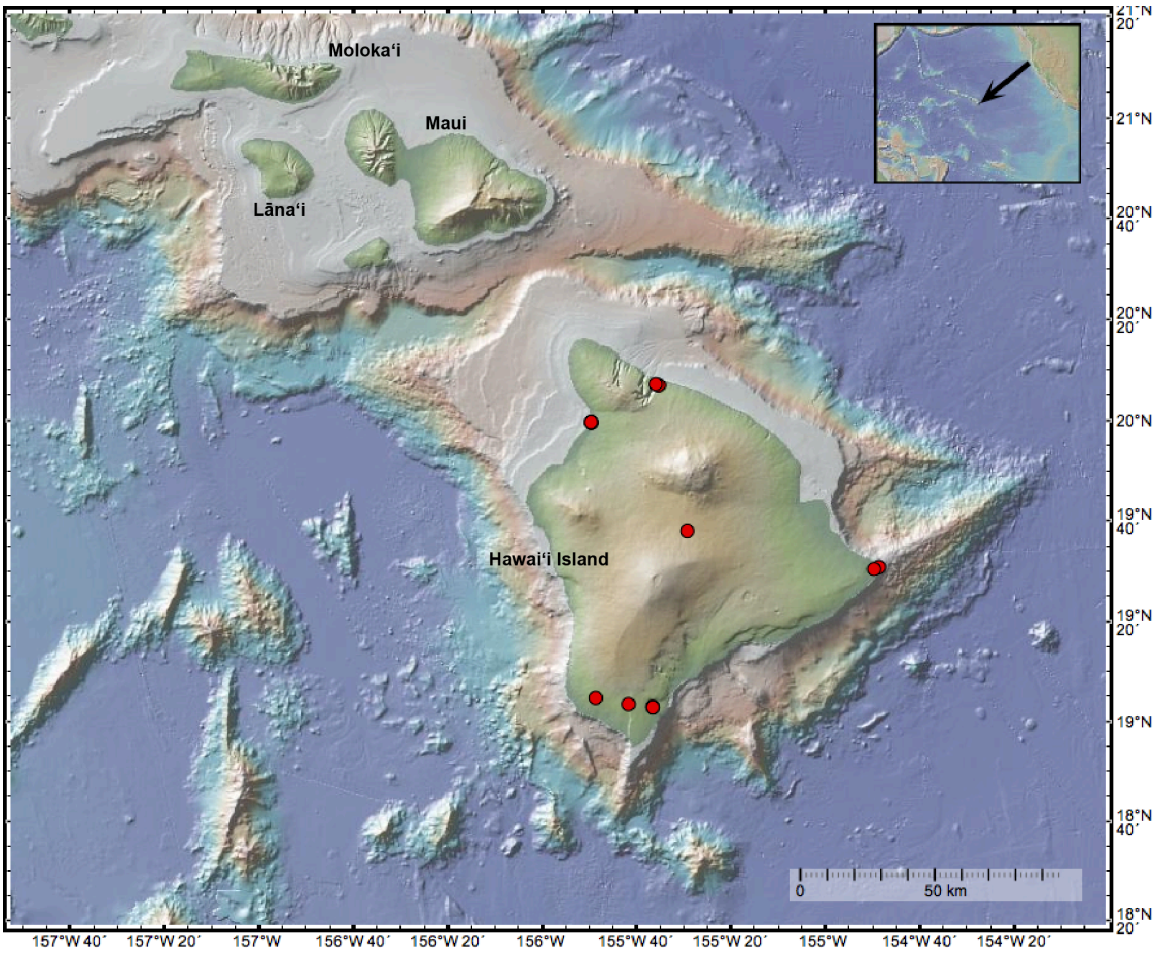

Figure 1. Overview map of sample locations on Hawai'i Island. Map generated in GeoMapApp (*Ryan et al.* [2009]; http://www.geomapapp.org)

Figure 2. Sample locations (refer to Table 1 for latitude and longitude information).

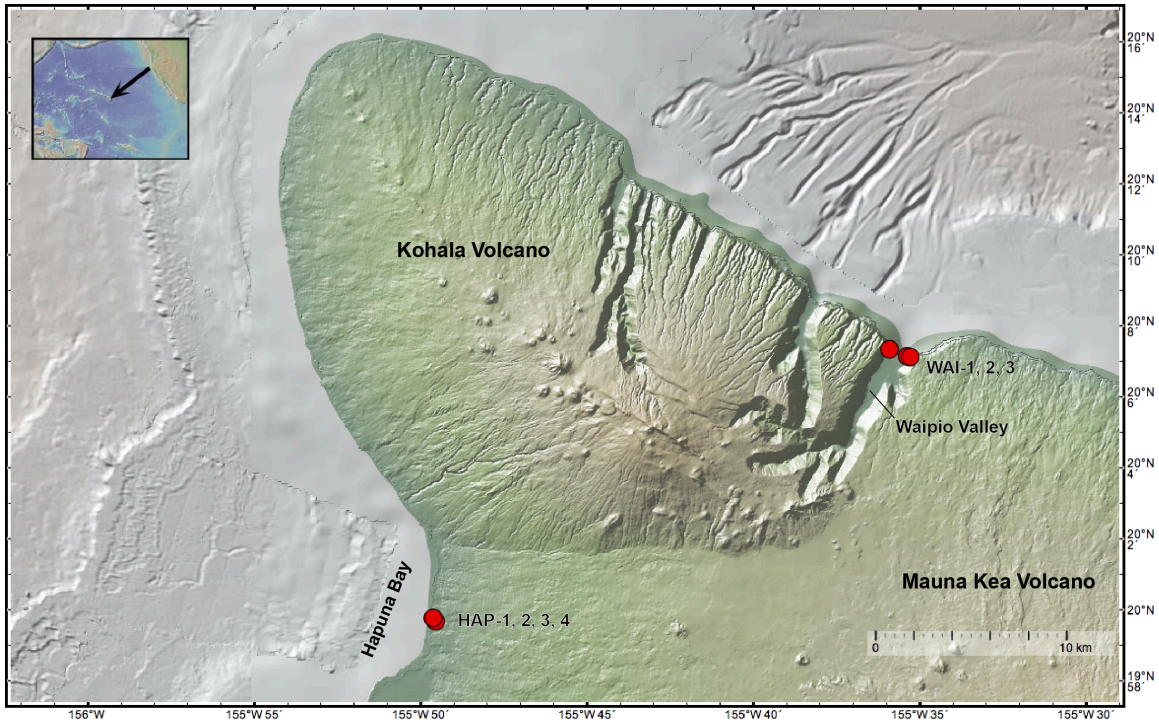

Figure 3. Locations of Waipio (WAI-1, 2, 3) and Hapuna (HAP-1, 2, 3, 4) samples. Map generated in GeoMapApp (*Ryan et al.* [2009]; http://www.geomapapp.org)

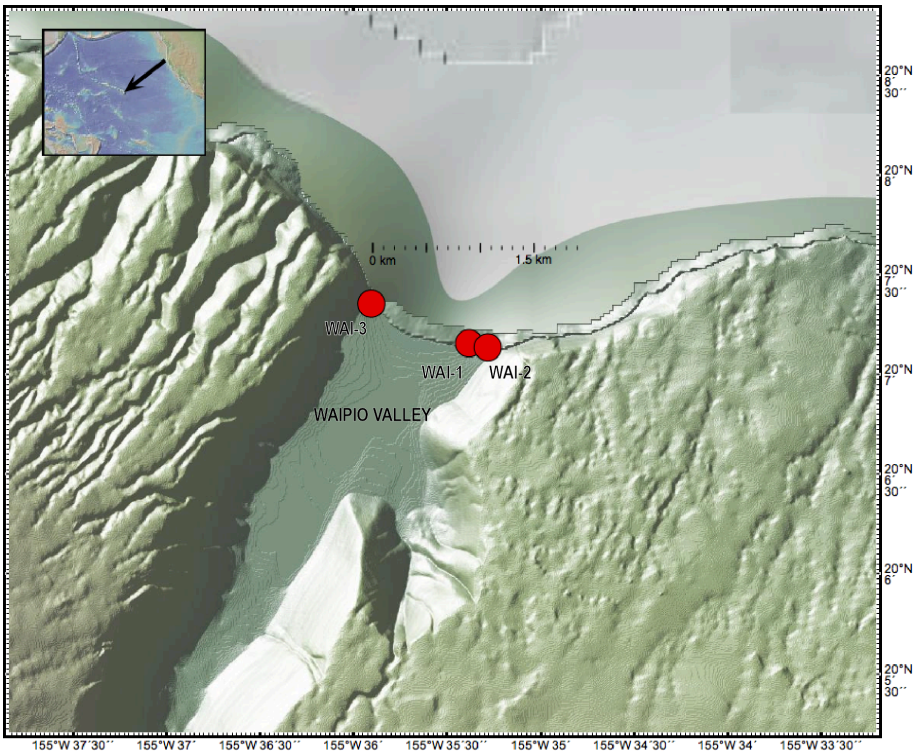

Figure 4. Location detail of Waipio Valley samples WAI-1, 2, 3. Map generated in GeoMapApp (*Ryan et al.* [2009]; http://www.geomapapp.org)

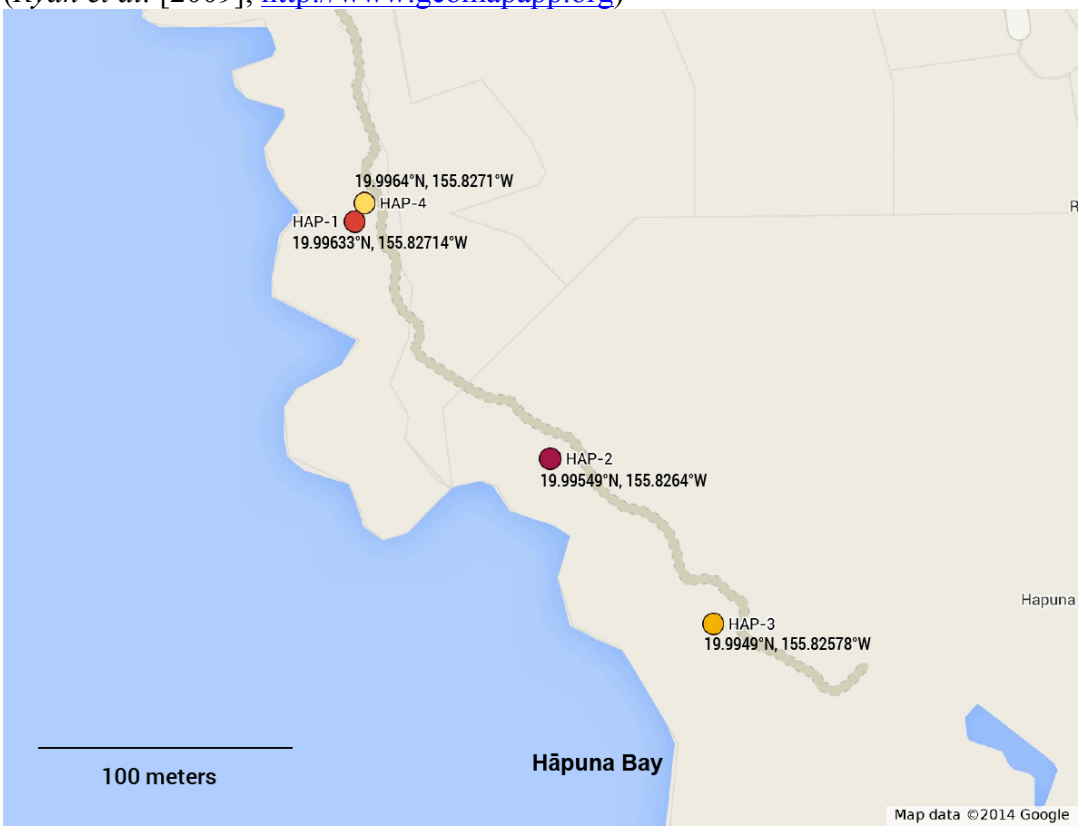

Figure 5. Location detail of Hapuna samples (HAP-1, 2, 3, 4).

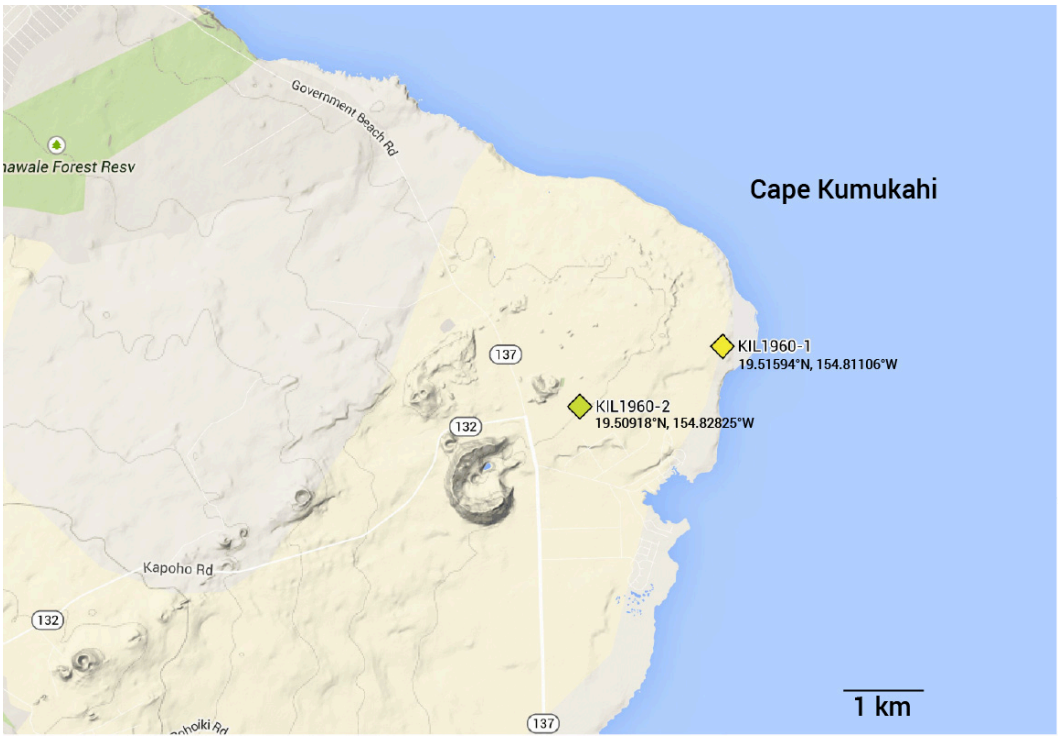

Figure 6. Location detail of Kīlauea samples (KIL1960-1, 2). Map made in GoogleMaps.

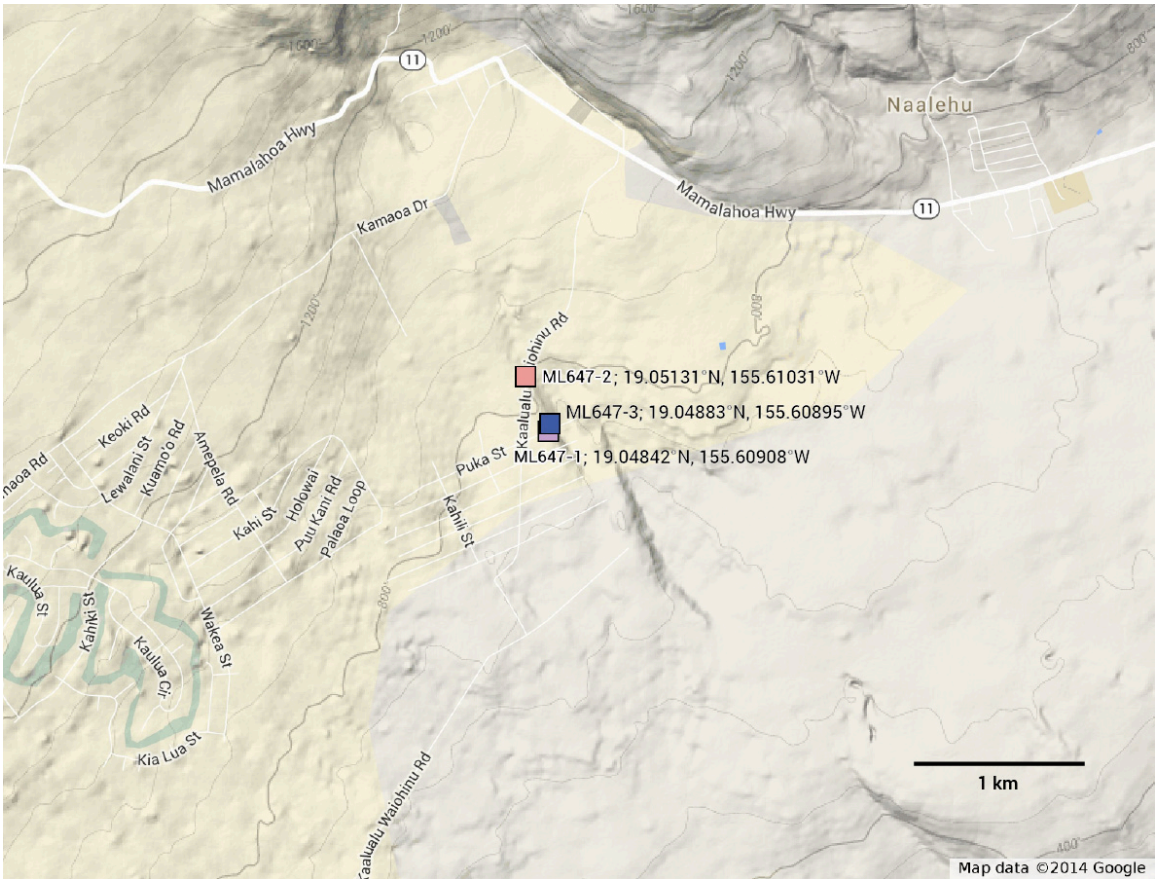

Figure 7. Location detail of site ML647 on Mauna Loa volcano (samples ML647-1, 2, 3).

Sample Analysis

Polished petrographic thin sections were made for samples collected in this study. The thin sections were used for sample description and electron microprobe mineral analyses. Geochemical analyses of mineral phases were made on the University of Hawai‘i JEOL Hyperprobe JXA-8500F field emission electron microprobe. Electron microprobe analyses are reported in Appendix 1 of this report.

Table 2. Sample Rocktypes and Mineral Assemblages

Sample	Rocktype, average mineral assemblage (phenocryst size) – vol%
HAP-1, 2, 3, 4	Ankaramite, Hāpuna Bay, Mauna Kea volcano; Olivine (6 mm) – 12 vol%; Clinopyroxene (5 mm) – 18 vol%; groundmass (cpx, plag, oxides) – 60 vol%; vesicles – 10 vol%
KIL1960-1, 2	Olivine basalt, Cape Kumukahi, Kilauea volcano; Olivine (4 mm) – 8 vol%; groundmass (cpx, oxides) – 80 vol%; vesicles – 12 vol%
ML494-2	Picrite basalt, 1868 flow, Mauna Loa volcano; Olivine (8 mm) – 20 vol%; groundmass (cpx, oxides, plag) – 75 vol%; vesicles – 5 vol%
ML499	Picrite basalt, 1750 flow, Mauna Loa volcano; Olivine (8 mm) – 25 vol%; groundmass (cpx, oxides, plag) – 70 vol%; vesicles – 5 vol%
ML647-1, 2, 3	Picrite basalt, Mauna Loa volcano; Olivine (11 mm) – 30 vol%; Clinopyroxene (2 mm) – 3 vol%; groundmass (cpx, oxides, plag) – 60 vol%; vesicles – 7 vol%
ML811-1	Olivine basalt, Mauna Loa; Olivine (5 mm) – 9 vol%; Clinopyroxene (2 mm) – 3 vol%; groundmass (plag, cpx) – 85 vol%; vesicles – 3 vol%
WAI-1, 2, 3	Plagioclase megacryst-bearing basalt, Waipio Valley, Kohala volcano; Plagioclase (1 cm) – 15 vol%; groundmass (plag, cpx, oxides) – 83 vol%; vesicles – 2 vol%

This suite of samples was subsampled for geochemical experiments reported in a separate section of the project final report. Sufficient material remains for further future studies.

Results and Discussion

The results of the University of Hawai‘i portion of the project are intended for incorporation into and synthesis with the project as a whole. As such, the mineralogical and chemical compositions of the samples reported here form the contextual starting point of the experimental and modeling results discussed in other chapters of the final project report.

The project goals were focused on assessing the carbonation potential of mafic silicate minerals and rocks for carbon capture to mitigate anthropogenic CO_2 buildup in the atmosphere. In addition to this work, Hawaiian basalts have been used in other mineral carbonation experiments [*Johnson et al.*, 2012; *Johnson et al.*, 2010; *Thompson et al.*, 2013; *Zhang et al.*, 2012; *Zhang et al.*, 2013]. These studies complement and, in some cases, serve as preliminary results of this study. Specifics of our experimental and modeling results in this project are discussed in separate sections of this final report, and in preliminary reports presented elsewhere (e.g., [*Zhang et al.*, 2012; *Zhang et al.*, 2013]).

Thermodynamics indicates that the high temperature igneous silicate phases olivine (Mg_2SiO_4), clinopyroxene ($CaMgSi_2O_6$), plagioclase ($CaAl_2Si_2O_8$) and orthopyroxene ($MgSiO_3$) are unstable at surface temperatures and pressures following eruption and emplacement at surface or near-surface conditions. These phases will naturally weather to stable carbonates (magnesite [$MgCO_3$], calcite [$CaCO_3$], siderite [$FeCO_3$]), clays, serpentine species, oxy-hydroxides, and other secondary phases depending on surface and near-surface T-P-X conditions. Consistent with other studies on the carbonation potential of mafic and ultramafic rocks in other geologic settings [*Goldberg et al.*, 2008; *Kelemen and Matter*, 2008; *Matter and Kelemen*, 2009; *McGrail et al.*, 2006; *Schaef et al.*, 2008], our results show favorable carbonation reaction conditions involving olivine and CO_2-bearing fluids at low temperatures and pressures (50 – 250°C, 100-500 bars) on short timescales (1-14 days). Previous studies have shown that carbonation reactions progress much more efficiently and to further extents when water is in the fluid phase with varying amounts of dissolved $CO_2 \pm SO_2$ [*Johnson et al.*, 2012; *Johnson et al.*, 2010; *Schaef et al.*, 2008] or $NaHCO_3$ at 200°C and 200 bars [*Zhang et al.*, 2012; *Zhang et al.*, 2013] to produce the stable carbonate minerals magnesite ($MgCO_3$) and calcite (CaCO3) from olivine, clinopyroxene, and plagioclase in Hawaiian basalts and picrites. Pure CO_2 in the supercritical phase (~35°C, ~78 bars) is substantially less reactive in experiments on Hawaiian basalts [*Johnson et al.*, 2012; *Johnson et al.*, 2010], suggesting the importance of water or dissolved ionic species in triggering or catalyzing natural weathering reactions involving mafic silicates and CO_2.

CO_2 Sequestration Potential of the Hawaiian Ridge

In this section I will use results from this study and from the literature to examine the potential for the Hawaiian volcanic ridge to permanently store CO_2,.
Assumptions:

1) Simplified mineral formulae
   a) Olivine: $(Mg, Fe)_2SiO_4$
   b) Orthopyroxene: $(Mg,Fe)_2Si_2O_6$
   c) Clinopyroxene: $Ca(Mg,Fe)Si_2O_6$
   d) Plagioclase Feldspar: $Na_{(1-x)}Ca_xAl_{(1+x)}Si_{(3-x)}O_8$
   e) Fe-Ti oxide: $(Fe,Ti)_3O_4$

2) Carbonation of olivine occurs together with hydration via the following simplified reactions:

$$4Mg_2SiO_4\,(\text{Mg-olivine}) + 4H_2O + 2CO_2 = 2Mg_3Si_2O_5(OH)_4\,(\text{serpentine}) + 2MgCO_3\,(\text{magnesite}) \quad (2a)$$
$$4Mg_2SiO_4 + H_2O + 5CO_2 = Mg_3Si_4O_{10}(OH)_2\,(\text{talc}) + 5MgCO_3 \quad (2b)$$
$$4Mg_2SiO_4 + 8CO_2 = 4SiO_2\,(\text{quartz}) + 8MgCO_3 \quad (2c)$$

After hydration, carbonation occurs via the simplified reactions:

$$4Mg_2SiO_4 + 6H_2O = 2Mg_3Si_2O_5(OH)_4 + 2Mg(OH)_2\,(\text{brucite}) \quad (2d)$$
$$\text{products of 1d} + 2CO_2 = 2Mg_3Si_2O_5(OH)_4 + 2MgCO_3 + 2H_2O \quad (2e)$$
$$\text{products of 1e} + 3CO_2 = Mg_3Si_4O_{10}(OH)_2 + 5MgCO_3 + 5H_2O \quad (2f)$$
$$\text{products of 1f} + 3CO_2 = 4SiO_2 + 8MgCO_3 + 6H_2O \quad (2g)$$

These reactions are written with no components other than H_2O andCO_2 in fluids, but can

include other key components, such as Ca^{2+}, aqueous SiO_2, H_2, sulfur species, and O_2.

Other important mafic silicate igneous rock-forming minerals are Ca-poor pyroxene (orthopyroxene or opx, with Mg-end-member enstatite, $MgSiO_3$) and Ca-rich pyroxene (clinopyroxene or cpx, with Mg-end-member diopside, $CaMgSi_2O_6$). To describe natural carbonation of mafic and ultramafic rocks, we add the simplified reaction:

$$4Mg_2SiO_4 + CaMgSi_2O_6 + 6H_2O + CO_2 = 3Mg_3Si_2O_5(OH)_4 + CaCO_3\,(calcite) \quad (2h)$$

This reaction often takes place in stages; that is,

$$4Mg_2SiO_4 + CaMgSi_2O_6 + 7H_2O = 3Mg_3Si_2O_5(OH)_4 + Ca^{2+}(aq) + 2OH^-(aq) \quad (2i)$$

which occurs in the subsurface, and then

$$Ca^{2+}(aq) + 2OH^-(aq) + CO_2\,(aq\ or\ gas) = CaCO_3 + H_2O \quad (2j)$$

occurs under certain conditions when fluids modified by the aforementioned reactions form carbonates at or near the surface [*Kelemen et al.*, 2011].

We can make use of the mineral carbonation results from this and other studies on Hawaiian basalts[*Johnson et al.*, 2012; *Johnson et al.*, 2010; *Schaef et al.*, 2008; *Thompson et al.*, 2013; *Zhang et al.*, 2013] to calculate the theoretical CO_2 storage capacity of the Hawaiian Ridge basalts. The calculated volume of Hawaiian basalts for the main Hawaiian Ridge (the islands Niʻihau, Kauaʻi, Ōʻahu, Moloka'i, Lānaʻi, Maui, Kahoʻolawe, Hawaiʻi and their submarine edifices built on the Pacific Plate, along with the young active Lōʻihi seamount) is 527,200 cubic kilometers[*Robinson and Eakins*, 2006]. This places the Hawaiian Ridge in the class of bona fide Large Igneous Provinces ("LIPs") comparable in volume to the Deccan Traps of India (a major LIP at 512,000 km^3), and exceeding the volume of many other major LIPS, including the Columbia River Flood Basalt Province in Washington.

To calculate the CO_2 storage capacity of the Hawaiian Ridge basalts, I assumed average mineral phenocryst abundances ("modes") of 12 volume% Mg-rich olivine, 25% plagioclase, and 20% cpx, along with an average porosity of 15%, with the remainder being fine-grained groundmass of glass, plagioclase, pyroxene, and oxides. However, modes are highly variable from picrites to aphyric basalts, resulting in variable storage capacities on small scales. As an upper limit, assuming complete carbonation of these three mineral phases (olivine, plagioclase, and pyroxene) and the reactions above, I calculated the carbonation potential of the Hawaiian Ridge (from the base of the volcanoes resting on the seafloor to the summits, as noted above). Based on those assumptions, I calculated that about 2.6×10^{17} kg CO_2 can be absorbed to convert all of these silicate phases to carbonates. Stated another way, 100 times the present-day atmospheric CO_2 ($2.2\text{-}2.9 \times 10^{15}$ kg CO_2) could be stably sequestered in Hawaiian Ridge basalts alone. As I mentioned, this number is a maximum value based on reasonable average compositions and 100% efficient chemical reactions. Considering that pre-industrial atmospheric CO_2 levels are estimated at $1.4\text{-}2.2 \times 10^{15}$ kg CO_2[*Barnola et al.*, 1987], the amount of anthropogenic CO_2 is $6.0\text{-}7.0 \times 10^{14}$ kg. Consequently, as much as 400 times the anthropogenic CO_2 production could

be stably sequestered in Hawaiian Ridge basalts alone. However, this maximum is predicated on complete carbonation efficiency of available silicate phases. Nevertheless, even at as little as 1% efficiency of the carbonation reactions or exposure volumes, Hawaiian basalts have the potential to significantly reduce the anthropogenic CO_2 load in the atmosphere.

Conclusions

Basalts were collected from 15 locations on the island of Hawai‘i. The samples were fully characterized by petrographic and geochemical analysis and were used as starting materials for experiments on basalt carbonation potential at 50 – 250°C and 50 – 200 bars in the presence of $NaHCO_3$. Details of these experiments are presented in other sections of the final report, but olivine was found to be highly reactive in the presence of CO_2. Based on results from this work and other studies, we conclude that basalts comprising the Hawaiian Ridge have the capacity to sequester most of the anthropogenic CO_2 currently produced, even at less than optimum carbonation efficiency.

References

Barnola, J. M., D. Raynaud, Y. S. Korotkevich, and C. Lorius (1987), Vostok ice core provides 160,000-year record of atmospheric CO_2, *Nature*, *329*, 408-414.

Goldberg, D. S., T. Takahashi, and A. L. Slagle (2008), Carbon dioxide sequestration in deep-sea basalt, *Proceedings of the National Academy of Sciences of the United States of America*, *105*(29), 9920-9925.

Johnson, K. T. M., B. P. McGrail, and H. T. Schaef (2012), CO_2 Reaction Experiments on Hawaiian Picrites, *Chapman Conference - Hawaiian Volcanoes: From Source to Surface*.

Johnson, K. T. M., B. P. McGrail, H. T. Schaef, and A. T. Owen (2010), Geologic Sequestration Studies with Hawaiian Picrites, *AGU Fall Meeting*.

Kelemen, P. B., and J. Matter (2008), In situ carbonation of peridotite for CO2 storage, *Proceedings of the National Academy of Sciences*, *105*(45), 17295-17300.

Kelemen, P. B., J. Matter, E. E. Streit, J. F. Rudge, W. B. Curry, and J. Blusztajn (2011), Rates and Mechanisms of Mineral Carbonation in Peridotite: Natural Processes and Recipes for Enhanced, in situ CO_2 Capture and Storage, *Ann Rev of Earth and Planet Sci*, *39*(1), 545-576.

Matter, J. M., and P. B. Kelemen (2009), Permanent storage of carbon dioxide in geological reservoirs by mineral carbonation, *Nature Geoscience*, *2*(12), 837-841.

McGrail, B. P., H. T. Schaef, A. M. Ho, Y.-J. Chien, J. J. Dooley, and C. L. Davidson (2006), Potential for carbon dioxide sequestration in flood basalts, *Journal of Geophysical Research*, *111*(B12).

Robinson, J. E., and B. W. Eakins (2006), Calculated volumes of individual shield volcanoes at the young end of the Hawaiian Ridge, *Journal of Volcanology and Geothermal Research*, *151*(1-3), 309-317.

Ryan, W. B. F., et al. (2009), Global Multi-Resolution Topography synthesis, *Geochemistry, Geophysics, Geosystems*, *10*(3), n/a-n/a.

Schaef, H. T., B. P. McGrail, and A. T. Owen (2008), Carbonate Mineralization of Volcanic Province Basalts, *Energy Procedia*, *GHGT-9*, 1-7.

Thompson, C., K. Gauglitz, J. Loring, H. T. Schaef, Q. Miller, K. T. M. Johnson, Z. Wang, K. Rosso, and B. P. McGrail (2013), Investigation of Plagioclase Reactivity in Wet Supercritical CO_2 by In Situ Infrared Spectroscopy, *AGU Fall Meeting*.

Zhang, S., L. Qiu, Z. Wang, S. Karato, K. T. M. Johnson, J. Ague, M. Oristaglio, E. W. Bolton, and D. Bercovici (2012), Experimental study of the kinetics of CO_2-sequestration by Hawaiian picrites, *AGU Fall Meeting*.

Zhang, S., Z. Wang, L. Qiu, S. Karato, K. T. M. Johnson, J. Ague, M. Oristaglio, E. W. Bolton, and D. Bercovici (2013), Experimental study of the reaction kinetics between CO_2-bearing solution and picrite cubes, *AGU Fall Meeting*.

Appendix 1. Geochemistry - Olivine, Pyroxene Electron Microprobe Analyses

SAMPLE	DAT/TIM	SiO2 WT%	TiO2 WT%	Al2O3 WT%	Cr2O3 WT%	FeO WT%	MnO WT%	MgO WT%	CaO WT%	NiO WT%	P2O5 WT%	TOTAL
Un 2 499_1_core	8/8/12 11:16	40.58	0.00	0.03	0.07	11.86	0.17	47.40	0.25	0.35	0.00	100.72
Un 2 499_1_core	8/8/12 11:19	40.60	0.00	0.04	0.07	11.90	0.16	47.35	0.23	0.33	0.00	100.68
Un 3 499_1_rim	8/8/12 11:54	40.66	0.00	0.04	0.07	11.57	0.16	47.57	0.23	0.34	0.00	100.65
Un 3 499_1_rim	8/8/12 11:57	40.69	0.00	0.03	0.09	11.75	0.17	47.59	0.23	0.33	0.02	100.91
Un 4 499_2_core	8/8/12 12:01	40.38	0.00	0.04	0.08	11.82	0.14	47.60	0.22	0.34	0.00	100.63
Un 4 499_2_core	8/8/12 12:04	40.43	0.01	0.05	0.08	11.72	0.16	47.73	0.22	0.33	0.00	100.74
Un 5 499_2_rim	8/8/12 12:07	40.28	0.00	0.06	0.08	12.97	0.16	46.63	0.26	0.31	0.00	100.75
Un 5 499_2_rim	8/8/12 12:11	40.34	0.00	0.05	0.07	12.97	0.17	46.64	0.24	0.32	0.00	100.82
Un 6 499_3_lo-Ca-px_core	8/8/12 12:14	53.03	0.49	1.44	0.14	13.86	0.29	27.49	2.36	0.08	0.00	99.19
Un 6 499_3_lo-Ca-px_core	8/8/12 12:17	52.99	0.48	1.32	0.14	13.80	0.28	27.74	2.37	0.07	0.00	99.20
Un 7 499_3_lo-Ca-px_rim	8/8/12 12:21	53.53	0.39	1.19	0.10	13.19	0.27	28.32	2.25	0.04	0.00	99.27
Un 7 499_3_lo-Ca-px_rim	8/8/12 12:24	53.45	0.39	1.15	0.09	13.07	0.29	28.22	2.24	0.05	0.00	98.95
Un 8 499_4_core	8/8/12 12:27	40.38	0.00	0.03	0.08	12.31	0.17	46.97	0.23	0.38	0.01	100.57
Un 8 499_4_core	8/8/12 12:31	40.41	0.00	0.03	0.07	12.29	0.16	46.81	0.23	0.38	0.01	100.40
Un 9 499_4_rim	8/8/12 12:34	40.16	0.01	0.05	0.07	13.18	0.19	46.24	0.24	0.33	0.02	100.49
Un 9 499_4_rim	8/8/12 12:37	40.21	0.00	0.04	0.07	12.65	0.15	46.86	0.23	0.35	0.03	100.59
Un 10 499_5_core	8/8/12 12:41	40.24	0.00	0.03	0.05	13.01	0.18	46.79	0.24	0.28	0.00	100.82
Un 10 499_5_core	8/8/12 12:44	40.02	0.00	0.03	0.11	12.93	0.19	46.58	0.24	0.24	0.02	100.36
Un 11 499_5_rim	8/8/12 12:47	39.68	0.01	0.03	0.04	15.47	0.19	44.77	0.26	0.27	0.02	100.74
Un 11 499_5_rim	8/8/12 12:51	39.72	0.01	0.03	0.06	14.98	0.20	45.32	0.25	0.27	0.01	100.84
Un 12 499_6_core	8/8/12 13:02	39.75	0.01	0.02	0.05	14.24	0.19	45.76	0.24	0.27	0.01	100.53
Un 12 499_6_core	8/8/12 13:06	39.90	0.01	0.04	0.05	14.31	0.22	45.91	0.23	0.28	0.00	100.95
Un 13 499_6_rim	8/8/12 13:28	39.77	0.00	0.03	0.05	14.87	0.19	45.06	0.24	0.31	0.01	100.53
Un 13 499_6_rim	8/8/12 13:32	39.52	0.01	0.05	0.04	16.65	0.22	43.71	0.27	0.27	0.00	100.74
Un 14 499_7_core	8/8/12 13:35	40.17	0.01	0.05	0.09	11.05	0.13	47.84	0.22	0.37	0.01	99.93
Un 14 499_7_core	8/8/12 13:38	40.18	0.00	0.05	0.09	11.06	0.16	47.79	0.21	0.39	0.00	99.94
Un 15 499_7_rim	8/8/12 13:42	39.94	0.01	0.06	0.07	13.23	0.18	46.41	0.23	0.36	0.01	100.50
Un 15 499_7_rim	8/8/12 13:45	39.71	0.01	0.05	0.07	14.44	0.20	45.53	0.26	0.31	0.01	100.59
Un 16 647_1_rim	8/8/12 13:48	40.27	0.00	0.04	0.07	13.30	0.17	46.32	0.24	0.35	0.00	100.78
Un 17 647_2_core	8/8/12 13:52	40.12	0.00	0.04	0.07	12.22	0.16	47.44	0.23	0.38	0.00	100.65
Un 17 647_2_core	8/8/12 13:55	40.23	0.00	0.03	0.08	12.12	0.18	47.39	0.22	0.38	0.00	100.63
Un 18 647_2_rim	8/8/12 13:58	39.41	0.00	0.04	0.04	14.32	0.19	45.83	0.26	0.31	0.01	100.42
Un 18 647_2_rim	8/8/12 14:02	39.20	0.01	0.02	0.06	14.72	0.20	45.50	0.26	0.32	0.01	100.30
Un 19 647_3_core	8/8/12 14:05	39.80	0.00	0.04	0.06	12.50	0.16	46.93	0.22	0.39	0.00	100.11
Un 19 647_3_core	8/8/12 14:09	40.15	0.01	0.04	0.09	12.66	0.17	46.84	0.21	0.37	0.01	100.55
Un 20 647_3_rim	8/8/12 14:12	39.53	0.02	0.04	0.06	14.15	0.16	45.60	0.25	0.33	0.01	100.14
Un 20 647_3_rim	8/8/12 14:15	39.40	0.00	0.03	0.04	13.96	0.17	45.83	0.24	0.31	0.00	99.99
Un 21 647_4_core	8/8/12 14:19	40.42	0.00	0.04	0.10	11.51	0.14	47.41	0.21	0.40	0.00	100.24
Un 21 647_4_core	8/8/12 14:22	40.27	0.00	0.04	0.10	11.53	0.17	47.46	0.21	0.40	0.00	100.17
Un 22 647_4_rim	8/8/12 14:25	39.94	0.02	0.05	0.09	13.39	0.18	46.15	0.24	0.37	0.00	100.43
Un 22 647_4_rim	8/8/12 14:29	39.76	0.01	0.05	0.07	14.54	0.19	45.16	0.26	0.29	0.03	100.37
Un 23 499_wehrl4_core	8/8/12 15:24	39.38	0.00	0.03	0.04	15.78	0.22	44.26	0.26	0.31	0.01	100.27
Un 23 499_wehrl4_core	8/8/12 15:27	39.39	0.00	0.02	0.03	15.66	0.24	44.42	0.26	0.30	0.01	100.33
Un 24 499_wehrl4-opx_core	8/8/12 15:30	53.49	0.31	1.43	0.45	10.73	0.24	29.58	2.12	0.08	0.01	98.43
Un 25 san carlos olivine before	8/8/12 16:35	40.42	0.00	0.02	0.02	9.51	0.13	48.76	0.10	0.37	0.01	99.35
Un 25 san carlos olivine before	8/8/12 16:39	40.38	0.00	0.03	0.00	9.52	0.13	48.80	0.10	0.36	0.01	99.33
Un 26 499_wehrl1_core	8/8/12 16:47	39.03	0.01	0.02	0.06	16.32	0.22	43.59	0.25	0.31	0.00	99.80
Un 26 499_wehrl1_core	8/8/12 16:50	39.17	0.02	0.03	0.04	16.23	0.21	43.71	0.25	0.33	0.00	99.99
Un 27 499_wehrl1_rim_to-cpx	8/8/12 16:53	39.26	0.02	0.03	0.04	15.84	0.22	44.19	0.28	0.29	0.00	100.17
Un 27 499_wehrl1_rim_to-cpx	8/8/12 16:57	39.45	0.00	0.02	0.03	15.53	0.23	44.52	0.26	0.31	0.01	100.36
Un 28 499_wehrl1_rim_to-groundmass	8/8/12 17:00	38.39	0.01	0.03	0.03	20.46	0.26	41.11	0.27	0.24	0.01	100.80
Un 28 499_wehrl1_rim_to-groundmass	8/8/12 17:04	38.84	0.00	0.03	0.04	18.16	0.24	42.86	0.26	0.26	0.01	100.70
Un 29 499_wehrl2_core	8/8/12 17:07	39.25	0.01	0.01	0.04	15.55	0.21	44.37	0.26	0.27	0.01	99.99
Un 29 499_wehrl2_core	8/8/12 17:10	39.12	0.00	0.03	0.04	15.63	0.23	44.51	0.27	0.30	0.09	100.21
Un 30 499_wehrl2_rim	8/8/12 17:14	39.23	0.00	0.04	0.05	15.58	0.22	44.47	0.29	0.30	0.01	100.19
Un 30 499_wehrl2_rim	8/8/12 17:17	39.31	0.01	0.04	0.04	15.74	0.21	44.13	0.30	0.30	0.00	100.08
Un 31 499_wehrl3_core	8/8/12 17:20	39.11	0.02	0.02	0.06	15.65	0.23	44.55	0.26	0.30	0.01	100.20
Un 31 499_wehrl3_core	8/8/12 17:24	39.12	0.00	0.02	0.05	15.61	0.24	44.57	0.26	0.29	0.00	100.16
Un 32 499_wehrl3_rim	8/8/12 17:27	39.04	0.02	0.04	0.06	15.64	0.21	44.18	0.31	0.29	0.00	99.80
Un 32 499_wehrl3_rim	8/8/12 17:30	39.11	0.01	0.03	0.05	15.63	0.26	44.50	0.32	0.29	0.00	100.20
Un 33 499_wehrl5_core	8/8/12 17:34	39.14	0.01	0.02	0.05	16.11	0.24	44.27	0.25	0.31	0.03	100.42
Un 33 499_wehrl5_core	8/8/12 17:37	39.01	0.01	0.03	0.02	16.05	0.23	43.99	0.26	0.31	0.02	99.93
Un 34 499_wehrl5_rim	8/8/12 17:40	39.09	0.00	0.03	0.04	15.68	0.23	44.40	0.31	0.27	0.02	100.07
Un 34 499_wehrl5_rim	8/8/12 17:44	39.18	0.00	0.03	0.06	15.81	0.21	44.27	0.30	0.29	0.01	100.17
Un 35 499_wehrl6_core	8/8/12 17:47	39.12	0.00	0.02	0.05	15.56	0.21	44.50	0.26	0.31	0.01	100.04
Un 35 499_wehrl6_core	8/8/12 17:50	39.04	0.00	0.02	0.03	15.59	0.23	44.64	0.26	0.30	0.00	100.12
Un 36 499_wehrl6_rim	8/8/12 17:54	38.96	0.01	0.03	0.04	16.21	0.21	44.19	0.30	0.26	0.00	100.22
Un 36 499_wehrl6_rim	8/8/12 17:57	38.95	0.01	0.04	0.05	15.55	0.20	44.59	0.29	0.30	0.01	100.00
Un 37 499_wehrl6_cpx	8/8/12 18:00	49.14	0.68	2.61	1.04	5.65	0.15	17.98	19.77	0.06	0.01	97.07
Un 37 499_wehrl6_cpx	8/8/12 18:04	50.06	0.46	2.03	0.92	5.26	0.15	19.17	18.70	0.07	0.01	96.83
Un 37 499_wehrl6_cpx	8/8/12 18:07	49.69	0.57	2.50	1.09	5.21	0.11	18.81	19.06	0.04	0.00	97.09
Un 37 499_wehrl6_cpx	8/8/12 18:10	49.40	0.71	2.51	1.03	5.21	0.17	18.41	19.57	0.08	0.00	97.08
Un 37 499_wehrl6_cpx	8/8/12 18:14	49.48	0.81	2.47	1.02	5.19	0.14	18.06	19.91	0.06	0.01	97.14
Un 38 499_wehrl6_cpx-exolved	8/8/12 18:17	49.16	0.69	2.47	1.03	6.13	0.13	18.24	19.17	0.05	0.01	97.09
Un 38 499_wehrl6_cpx-exolved	8/8/12 18:20	49.33	0.56	2.54	1.11	5.41	0.18	18.56	19.29	0.04	0.01	97.04
Un 38 499_wehrl6_cpx-exolved	8/8/12 18:24	49.53	0.56	2.53	1.11	5.71	0.14	18.54	18.98	0.06	0.01	97.17
Un 38 499_wehrl6_cpx-exolved	8/8/12 18:27	49.61	0.51	2.45	1.08	5.61	0.13	19.18	18.41	0.07	0.01	97.06
Un 39 499_opx-cpx8	8/8/12 18:30	49.21	0.68	2.37	0.51	7.73	0.21	17.71	18.50	0.04	0.01	96.97
Un 39 499_opx-cpx8	8/8/12 18:34	48.61	0.83	2.40	0.47	8.25	0.18	16.75	19.48	0.03	0.01	97.01
Un 39 499_opx-cpx8	8/8/12 18:37	48.52	0.78	2.63	0.56	8.24	0.20	16.87	19.15	0.03	0.01	96.98
Un 39 499_opx-cpx8	8/8/12 18:40	49.17	0.73	2.28	0.44	9.57	0.20	18.21	16.50	0.03	0.01	97.15
Un 39 499_opx-cpx8	8/8/12 18:44	51.70	0.42	1.49	0.22	14.54	0.29	26.51	2.52	0.06	0.00	97.75
Un 39 499_opx-cpx8	8/8/12 18:47	51.37	0.32	1.51	0.29	13.21	0.27	27.12	2.40	0.07	0.01	96.58
Un 39 499_opx-cpx8	8/8/12 18:50	52.83	0.28	1.09	0.22	12.85	0.23	28.16	2.34	0.04	0.00	98.03
Un 39 499_opx-cpx8	8/8/12 18:54	52.63	0.29	1.07	0.21	13.63	0.29	27.67	2.32	0.04	0.00	98.15
Un 40 499_ol9_core	8/8/12 18:57	39.84	0.00	0.05	0.07	10.94	0.13	48.03	0.22	0.36	0.01	99.64
Un 40 499_ol9_core	8/8/12 19:00	39.72	0.00	0.05	0.10	10.95	0.14	48.20	0.21	0.36	0.00	99.73
Un 41 499_ol9_rim	8/8/12 19:04	38.88	0.01	0.04	0.03	16.23	0.25	44.16	0.24	0.29	0.04	100.18
Un 41 499_ol9_rim	8/8/12 19:07	38.94	0.02	0.03	0.03	15.85	0.21	44.40	0.25	0.27	0.05	100.06
Un 42 499_rounded-opx_profile-rim-core	8/8/12 19:10	49.88	0.78	2.01	0.38	9.58	0.23	20.00	14.23	0.05	0.01	97.14
Un 42 499_rounded-opx_profile-rim-core	8/8/12 19:14	51.94	0.50	2.06	0.53	11.09	0.24	28.01	3.72	0.08	0.01	98.17
Un 42 499_rounded-opx_profile-rim-core	8/8/12 19:17	52.52	0.40	1.65	0.55	10.81	0.23	28.88	2.88	0.05	0.01	97.99
Un 42 499_rounded-opx_profile-rim-core	8/8/12 19:20	51.94	0.51	1.59	0.17	13.85	0.29	27.45	2.41	0.07	0.00	98.29

Appendix 1. Geochemistry - Olivine, Pyroxene Electron Microprobe Analyses

SAMPLE	DAT/TIM	SiO2 WT%	TiO2 WT%	Al2O3 WT%	Cr2O3 WT%	FeO WT%	MnO WT%	MgO WT%	CaO WT%	NiO WT%	P2O5 WT%	TOTAL
Un 42 499_rounded-opx_profile-rim-core	8/8/12 19:24	46.87	0.47	1.49	0.14	12.50	0.28	24.72	2.18	0.07	0.00	88.72
Un 42 499_rounded-opx_profile-rim-core	8/8/12 19:27	52.14	0.53	1.53	0.16	13.85	0.31	27.47	2.38	0.06	0.00	98.44
Un 42 499_rounded-opx_profile-rim-core	8/8/12 19:30	51.77	0.52	1.51	0.15	13.94	0.26	27.37	2.36	0.05	0.00	97.95
Un 42 499_rounded-opx_profile-rim-core	8/8/12 19:34	51.89	0.51	1.52	0.15	14.00	0.30	27.37	2.37	0.08	0.00	98.18
Un 42 499_rounded-opx_profile-rim-core	8/8/12 19:37	52.12	0.53	1.53	0.15	13.81	0.27	27.16	2.72	0.06	0.00	98.34
Un 42 499_rounded-opx_profile-rim-core	8/8/12 19:41	52.05	0.51	1.46	0.15	13.91	0.27	27.08	2.78	0.09	0.00	98.29
Un 42 499_rounded-opx_profile-rim-core	8/8/12 19:44	52.12	0.51	1.43	0.13	13.82	0.26	27.15	2.66	0.08	0.00	98.16
Un 42 499_rounded-opx_profile-rim-core	8/8/12 19:47	51.99	0.50	1.47	0.15	13.78	0.30	27.11	2.78	0.07	0.01	98.15
Un 42 499_rounded-opx_profile-rim-core	8/8/12 19:51	51.98	0.53	1.48	0.16	13.85	0.28	27.16	2.78	0.09	0.00	98.31
Un 42 499_rounded-opx_profile-rim-core	8/8/12 19:54	50.96	0.60	2.38	0.68	10.02	0.25	24.00	8.75	0.06	0.01	97.69
Un 42 499_rounded-opx_profile-rim-core	8/8/12 19:57	48.91	0.93	3.04	0.54	9.08	0.19	19.66	14.72	0.05	0.02	97.13
Un 43 499_opx11_core	8/8/12 20:01	52.57	0.39	0.98	0.02	15.45	0.31	26.85	2.18	0.05	0.01	98.81
Un 43 499_opx11_core	8/8/12 20:04	52.23	0.45	1.34	0.04	14.91	0.33	27.02	2.24	0.05	0.00	98.60
Un 44 499_opx11_rim	8/8/12 20:07	52.24	0.49	1.24	0.03	16.09	0.32	26.35	2.22	0.04	0.01	99.02
Un 44 499_opx11_rim	8/8/12 20:11	52.16	0.49	1.23	0.03	16.01	0.33	26.40	2.26	0.03	0.00	98.95
Un 45 647_5_core	8/8/12 20:14	40.28	0.00	0.04	0.06	11.83	0.18	47.55	0.23	0.35	0.01	100.53
Un 45 647_5_core	8/8/12 20:17	40.14	0.02	0.05	0.06	11.85	0.15	47.37	0.24	0.34	0.09	100.32
Un 45 647_5_core	8/8/12 20:21	39.98	0.00	0.04	0.08	11.68	0.17	47.73	0.23	0.38	0.00	100.29
Un 46 647_5_rim	8/8/12 20:24	39.40	0.02	0.03	0.06	13.83	0.20	46.26	0.22	0.33	0.00	100.34
Un 46 647_5_rim	8/8/12 20:28	39.39	0.00	0.04	0.06	14.06	0.19	46.13	0.25	0.31	0.00	100.43
Un 47 647_6_core	8/8/12 20:31	39.99	0.00	0.06	0.09	11.75	0.17	47.56	0.22	0.39	0.00	100.23
Un 47 647_6_core	8/8/12 20:34	39.96	0.01	0.04	0.11	11.79	0.15	47.48	0.22	0.40	0.01	100.17
Un 48 647_6_rim	8/8/12 20:38	39.76	0.02	0.05	0.07	12.83	0.18	46.86	0.23	0.35	0.00	100.34
Un 48 647_6_rim	8/8/12 20:41	39.30	0.01	0.05	0.08	13.40	0.17	46.52	0.24	0.38	0.03	100.18
Un 49 647_7_core	8/8/12 20:44	39.84	0.00	0.04	0.09	12.23	0.16	47.33	0.22	0.39	0.01	100.30
Un 49 647_7_core	8/8/12 20:48	39.94	0.00	0.04	0.08	12.41	0.22	47.38	0.22	0.38	0.01	100.69
Un 50 647_7_rim	8/8/12 20:51	39.47	0.01	0.04	0.06	14.64	0.19	45.80	0.26	0.37	0.02	100.85
Un 50 647_7_rim	8/8/12 20:54	39.29	0.01	0.06	0.07	14.70	0.22	45.73	0.28	0.33	0.03	100.72
Un 51 647_8_core	8/8/12 20:58	39.66	0.00	0.03	0.06	13.50	0.19	46.38	0.27	0.28	0.01	100.39
Un 51 647_8_core	8/8/12 21:01	39.67	0.01	0.02	0.05	13.43	0.21	46.55	0.26	0.26	0.04	100.50
Un 52 647_8_rim	8/8/12 21:04	39.50	0.02	0.03	0.06	14.75	0.20	45.21	0.27	0.31	0.01	100.37
Un 52 647_8_rim	8/8/12 21:08	39.56	0.02	0.05	0.05	14.12	0.19	45.86	0.27	0.31	0.02	100.45
Un 53 647_9_core	8/8/12 21:11	39.32	0.00	0.04	0.06	14.53	0.19	45.80	0.24	0.29	0.00	100.49
Un 53 647_9_core	8/8/12 21:15	39.48	0.00	0.05	0.08	14.50	0.19	45.78	0.23	0.31	0.00	100.62
Un 54 647_9_rim	8/8/12 21:18	39.31	0.00	0.04	0.05	14.30	0.19	45.95	0.25	0.30	0.01	100.39
Un 54 647_9_rim	8/8/12 21:21	39.72	0.01	0.05	0.06	14.91	0.21	45.36	0.28	0.28	0.00	100.89
Un 55 san carlos olivine after	8/8/12 21:25	40.43	0.00	0.04	0.02	9.55	0.11	49.12	0.09	0.34	0.00	99.71
Un 55 san carlos olivine after	8/8/12 21:28	40.45	0.00	0.02	0.03	9.45	0.15	49.12	0.10	0.34	0.00	99.66
Un 55 san carlos olivine after	8/8/12 21:31	40.44	0.00	0.03	0.01	9.65	0.14	49.34	0.10	0.37	0.01	100.09
Un 56 SanCarlos-ol	8/10/12 11:28	40.75	0.00	0.02	0.02	9.48	0.14	49.28	0.09	0.35	0.00	100.13
Un 56 SanCarlos-ol	8/10/12 11:32	40.89	0.00	0.03	0.01	9.57	0.15	49.17	0.10	0.37	0.00	100.28
Un 57 SanCarlos-ol	8/10/12 12:07	40.68	0.00	0.02	0.01	9.61	0.16	49.20	0.09	0.35	0.00	100.13
Un 57 SanCarlos-ol	8/10/12 12:10	40.74	0.01	0.03	0.02	9.52	0.14	49.29	0.10	0.38	0.00	100.21
Un 58 Wai1_ol1_core	8/10/12 12:14	37.54	0.01	0.07	0.01	23.64	0.28	37.68	0.32	0.19	0.04	99.78
Un 58 Wai1_ol1_core	8/10/12 12:17	45.86	7.61	18.84	0.01	7.80	0.12	0.31	7.08	0.00	0.02	87.67
Un 59 Wai1_ol1_rim	8/10/12 12:20	36.77	0.05	0.04	0.02	31.85	0.41	31.79	0.32	0.13	0.00	101.39
Un 59 Wai1_ol1_rim	8/10/12 12:24	36.43	0.07	0.27	0.01	27.96	0.29	32.75	0.41	0.13	0.07	98.40
Un 60 Wai1_ol2_core	8/10/12 12:27	38.17	0.01	0.01	0.03	23.07	0.29	38.77	0.28	0.20	0.01	100.84
Un 60 Wai1_ol2_core	8/10/12 12:30	38.00	0.02	0.02	0.03	23.22	0.30	38.67	0.30	0.16	0.00	100.71
Un 61 Wai1_ol2_rim	8/10/12 12:34	35.31	0.09	0.24	0.02	36.19	0.45	26.96	0.31	0.09	0.11	99.77
Un 61 Wai1_ol2_rim	8/10/12 12:37	36.00	0.10	0.81	0.03	28.89	0.34	29.25	0.39	0.16	0.14	96.11
Un 61 Wai1_ol2_rim	8/10/12 12:40	35.33	0.18	0.50	0.01	42.09	0.38	17.39	0.41	0.05	0.09	96.42
Un 62 Wai1_ol3_inclusion-in-plag	8/10/12 12:44	38.13	0.01	0.04	0.03	22.10	0.27	38.94	0.31	0.17	0.02	100.02
Un 62 Wai1_ol3_inclusion-in-plag	8/10/12 12:47	38.02	0.02	0.05	0.02	22.17	0.28	39.06	0.31	0.18	0.02	100.12
Un 63 Wai1_ol4a_inside-plag-cpx-patch	8/10/12 12:50	38.24	0.01	0.04	0.02	22.94	0.30	38.01	0.32	0.19	0.01	100.08
Un 63 Wai1_ol4a_inside-plag-cpx-patch	8/10/12 12:54	38.19	0.01	0.02	0.02	22.86	0.28	38.54	0.31	0.18	0.01	100.43
Un 64 Wai1_ol4b_inside-plag-cpx-patch	8/10/12 12:57	38.17	0.02	0.03	0.02	22.76	0.28	38.65	0.29	0.19	0.04	100.45
Un 64 Wai1_ol4b_inside-plag-cpx-patch	8/10/12 13:00	38.25	0.01	0.03	0.03	22.75	0.27	38.72	0.30	0.18	0.02	100.55
Un 65 Wai1_ol5_left-edge-of-plag-cpx-patch	8/10/12 13:04	38.11	0.00	0.02	0.03	23.09	0.27	38.66	0.31	0.17	0.02	100.68
Un 65 Wai1_ol5_left-edge-of-plag-cpx-patch	8/10/12 13:07	38.08	0.00	0.03	0.02	23.12	0.29	38.61	0.29	0.21	0.00	100.65
Un 66 Wai1_ol5-rim_left-edge-of-plag-cpx-patch	8/10/12 13:10	36.80	0.05	0.94	0.04	26.74	0.33	31.43	0.41	0.14	0.13	97.00
Un 66 Wai1_ol5-rim_left-edge-of-plag-cpx-patch	8/10/12 13:14	35.38	0.06	0.57	0.02	30.91	0.48	27.29	0.59	0.12	0.12	95.54
Un 67 Wai1_ol6_core	8/10/12 13:17	38.17	0.02	0.01	0.02	22.78	0.31	38.71	0.28	0.20	0.02	100.50
Un 67 Wai1_ol6_core	8/10/12 13:20	38.35	0.02	0.03	0.00	22.73	0.27	38.61	0.33	0.19	0.02	100.56
Un 68 Wai1_ol6_rim	8/10/12 13:24	36.47	0.04	0.07	0.02	32.81	0.40	30.39	0.42	0.13	0.02	100.76
Un 68 Wai1_ol6_rim	8/10/12 13:27	35.83	0.16	0.17	0.02	31.40	0.39	28.82	0.34	0.12	0.06	97.32
Un 69 Wai1_ol7a_inside-plag-cpx-patch	8/10/12 13:30	38.11	0.01	0.02	0.01	22.64	0.29	38.77	0.29	0.21	0.00	100.35
Un 69 Wai1_ol7a_inside-plag-cpx-patch	8/10/12 13:34	37.94	0.01	0.02	0.02	22.71	0.31	38.64	0.29	0.20	0.01	100.15
Un 70 Wai1_ol8_quite-small_150mu	8/10/12 13:37	37.95	0.02	0.03	0.02	23.06	0.30	38.40	0.32	0.18	0.02	100.27
Un 70 Wai1_ol8_quite-small_150mu	8/10/12 13:40	37.92	0.01	0.03	0.02	22.81	0.29	38.43	0.31	0.19	0.02	100.04
Un 71 Wai1_ol8-rim_quite-small_150mu	8/10/12 13:44	34.70	0.08	0.32	0.02	33.80	0.33	25.42	0.46	0.11	0.18	95.42
Un 72 Wai1_ol8-rim_quite-small_150mu_alt?	8/10/12 13:47	35.25	0.15	0.29	0.01	33.62	0.37	28.26	0.28	0.13	0.06	98.42
Un 73 Hap1_ol1_core	8/10/12 14:50	39.84	0.01	0.04	0.05	12.97	0.19	46.55	0.32	0.25	0.00	100.21
Un 73 Hap1_ol1_core	8/10/12 14:54	39.85	0.01	0.04	0.05	12.81	0.17	46.49	0.32	0.26	0.00	99.99
Un 74 Hap1_ol1_rim	8/10/12 14:57	38.88	0.02	0.05	0.02	15.97	0.23	44.03	0.37	0.22	0.00	99.78
Un 74 Hap1_ol1_rim	8/10/12 15:00	39.34	0.01	0.04	0.04	15.75	0.22	44.04	0.35	0.23	0.00	100.02
Un 75 Hap1_ol2-core	8/10/12 15:04	39.37	0.00	0.03	0.02	14.18	0.21	45.35	0.34	0.23	0.02	99.75
Un 75 Hap1_ol2-core	8/10/12 15:07	39.60	0.00	0.03	0.06	13.82	0.21	45.53	0.35	0.27	0.02	99.90
Un 76 Hap1_ol2_rim	8/10/12 15:11	39.64	0.00	0.05	0.06	13.96	0.21	45.51	0.36	0.29	0.01	100.09
Un 76 Hap1_ol2_rim	8/10/12 15:14	39.65	0.01	0.03	0.04	14.14	0.17	45.33	0.38	0.27	0.00	100.04
Un 77 Hap1_ol3_core	8/10/12 15:17	39.55	0.01	0.03	0.03	13.61	0.18	45.53	0.35	0.27	0.00	99.56
Un 77 Hap1_ol3_core	8/10/12 15:21	39.61	0.01	0.02	0.03	13.36	0.20	45.51	0.35	0.25	0.00	99.33
Un 78 Hap1_ol3_rim	8/10/12 15:24	39.58	0.01	0.04	0.03	14.30	0.19	44.69	0.38	0.25	0.00	99.48
Un 78 Hap1_ol3_rim	8/10/12 15:27	39.54	0.00	0.06	0.03	14.21	0.19	45.11	0.39	0.23	0.00	99.75
Un 79 Hap1_ol4_core	8/10/12 15:31	39.20	0.00	0.02	0.03	14.59	0.19	44.68	0.33	0.26	0.00	99.30
Un 79 Hap1_ol4_core	8/10/12 15:34	39.51	0.00	0.03	0.03	14.57	0.23	44.77	0.33	0.26	0.01	99.74
Un 80 Hap1_ol4_rim	8/10/12 15:37	39.45	0.02	0.04	0.03	14.57	0.20	44.57	0.36	0.27	0.01	99.51
Un 80 Hap1_ol4_rim	8/10/12 15:41	39.44	0.02	0.06	0.04	14.75	0.22	44.77	0.36	0.26	0.03	99.96
Un 81 Hap1_cpx5_huge_core	8/10/12 15:44	48.52	0.88	2.76	0.61	5.53	0.12	16.52	21.60	0.03	0.01	96.58
Un 82 Hap1_cpx5_huge_darker-rim	8/10/12 15:47	48.00	0.86	3.39	1.05	5.05	0.11	16.39	21.60	0.03	0.00	96.49
Un 83 Hap1_ol6_core	8/10/12 15:51	39.57	0.01	0.04	0.04	14.07	0.19	45.56	0.31	0.29	0.02	100.11
Un 83 Hap1_ol6_core	8/10/12 15:54	39.51	0.00	0.02	0.04	14.08	0.18	45.41	0.29	0.27	0.01	99.80
Un 83 Hap1_ol6_core	8/10/12 15:57	39.49	0.02	0.02	0.04	14.08	0.19	45.14	0.33	0.26	0.00	99.58

Appendix 1. Geochemistry - Olivine, Pyroxene Electron Microprobe Analyses

SAMPLE	DAT/TIM	SiO2 WT%	TiO2 WT%	Al2O3 WT%	Cr2O3 WT%	FeO WT%	MnO WT%	MgO WT%	CaO WT%	NiO WT%	P2O5 WT%	TOTAL	
Un 84 Hap1_ol6_rim	8/10/12 16:01	39.50	0.01	0.03	0.04	14.47	0.20	45.40	0.34	0.30	0.00	100.28	
Un 84 Hap1_ol6_rim	8/10/12 16:04	39.33	0.00	0.04	0.03	14.35	0.20	45.21	0.33	0.26	0.00	99.74	
Un 85 Hap1_ol7_core	8/10/12 16:08	39.79	0.01	0.04	0.06	13.34	0.16	45.71	0.35	0.28	0.01	99.75	
Un 85 Hap1_ol7_core	8/10/12 16:11	39.64	0.00	0.02	0.05	13.32	0.20	45.84	0.36	0.30	0.00	99.73	
Un 85 Hap1_ol7_core	8/10/12 16:14	39.50	0.01	0.04	0.04	13.28	0.22	46.01	0.34	0.28	0.01	99.72	
Un 86 Hap1_ol7_rim	8/10/12 16:18	39.18	0.01	0.02	0.04	14.96	0.20	44.89	0.37	0.27	0.00	99.93	
Un 86 Hap1_ol7_rim	8/10/12 16:21	39.20	0.01	0.05	0.03	15.15	0.20	44.78	0.37	0.26	0.00	100.05	
Un 87 Hap1_ol8_core	8/10/12 16:24	38.89	0.02	0.05	0.04	15.50	0.20	44.16	0.30	0.26	0.04	99.45	
Un 87 Hap1_ol8_core	8/10/12 16:28	39.12	0.02	0.05	0.03	15.56	0.20	44.16	0.31	0.26	0.02	99.72	
Un 88 Hap1_ol8_rim	8/10/12 16:31	39.21	0.01	0.05	0.09	14.52	0.21	44.73	0.33	0.29	0.04	99.50	
Un 88 Hap1_ol8_rim	8/10/12 16:34	39.51	0.00	0.05	0.06	13.87	0.18	45.44	0.34	0.32	0.02	99.80	
Un 89 Hap1_ol9_core	8/10/12 16:38	39.32	0.01	0.04	0.06	13.70	0.17	45.81	0.35	0.26	0.00	99.72	
Un 89 Hap1_ol9_core	8/10/12 16:41	39.19	0.00	0.03	0.04	13.79	0.19	45.60	0.35	0.28	0.01	99.46	
Un 89 Hap1_ol9_core	8/10/12 16:44	39.49	0.01	0.04	0.03	13.81	0.21	45.78	0.34	0.28	0.00	100.00	
Un 90 Hap1_ol9_rim	8/10/12 16:48	39.38	0.01	0.05	0.04	14.45	0.19	44.98	0.39	0.27	0.00	99.76	
Un 90 Hap1_ol9_rim	8/10/12 16:51	39.33	0.02	0.05	0.03	14.19	0.22	45.03	0.37	0.25	0.00	99.50	
Un 91 Hap1_ol10_core	8/10/12 16:55	39.65	0.00	0.02	0.07	11.92	0.19	46.85	0.37	0.29	0.01	99.36	
Un 91 Hap1_ol10_core	8/10/12 16:58	39.36	0.02	0.04	0.06	12.16	0.17	45.96	0.37	0.27	0.00	98.41	
Un 92 Hap1_ol10_rim	8/10/12 17:01	39.70	0.02	0.04	0.06	12.98	0.19	45.71	0.38	0.27	0.01	99.34	
Un 92 Hap1_ol10_rim	8/10/12 17:05	39.39	0.00	0.04	0.03	14.24	0.20	45.22	0.37	0.26	0.01	99.78	
Un 93 SanCarlos-ol	8/10/12 17:08	40.14	0.00	0.03	0.01	9.52	0.15	48.85	0.10	0.37	0.00	99.17	
Un 93 SanCarlos-ol	8/10/12 17:11	40.05	0.00	0.02	0.02	9.49	0.13	48.87	0.10	0.38	0.00	99.07	
Un 93 SanCarlos-ol	8/10/12 17:15	40.61	0.00	0.02	0.02	9.60	0.15	49.16	0.10	0.39	0.01	100.05	
San Carlos olivine before	9/27/13 9:04	40.71	0.00	0.02	0.02	9.57	0.14	49.11	0.10	0.37	0.01	100.05	
San Carlos olivine before	9/27/13 9:07	40.68	0.00	0.03	0.00	9.59	0.13	49.15	0.10	0.36	0.01	100.05	
ML647-3_ol_random	9/27/13 9:11	39.86	0.00	0.04	0.07	13.16	0.17	45.84	0.24	0.35	0.00	99.74	
ML647-3_ol_random	9/27/13 9:14	39.75	0.00	0.04	0.07	12.11	0.16	47.01	0.22	0.37	0.00	99.75	
ML647-3_ol_random	9/27/13 9:18	39.87	0.00	0.03	0.08	12.01	0.17	46.96	0.21	0.38	0.00	99.73	
ML647-3_ol_random	9/27/13 9:22	39.13	0.00	0.04	0.04	14.22	0.19	45.51	0.26	0.31	0.01	99.72	
ML647-3_ol_random	9/27/13 9:25	39.05	0.01	0.02	0.06	14.66	0.20	45.33	0.26	0.32	0.01	99.93	
ML647-3_ol_random	9/27/13 9:29	39.78	0.00	0.04	0.06	12.50	0.16	46.90	0.22	0.39	0.00	100.05	
ML647-3_ol_random	9/27/13 9:32	39.71	0.01	0.04	0.08	12.52	0.17	46.33	0.21	0.37	0.01	99.45	
ML647-3_ol_random	9/27/13 9:36	39.36	0.02	0.04	0.06	14.09	0.16	45.41	0.25	0.33	0.01	99.72	
ML647-3_ol_random	9/27/13 9:40	39.21	0.00	0.03	0.04	13.89	0.17	45.61	0.24	0.31	0.00	99.50	
ML647-3_ol_random	9/27/13 9:43	40.24	0.00	0.04	0.10	11.46	0.14	47.20	0.21	0.40	0.00	99.80	
ML647-3_ol_random	9/27/13 9:47	40.09	0.00	0.04	0.10	11.47	0.17	47.25	0.21	0.40	0.00	99.72	
ML647-3_ol_random	9/27/13 9:50	39.55	0.02	0.05	0.09	13.26	0.18	45.70	0.24	0.37	0.00	99.46	
ML647-3_ol_random	9/27/13 9:54	39.61	0.01	0.05	0.07	14.48	0.19	45.00	0.26	0.29	0.03	100.00	
ML647-3_ol_random	9/27/13 9:58	39.68	0.10	0.20	0.01	17.96	0.27	41.37	0.40	0.01	0.00	99.99	
ML647-3_px_random	9/27/13 10:01	53.86	0.69	2.27	0.47	10.01	0.23	21.67	10.40	0.17	0.02	99.78	
ML647-3_px_random	9/27/13 10:05	52.37	1.03	3.03	0.31	10.66	0.24	20.05	12.14	0.18	0.01	100.02	
ML647-3_px_random	9/27/13 10:08	47.42	2.51	5.06	0.00	12.39	0.32	13.30	18.42	0.34	0.01	99.75	
ML647-3_px_random	9/27/13 10:12	53.19	0.79	2.80	0.65	8.94	0.19	20.14	12.99	0.19	0.00	99.90	
ML647-3_px_random	9/27/13 10:16	51.23	1.37	4.18	0.05	10.29	0.28	15.50	16.85	0.28	0.05	100.09	
ML647-3_px_random	9/27/13 10:19	39.95	0.16	0.26	0.06	17.34	0.27	41.47	0.49	0.03	0.01	100.04	
ML647-3_px_random	9/27/13 10:23	49.27	1.91	4.65	0.05	11.90	0.30	14.91	16.24	0.32	0.03	99.56	
ML647-3_px_random	9/27/13 10:26	51.38	1.15	3.71	0.59	7.88	0.16	16.68	17.52	0.25	0.00	99.33	
ML647-3_px_random	9/27/13 10:30	54.63	0.44	1.48	0.19	12.08	0.24	24.54	5.76	0.08	0.03	99.48	
HAP-4_ol1	9/27/13 10:34	39.75	0.00	0.03	0.06	13.88	0.21	45.70	0.36	0.28	0.02	100.28	
HAP-4_ol1	9/27/13 10:37	38.25	0.00	0.05	0.05	13.47	0.20	43.92	0.35	0.28	0.01	96.58	
HAP-4_ol1	9/27/13 10:41	39.47	0.01	0.03	0.04	14.08	0.17	45.12	0.38	0.27	0.00	99.57	
HAP-4_ol1	9/27/13 10:44	39.65	0.01	0.03	0.03	13.64	0.18	45.64	0.35	0.27	0.00	99.80	
HAP-4_ol1	9/27/13 10:48	39.86	0.01	0.02	0.03	13.44	0.20	45.79	0.35	0.25	0.00	99.96	
HAP-4_ol1	9/27/13 10:52	39.60	0.01	0.04	0.03	14.30	0.19	44.70	0.38	0.25	0.00	99.51	
HAP-4_ol1	9/27/13 10:55	39.68	0.00	0.06	0.03	14.26	0.19	45.27	0.39	0.23	0.00	100.11	
HAP-4_ol1	9/27/13 10:59	38.09	0.00	0.02	0.03	14.18	0.18	43.42	0.32	0.25	0.00	96.49	
HAP-4_ol1	9/27/13 11:02	39.67	0.00	0.03	0.03	14.63	0.23	44.96	0.33	0.26	0.01	100.16	

Appendix 1. Geochemistry - Plagioclase, Pyroxene Electron Microprobe Analyses

SAMPLE	DAT/TIM	SiO2 WT%	TiO2 WT%	Al2O3 WT%	Cr2O3 WT%	FeO WT%	MnO WT%	MgO WT%	CaO WT%	Na2O WT%	K2O WT%	TOTAL
Lake-County-plag-std1	9/24/13 11:14	51.20	0.04	30.27	0.00	0.48	0.00	0.13	13.33	3.74	0.11	99.30
Lake-County-plag-std1	9/24/13 11:17	51.41	0.04	30.33	0.04	0.42	0.01	0.13	13.37	3.70	0.11	99.56
Lake-County-plag-std1	9/24/13 11:20	51.32	0.01	30.35	0.01	0.42	0.04	0.15	13.37	3.64	0.12	99.42
ML499-needle-test	9/24/13 11:55	54.53	0.51	1.47	0.13	14.26	0.27	26.83	2.18	0.04	0.01	100.23
ML499-needle-test	9/24/13 11:58	51.83	1.07	2.63	0.25	8.97	0.22	16.56	18.25	0.29	0.00	100.06
ML499-wehrlite	9/24/13 12:18	53.62	0.49	2.04	0.87	5.14	0.10	18.95	18.87	0.25	0.00	100.31
ML499-wehrlite	9/24/13 12:21	53.01	0.57	2.69	1.06	5.66	0.11	18.75	17.79	0.28	0.01	99.93
ML499-wehrlite	9/24/13 12:24	53.07	0.59	2.81	1.11	5.21	0.15	18.35	18.74	0.25	0.01	100.29
ML499-wehrlite	9/24/13 12:27	53.22	0.53	2.43	1.02	5.15	0.12	18.73	18.94	0.23	0.02	100.38
ML499-wehrlite-rim	9/24/13 12:31	52.52	0.59	2.91	0.72	6.14	0.14	17.98	18.50	0.23	0.01	99.73
ML499-wehrlite-rim	9/24/13 12:34	52.73	0.47	2.73	0.84	6.31	0.13	17.90	18.84	0.21	0.00	100.16
ML499-wehrlite-rim	9/24/13 12:37	52.60	0.71	3.18	0.55	6.90	0.19	17.93	18.28	0.23	0.00	100.59
ML499-plag@wehrlite-rim	9/24/13 12:40	48.63	0.05	32.08	0.02	0.71	0.02	0.23	15.71	2.44	0.04	99.94
ML499-plag@wehrlite-rim	9/24/13 12:43	49.05	0.01	31.66	0.01	0.73	0.05	0.23	15.45	2.59	0.06	99.84
ML499-plag@wehrlite-rim	9/24/13 12:46	49.77	0.07	31.25	0.02	0.63	0.02	0.23	15.08	2.76	0.07	99.91
ML499-cpx@wehrlite-rim	9/24/13 12:49	52.10	1.09	2.78	0.90	5.53	0.10	17.19	19.65	0.34	0.00	99.68
ML499-cpx@wehrlite-rim	9/24/13 12:53	52.39	0.68	2.63	0.99	5.31	0.08	17.74	19.02	0.25	0.00	99.09
ML499-cpx@wehrlite-rim	9/24/13 12:56	52.16	0.96	2.67	0.94	5.74	0.11	17.10	19.41	0.28	0.01	99.37
HAP-1_plag	9/24/13 12:59	47.61	0.07	32.37	0.01	0.67	0.06	0.16	16.19	2.01	0.05	99.21
HAP-1_cpx	9/24/13 13:02	50.18	1.26	4.84	0.61	5.64	0.15	15.61	20.78	0.26	0.00	99.33
Lake-County-plag-std2	9/24/13 13:55	51.34	0.05	30.49	0.00	0.43	0.00	0.12	13.35	3.62	0.12	99.54
Lake-County-plag-std2	9/24/13 13:58	51.33	0.01	30.40	0.00	0.39	0.00	0.15	13.37	3.65	0.13	99.43
Lake-County-plag-std2	9/24/13 14:01	51.51	0.05	30.48	0.02	0.38	0.00	0.14	13.34	3.74	0.10	99.77
Kakanui-augite_std1	9/24/13 14:04	50.45	0.82	8.66	0.18	6.29	0.10	15.83	15.97	1.34	0.00	99.63
Kakanui-augite_std1	9/24/13 14:07	50.42	0.90	8.67	0.15	6.27	0.19	15.79	15.91	1.29	0.00	99.60
Kakanui-augite_std1	9/24/13 14:11	50.50	0.90	8.62	0.17	6.21	0.13	15.87	15.92	1.33	0.00	99.67
HAP-1_cpx2_zoned	9/24/13 15:32	50.55	1.54	3.29	0.26	6.60	0.08	15.18	20.75	0.29	0.00	98.56
HAP-1_cpx2_zoned	9/24/13 15:35	50.85	1.48	3.23	0.30	6.66	0.19	15.04	20.83	0.33	0.00	98.89
HAP-1_cpx2_zoned	9/24/13 15:38	50.73	1.46	3.25	0.25	6.72	0.12	15.15	20.68	0.33	0.00	98.66
HAP-1_cpx2_zoned	9/24/13 15:41	50.65	1.49	3.34	0.34	6.76	0.13	15.17	20.71	0.34	0.00	98.94
HAP-1_cpx2_zoned	9/24/13 15:44	50.55	1.46	3.43	0.41	6.78	0.13	15.28	20.69	0.33	0.00	99.08
HAP-1_cpx2_zoned	9/24/13 15:47	51.27	0.92	3.40	1.02	5.19	0.10	15.77	21.27	0.28	0.00	99.21
HAP-1_cpx2_zoned	9/24/13 15:51	48.48	0.81	3.38	0.95	4.60	0.10	14.90	19.91	0.25	0.02	93.39
HAP-1_cpx2_zoned	9/24/13 15:54	51.09	0.94	3.65	1.01	5.03	0.14	15.77	21.24	0.25	0.00	99.12
HAP-1_cpx2_zoned	9/24/13 15:57	51.06	0.94	3.68	1.03	5.13	0.12	15.77	21.38	0.26	0.00	99.38
HAP-1_cpx2_zoned	9/24/13 16:00	51.07	0.96	3.68	1.00	5.00	0.12	15.74	21.29	0.27	0.00	99.14
HAP-1_cpx2_zoned	9/24/13 16:03	51.21	0.99	3.60	1.06	4.94	0.15	15.61	21.42	0.28	0.01	99.27
HAP-1_cpx2_zoned	9/24/13 16:06	51.01	0.95	3.64	1.02	5.10	0.10	15.69	21.23	0.25	0.00	98.99
HAP-1_cpx2_zoned	9/24/13 16:09	50.95	0.96	3.62	1.04	4.95	0.14	15.61	21.35	0.25	0.01	98.87
HAP-1_cpx2_zoned	9/24/13 16:13	52.22	0.66	2.72	1.18	4.01	0.10	16.51	21.58	0.27	0.00	99.27
HAP-1_cpx2_zoned	9/24/13 16:16	52.42	0.62	2.50	1.04	4.11	0.11	16.63	21.62	0.26	0.00	99.31
HAP-1_cpx2_zoned	9/24/13 16:19	51.09	0.68	3.17	1.13	4.08	0.10	15.99	21.31	0.25	0.00	97.81
HAP-1_cpx2_zoned	9/24/13 16:22	51.88	0.68	2.94	1.14	4.17	0.09	16.32	21.71	0.22	0.00	99.14
HAP-1_cpx2_zoned	9/24/13 16:25	51.92	0.63	3.05	1.21	4.02	0.09	16.30	21.74	0.21	0.00	99.17
HAP-1_cpx2_zoned	9/24/13 16:28	51.49	0.82	3.64	1.18	4.52	0.11	15.87	21.61	0.23	0.00	99.48
HAP-1_cpx2_zoned	9/24/13 16:31	50.37	1.35	4.42	0.44	7.05	0.08	14.88	20.54	0.31	0.01	99.45
Kil1960_pl-px-cluster_pl-core	9/24/13 16:35	48.58	0.04	32.69	0.02	0.75	0.00	0.13	15.35	2.46	0.07	100.10
Kil1960_pl-px-cluster_pl-core	9/24/13 16:38	48.18	0.07	32.76	0.01	0.72	0.02	0.12	15.38	2.48	0.07	99.80
Kil1960_pl-px-cluster_pl-dark-core	9/24/13 16:41	52.39	0.08	30.28	0.00	0.62	0.00	0.15	12.58	4.07	0.17	100.34
Kil1960_pl-px-cluster_pl-dark-core	9/24/13 16:44	52.59	0.14	29.94	0.01	0.58	0.00	0.16	12.29	4.11	0.16	99.96
Kil1960_pl-px-cluster_pl-dark-rim@cpx	9/24/13 16:47	52.28	0.13	30.09	0.00	0.86	0.00	0.23	12.69	3.95	0.18	100.42
Kil1960_pl-px-cluster_pl-dark-rim@cpx	9/24/13 16:51	51.90	0.14	30.04	0.00	0.88	0.01	0.24	12.79	3.87	0.17	100.04
Kil1960_matrix-plag@pl-px-cluster	9/24/13 16:54	51.92	0.17	29.89	0.00	1.04	0.03	0.28	12.56	3.97	0.17	100.02
Kil1960_matrix-plag@pl-px-cluster	9/24/13 16:57	52.68	0.27	28.91	0.01	1.26	0.00	0.37	12.12	4.27	0.18	100.10
Kil1960_matrix-plag@pl-px-cluster	9/24/13 17:00	52.94	0.24	29.07	0.00	1.16	0.00	0.24	12.05	4.22	0.21	100.13
Kil1960_pl-px-cluster_cpx	9/24/13 17:03	48.84	1.84	4.13	0.15	9.07	0.18	14.61	19.02	0.30	0.00	98.14
Kil1960_pl-px-cluster_cpx	9/24/13 17:06	50.41	1.39	3.50	0.26	8.67	0.24	15.60	18.67	0.30	0.00	99.03
Kil1960_pl-px-cluster_cpx-rim	9/24/13 17:10	51.20	1.35	2.21	0.09	10.00	0.30	15.49	17.69	0.25	0.00	98.58
Kil1960_pl-px-cluster_cpx-rim	9/24/13 17:13	49.11	2.09	4.01	0.14	9.93	0.27	14.87	17.93	0.29	0.01	98.64
Kil1960_pl-px-cluster_cpx2	9/24/13 17:16	49.59	1.60	4.11	0.21	9.10	0.23	15.37	18.07	0.32	0.01	98.61
Kil1960_pl-px-cluster_cpx2	9/24/13 17:19	49.37	1.85	4.20	0.20	9.42	0.20	14.99	18.05	0.29	0.00	98.56
Kil1960_pl-px-cluster_cpx2	9/24/13 17:22	50.71	1.42	4.58	0.08	10.01	0.22	13.81	16.76	0.72	0.04	98.34
Lake-County-plag-std2	9/24/13 17:25	51.30	0.02	31.48	0.02	0.40	0.03	0.14	13.35	3.69	0.10	100.53
Lake-County-plag-std2	9/24/13 17:29	51.07	0.08	31.47	0.00	0.33	0.00	0.14	13.27	3.72	0.12	100.20
Lake-County-plag-std2	9/24/13 17:32	50.96	0.01	31.34	0.00	0.46	0.02	0.14	13.31	3.68	0.10	100.02
Kakanui-augite_std1	9/24/13 17:35	49.85	0.88	8.56	0.15	6.22	0.16	15.83	15.84	1.35	0.00	98.83
Kakanui-augite_std1	9/24/13 17:38	50.06	0.85	8.67	0.18	6.23	0.15	15.82	15.95	1.31	0.01	99.23
Kakanui-augite_std1	9/24/13 17:41	49.98	0.95	8.59	0.14	6.21	0.13	15.92	15.97	1.29	0.01	99.19
Kil1960_cpx2	9/24/13 17:44	51.87	0.91	2.51	0.44	6.42	0.15	16.79	19.68	0.24	0.00	99.01
Kil1960_cpx2	9/24/13 17:48	52.01	0.88	2.59	0.41	6.37	0.15	16.61	19.77	0.25	0.01	99.02
Kil1960_plag2	9/24/13 17:51	51.65	0.08	30.41	0.00	0.75	0.01	0.18	13.08	3.73	0.15	100.05
Kil1960_plag2	9/24/13 17:54	51.66	0.12	30.50	0.00	0.82	0.00	0.19	13.05	3.77	0.13	100.24
Kil1960_plag2	9/24/13 17:57	51.50	0.08	30.65	0.00	0.75	0.02	0.18	13.00	3.69	0.13	100.01
Kil1960_plag2	9/24/13 18:00	51.76	0.08	30.76	0.01	0.83	0.00	0.19	13.01	3.76	0.13	100.53
Kil1960_matrix-plag3	9/24/13 18:03	52.91	0.24	28.17	0.00	1.06	0.00	0.21	12.26	4.20	0.21	99.25
Kil1960_matrix-plag3	9/24/13 18:07	52.63	0.18	28.55	0.00	0.94	0.03	0.20	12.17	4.22	0.20	99.12
Kil1960_matrix-plag3	9/24/13 18:10	52.57	0.28	28.25	0.02	1.12	0.02	0.28	12.34	4.16	0.20	99.23
Kil1960_matrix-cpx3	9/24/13 18:13	50.70	1.57	3.10	0.17	9.52	0.19	15.58	17.10	0.24	0.01	98.18
Kil1960_matrix-cpx3	9/24/13 18:16	55.54	1.56	7.92	0.03	12.91	0.23	6.99	10.64	1.72	1.35	98.90
Kil1960_matrix-cpx3	9/24/13 18:19	50.49	1.60	3.13	0.25	9.53	0.28	15.92	17.37	0.28	0.02	98.86
Kil1960_matrix-cpx3	9/24/13 18:22	47.00	3.10	7.22	0.16	8.71	0.21	13.63	17.64	0.50	0.04	98.21
Kil1960_plag4	9/24/13 18:26	51.43	0.05	30.57	0.00	0.84	0.00	0.14	12.98	3.85	0.13	99.99
Kil1960_plag4	9/24/13 18:29	51.17	0.09	30.74	0.00	0.68	0.00	0.14	13.21	3.78	0.12	99.93
Kil1960_plag4	9/24/13 18:32	51.15	0.09	30.77	0.00	0.73	0.01	0.12	13.21	3.80	0.12	100.00
Kil1960_plag4	9/24/13 18:35	50.06	0.10	31.43	0.00	0.72	0.00	0.12	13.81	3.33	0.11	99.67
Kil1960_plag4	9/24/13 18:38	50.81	0.07	30.95	0.02	0.70	0.00	0.13	13.46	3.53	0.12	99.79

Appendix 1. Geochemistry - Plagioclase, Pyroxene Electron Microprobe Analyses

SAMPLE	DAT/TIM	SiO2 WT%	TiO2 WT%	Al2O3 WT%	Cr2O3 WT%	FeO WT%	MnO WT%	MgO WT%	CaO WT%	Na2O WT%	K2O WT%	TOTAL
Kil1960_plag4	9/24/13 18:41	50.78	0.10	30.96	0.01	0.66	0.00	0.14	13.54	3.57	0.12	99.88
Kil1960_plag4	9/24/13 18:45	51.32	0.09	30.62	0.01	0.72	0.01	0.14	13.11	3.80	0.14	99.96
Kil1960_plag4	9/24/13 18:48	51.27	0.11	30.65	0.01	0.79	0.01	0.12	13.15	3.73	0.12	99.96
Kil1960_plag4	9/24/13 18:51	51.27	0.09	30.71	0.01	0.89	0.04	0.13	13.10	3.65	0.12	100.01
Kil1960_plag4	9/24/13 18:54	52.70	0.19	27.89	0.00	1.86	0.01	1.20	11.63	4.14	0.20	99.83
Kil1960_cpx4	9/24/13 18:57	49.17	1.96	4.53	0.39	8.64	0.18	15.21	18.04	0.29	0.01	98.42
Kil1960_cpx4	9/24/13 19:00	48.61	2.20	4.98	0.35	8.54	0.15	14.65	19.04	0.31	0.01	98.82
Kil1960_cpx4	9/24/13 19:03	50.69	1.40	3.69	0.63	8.18	0.15	16.65	17.64	0.25	0.00	99.28
Kil1960_cpx4	9/24/13 19:06	50.55	1.36	3.55	0.27	8.82	0.18	14.52	16.97	0.40	0.24	96.86
Kil1960_cpx4	9/24/13 19:10	49.48	1.44	3.01	0.08	10.54	0.29	14.63	18.01	0.26	0.00	97.73
Kil1960_cpx4	9/24/13 19:13	50.71	1.17	2.52	0.07	10.48	0.25	15.03	17.73	0.29	0.00	98.25
Kil1960_cpx4	9/24/13 19:16	50.33	1.87	5.23	0.14	9.97	0.21	12.82	17.06	0.58	0.42	98.62
Kil1960_cpx4	9/24/13 19:19	48.60	2.29	4.78	0.11	9.93	0.19	13.43	18.71	0.44	0.03	98.52
Kil1960_cpx4	9/24/13 19:22	49.36	1.44	2.99	0.14	9.75	0.28	14.52	17.84	0.30	0.00	96.62
Kil1960_cpx4	9/24/13 19:25	49.99	1.54	4.12	0.71	8.01	0.25	15.17	18.81	0.32	0.01	98.93
Kil1960_cpx4	9/24/13 19:28	49.02	2.10	5.28	0.48	8.53	0.18	14.09	18.73	0.36	0.04	98.82
Kil1960_cpx4	9/24/13 19:32	49.09	2.04	5.10	0.38	8.56	0.18	14.50	18.64	0.30	0.01	98.80
Kil1960_cpx4	9/24/13 19:35	51.15	1.37	2.64	0.24	9.37	0.22	16.12	17.10	0.25	0.02	98.49
Kil1960_cpx4	9/24/13 19:38	49.52	2.23	3.01	0.01	15.00	0.31	13.43	15.00	0.32	0.09	98.93
Kil1960_cpx4	9/24/13 19:41	53.29	1.29	18.14	0.02	6.03	0.09	3.78	12.18	4.03	0.28	99.14
Lake-County-plag-std3	9/24/13 19:44	51.19	0.02	31.46	0.01	0.41	0.00	0.15	13.31	3.66	0.11	100.32
Lake-County-plag-std3	9/24/13 19:47	51.18	0.05	31.58	0.01	0.49	0.03	0.14	13.34	3.71	0.11	100.65
Lake-County-plag-std3	9/24/13 19:51	51.18	0.05	31.53	0.01	0.44	0.01	0.13	13.33	3.67	0.10	100.46
Kakanui-augite_std2	9/24/13 19:54	50.38	0.92	8.28	0.15	6.30	0.17	15.92	15.89	1.32	0.00	99.32
Kakanui-augite_std2	9/24/13 19:57	50.36	0.84	8.26	0.15	6.23	0.14	15.84	15.89	1.35	0.02	99.07
Kakanui-augite_std2	9/24/13 20:00	50.43	0.84	8.20	0.14	6.30	0.14	15.89	15.91	1.28	0.02	99.15
HAP-1_cpx3_extremes	9/24/13 20:03	50.65	0.97	3.86	1.01	5.08	0.14	15.60	21.57	0.25	0.00	99.14
HAP-1_cpx3_extremes	9/24/13 20:07	50.65	1.01	3.98	1.08	4.97	0.08	15.59	21.61	0.25	0.00	99.21
HAP-1_cpx3_extremes	9/24/13 20:10	50.72	1.30	3.40	0.48	5.83	0.07	15.58	21.23	0.32	0.00	98.93
HAP-1_cpx3_extremes	9/24/13 20:13	49.65	1.87	4.13	0.15	7.72	0.18	14.89	20.45	0.33	0.00	99.36
HAP-1_cpx3_extremes	9/24/13 20:16	51.82	1.05	2.13	0.11	7.48	0.16	16.41	19.86	0.24	0.00	99.26
HAP-1_cpx3_extremes	9/24/13 20:19	50.95	0.93	3.60	1.00	4.82	0.08	16.05	21.69	0.27	0.01	99.41
HAP-1_cpx3_extremes	9/24/13 20:22	51.19	1.06	3.31	0.41	5.94	0.08	15.91	21.01	0.29	0.00	99.19
HAP-1_cpx3_extremes	9/24/13 20:25	51.54	1.16	3.11	0.49	5.93	0.13	16.06	20.89	0.29	0.00	99.60
HAP-1_cpx3_extremes	9/24/13 20:29	52.32	0.86	2.59	0.47	5.48	0.10	16.60	21.00	0.20	0.00	99.61
HAP-1_cpx3_extremes	9/24/13 20:32	51.42	1.17	2.61	0.11	7.91	0.14	15.38	19.62	0.26	0.02	98.64
HAP-1_cpx3_rim-profile	9/24/13 20:35	50.76	1.22	3.76	0.71	5.73	0.13	15.37	21.28	0.33	0.00	99.29
HAP-1_cpx3_rim-profile	9/24/13 20:38	50.87	1.25	3.49	0.55	5.70	0.07	15.61	21.11	0.32	0.00	98.98
HAP-1_cpx3_rim-profile	9/24/13 20:41	51.06	1.25	3.51	0.56	5.85	0.15	15.57	21.18	0.32	0.00	99.45
HAP-1_cpx3_rim-profile	9/24/13 20:44	50.94	1.30	3.54	0.54	5.73	0.11	15.63	21.25	0.28	0.00	99.32
HAP-1_cpx3_rim-profile	9/24/13 20:47	49.57	1.74	4.35	0.28	7.40	0.12	14.49	20.43	0.32	0.00	98.71
HAP-1_cpx3_rim-profile	9/24/13 20:51	50.02	1.83	3.66	0.02	8.96	0.17	14.17	19.92	0.32	0.01	99.08
HAP-1_big-cpx4_extremes	9/24/13 20:54	50.86	1.21	3.54	0.75	6.01	0.11	15.25	21.21	0.29	0.00	99.22
HAP-1_big-cpx4_extremes	9/24/13 20:57	50.97	1.19	3.49	0.62	6.30	0.14	15.41	20.83	0.26	0.00	99.21
HAP-1_big-cpx4_extremes	9/24/13 21:00	52.28	0.70	2.79	0.81	4.86	0.06	16.51	21.14	0.25	0.00	99.40
HAP-1_big-cpx4_extremes	9/24/13 21:03	51.95	0.81	3.07	0.83	4.77	0.09	16.25	21.45	0.23	0.00	99.45
HAP-1_big-cpx4_extremes	9/24/13 21:06	52.58	0.66	2.69	1.00	4.38	0.11	16.90	21.20	0.22	0.00	99.73
HAP-1_big-cpx4_extremes	9/24/13 21:10	51.49	0.84	3.49	1.11	4.85	0.10	16.02	21.43	0.25	0.00	99.59
HAP-1_big-cpx4_rim-prof1	9/24/13 21:13	51.91	0.72	3.02	1.09	4.25	0.06	16.64	21.58	0.25	0.00	99.52
HAP-1_big-cpx4_rim-prof1	9/24/13 21:16	51.71	0.72	3.02	1.08	4.11	0.12	16.61	21.58	0.24	0.00	99.18
HAP-1_big-cpx4_rim-prof1	9/24/13 21:19	51.87	0.65	2.76	1.07	4.09	0.09	16.92	21.68	0.26	0.00	99.39
HAP-1_big-cpx4_rim-prof1	9/24/13 21:22	52.04	0.67	2.70	1.03	4.26	0.09	17.05	21.67	0.23	0.00	99.74
HAP-1_big-cpx4_rim-prof1	9/24/13 21:25	51.72	0.77	2.87	0.96	4.74	0.15	16.54	21.35	0.24	0.00	99.34
HAP-1_big-cpx4_rim-prof1	9/24/13 21:28	51.22	0.88	3.62	1.02	5.03	0.10	15.92	21.45	0.24	0.00	99.47
HAP-1_big-cpx4_rim-prof1	9/24/13 21:32	51.54	0.82	3.42	0.94	5.09	0.12	16.18	21.33	0.25	0.00	99.69
HAP-1_big-cpx4_rim-prof1	9/24/13 21:35	51.90	0.78	3.20	1.05	4.89	0.12	16.16	21.39	0.24	0.00	99.74
HAP-1_big-cpx4_rim-prof1	9/24/13 21:38	51.66	0.88	3.46	0.83	5.22	0.09	16.26	21.31	0.25	0.00	99.97
HAP-1_big-cpx4_rim-prof1	9/24/13 21:41	51.62	0.77	3.47	1.03	4.90	0.13	16.27	21.29	0.26	0.00	99.74
HAP-1_big-cpx4_rim-prof1	9/24/13 21:44	51.81	0.78	3.32	1.03	4.88	0.11	16.31	21.18	0.24	0.00	99.66
HAP-1_big-cpx4_center-prof2_bands	9/24/13 21:47	50.95	1.22	3.64	0.76	5.81	0.10	15.67	21.06	0.29	0.00	99.51
HAP-1_big-cpx4_center-prof2_bands	9/24/13 21:51	51.26	1.11	3.24	0.65	5.70	0.11	16.01	21.07	0.25	0.01	99.40
HAP-1_big-cpx4_center-prof2_bands	9/24/13 21:54	51.81	0.98	2.86	0.63	5.33	0.14	16.33	21.04	0.26	0.00	99.39
HAP-1_big-cpx4_center-prof2_bands	9/24/13 21:57	52.80	0.68	2.30	0.69	5.33	0.11	16.71	20.76	0.25	0.00	99.64
HAP-1_big-cpx4_center-prof2_bands	9/24/13 22:00	52.16	0.70	2.75	0.86	4.94	0.15	16.69	21.07	0.23	0.00	99.55
HAP-1_big-cpx4_center-prof2_bands	9/24/13 22:03	52.55	0.71	2.77	0.77	4.81	0.10	16.79	21.18	0.23	0.00	99.91
HAP-1_big-cpx4_center-prof2_bands	9/24/13 22:06	51.92	0.78	2.93	1.01	4.60	0.10	16.59	21.10	0.23	0.00	99.24
HAP-1_big-cpx4_center-prof2_bands	9/24/13 22:09	52.75	0.56	2.40	1.04	4.35	0.06	16.96	21.07	0.21	0.00	99.41
HAP-1_big-cpx4_center-prof2_bands	9/24/13 22:13	52.82	0.61	2.40	1.06	4.60	0.13	17.05	21.08	0.24	0.00	99.99
HAP-1_big-cpx4_center-prof2_bands	9/24/13 22:16	52.48	0.62	2.72	1.02	4.70	0.08	16.88	21.16	0.22	0.01	99.87
Kakanui-augite_std4	9/24/13 22:19	50.70	0.90	8.33	0.20	6.23	0.10	16.07	15.89	1.34	0.01	99.77
Kakanui-augite_std4	9/24/13 22:22	50.87	0.90	8.33	0.18	6.37	0.16	16.15	15.94	1.34	0.00	100.24
Kakanui-augite_std4	9/24/13 22:25	50.69	0.86	8.27	0.16	6.20	0.18	16.07	15.91	1.32	0.00	99.66
Lake-County-plag-std4	9/24/13 22:28	51.38	0.04	30.24	0.00	0.43	0.01	0.14	13.28	3.72	0.10	99.34
Lake-County-plag-std4	9/24/13 22:32	51.40	0.01	30.06	0.00	0.47	0.00	0.14	13.39	3.68	0.11	99.25
Lake-County-plag-std4	9/24/13 22:35	51.35	0.05	30.06	0.00	0.43	0.00	0.12	13.31	3.70	0.12	99.14
Kakanui-augite_std	9/25/13 9:22	50.99	0.86	8.33	0.17	6.36	0.11	16.12	15.76	1.33	0.00	100.03
Kakanui-augite_std	9/25/13 9:26	51.17	0.90	8.36	0.15	6.29	0.12	16.30	15.83	1.36	0.01	100.49
Kakanui-augite_std	9/25/13 9:29	51.13	0.86	8.42	0.15	6.31	0.13	16.36	15.88	1.34	0.00	100.58
Lake-County-plag-std	9/25/13 9:32	51.78	0.05	30.32	0.03	0.42	0.00	0.15	13.33	3.74	0.10	99.93
Lake-County-plag-std	9/25/13 9:35	51.82	0.01	30.21	0.02	0.47	0.02	0.12	13.26	3.71	0.11	99.74
Lake-County-plag-std	9/25/13 9:38	51.71	0.03	30.19	0.00	0.40	0.00	0.12	13.29	3.69	0.10	99.53
HAP-1_matrix-plag@cpx3	9/25/13 10:17	51.67	0.17	29.74	0.00	1.10	0.00	0.26	13.39	3.59	0.22	100.13
HAP-1_matrix-plag@cpx3	9/25/13 10:20	52.76	0.20	29.01	0.01	1.00	0.01	0.23	12.65	3.95	0.27	100.09
HAP-1_matrix-plag@cpx3	9/25/13 10:23	51.99	0.20	29.24	0.02	1.12	0.01	0.30	12.99	3.75	0.23	99.85
HAP-1_matrix-plag@cpx3	9/25/13 10:26	52.03	0.16	29.28	0.00	1.06	0.02	0.26	12.95	3.89	0.25	99.89
HAP-1_matrix-plag@cpx3	9/25/13 10:29	51.37	0.15	29.84	0.04	0.95	0.01	0.25	13.45	3.58	0.20	99.83

Appendix 1. Geochemistry - Plagioclase, Pyroxene Electron Microprobe Analyses

SAMPLE	DAT/TIM	SiO2 WT%	TiO2 WT%	Al2O3 WT%	Cr2O3 WT%	FeO WT%	MnO WT%	MgO WT%	CaO WT%	Na2O WT%	K2O WT%	TOTAL
HAP-1_matrix-cpx@cpx3	9/25/13 10:32	50.69	1.68	3.97	0.24	7.60	0.17	14.86	20.01	0.31	0.01	99.54
HAP-1_matrix-cpx@cpx3	9/25/13 10:36	49.66	1.95	5.01	0.29	7.93	0.11	14.56	19.58	0.32	0.02	99.44
HAP-1_matrix-cpx@cpx3	9/25/13 10:39	51.25	1.38	3.54	0.29	7.49	0.10	15.53	19.75	0.30	0.01	99.64
HAP-1_cpx3a_core-to-rim	9/25/13 10:42	52.71	0.91	2.83	0.29	7.20	0.20	17.84	17.93	0.21	0.00	100.12
HAP-1_cpx3a_core-to-rim	9/25/13 10:45	52.52	0.92	3.03	0.34	6.99	0.19	17.98	17.67	0.20	0.00	99.85
HAP-1_cpx3a_core-to-rim	9/25/13 10:48	48.67	1.90	6.17	0.72	6.50	0.13	14.55	20.33	0.31	0.00	99.29
HAP-1_cpx3a_core-to-rim	9/25/13 10:51	50.93	1.30	4.11	0.63	5.83	0.13	15.69	20.70	0.24	0.00	99.55
HAP-1_cpx3a_core-to-rim	9/25/13 10:55	49.85	1.81	3.95	0.09	8.63	0.10	14.25	20.17	0.33	0.00	99.17
ML499-random-matrix-plag_5mu	9/25/13 11:34	52.89	0.11	28.86	0.00	0.82	0.00	0.31	12.66	3.98	0.12	99.76
ML499-random-matrix-plag_5mu	9/25/13 11:37	53.93	0.19	27.91	0.02	1.32	0.03	0.35	11.83	4.45	0.18	100.20
ML499-random-matrix-plag_5mu	9/25/13 11:40	53.25	0.15	28.72	0.00	0.82	0.00	0.37	12.68	4.02	0.13	100.15
ML499-random-matrix-plag_5mu	9/25/13 11:43	53.12	0.15	28.75	0.00	1.00	0.00	0.29	12.61	4.15	0.13	100.21
ML499-random-matrix-plag_5mu	9/25/13 11:46	53.15	0.19	28.42	0.01	1.11	0.00	0.34	12.42	4.15	0.17	99.98
ML499-random-matrix-plag_5mu	9/25/13 11:50	53.93	0.17	28.29	0.00	1.14	0.01	0.28	12.14	4.38	0.18	100.52
ML499-random-matrix-plag_5mu	9/25/13 11:53	53.69	0.22	28.18	0.00	1.20	0.04	0.26	12.00	4.33	0.18	100.11
ML499-random-matrix-plag_5mu	9/25/13 11:56	53.47	0.14	28.30	0.01	1.12	0.02	0.35	12.28	4.20	0.16	100.05
ML499-random-matrix-plag_5mu	9/25/13 11:59	52.51	0.16	28.87	0.00	1.00	0.01	0.28	12.72	3.98	0.14	99.68
ML499-random-matrix-plag_5mu	9/25/13 12:02	53.63	0.18	28.55	0.00	0.95	0.06	0.27	12.31	4.29	0.15	100.39
ML499-random-matrix-cpx_2mu	9/25/13 12:27	49.90	1.89	5.35	0.24	10.07	0.21	16.78	15.34	0.29	0.02	100.08
ML499-random-matrix-cpx_2mu	9/25/13 12:30	52.91	0.90	2.22	0.25	9.80	0.18	18.13	15.32	0.18	0.02	99.91
ML499-random-matrix-cpx_2mu	9/25/13 12:33	51.42	1.45	3.84	0.24	11.27	0.25	18.55	12.65	0.21	0.02	99.92
ML499-random-matrix-cpx_2mu	9/25/13 12:36	52.62	0.99	2.99	0.61	10.60	0.29	20.54	11.54	0.20	0.01	100.37
ML499-random-matrix-cpx_2mu	9/25/13 12:40	50.73	1.96	4.08	0.00	14.94	0.36	12.63	14.92	0.55	0.13	100.31
ML499-random-matrix-cpx_2mu	9/25/13 12:43	52.38	1.06	3.16	0.78	9.43	0.21	18.84	14.22	0.24	0.03	100.35
ML499-random-matrix-cpx_2mu	9/25/13 12:46	51.46	1.25	3.58	0.30	11.75	0.25	20.03	10.44	0.18	0.01	99.24
ML499-random-matrix-cpx_2mu	9/25/13 12:49	49.91	1.71	2.76	0.01	15.98	0.25	14.08	14.77	0.27	0.02	99.76
ML499-random-matrix-cpx_2mu	9/25/13 12:52	52.11	1.09	2.62	0.16	11.22	0.26	17.48	14.85	0.24	0.02	100.04
ML499-random-matrix-cpx_2mu	9/25/13 12:55	51.56	1.25	2.99	0.10	11.71	0.23	17.19	14.54	0.25	0.01	99.84
ML499-random-matrix-cpx_2mu	9/25/13 12:59	52.94	0.92	2.30	0.11	13.20	0.29	19.49	10.08	0.20	0.05	99.59
ML499-random-matrix-cpx_2mu	9/25/13 13:02	52.18	1.17	3.18	0.42	9.47	0.22	17.75	15.54	0.23	0.02	100.18
ML499-random-matrix-cpx_2mu	9/25/13 13:05	52.30	1.05	2.77	0.33	10.51	0.28	18.73	13.76	0.22	0.03	99.97
ML499-random-matrix-cpx_2mu	9/25/13 13:08	50.14	1.80	4.73	0.20	10.24	0.24	15.74	16.28	0.29	0.01	99.67
ML499-random-matrix-cpx_2mu	9/25/13 13:11	48.77	2.15	3.19	0.00	16.67	0.25	11.81	15.97	0.34	0.02	99.16
494-2_dark-ol	9/25/13 14:40	39.94	0.02	0.02	0.06	14.12	0.19	44.14	0.20	0.00	0.00	98.69
494-2_resorbed-bright-ol	9/25/13 14:44	38.15	0.01	0.03	0.01	25.68	0.27	34.56	0.23	0.00	0.00	98.94
494-2_resorbed-bright-ol	9/25/13 14:47	37.73	0.02	0.02	0.02	26.04	0.35	33.98	0.19	0.01	0.01	98.37
Kakanui-augite_std	9/25/13 16:20	49.94	0.84	8.13	0.17	6.15	0.11	15.76	15.77	1.28	0.00	98.16
Kakanui-augite_std	9/25/13 16:23	50.04	0.89	8.16	0.16	6.13	0.17	15.66	15.87	1.33	0.01	98.43
Kakanui-augite_std	9/25/13 16:26	49.91	0.84	8.23	0.17	6.14	0.16	15.80	15.92	1.29	0.00	98.44
Lake-County-plag-std	9/25/13 16:29	50.57	0.00	29.86	0.01	0.38	0.00	0.14	13.26	3.70	0.11	98.03
Lake-County-plag-std	9/25/13 16:32	50.93	0.00	29.83	0.01	0.44	0.02	0.14	13.28	3.70	0.12	98.47
Lake-County-plag-std	9/25/13 16:35	50.93	0.07	29.92	0.00	0.50	0.02	0.13	13.27	3.69	0.10	98.64
ML647-1_area1_random-matrix-cpx	9/25/13 16:39	52.65	0.60	2.39	0.88	7.69	0.21	18.58	15.86	0.19	0.00	99.04
ML647-1_area1_random-matrix-cpx	9/25/13 16:42	51.76	0.83	2.91	0.95	7.55	0.22	17.96	16.31	0.21	0.00	98.70
ML647-1_area1_random-matrix-cpx	9/25/13 16:45	54.33	0.42	1.19	0.29	11.17	0.25	24.45	6.37	0.09	0.01	98.58
ML647-1_area1_random-matrix-cpx	9/25/13 16:48	49.24	1.70	5.41	0.55	8.07	0.16	15.72	17.50	0.25	0.01	98.62
ML647-1_area1_random-matrix-cpx	9/25/13 16:51	51.17	1.23	2.80	0.21	9.60	0.21	17.72	15.03	0.19	0.02	98.19
ML647-1_area1_random-matrix-cpx	9/25/13 16:54	51.70	0.90	2.90	0.63	8.56	0.21	18.39	15.26	0.19	0.00	98.75
ML647-1_area1_random-matrix-cpx	9/25/13 16:58	51.78	1.03	2.94	0.51	8.33	0.19	17.74	16.18	0.21	0.01	98.93
ML647-1_area1_random-matrix-cpx	9/25/13 17:01	49.82	1.57	5.33	0.34	10.71	0.21	18.97	10.91	0.17	0.01	98.03
ML647-1_area1_random-matrix-plag	9/25/13 17:04	52.34	0.15	29.66	0.02	1.21	0.03	0.40	12.87	3.72	0.09	100.49
ML647-1_area1_random-matrix-plag	9/25/13 17:07	52.63	0.12	29.73	0.00	0.92	0.00	0.30	12.43	3.94	0.10	100.18
ML647-1_area1_random-matrix-plag	9/25/13 17:10	52.64	0.49	25.04	0.00	2.77	0.02	2.17	13.08	3.67	0.11	100.00
ML647-1_area1_random-matrix-plag	9/25/13 17:13	51.31	0.14	30.76	0.00	0.95	0.01	0.34	13.58	3.42	0.08	100.59
ML647-1_area1_random-matrix-plag	9/25/13 17:17	52.65	0.16	29.78	0.03	0.97	0.01	0.34	12.67	3.85	0.09	100.55
ML647-1_area1_random-matrix-plag	9/25/13 17:20	52.72	0.16	29.50	0.00	1.08	0.02	0.37	12.49	3.89	0.11	100.32
ML647-1_area1_random-matrix-plag	9/25/13 17:23	51.80	0.17	30.28	0.02	0.86	0.00	0.35	13.29	3.55	0.09	100.41
ML647-1_area1_random-matrix-plag	9/25/13 17:26	52.86	0.17	29.28	0.00	1.13	0.02	0.43	12.69	3.83	0.11	100.52
ML647-1_area1_random-matrix-plag	9/25/13 17:29	53.14	0.19	29.26	0.00	1.01	0.00	0.30	12.23	4.02	0.12	100.28
ML647-1_area1_random-matrix-plag	9/25/13 17:32	56.81	0.54	25.50	0.01	1.74	0.05	0.46	10.05	4.56	0.25	99.98
ML647-1_area2_random-matrix-plag	9/25/13 17:36	56.35	0.56	24.88	0.00	2.43	0.03	0.43	10.59	3.97	0.32	99.56
ML647-1_area2_random-matrix-plag	9/25/13 17:39	51.54	0.12	30.60	0.00	0.91	0.00	0.35	13.40	3.44	0.09	100.46
ML647-1_area2_random-matrix-plag	9/25/13 17:42	53.17	0.20	28.32	0.00	2.05	0.00	0.29	12.20	4.03	0.13	100.38
ML647-1_area2_random-matrix-plag	9/25/13 17:45	52.32	0.14	29.19	0.01	1.22	0.01	0.34	12.66	3.76	0.12	99.77
ML647-1_area2_random-matrix-plag	9/25/13 17:48	52.09	0.10	29.85	0.00	0.96	0.01	0.41	13.07	3.62	0.10	100.23
ML647-1_area2_random-matrix-plag	9/25/13 17:51	52.72	0.13	29.51	0.02	0.99	0.03	0.34	12.53	3.85	0.11	100.23
ML647-1_area2_random-matrix-plag	9/25/13 17:55	51.27	0.09	30.35	0.00	0.75	0.00	0.36	13.40	3.44	0.08	99.75
ML647-1_area2_random-matrix-plag	9/25/13 17:58	52.34	0.14	29.57	0.00	0.94	0.03	0.34	12.65	3.75	0.10	99.85
ML647-1_area2_random-matrix-plag	9/25/13 18:01	51.11	0.17	30.32	0.00	1.05	0.03	0.37	13.47	3.27	0.09	99.88
ML647-1_area2_random-matrix-plag	9/25/13 18:04	53.66	0.28	27.41	0.01	2.19	0.01	0.39	11.74	4.01	0.18	99.87
ML647-1_area2_random-matrix-cpx	9/25/13 18:07	38.84	0.09	0.20	0.01	17.58	0.26	40.49	0.39	0.01	0.00	97.87
ML647-1_area2_random-matrix-cpx	9/25/13 18:10	52.94	0.68	2.23	0.46	9.84	0.23	21.30	10.22	0.17	0.02	98.08
ML647-1_area2_random-matrix-cpx	9/25/13 18:14	51.77	1.01	3.00	0.31	10.54	0.23	19.82	12.00	0.18	0.01	98.87
ML647-1_area2_random-matrix-cpx	9/25/13 18:17	46.54	2.46	4.96	0.00	12.16	0.31	13.05	18.08	0.33	0.01	97.90
ML647-1_area2_random-matrix-cpx	9/25/13 18:20	52.55	0.78	2.77	0.64	8.83	0.19	19.90	12.83	0.19	0.00	98.69
ML647-1_area2_random-matrix-cpx	9/25/13 18:23	50.20	1.34	4.10	0.05	10.08	0.27	15.19	16.51	0.28	0.05	98.07
ML647-1_area2_random-matrix-cpx	9/25/13 18:26	39.28	0.16	0.26	0.06	17.05	0.27	40.78	0.49	0.03	0.01	98.38
ML647-1_area2_random-matrix-cpx	9/25/13 18:29	48.87	1.90	4.61	0.05	11.80	0.29	14.79	16.11	0.32	0.02	98.76
ML647-1_area2_random-matrix-cpx	9/25/13 18:32	51.10	1.14	3.69	0.59	7.84	0.16	16.59	17.42	0.25	0.00	98.79
ML647-1_area2_random-matrix-cpx	9/25/13 18:36	54.23	0.44	1.47	0.19	11.99	0.24	24.37	5.71	0.08	0.03	98.76
Kakanui-augite_std	9/25/13 18:39	50.28	0.90	8.63	0.11	6.33	0.13	15.83	15.88	1.28	0.00	99.37
Kakanui-augite_std	9/25/13 18:42	50.19	0.90	8.63	0.16	6.04	0.14	15.80	15.90	1.32	0.02	99.10
Kakanui-augite_std	9/25/13 18:45	50.23	0.89	8.60	0.16	6.26	0.11	15.89	15.83	1.37	0.01	99.34
Lake-County-plag-std	9/25/13 18:48	50.92	0.03	31.39	0.00	0.40	0.04	0.13	13.36	3.69	0.12	100.07
Lake-County-plag-std	9/25/13 18:52	50.65	0.04	31.28	0.00	0.39	0.05	0.15	13.30	3.62	0.11	99.58
Lake-County-plag-std	9/25/13 18:55	51.11	0.04	31.30	0.00	0.42	0.06	0.14	13.29	3.71	0.10	100.18

Appendix 1. Geochemistry - Plagioclase, Pyroxene Electron Microprobe Analyses

SAMPLE	DAT/TIM	SiO2 WT%	TiO2 WT%	Al2O3 WT%	Cr2O3 WT%	FeO WT%	MnO WT%	MgO WT%	CaO WT%	Na2O WT%	K2O WT%	TOTAL
ML647-1_area3_random-matrix-CPX	9/25/13 18:58	51.96	1.05	3.17	0.46	8.97	0.21	18.66	14.67	0.21	0.00	99.36
ML647-1_area3_random-matrix-CPX	9/25/13 19:01	52.65	0.71	2.79	0.73	8.13	0.18	19.05	14.66	0.23	0.01	99.13
ML647-1_area3_random-matrix-CPX	9/25/13 19:04	52.83	0.85	2.93	0.24	9.66	0.24	19.85	12.25	0.21	0.03	99.10
ML647-1_area3_random-matrix-CPX	9/25/13 19:07	47.43	2.15	7.75	0.00	11.42	0.20	12.00	17.01	0.78	0.04	98.76
ML647-1_area3_random-matrix-CPX	9/25/13 19:11	52.90	0.77	2.32	0.03	14.51	0.32	22.48	6.37	0.13	0.00	99.83
ML647-1_area3_random-matrix-CPX	9/25/13 19:14	54.22	0.50	3.76	0.24	11.12	0.28	22.20	6.20	0.41	0.02	98.95
ML647-1_area3_random-matrix-CPX	9/25/13 19:17	51.24	1.07	3.76	0.48	8.50	0.15	17.20	16.31	0.28	0.01	98.99
ML647-1_area3_random-matrix-CPX	9/25/13 19:20	48.94	1.78	4.19	0.05	11.41	0.22	14.86	17.10	0.27	0.01	98.81
ML647-1_area3_random-matrix-CPX	9/25/13 19:23	53.24	1.67	11.62	0.00	8.44	0.19	8.05	14.57	1.23	0.25	99.25
ML647-1_area3_random-matrix-CPX	9/25/13 19:26	51.03	1.31	3.20	0.04	11.01	0.27	17.04	14.56	0.20	0.02	98.67
ML647-1_area3_random-matrix-plag	9/25/13 19:29	52.54	0.17	29.77	0.02	1.03	0.04	0.41	12.55	3.64	0.11	100.28
ML647-1_area3_random-matrix-plag	9/25/13 19:33	53.34	0.17	28.76	0.01	1.54	0.00	0.38	12.33	3.87	0.13	100.54
ML647-1_area3_random-matrix-plag	9/25/13 19:36	53.36	0.20	28.61	0.00	1.50	0.01	0.34	12.31	3.81	0.12	100.24
ML647-1_area3_random-matrix-plag	9/25/13 19:39	52.65	0.13	29.83	0.01	0.88	0.02	0.43	12.82	3.56	0.10	100.42
ML647-1_area3_random-matrix-plag	9/25/13 19:42	52.39	0.13	29.66	0.00	1.00	0.00	0.35	12.86	3.65	0.10	100.16
ML647-1_area3_random-matrix-plag	9/25/13 19:45	53.33	0.88	27.86	0.01	1.60	0.06	0.63	12.44	3.15	0.21	100.16
ML647-1_area3_random-matrix-plag	9/25/13 19:48	53.18	0.10	29.82	0.01	1.10	0.03	0.34	12.57	3.81	0.13	101.10
ML647-1_area3_random-matrix-plag	9/25/13 19:51	51.83	0.11	30.33	0.00	0.93	0.01	0.36	13.23	3.49	0.08	100.37
ML647-1_area3_random-matrix-plag	9/25/13 19:55	53.33	0.17	29.03	0.01	1.21	0.03	0.34	12.21	3.94	0.13	100.40
ML647-1_area3_random-matrix-plag	9/25/13 19:58	53.55	0.36	27.94	0.00	1.90	0.04	0.35	12.03	3.91	0.16	100.24
WAI-1_area1_random-matrix-plag	9/25/13 20:01	53.25	0.17	29.20	0.01	0.83	0.01	0.18	11.65	4.44	0.17	99.91
WAI-1_area1_random-matrix-plag	9/25/13 20:04	55.49	0.21	27.59	0.00	0.88	0.00	0.11	9.90	5.40	0.26	99.85
WAI-1_area1_random-matrix-plag	9/25/13 20:07	53.83	0.16	28.72	0.00	0.98	0.03	0.18	11.30	4.74	0.18	100.10
WAI-1_area1_random-matrix-plag	9/25/13 20:11	55.27	0.20	28.03	0.03	1.07	0.00	0.19	10.41	4.93	0.28	100.40
WAI-1_area1_random-matrix-plag	9/25/13 20:14	52.95	0.12	29.41	0.00	0.91	0.00	0.30	12.13	4.24	0.15	100.21
WAI-1_area1_random-matrix-plag	9/25/13 20:17	53.39	0.15	28.96	0.02	0.97	0.02	0.23	11.70	4.40	0.18	100.04
WAI-1_area1_random-matrix-plag	9/25/13 20:20	52.38	0.16	29.53	0.03	0.78	0.00	0.24	12.21	4.17	0.16	99.65
WAI-1_area1_random-matrix-plag	9/25/13 20:23	53.05	0.15	29.51	0.01	0.81	0.00	0.27	12.25	4.21	0.15	100.40
WAI-1_area1_random-matrix-plag	9/25/13 20:26	53.96	0.20	28.54	0.00	1.02	0.00	0.21	11.26	4.66	0.20	100.06
WAI-1_area1_random-matrix-plag	9/25/13 20:30	54.76	0.18	28.01	0.00	1.07	0.00	0.17	10.61	5.07	0.25	100.12
WAI-1_area1_random-matrix-cpx	9/25/13 20:33	49.09	2.08	3.89	0.10	10.71	0.24	14.27	17.66	0.29	0.00	98.35
WAI-1_area1_random-matrix-cpx	9/25/13 20:36	49.72	1.69	3.62	0.18	11.16	0.30	15.45	16.24	0.28	0.00	98.66
WAI-1_area1_random-matrix-cpx	9/25/13 20:39	49.79	1.64	3.76	0.33	9.75	0.20	15.21	17.38	0.28	0.01	98.35
WAI-1_area1_random-matrix-cpx	9/25/13 20:42	49.52	1.88	4.02	0.32	10.69	0.32	15.29	16.47	0.21	0.00	98.74
WAI-1_area1_random-matrix-cpx	9/25/13 20:45	49.51	1.89	3.28	0.09	11.01	0.22	14.29	18.00	0.27	0.01	98.58
WAI-1_area1_random-matrix-cpx	9/25/13 20:48	48.84	1.91	3.72	0.07	13.29	0.28	14.84	15.35	0.26	0.00	98.56
WAI-1_area1_random-matrix-cpx	9/25/13 20:52	48.86	1.89	3.29	0.01	14.63	0.29	11.95	17.06	0.31	0.02	98.31
WAI-1_area1_random-matrix-cpx	9/25/13 20:55	49.78	1.68	3.26	0.06	11.80	0.22	14.78	16.89	0.25	0.00	98.72
WAI-1_area1_random-matrix-cpx	9/25/13 20:58	48.84	2.01	3.70	0.08	13.46	0.33	14.82	15.28	0.24	0.00	98.76
WAI-1_area1_random-matrix-cpx	9/25/13 21:01	49.05	1.49	2.23	0.00	20.04	0.43	12.01	13.33	0.21	0.00	98.79
WAI-1_area2_random-matrix-cpx	9/25/13 21:04	49.77	1.98	4.00	0.29	11.22	0.20	15.57	16.05	0.26	0.01	99.35
WAI-1_area2_random-matrix-cpx	9/25/13 21:08	52.85	0.72	1.54	0.21	12.41	0.29	19.65	11.54	0.11	0.00	99.31
WAI-1_area2_random-matrix-cpx	9/25/13 21:11	49.27	2.07	4.17	0.39	9.34	0.22	14.44	18.56	0.27	0.00	98.73
WAI-1_area2_random-matrix-cpx	9/25/13 21:14	49.61	1.91	3.17	0.02	12.77	0.24	13.69	17.20	0.28	0.01	98.91
WAI-1_area2_random-matrix-cpx	9/25/13 21:17	53.02	0.67	1.43	0.25	11.83	0.29	19.69	11.71	0.12	0.00	99.00
WAI-1_area2_random-matrix-cpx	9/25/13 21:20	49.66	1.90	3.69	0.17	9.83	0.19	14.63	18.37	0.28	0.00	98.72
WAI-1_area2_random-matrix-cpx	9/25/13 21:23	48.79	1.70	2.86	0.00	18.83	0.34	11.63	14.51	0.26	0.00	98.92
WAI-1_area2_random-matrix-cpx	9/25/13 21:26	49.56	1.23	1.90	0.01	20.39	0.45	10.92	14.24	0.21	0.00	98.90
WAI-1_area2_random-matrix-cpx	9/25/13 21:30	49.74	1.83	3.83	0.29	9.44	0.17	14.80	18.28	0.29	0.00	98.67
WAI-1_area2_random-matrix-cpx	9/25/13 21:33	49.68	1.91	2.88	0.02	14.37	0.31	14.01	15.47	0.24	0.01	98.91
WAI-1_area2_random-matrix-plag	9/25/13 21:36	57.39	0.11	26.74	0.00	1.01	0.00	0.10	8.95	5.75	0.37	100.43
WAI-1_area2_random-matrix-plag	9/25/13 21:39	52.75	0.16	29.98	0.01	0.80	0.01	0.22	12.44	4.19	0.14	100.69
WAI-1_area2_random-matrix-plag	9/25/13 21:42	51.87	0.15	30.09	0.00	0.77	0.00	0.22	12.63	3.85	0.13	99.72
WAI-1_area2_random-matrix-plag	9/25/13 21:46	53.23	0.15	29.50	0.01	0.79	0.00	0.22	12.03	4.38	0.16	100.48
WAI-1_area2_random-matrix-plag	9/25/13 21:49	53.43	0.16	29.31	0.00	0.86	0.02	0.25	11.92	4.30	0.15	100.39
WAI-1_area2_random-matrix-plag	9/25/13 21:52	53.89	0.20	28.84	0.00	0.89	0.04	0.21	11.39	4.65	0.19	100.30
WAI-1_area2_random-matrix-plag	9/25/13 21:55	54.63	0.23	28.50	0.00	1.07	0.02	0.15	10.82	4.78	0.24	100.46
WAI-1_area2_random-matrix-plag	9/25/13 21:58	53.32	0.13	29.40	0.01	0.82	0.04	0.26	11.96	4.30	0.14	100.40
WAI-1_area2_random-matrix-plag	9/25/13 22:01	54.83	0.18	28.56	0.00	0.93	0.00	0.15	10.83	4.85	0.25	100.57
WAI-1_area2_random-matrix-plag	9/25/13 22:04	54.65	0.18	28.66	0.00	0.86	0.04	0.17	10.98	4.91	0.23	100.67
WAI-1_area3_random-matrix-plag	9/25/13 22:08	52.20	0.10	30.45	0.02	0.76	0.03	0.27	12.76	3.83	0.13	100.55
WAI-1_area3_random-matrix-plag	9/25/13 22:11	55.52	0.24	28.08	0.00	1.15	0.02	0.17	10.40	5.21	0.25	101.03
WAI-1_area3_random-matrix-plag	9/25/13 22:14	56.24	0.21	27.57	0.00	0.97	0.00	0.14	9.78	5.38	0.29	100.58
WAI-1_area3_random-matrix-plag	9/25/13 22:17	56.66	0.20	27.19	0.00	0.97	0.01	0.12	9.50	5.63	0.33	100.62
WAI-1_area3_random-matrix-plag	9/25/13 22:20	54.48	0.12	28.81	0.01	0.96	0.00	0.22	11.15	4.73	0.18	100.66
WAI-1_area3_random-matrix-cpx	9/25/13 22:23	50.17	1.68	3.63	0.13	10.74	0.20	15.04	17.35	0.26	0.01	99.21
WAI-1_area3_random-matrix-cpx	9/25/13 22:27	49.61	1.60	2.41	0.01	19.63	0.37	13.24	12.42	0.26	0.00	99.56
WAI-1_area3_random-matrix-cpx	9/25/13 22:30	49.83	1.76	2.97	0.07	14.04	0.30	15.54	14.36	0.21	0.00	99.08
WAI-1_area3_random-matrix-cpx	9/25/13 22:33	50.25	1.66	3.65	0.26	9.72	0.21	15.33	17.63	0.28	0.00	98.99
WAI-1_area3_random-matrix-cpx	9/25/13 22:36	50.01	1.87	3.42	0.12	11.76	0.26	15.72	15.81	0.22	0.00	99.20
WAI-1_area3_random-matrix-cpx	9/25/13 22:39	50.18	1.62	3.95	0.44	9.71	0.19	15.62	17.03	0.27	0.01	99.03
Kakanui-augite_std	9/25/13 22:42	50.75	0.86	8.61	0.16	6.16	0.16	16.03	15.87	1.29	0.01	99.89
Kakanui-augite_std	9/25/13 22:46	50.51	0.88	8.70	0.16	6.16	0.14	16.06	15.81	1.29	0.00	99.72
Kakanui-augite_std	9/25/13 22:49	50.47	0.82	8.64	0.16	6.15	0.18	16.10	15.93	1.32	0.00	99.77
Lake-County-plag-std	9/25/13 22:52	51.28	0.05	31.58	0.00	0.46	0.00	0.12	13.34	3.62	0.12	100.57
Lake-County-plag-std	9/25/13 22:55	51.55	0.05	31.70	0.01	0.42	0.01	0.13	13.40	3.71	0.09	101.07
Lake-County-plag-std	9/25/13 22:58	51.45	0.04	31.50	0.01	0.44	0.00	0.13	13.28	3.68	0.11	100.64
WAI-1_area1_big-plag_core-rim	9/25/13 23:01	52.10	0.09	30.40	0.00	0.42	0.01	0.17	12.66	3.88	0.12	99.85
WAI-1_area1_big-plag_core-rim	9/25/13 23:05	51.23	0.09	30.72	0.00	0.45	0.02	0.17	13.16	3.65	0.11	99.61
WAI-1_area1_big-plag_core-rim	9/25/13 23:08	50.25	0.07	31.65	0.00	0.52	0.00	0.17	13.78	3.34	0.11	99.89
WAI-1_area1_big-plag_core-rim	9/25/13 23:11	50.65	0.11	31.23	0.00	0.43	0.03	0.16	13.55	3.48	0.11	99.73
WAI-1_area1_big-plag_core-rim	9/25/13 23:14	50.50	0.07	31.43	0.01	0.47	0.00	0.15	13.71	3.40	0.10	99.85
WAI-1_area1_big-plag_core-rim	9/25/13 23:17	51.29	0.10	30.92	0.02	0.49	0.04	0.17	13.13	3.71	0.12	99.99
WAI-1_area1_big-plag_core-rim	9/25/13 23:20	51.65	0.08	30.61	0.00	0.46	0.01	0.18	12.92	3.86	0.12	99.88
WAI-1_area1_big-plag_core-rim	9/25/13 23:23	50.59	0.09	31.16	0.00	0.46	0.00	0.15	13.62	3.44	0.10	99.61
WAI-1_area1_big-plag_core-rim	9/25/13 23:26	51.27	0.06	31.23	0.00	0.40	0.00	0.19	13.47	3.47	0.09	100.18

Appendix 1. Geochemistry - Plagioclase, Pyroxene Electron Microprobe Analyses

SAMPLE	DAT/TIM	SiO2 WT%	TiO2 WT%	Al2O3 WT%	Cr2O3 WT%	FeO WT%	MnO WT%	MgO WT%	CaO WT%	Na2O WT%	K2O WT%	TOTAL
WAI-1_area1_big-plag_core-rim	9/25/13 23:30	51.74	0.10	31.01	0.01	0.47	0.00	0.19	13.15	3.69	0.09	100.44
WAI-1_area1_big-plag_core-rim	9/25/13 23:33	51.37	0.06	31.19	0.00	0.47	0.00	0.16	13.51	3.49	0.09	100.33
WAI-1_area1_big-plag_core-rim	9/25/13 23:36	51.08	0.07	31.32	0.00	0.45	0.01	0.18	13.50	3.42	0.11	100.15
WAI-1_area1_big-plag_core-rim	9/25/13 23:39	51.19	0.10	31.25	0.00	0.52	0.00	0.17	13.48	3.50	0.10	100.32
WAI-1_area1_big-plag_core-rim	9/25/13 23:42	51.66	0.10	30.84	0.00	0.46	0.05	0.18	13.11	3.75	0.10	100.25
WAI-1_area1_big-plag_core-rim	9/25/13 23:45	51.63	0.11	31.01	0.01	0.46	0.01	0.18	13.24	3.62	0.11	100.38
WAI-1_area1_big-plag_core-rim	9/25/13 23:48	51.40	0.09	31.17	0.01	0.46	0.01	0.18	13.34	3.62	0.11	100.37
WAI-1_area1_big-plag_core-rim	9/25/13 23:52	51.35	0.08	31.20	0.00	0.46	0.05	0.18	13.40	3.58	0.11	100.40
WAI-1_area1_big-plag_core-rim	9/25/13 23:55	51.75	0.08	31.02	0.01	0.50	0.00	0.19	13.25	3.67	0.12	100.60
WAI-1_area1_big-plag_core-rim	9/25/13 23:58	51.84	0.13	30.89	0.00	0.51	0.01	0.18	13.17	3.72	0.11	100.58
WAI-1_area1_big-plag_core-rim	9/26/13 0:01	52.53	0.12	30.31	0.00	0.46	0.00	0.19	12.54	4.05	0.13	100.32
WAI-1_area1_big-plag_core-rim	9/26/13 0:04	51.54	0.10	31.12	0.01	0.63	0.00	0.21	13.32	3.62	0.11	100.66
WAI-1_area1_big-plag_core-rim	9/26/13 0:07	51.58	0.09	30.84	0.01	0.62	0.00	0.22	13.33	3.64	0.11	100.44
WAI-1_area3_big-plag_rim-core-rim	9/26/13 0:11	51.42	0.08	30.90	0.00	0.47	0.00	0.17	13.35	3.64	0.10	100.14
WAI-1_area3_big-plag_rim-core-rim	9/26/13 0:14	51.44	0.06	30.94	0.00	0.51	0.00	0.18	13.27	3.62	0.12	100.13
WAI-1_area3_big-plag_rim-core-rim	9/26/13 0:17	52.12	0.09	30.73	0.00	0.42	0.03	0.19	12.95	3.81	0.12	100.47
WAI-1_area3_big-plag_rim-core-rim	9/26/13 0:20	51.25	0.11	31.00	0.01	0.51	0.00	0.18	13.28	3.62	0.11	100.07
WAI-1_area3_big-plag_rim-core-rim	9/26/13 0:23	51.39	0.09	31.11	0.00	0.47	0.01	0.19	13.36	3.53	0.10	100.25
WAI-1_area3_big-plag_rim-core-rim	9/26/13 0:27	51.91	0.09	30.72	0.00	0.46	0.00	0.18	13.00	3.78	0.12	100.27
WAI-1_area3_big-plag_rim-core-rim	9/26/13 0:30	51.78	0.11	30.81	0.00	0.43	0.00	0.18	13.06	3.82	0.12	100.31
WAI-1_area3_big-plag_rim-core-rim	9/26/13 0:33	51.28	0.07	31.11	0.02	0.53	0.00	0.20	13.46	3.49	0.10	100.25
WAI-1_area3_big-plag_rim-core-rim	9/26/13 0:36	51.43	0.11	30.96	0.00	0.48	0.04	0.20	13.29	3.50	0.11	100.12
WAI-1_area3_big-plag_rim-core-rim	9/26/13 0:39	51.54	0.08	31.18	0.02	0.47	0.00	0.18	13.49	3.53	0.11	100.60
WAI-1_area3_big-plag_rim-core-rim	9/26/13 0:42	52.02	0.08	30.78	0.00	0.47	0.00	0.18	13.02	3.79	0.12	100.46
WAI-1_area3_big-plag_rim-core-rim	9/26/13 0:46	51.67	0.08	30.97	0.01	0.52	0.02	0.19	13.20	3.64	0.11	100.41
WAI-1_area3_big-plag_rim-core-rim	9/26/13 0:49	52.03	0.10	30.71	0.00	0.64	0.01	0.19	13.05	3.82	0.12	100.67
ML494-2_area1_random-matrix-cpx	9/26/13 0:52	54.69	0.36	1.95	0.56	10.72	0.23	28.86	2.45	0.04	0.01	99.86
ML494-2_area1_random-matrix-cpx	9/26/13 0:55	54.26	0.37	2.13	0.68	10.43	0.15	28.28	2.94	0.06	0.00	99.31
ML494-2_area1_random-matrix-cpx	9/26/13 0:58	54.28	0.40	2.28	0.68	10.78	0.25	28.59	2.52	0.04	0.00	99.83
ML494-2_area1_random-matrix-cpx	9/26/13 1:02	54.05	0.41	2.54	0.71	11.01	0.21	28.42	2.46	0.07	0.00	99.87
ML494-2_area1_random-matrix-cpx	9/26/13 1:05	51.23	0.99	3.29	0.38	8.96	0.21	17.32	16.64	0.24	0.00	99.25
ML494-2_area1_random-matrix-cpx	9/26/13 1:08	54.37	0.45	1.50	0.23	14.25	0.26	26.51	2.31	0.03	0.01	99.91
ML494-2_area1_random-matrix-cpx	9/26/13 1:11	54.65	0.46	1.30	0.19	14.01	0.26	26.77	2.35	0.05	0.00	100.03
ML494-2_area1_random-matrix-cpx	9/26/13 1:14	54.43	0.51	1.49	0.20	13.82	0.25	26.46	2.33	0.05	0.00	99.54
ML494-2_area1_random-matrix-cpx	9/26/13 1:17	51.27	0.92	1.21	0.03	17.54	0.36	15.56	11.47	0.23	0.02	98.60
ML494-2_area1_random-matrix-cpx	9/26/13 1:21	50.55	0.87	2.22	0.16	17.92	0.36	16.40	9.57	0.20	0.01	98.27
ML494-2_area1_random-matrix-plag	9/26/13 1:24	51.99	0.14	28.94	0.02	1.07	0.00	0.22	12.73	3.92	0.15	99.19
ML494-2_area1_random-matrix-plag	9/26/13 1:27	54.16	0.12	27.34	0.02	1.11	0.01	0.16	11.04	4.91	0.21	99.08
ML494-2_area1_random-matrix-plag	9/26/13 1:30	52.58	0.09	28.49	0.00	1.13	0.00	0.19	12.29	4.15	0.18	99.10
ML494-2_area1_random-matrix-plag	9/26/13 1:33	55.68	0.14	26.43	0.00	1.18	0.00	0.22	9.87	5.48	0.25	99.27
ML494-2_area1_random-matrix-plag	9/26/13 1:36	51.61	0.13	29.05	0.00	1.28	0.00	0.23	12.80	3.87	0.13	99.11
ML494-2_area1_random-matrix-plag	9/26/13 1:40	52.01	0.15	29.07	0.00	1.07	0.00	0.20	12.72	3.94	0.15	99.32
ML494-2_area1_random-matrix-plag	9/26/13 1:43	51.84	0.12	28.78	0.01	1.27	0.03	0.20	12.61	4.01	0.15	99.02
ML494-2_area1_random-matrix-plag	9/26/13 1:46	76.37	1.40	11.51	0.00	1.32	0.02	0.15	0.72	2.09	4.11	97.69
ML494-2_area1_random-matrix-plag	9/26/13 1:49	54.15	0.15	27.55	0.00	1.16	0.02	0.18	10.99	4.89	0.24	99.33
ML494-2_area1_random-matrix-plag	9/26/13 1:52	52.15	0.15	28.66	0.01	1.17	0.00	0.22	12.51	4.05	0.16	99.08
ML494-2_area1_random-matrix-plag	9/26/13 1:55	52.15	0.14	28.59	0.01	1.12	0.00	0.15	12.49	4.08	0.17	98.91
ML494-2_area1_random-matrix-plag	9/26/13 1:58	51.86	0.10	28.70	0.02	1.16	0.01	0.19	12.63	4.03	0.16	98.86
ML494-2_area1_random-matrix-plag	9/26/13 2:02	51.43	0.08	29.20	0.00	1.17	0.01	0.17	13.01	3.74	0.14	98.96
ML494-2_area1_random-matrix-plag	9/26/13 2:05	56.12	0.12	26.44	0.01	1.02	0.00	0.12	9.72	5.59	0.31	99.44
ML494-2_area1_random-matrix-plag	9/26/13 2:08	53.28	0.17	27.84	0.00	1.35	0.00	0.17	11.69	4.45	0.21	99.16
ML494-2_area1_random-matrix-plag	9/26/13 2:11	51.24	0.09	29.12	0.00	1.13	0.04	0.15	12.98	3.76	0.16	98.67
ML494-2_area1_random-matrix-plag	9/26/13 2:14	51.54	0.10	28.81	0.00	1.10	0.03	0.17	12.83	3.83	0.14	98.54
ML494-2_area1_random-matrix-plag	9/26/13 2:17	52.16	0.18	28.69	0.00	1.31	0.01	0.13	12.55	4.04	0.17	99.25
ML494-2_area1_random-matrix-plag	9/26/13 2:21	52.28	0.15	28.46	0.01	1.18	0.01	0.21	12.42	4.06	0.18	98.96
ML494-2_area1_random-matrix-plag	9/26/13 2:24	55.21	0.17	26.65	0.00	1.12	0.00	0.16	10.13	5.34	0.29	99.09
ML494-2_area2_random-matrix-cpx	9/26/13 2:27	51.54	0.95	1.94	0.10	11.29	0.27	15.93	16.43	0.27	0.02	98.76
ML494-2_area2_random-matrix-cpx	9/26/13 2:30	51.82	0.95	1.81	0.11	11.41	0.24	16.13	16.32	0.25	0.02	99.06
ML494-2_area2_random-matrix-cpx	9/26/13 2:33	51.62	0.99	2.21	0.24	14.28	0.27	14.07	14.85	0.31	0.07	98.90
ML494-2_area2_random-matrix-cpx	9/26/13 2:36	51.46	1.07	2.32	0.12	11.05	0.26	15.71	16.59	0.27	0.01	98.86
ML494-2_area2_random-matrix-cpx	9/26/13 2:40	53.69	0.42	1.14	0.08	16.33	0.33	23.11	4.03	0.08	0.01	99.24
ML494-2_area2_random-matrix-cpx	9/26/13 2:43	53.60	0.43	1.17	0.10	15.37	0.31	22.94	4.76	0.09	0.00	98.77
ML494-2_area2_random-matrix-cpx	9/26/13 2:46	54.52	0.31	0.90	0.10	14.18	0.31	25.08	3.77	0.09	0.00	99.28
ML494-2_area2_random-matrix-cpx	9/26/13 2:49	50.83	0.68	1.11	0.05	21.52	0.43	17.73	5.54	0.15	0.05	98.08
ML494-2_area2_random-matrix-cpx	9/26/13 2:52	51.82	1.00	1.99	0.07	11.82	0.24	15.45	16.56	0.28	0.02	99.25
ML494-2_area2_random-matrix-cpx	9/26/13 2:55	51.30	1.10	2.25	0.10	11.50	0.26	15.34	16.71	0.27	0.01	98.84
Kakanui-augite_std	9/26/13 2:59	50.75	0.86	8.33	0.14	6.22	0.13	16.12	15.88	1.29	0.00	99.72
Kakanui-augite_std	9/26/13 3:02	50.67	0.92	8.30	0.16	6.38	0.14	16.07	15.88	1.31	0.00	99.84
Kakanui-augite_std	9/26/13 3:05	50.47	0.90	8.30	0.19	6.09	0.09	16.14	15.78	1.30	0.01	99.28
Lake-County-plag-std	9/26/13 3:08	51.39	0.06	30.02	0.03	0.40	0.05	0.14	13.27	3.72	0.11	99.17
Lake-County-plag-std	9/26/13 3:11	51.49	0.03	30.02	0.00	0.41	0.02	0.13	13.36	3.70	0.12	99.29
Lake-County-plag-std	9/26/13 3:15	51.40	0.03	30.19	0.02	0.47	0.01	0.13	13.30	3.72	0.10	99.38
HAP-4_cpx1	9/26/13 3:19	50.79	1.55	3.30	0.26	6.63	0.08	15.26	20.85	0.30	0.00	99.02
HAP-4_cpx1	9/26/13 3:22	50.23	1.47	3.19	0.30	6.58	0.18	14.85	20.58	0.33	0.00	97.69
HAP-4_cpx1	9/26/13 3:26	51.07	1.47	3.27	0.25	6.76	0.12	15.25	20.82	0.33	0.00	99.33
HAP-4_cpx1	9/26/13 3:30	50.72	1.49	3.35	0.34	6.77	0.13	15.19	20.74	0.34	0.00	99.07
HAP-4_cpx1	9/26/13 3:33	50.47	1.46	3.43	0.41	6.77	0.13	15.25	20.66	0.33	0.00	98.91
HAP-4_cpx2	9/26/13 3:37	51.08	0.91	3.38	1.02	5.17	0.10	15.72	21.20	0.28	0.00	98.86
HAP-4_cpx3	9/26/13 3:40	51.37	0.86	3.58	1.01	4.88	0.10	15.79	21.09	0.27	0.02	98.96
HAP-4_cpx4	9/26/13 3:44	51.25	0.94	3.66	1.02	5.05	0.14	15.82	21.31	0.25	0.00	99.44
HAP-4_cpx4	9/26/13 3:48	50.95	0.94	3.68	1.02	5.12	0.12	15.74	21.34	0.26	0.00	99.16
HAP-4_cpx5_zoned	9/26/13 3:51	50.83	0.95	3.67	1.00	4.97	0.12	15.67	21.19	0.27	0.00	98.67
HAP-4_cpx5_zoned	9/26/13 3:55	50.83	0.98	3.57	1.06	4.91	0.14	15.50	21.26	0.28	0.01	98.54
HAP-4_cpx5_zoned	9/26/13 3:58	51.14	0.95	3.65	1.02	5.11	0.10	15.73	21.28	0.26	0.00	99.25
HAP-4_cpx5_zoned	9/26/13 4:02	50.99	0.96	3.62	1.04	4.95	0.14	15.62	21.37	0.25	0.01	98.96
HAP-4_cpx5_zoned	9/26/13 4:06	52.13	0.66	2.72	1.17	4.01	0.10	16.48	21.54	0.27	0.00	99.09

Appendix 1. Geochemistry - Plagioclase, Pyroxene Electron Microprobe Analyses

SAMPLE	DAT/TIM	SiO2 WT%	TiO2 WT%	Al2O3 WT%	Cr2O3 WT%	FeO WT%	MnO WT%	MgO WT%	CaO WT%	Na2O WT%	K2O WT%	TOTAL
HAP-4_cpx5_zoned	9/26/13 4:09	52.13	0.62	2.49	1.03	4.09	0.11	16.53	21.50	0.26	0.00	98.76
HAP-4_cpx5_zoned	9/26/13 4:13	51.74	0.69	3.21	1.14	4.13	0.10	16.19	21.58	0.25	0.00	99.06
HAP-4_cpx5_zoned	9/26/13 4:16	51.75	0.68	2.93	1.14	4.16	0.09	16.28	21.65	0.22	0.00	98.90
HAP-4_cpx5_zoned	9/26/13 4:20	51.75	0.63	3.04	1.20	4.00	0.09	16.25	21.67	0.21	0.00	98.86
HAP-4_cpx5_zoned	9/26/13 4:24	51.36	0.81	3.63	1.18	4.51	0.11	15.83	21.56	0.23	0.00	99.24
HAP-4_cpx5_zoned	9/26/13 4:27	50.03	1.34	4.39	0.43	7.00	0.08	14.78	20.40	0.31	0.01	98.77
WAI-3_random-matrix-plag	9/26/13 4:31	56.79	0.11	26.46	0.00	1.00	0.00	0.10	8.86	5.69	0.36	99.38
WAI-3_random-matrix-plag	9/26/13 4:34	51.88	0.16	29.48	0.01	0.79	0.01	0.21	12.23	4.12	0.14	99.02
WAI-3_random-matrix-plag	9/26/13 4:38	50.82	0.15	29.48	0.00	0.75	0.00	0.21	12.37	3.77	0.13	97.69
WAI-3_random-matrix-plag	9/26/13 4:42	52.62	0.14	29.17	0.01	0.78	0.00	0.22	11.90	4.33	0.16	99.33
WAI-3_random-matrix-plag	9/26/13 4:45	52.73	0.16	28.93	0.00	0.85	0.02	0.24	11.76	4.24	0.14	99.07
WAI-3_random-matrix-plag	9/26/13 4:49	53.15	0.20	28.44	0.00	0.87	0.04	0.21	11.24	4.59	0.18	98.91
WAI-3_random-matrix-plag	9/26/13 4:52	53.76	0.23	28.05	0.00	1.05	0.02	0.15	10.65	4.71	0.24	98.86
WAI-3_random-matrix-plag	9/26/13 4:56	52.56	0.13	28.98	0.01	0.80	0.04	0.26	11.79	4.24	0.14	98.96
WAI-3_random-matrix-plag	9/26/13 5:00	54.22	0.18	28.24	0.00	0.92	0.00	0.14	10.71	4.79	0.24	99.44
WAI-3_random-matrix-plag	9/26/13 5:03	53.83	0.18	28.23	0.00	0.84	0.04	0.17	10.82	4.83	0.22	99.16
WAI-3_random-matrix-plag	9/26/13 5:07	51.23	0.10	29.88	0.02	0.74	0.03	0.27	12.52	3.75	0.12	98.67
WAI-3_random-matrix-plag	9/26/13 5:10	54.15	0.23	27.38	0.00	1.12	0.02	0.17	10.15	5.08	0.25	98.54
WAI-3_random-matrix-plag	9/26/13 5:14	55.50	0.20	27.21	0.00	0.96	0.00	0.14	9.65	5.31	0.29	99.25
WAI-3_random-matrix-plag	9/26/13 5:18	55.73	0.20	26.74	0.00	0.95	0.01	0.12	9.35	5.54	0.33	98.96
WAI-3_random-matrix-plag	9/26/13 5:21	53.63	0.12	28.36	0.01	0.95	0.00	0.21	10.97	4.66	0.18	99.09

Appendix 1. Geochemistry - XRF Analyses

SAMPLE	Date	SiO2	TiO2	Al2O3	Fe2O3	MnO	MgO	CaO	Na2O	K2O	P2O5	SUM
HAP-1A (new)	9/5/13	45.56	2.06	11.32	12.07	0.15	13.5	11.84	1.29	0.24	0.22	98.25
HAP-1B	8/15/13	46.39	2.12	11.74	12.24	0.15	13.08	11.97	1.12	0.24	0.23	99.28
HAP-1B	9/5/13	45.78	2.1	11.51	12.15	0.15	13.4	11.91	1.28	0.24	0.22	98.74
HAP-1C	9/5/13	45.55	2.05	11.26	12.15	0.15	13.6	11.83	1.23	0.23	0.21	98.27
HAP-2A	8/15/13	45.84	2	11.09	12.57	0.16	14.81	11.22	1.03	0.26	0.22	99.2
HAP-2B	8/15/13	45.85	2.01	11.06	12.57	0.15	14.88	11.22	0.93	0.26	0.21	99.13
HAP-3	9/23/13	46.2	2.02	11.18	12.67	0.16	14.93	11.31	1.04	0.26	0.22	99.98
HAP-4	9/23/13	45.23	2.15	11.14	12.79	0.15	15.11	11.64	0.94	0.26	0.21	99.63
KIL1960AA	9/5/13	48.57	2.76	12.31	12.96	0.16	9.24	9.67	1.94	0.57	0.3	98.48
KIL1960AB	8/15/13	49.03	2.81	12.52	13.17	0.16	8.98	9.84	1.7	0.58	0.31	99.1
KIL1960-2	9/23/13	48.97	2.78	12.41	13.07	0.16	9.32	9.75	1.96	0.57	0.3	99.28
ML494-1A	8/15/13	49.24	1.75	11.29	12.46	0.16	13.27	8.74	1.23	0.35	0.2	98.68
ML494-1B	8/15/13	49.65	1.76	11.42	12.51	0.16	13.47	8.71	1.21	0.34	0.2	99.43
ML494-2A	8/17/13	51.43	1.99	12.65	12.14	0.15	10.01	9.76	1.52	0.41	0.24	100.31
ML494-2A	9/4/13	50.39	1.97	12.81	12.13	0.16	9.84	9.66	1.83	0.39	0.24	99.41
ML494-2A	9/5/13	50.22	1.97	12.56	12.15	0.15	9.75	9.68	1.81	0.39	0.23	98.91
ML494-2A	9/5/13	50.45	1.99	12.69	12.15	0.15	9.64	9.71	1.7	0.4	0.23	99.1
ML494-2B	8/15/13	50.98	2	12.76	12.24	0.15	9.63	9.77	1.55	0.41	0.24	99.74
ML494-2C	9/4/13	50.38	1.96	12.68	12.17	0.16	10.08	9.63	1.83	0.39	0.24	99.5
ML494-2C	9/5/13	50.54	1.97	12.65	12.2	0.15	9.87	9.68	1.71	0.39	0.23	99.39
ML499-1A	8/15/13	50.82	2.11	12.5	12.4	0.16	9.58	9.42	1.5	0.47	0.28	99.23
ML499-1B	8/15/13	51.07	2.11	12.45	12.44	0.16	9.79	9.42	1.51	0.47	0.29	99.71
ML647-2A	9/5/13	45.54	1.09	7.46	13.08	0.16	25.17	5.7	0.73	0.18	0.12	99.23
ML647-2B	8/15/13	45.84	1.08	7.53	13.27	0.16	25	5.67	0.48	0.17	0.13	99.34
ML647-2B	8/17/13	45.81	1.08	7.49	13.29	0.16	24.98	5.67	0.48	0.17	0.13	99.27
ML647-3	9/23/13	44.96	1.1	7.23	13.87	0.16	25.68	5.53	0.41	0.16	0.12	99.22
WAI-1A	8/15/13	49.07	2.06	18.75	11.06	0.13	5.22	10.86	2.04	0.19	0.2	99.57
WAI-1B	8/15/13	49.03	2.05	18.84	11.05	0.13	5.2	10.87	2.12	0.19	0.2	99.7
WAI-2A	8/15/13	45.92	3.49	15.48	16.38	0.18	6.2	9.28	2.1	0.29	0.36	99.69
WAI-2B	8/15/13	45.77	3.48	15.42	16.28	0.18	6.2	9.25	2.08	0.28	0.36	99.32
WAI-3	9/23/13	46.03	3.5	15.51	16.37	0.18	6.24	9.3	2.09	0.28	0.36	99.87
Standards												
BCR-1B	8/15/13	54.99	2.25	13.72	13.74	0.17	3.43	7.04	3.19	1.73	0.37	100.65
BCR-1B	9/4/13	54.55	2.22	13.84	13.65	0.17	3.58	6.94	3.59	1.71	0.38	100.63
BCR-1B	9/5/13	54.59	2.25	13.54	13.66	0.17	3.5	7	3.44	1.73	0.38	100.26
BCR-1C	8/15/13	54.97	2.25	13.86	13.74	0.18	3.46	7.02	3.24	1.74	0.37	100.84
BCR-1C	9/4/13	54.52	2.22	13.88	13.69	0.17	3.62	6.95	3.7	1.71	0.38	100.86
BCR-1C	9/5/13	54.54	2.24	13.54	13.72	0.17	3.55	7.01	3.51	1.74	0.38	100.39
BCR-1C	9/23/13	54.27	2.23	13.47	13.65	0.17	3.53	6.98	3.49	1.73	0.38	99.9
BCR-1 avg		**54.63**	**2.24**	**13.69**	**13.69**	**0.17**	**3.52**	**6.99**	**3.45**	**1.73**	**0.38**	
BCR-1_publ		**54.39**	**2.25**	**13.72**	**13.67**	**0.18**	**3.5**	**6.99**	**3.29**	**1.7**	**0.36**	
BHVO-1B	8/15/13	49.68	2.74	13.7	12.49	0.16	7.02	11.33	2.04	0.52	0.27	99.96
BHVO-1B	9/4/13	49.27	2.69	13.77	12.38	0.16	7.27	11.15	2.36	0.51	0.27	99.85
BHVO-1B	9/5/13	49.23	2.72	13.5	12.4	0.16	7.13	11.23	2.23	0.52	0.27	99.37
BHVO-1B	9/23/13	49.43	2.73	13.55	12.45	0.16	7.16	11.28	2.24	0.52	0.27	99.79
BHVO-1 avg		**49.40**	**2.72**	**13.63**	**12.43**	**0.16**	**7.15**	**11.25**	**2.22**	**0.52**	**0.27**	
BHVO-1_publ		**49.59**	**2.69**	**13.7**	**12.39**	**0.17**	**7.22**	**11.32**	**2.24**	**0.52**	**0.27**	
UH-1F	8/15/13	47.89	4.1	15.75	14.73	0.17	4.34	7.84	3.96	1.44	0.8	101.02
UH-1F	9/4/13	47.57	4.05	15.97	14.65	0.17	4.51	7.73	4.37	1.42	0.81	101.25
UH-1F	9/5/13	47.54	4.07	15.47	14.67	0.17	4.41	7.79	4.19	1.44	0.8	100.55
UH-1N	8/15/13	47.49	4.04	15.62	14.52	0.17	4.25	7.73	3.61	1.41	0.8	99.63
UH-1N	9/4/13	47.13	3.99	15.81	14.42	0.17	4.44	7.6	4.02	1.39	0.78	99.75
UH-1N	9/5/13	46.98	4.01	15.28	14.41	0.17	4.31	7.68	3.83	1.41	0.8	98.87
UH-1N	9/23/13	47.32	4.04	15.39	14.51	0.17	4.34	7.74	3.86	1.42	0.81	99.59
UH avg		**47.42**	**4.04**	**15.61**	**14.56**	**0.17**	**4.37**	**7.73**	**3.98**	**1.42**	**0.80**	
UH-1_publ		**47.42**	**4.04**	**15.6**	**14.48**	**0.17**	**4.35**	**7.8**	**3.81**	**1.41**	**0.81**	
W2B	8/15/13	52.65	1.09	15.5	11.1	0.16	6.17	10.96	2.35	0.65	0.13	100.75
W2B	9/4/13	52.06	1.07	15.45	11.02	0.16	6.42	10.85	2.76	0.63	0.13	100.56
W2B	9/5/13	52.19	1.08	15.34	11.03	0.16	6.27	10.89	2.63	0.64	0.12	100.36
W2F	8/15/13	52.87	1.08	15.65	11.23	0.16	6.24	11	2.16	0.64	0.13	101.16
W2F	9/4/13	52.39	1.06	15.6	11.16	0.16	6.48	10.86	2.58	0.62	0.14	101.04
W2F	9/5/13	52.45	1.08	15.4	11.16	0.16	6.34	10.93	2.43	0.63	0.13	100.69
W2F	9/23/13	52.16	1.07	15.32	11.1	0.16	6.31	10.87	2.42	0.63	0.13	100.16
W2 avg		**52.40**	**1.08**	**15.47**	**11.11**	**0.16**	**6.32**	**10.91**	**2.48**	**0.63**	**0.13**	
W2_publ		**52.61**	**1.06**	**15.43**	**10.88**	**0.17**	**6.36**	**10.85**	**2.2**	**0.63**	**0.14**	100.40

APPENDIX E – MODELING CODES

In addition to the experimental work, the project developed several modeling codes to understand the theoretical and numerical issues of simulating reactive flow and deformation processes of mineral carbonation reactions occurring at realistic pressures and temperatures underground. The original project plan called for a series of two-dimensional (2D) and three-dimensional (3D) scaling-up simulations to test the feasibility of modeling an actual field test of in situ carbonation. As described in the project's quarterly status reports, these original plans had to be curtailed, in part, because of the difficulty of implementing the 2D and 3D codes and, in part, because of health issues that interrupted participation in the project of the principal investigator responsible for this work (Edward Bolton, Yale University).

Nevertheless, by the end of the project, several novel codes had been developed and were in the early stages of stages of testing and validation. These codes, described below, are part of the deliverables of the research. The document ("KINFLOW formulation") that follows this section outlines the mathematical basis of these numerical models.

Modeling Codes

The following codes are part of the package of deliverables for the project:

- KINFLOW1D is a code that can simulate 0D (zero-dimensional) and 1D (one-dimensional) reaction and transport under kinetic control. The 0D formulation is described in detail in the document "KINFLOW formulation". The deliverables include Makefiles, input files, FORTRAN code, and example runs for this code and the others described below. Advection and diffusion of solutes in 1D are calculated with this code, with injection of arbitrary fluid compositions from above or below the computational domain. The code allows for thermal evolution. Specialized input files for aqueous phase equilibrium reactions were created to match EQ3/6 at 1 bar and arbitrary temperature, as well as at 150 bar and 200°C to compare to some of the mineral carbonation experiments. Most of the kinetic data is drawn from Palandri and Kharaka (2004), except for additional kinetic data from Hanchen et al. (2006) and Saldi et al. (2010, 2012). Our sub-gridscale grain models allow for arbitrary rectangular prism grain shapes, and armoring of one mineral by another.

- COMPNEARLIN is a 1D coupled reaction and poroelastic compaction, using a simple reaction term in the lower portion of the model domain. This model adds reactive exchange between the solid and the fluid to a simplified version of the model of Cai and Bercovici (2014). With no reactions or gravity, the code recovers the error function solution shown in Figure 1 of Cai and Bercovici (2014).

- COUPLED-POROELASTIC-KINFLOW1D is a coupling of COMPNEARLIN and KINFLOW1D, where the reactions create porosity changes. Compaction modifies the porosity as well. The reactions are under kinetic control. Compaction also modifies the nucleation density of the minerals, reducing the distance between grains in the *z*-direction. The reactive term is calculated from the porosity change, which would occur with reactions only. This is then used to provide the compaction routine with the necessary volume changes between the fluid and the solid phases. A reformulation is necessary before boundary conditions can accommodate fixed strain-rates or increasing stresses at the boundaries for comparison to the experiments performed at the University of Maryland.

- MOREMINERALS2DCO2 is a 2-dimensional, 2-fluid phase extension of kinflow1d. We allow multiple simulated injection and extraction wells, where the injection fluid compositions can be specified. The fluid density is calculated from the PVTBO1 FORTRAN code (Hassanzadeh et al., 2004). The phase split and CO_2-H_2O partitioning is calculated via RKCO2_V2 FORTRAN code (Spycher et al., 2003; and Spycher and Pruess, 2005). This code also allows the relative saturation of a CO_2 rich phase to be calculated, which can be either a vapor phase or a supercritical fluid. Pressure is calculated using an IMPES routine as described in Bolton and Firoozabadi (2014). Salinities are estimated from the total concentration of all species except for H_2O, CO_2, H^+ and OH^-. Zero capillary pressure has been assumed. The two-phase compressibility and partial molar volumes used are currently quite rough estimates. This code is still in beta testing; updated versions can be provided upon request.

Appendix E References

Bolton, E.W., and Firoozabadi, A., 2014. Numerical modeling of temperature and species distributions in hydrocarbon reservoirs. *Journal of Geophysical Research Solid Earth* **119**: 18-31, doi:10.1002/2013JB010043.

Cai, Z., and Bercovici, D., 2014. Two-phase viscoelastic damage theory, with applications to subsurface fluid injection. *Geophys. J. Int.* **199**: 1481–1496, doi: 10.1093/gji/ggu344.

Hanchen, M., Prigiobbe, V., Storti, G., Seward, T.M., Mazzotti, M., 2006. Dissolution kinetics of fosteritic olivine at 90-150 degrees C including effects of the presence of CO_2. *Geochimica Cosmochimica Acta* **70**: 4403-4416.

Hassanzadeh, H., Pooladi-Darvish, M., Elsharkawy, A.M., Keith, D.W., and Leonenko, Y., 2008. Predicting PVT data for CO_2 brine mixtures for black-oil simulation of CO_2 geological storage. *International Journal of Greenhouse Gas Control* **2**(1): 65-77.

Palandri, J.L., and Kharaka, Y.K., 2004. A compilation of rate parameters of water-mineral interaction kinetics for application to geochemical modeling Open File Report 2004-1068, U.S. Geological Survey.

Saldi, G.D., Schott, J., Pokrovsky, O.S., and Oelkers, E.H., 2010. An experimental study of magnesite dissolution rates at neutral to alkaline conditions and 150 and 200°C as a function of pH, total dissolved carbonate concentration, and chemical affinity. *Geochimica Cosmochimica Acta* **74**: 6344–6356.

Saldi, G.D., Schott, J., Pokrovsky, O.S., Gautier, Q., and Oelkers, E.H., 2012. An experimental study of magnesite precipitation rates at neutral to alkaline conditions and 100–200°C as a function of pH, aqueous solution composition and chemical affinity. *Geochimica Cosmochimica Acta* **83**: 93–109.

Spycher, N., Pruess, K., and Ennis-King, J., 2003. CO_2-H_2O mixtures in the geological sequestration of CO2. I. Assessment and calculation of mutual solubilities from 12°C to 100°C and up to 600 bar. *Geochimica Cosmochimica Acta* **67**: 3015-3031.

Spycher, N., and Pruess, K. (2005) Mixtures in the geological sequestration of CO_2. II. Partitioning in chloride brines at 12–100°C and up to 600 bar. *Geochimica Cosmochimica Acta* **69**: 3309–3320.

KINFLOW formulation

Edward W. Bolton

Department of Geology and Geophysics

Yale University, New Haven, Connecticut 06511, U.S.A.

24 November 2014 Draft

We present a model for comparisons to geochemical experiments of forsterite dissolution and magnesite precipitation. The model, developed at Yale, is dubbed KINFLOW. We also included additional secondary minerals. Besides mineral reactions, we consider the aqueous phase speciation reactions that are assumed to be in equilibrium (see Table 1).

Table 1. Aqueous speciation reactions assumed to be in equilibrium

Aqueous Reaction	Eq. #
$H^+ + OH^- \rightleftharpoons H_2O$	aq 1
$H_3SiO_4^- + H^+ \rightleftharpoons SiO_2(aq) + 2H_2O$	aq 2
$HCO_3^- + H^+ \rightleftharpoons CO_2(aq) + H_2O$	aq 3
$CO_3^{2-} + 2H^+ \rightleftharpoons CO_2(aq) + H_2O$	aq 4
$MgCO_3(aq) + 2H^+ \rightleftharpoons Mg^{2+} + CO_2(aq) + H_2O$	aq 5
$NaCO_3^- + 2H^+ \rightleftharpoons Na^+ + CO_2(aq) + H_2O$	aq 6
$MgHCO_3^+ + H^+ \rightleftharpoons Mg^{2+} + CO_2(aq) + H_2O$	aq 7
$MgOH^+ + H^+ \rightleftharpoons Mg^{2+} + H_2O$	aq 8
$NaOH(aq) + H^+ \rightleftharpoons Na^+ + H_2O$	aq 9
$NaHSiO_3(aq) + H^+ \rightleftharpoons Na^+ + SiO_2(aq) + H_2O$	aq 10
$NaHCO_3(aq) + H^+ \rightleftharpoons Na^+ + CO_2(aq) + H_2O$	aq 11

This set of species was chosen to include all species for this set of elements of concentration higher than 10^{-10} molal predicted by a run of EQ3NR (Wolery, 1979, 1992) that included 1 molar $NaHCO_3$ (as used in the experiments) and experimentally observed total concentration of Si and Mg. It should be mentioned that we here write CO_2(aq) to mean the same thing as H_2CO_3 as used by Garrels and Christ (1990) p. 76, (see also footnote and references there discussed) which is to include the sum of both species in solution (typically dominated by CO_2 molecules). Some authors use the notation $H_2CO_3^*$ for the sum of these two species.

We partition the system into primary and secondary species (Reed 1982, Lichtner 1985, and Kirkner and Reeves 1988). This is purely a mathematical convenience arising from the fact that not all species need be calculated simultaneously, and one species can be eliminated for each homogeneous reaction that

is in equilibrium. The choice of the partition is arbitrary. We choose the following primary species: $0 : \mathrm{H_2O},\ 1 : \mathrm{H^+},\ 2 : \mathrm{SiO_2(aq)},\ 3 : \mathrm{Na^+},\ 4 : \mathrm{Mg^{2+}},\ 5 : \mathrm{CO_2(aq)}$. We also used $\mathrm{Cl^-}$ in simulations to compare to cases when HCl was added to make acidic conditions. The remaining secondary species are: $1 : \mathrm{OH^-},\ 2 : \mathrm{H_3SiO_4^-},\ 3 : \mathrm{HCO_3^-},\ 4 : \mathrm{CO_3^2-},\ 5 : \mathrm{MgCO_3(aq)},\ 6 : \mathrm{NaCO_3^-},\ 7 : \mathrm{MgHCO_3^+},\ 8 : \mathrm{MgOH^+},$ $9 : \mathrm{NaOH(aq)},\ \ 10 : \mathrm{NaHSiO_3(aq)},\ 11 : \mathrm{NaHCO_3(aq)}$. We assume all charged species are in the aqueous phase, while uncharged species (except for water) are written explicitly to include their phase (aq for aqueous). We assume the secondary species in the homogeneous equilibrium reactions have a stoichiometric coefficient of -1 (as it is on the left-hand side of the reaction equation), so that we write the reaction in the form of the destruction of the secondary species:

$$A_{s:i} \rightleftharpoons \sum_{j=0}^{N_p} \nu_{n:ij} A_{p:j} \tag{1}$$

for each of the N_s secondary species, where $\nu_{n:ij}$ (often zero) is the number of moles of primary species j for the reaction n of one mole of secondary species i, $A_{p:j}$ and $A_{s:i}$ are the chemical formulae of the primary and secondary species, respectively, and N_p is the number of primary species. The notation is somewhat modified from Bolton et al., (1996), where the secondary species were on the right-hand-side of the equation. For simplicity, here we number the equilibrium reactions such that $n = i$, with one secondary species for each reaction of the same number, so that $\nu_{n:ij} \equiv \nu_{ij}$.

To be specific, given the equations above, and the choice of primary and secondary species above, we may write for the first 5 speciation reactions:

$$\begin{bmatrix} \nu_{10} & \nu_{11} & \nu_{12} & \nu_{13} & \nu_{14} & \nu_{15} \\ \nu_{20} & \nu_{21} & \nu_{22} & \nu_{23} & \nu_{24} & \nu_{25} \\ \nu_{30} & \nu_{31} & \nu_{32} & \nu_{33} & \nu_{34} & \nu_{35} \\ \nu_{40} & \nu_{41} & \nu_{42} & \nu_{43} & \nu_{44} & \nu_{45} \\ \nu_{50} & \nu_{51} & \nu_{52} & \nu_{53} & \nu_{54} & \nu_{55} \end{bmatrix} = \begin{bmatrix} 1 & -1 & 0 & 0 & 0 & 0 \\ 1 & -2 & 0 & 1 & 0 & 1 \\ 1 & -1 & 0 & 0 & 0 & 1 \\ 1 & -2 & 0 & 0 & 0 & 1 \\ 1 & -2 & 0 & 0 & 1 & 1 \end{bmatrix}.$$

with other reactions of analogous forms. For aqueous solutions, the concentrations of the secondary species, $m_{s:i}$ (in molality: moles of solute i in 1 kg of water), may be expressed in terms of the concentrations of primary species j, $m_{p:j}$ (also in molality), and the activity of water, $a_{H2\,0} = a_{p:0}$, through the equilibrium "constants" $\hat{K}_{s:i}$ of the homogeneous reactions, and the practical activity coefficients (Garrels & Christ, 1990), $\gamma_{p:j}$ and $\gamma_{s:i}$ (primary and secondary species, respectively). For either species (except for water), $a_k = \gamma_k m_k$. The presence of water (also chosen as one of the primary species of index 0) as the dominant fluid phase needs special treatment. The current treatment assumes the water activity can be

approximated by its mole fraction in the aqueous phase. We note that the more extensive formulation for the activity of water in EQ3/6 differs from the mole fraction approach by only 0.5% for a 1 molal solution of NaCl. The activity coefficients for the dissolved species are calculated by the Extended Debye Hückel (b-dot) relations (cf. Helgeson and Kirkham, 1974):

$$\log_{10} \gamma_i = -\frac{A z_i^2 I^{1/2}}{1 + B \, \mathring{a}_i \, I^{1/2}} + \dot{b} I \tag{2}$$

where I is the ionic strength

$$I = \frac{1}{2} \prod m_i z_i^2 \tag{3}$$

with z_i as the ionic charge of species i. The other symbols are as follows: A, B and $\dot{b}$ are temperature dependent parameters (A and B with units of kg$^{1/2}$ mole$^{-1/2}$), and $\mathring{a}_i$ is the ion size parameter commonly expressed in angstroms.

For our choice of numbering the homogeneous reactions and the secondary species, the equilibrium constants are written as:

$$\hat{K}_{s:i} = \frac{\prod_{j=0}^{N_p} (a_{p:j})^{\nu_{ij}}}{a_{s:i}} \tag{4}$$

so that the molality of the secondary species may be calculated from the activities of the primary species directly, when they are known:

$$m_{s:i} = \hat{K}_{s:i}^{-1} \gamma_{s:i}^{-1} \prod_{j=0}^{N_p} (a_{p:j})^{\nu_{ij}} \tag{5}$$

The reactive transport formulations for one and higher dimensions are more conveniently formulated in terms of molarity rather than molality. Although this makes little difference for a zero-dimensional code, with an equation of state for the fluid, it is simple to transform one formulation into the other. For instance, M_i in molarity (moles i per liter of solution) for the non-water species can be calculated from m_i in molality via

$$M_i = m_i \omega_w \rho_{liq} \cdot \left(\frac{1}{1000} \right) \left(\frac{\text{m}^3 \text{ liq}}{\text{L liq}} \right) \tag{6}$$

where ω_w is the mass fraction of water in solution, ρ_{liq} is the density of the liquid (in kg/m^3) .

Mineral reactions are comparatively slow, so governed by kinetic control. The six mineral set under current consideration are as in Table 2.

Table 2. Mineral dissolution/precipitation reactions under kinetic control

Mineral Reaction	Eq. #	Mineral
$Mg(OH)_2(s) + 2H^+ \rightleftharpoons Mg^{2+} + 2H_2O$	min rxn 1	brucite
$SiO_2(amrph:s) \rightleftharpoons SiO_2(aq)$	min rxn 2	amorphous silica
$Mg_3Si_4O_{10}(OH)_2(s) + 6H^+ \rightleftharpoons 3Mg^{2+} + 4SiO_2(aq) + 4H_2O$	min rxn 3	talc
$Mg_2SiO_4(s) + 4H^+ \rightleftharpoons 2Mg^{2+} + SiO_2(aq) + 2H_2O$	min rxn 4	forsterite
$Mg_3Si_2O_5(OH)_4(s) + 6H^+ \rightleftharpoons 3Mg^{2+} + 2SiO_2(aq) + 5H_2O$	min rxn 5	chrysotile
$MgCO_3(s) + 2H^+ \rightleftharpoons Mg^{2+} + CO_2(aq) + H_2O$	min rxn 6	magnesite

Here we assume end-member forsterite. Note that we have written the mineral reactions in terms of the primary species. We also have chosen a stoichiometric coefficient of the mineral to be unity. These reaction may be written as:

$$A_{min:m} \rightleftharpoons \sum_{j=0}^{N_p} \hat{\nu}_{mj} A_{p:j} \tag{7}$$

where $A_{min:m}$ are the chemical formulae of the minerals. If the mineral is in equilibrium with the fluid, the ion activity product for the reaction $Q_{min:m}$ is equal to the equilibrium constant $K_{min:m}$ for the mineral reaction written in terms of the primary species.

$$Q_{min:m} \equiv \frac{\prod_{j=0}^{N_p} (a_{p:j})^{\hat{\nu}_{mj}}}{a_{min:m}} \tag{8}$$

and

$$Q_{min:m} = K_{min:m} \text{ at equilibrium} \tag{9}$$

where $a_{min:m}$ is the activity of the mineral. Dissolution of the mineral occurs for $Q_{min:m} < K_{min:m}$. For pure end-member minerals, we may assume unit activity for $a_{min:m}$.

For the mineral reactions given in Table 2, and the choice of primary species above, the form of $\hat{\nu}_{mj}$ is:

$$\begin{bmatrix} \hat{\nu}_{10} & \hat{\nu}_{11} & \hat{\nu}_{12} & \hat{\nu}_{13} & \hat{\nu}_{14} & \hat{\nu}_{15} \\ \hat{\nu}_{20} & \hat{\nu}_{21} & \hat{\nu}_{22} & \hat{\nu}_{23} & \hat{\nu}_{24} & \hat{\nu}_{25} \\ \hat{\nu}_{30} & \hat{\nu}_{31} & \hat{\nu}_{32} & \hat{\nu}_{33} & \hat{\nu}_{34} & \hat{\nu}_{35} \\ \hat{\nu}_{40} & \hat{\nu}_{41} & \hat{\nu}_{42} & \hat{\nu}_{43} & \hat{\nu}_{44} & \hat{\nu}_{45} \\ \hat{\nu}_{50} & \hat{\nu}_{51} & \hat{\nu}_{52} & \hat{\nu}_{53} & \hat{\nu}_{54} & \hat{\nu}_{55} \\ \hat{\nu}_{60} & \hat{\nu}_{61} & \hat{\nu}_{62} & \hat{\nu}_{63} & \hat{\nu}_{64} & \hat{\nu}_{65} \end{bmatrix} = \begin{bmatrix} 2 & -2 & 0 & 0 & 1 & 0 \\ 0 & 0 & 1 & 0 & 0 & 0 \\ 4 & -6 & 4 & 0 & 3 & 0 \\ 2 & -4 & 1 & 0 & 2 & 0 \\ 5 & -6 & 2 & 0 & 3 & 0 \\ 1 & -2 & 0 & 0 & 1 & 1 \end{bmatrix}.$$

We write the rate $R_{min:m}$ of the mineral reactions to be positive when the mineral dissolves (mineral reactions as written in Table 2 running to the right) with $R_{min:m}$ as the rate of mineral reaction m (in moles of mineral consumed/(kg water)/sec). The direct rate of production of primary species j by all the mineral reactions is

$$P_{p:j}^{min} = \sum_{m=1}^{N_{min}} (\hat{\nu}_{mj} R_{min:m}) \tag{10}$$

(although this is not the entire story, as equilibrium reactions can simultaneously modify the primary species as well: see below). In the same units, the rate of change of mineral m is:

$$\dot{m}_{min:m} = -R_{min:m} \tag{11}$$

When $R_{min:m} < 0$ the mineral increases in mass.

Changes in the concentrations of the primary species also cause changes in the concentrations of the secondary species. Although the secondary species are connected to the primary species by equilibrium reactions, and we view their adjustment as instantaneous, in fact the rates of change of the secondary species are slaved to the rates of the mineral reactions. The notation to deal with all these rates is expressed as explicitly as possible to avoid confusion and conflicts with other notations present in the literature. Referring to the aqueous phase equilibrium reactions (Table 1 and Eq. 1), the rate of this reaction (slaved to the mineral reactions) is written positive to the right, with primary species produced (when the ν_{kj} are positive) while secondary species are destroyed, so that: $R^{aq}_{s:k}$ is the rate of the equilibrium reaction k (in moles/(kg water)/sec), which given our choice of stoichiometry implies changes in the secondary species concentration as:

$$\dot{m}^{aq}_{s:k} = -R^{aq}_{s:k} \tag{12}$$

The direct rate of production of primary species j by all the secondary equilibrium reactions is

$$P^{aq}_{p:j} = \sum_{k=1}^{N_s} (\nu_{kj} R^{aq}_{s:k}) \tag{13}$$

So the net rate of production of primary species for both the mineral and the aqueous phase equilibrium reactions is

$$\dot{m}_{p:j} = P^{min}_{p:j} + P^{aq}_{p:j} = \sum_{m=1}^{N_{min}} (\hat{\nu}_{mj} R_{min:m}) + \sum_{k=1}^{N_s} (\nu_{kj} R^{aq}_{s:k}) = -\sum_{m=1}^{N_{min}} \hat{\nu}_{mj} \dot{m}_{min:m} - \sum_{k=1}^{N_s} \nu_{kj} \dot{m}_{s:k} \tag{14}$$

We now define the so-called total concentrations (Kirkner and Reeves, 1988), not to be confused with typical definitions of total carbonate, etc. (although it turns out that U_5 is in fact the total carbon species concentration in the aqueous solution). For convenience in use of reactive transport modeling, we define both the molality and molarity forms of this quantity. In molality units, the total concentration is

$$\hat{U}_j = m_{p:j} + \sum_{k=1}^{N_s} \nu_{kj} m_{s:k} \tag{15}$$

and in molarity units

$$\bar{U}_j = M_{p:j} + \sum_{k=1}^{N_s} \nu_{kj} M_{s:k} \tag{16}$$

with the relationship

$$\bar{U}_j = \hat{U}_j \omega_w \rho_{liq} \cdot \left(\frac{1}{1000}\right)\left(\frac{\text{m}^3 \text{ liq}}{\text{L liq}}\right) \tag{17}$$

We also define

$$\bar{P}_{p:j} = P_{p:j} \omega_w \rho_{liq} \cdot \left(\frac{1}{1000}\right)\left(\frac{\text{m}^3 \text{ liq}}{\text{L liq}}\right) \tag{18}$$

and

$$\bar{R}_{min:m} = R_{min:m} \omega_w \rho_{liq} \cdot \left(\frac{1}{1000}\right)\left(\frac{\text{m}^3 \text{ liq}}{\text{L liq}}\right) \tag{19}$$

with $\bar{R}_{min:m}$ in moles mineral consumed per liter liquid per second.

The time derivative (dot) of the U's may be written as

$$\dot{\hat{U}}_j = \dot{m}_{p:j} + \sum_{k=1}^{N_s} \nu_{kj} \dot{m}_{s:k} \tag{20}$$

so that (and using Eq 14)

$$\dot{\hat{U}}_j = \sum_{m=1}^{N_{min}} (\hat{\nu}_{mj} R_{min:m}) - \sum_{k=1}^{N_s} \nu_{kj} \dot{m}_{s:k} + \sum_{k=1}^{N_s} \nu_{kj} \dot{m}_{s:k} \tag{21}$$

leading to

$$\dot{\hat{U}}_j = \sum_{m=1}^{N_{min}} (\hat{\nu}_{mj} R_{min:m}) \tag{22}$$

and

$$\dot{\bar{U}}_j = \sum_{m=1}^{N_{min}} (\hat{\nu}_{mj} \bar{R}_{min:m}) \tag{23}$$

Note that the equilibrium reactions cancel so that the time dependence of the Us depend directly only on the mineral reactions. These forms show how the total concentrations change due to mineral reactions and speciation. The full form for such changes will later be written to also include transport, diffusion, and porosity changes. If the Us are known, one can solve a system of nonlinear equations for the molarities or molalities of the primary species (using Eq 5 and Eq 17 or Eq **??**). As mentioned before, once the primary species are known, the secondary species can be calculated via the aqueous phase equilibrium relations.

Multimineralic Grain Model for Fluid Bathed Cubes

Here we assume that the distance between grain centers can be assigned at an initial time. We show here various relations for the special case that the grains are cubic, but other more realistic grain shapes based on arbitrarily shaped rectangular prisms is coded.

$\ell_m =$ characteristic distance between grain centers of mineral m in the bulk.

$V_B =$ a reference volume in units of choice (e.g. 1 m^3)

$\bar{N}_m = (1/\ell_m^3) =$ nuclei density for m (grains/volume)

$d_m =$ effective grain size of mineral m (grain width for cubes)

$N_{min} =$ total number of mineral types

Porosity fraction

$$\phi = 1 - \sum_{m=1}^{N_{min}} \bar{N}_m F_V d_m^3$$

$F_V =$ volume form factor: (1 for cubes)

Surface area of mineral m compared to fluid volume

$$\frac{A_m}{V_f} = \frac{1}{\phi}(\bar{N}_m F_A d_m^2)\mathcal{R}_m$$

$F_A =$ area form factor: (6 for cubes) where $\mathcal{R}_m$ is a parameter to account for potential roughness of the mineral surfaces that may have more actual surface area than the geometric surface area.

We have implemented a simple model for armoring to compare to the experiments where a single crystal of forsterite (Fo) is dissolving and the precipitated minerals form on the surface of forsterite. This occludes the forsterite where other minerals grow, reducing the Fo surface area available for exchange with the fluid. Our first approach to capture this effect is to reduce the Fo area by the area of a cubic face of the growing attached minerals. Mathematically, this may be written as

$$\frac{A_{Fo}}{V_f} = \left(\frac{1}{\phi}(\bar{N}_{Fo} F_A d_{Fo}^2)\mathcal{R}_{Fo} - \sum_{m \neq Fo}^{N_{min}} \frac{1}{\phi}(\bar{N}_m d_m^2) \right)$$

Relation of this notation to kinetic mineral data

Most mineral kinetic data is presented in (or could be converted to) units of the change of the number of moles of mineral m per m^2 mineral surface area per second (positive for precipitation), which we call

here $k_{min:m}$. As our initial guess of mineral kinetics, we have used the compilation of Palandri and Kharaka (2004) (that we here dub PK04). In terms of fluid concentration changes in molarity/time, we use:

$$\dot{\bar{U}}_j = \sum_{m=1}^{N_{min}} (\hat{\nu}_{mj} \bar{R}_{min:m}) \tag{24}$$

and

$$\bar{R}_{min:m} = -\frac{A_m}{V_f} \left[\frac{\text{m}^2 \text{ mineral}}{\text{m}^3 \text{ liquid}}\right] \cdot 10^{-3} \cdot \left[\frac{\text{m}^3 \text{ liquid}}{\text{liter liquid}}\right] \cdot k_{min:m} \cdot \left[\frac{\text{moles mineral } m}{\text{m}^2 \text{ mineral*seconds}}\right] \tag{25}$$

The kinetic rates are written as the sum over mechanisms, typically and acid, neutral, and basic (or other) mechanism (i) as (for mineral m):

$$k_{min:m} = -\sum_{i}^{mechanisms} \left[k_{i:m}^{298.15K} \exp\left(\frac{-E_{act:i:m}}{R} \left(\frac{1}{T(K)} - \frac{1}{298.15K} \right) \right) \prod_{j}^{cat\ inib} a_{i,j}^{n_{i,j:m}} (1 - (Q_{min:m}/K_{min:m})^{p_{i:m}})^{q_{i:m}} \right] \tag{26}$$

where multiple catalysts or inhibitors are allowed. $k_{min:m}$ and $k_{i:m}^{298.15K}$ are in (moles of mineral m) / m^2 / second. Recall that dissolution of the mineral occurs for $Q_{min:m} < K_{min:m}$, $k_{min:m} < 0$, and $\bar{R}_{min:m} < 0$. Mineral growth, as change of grain diameter (in meters):

$$\frac{\partial d_m}{\partial t} = \bar{V}_m \cdot k_{min:m} \left[\frac{\text{moles mineral } m}{\text{m}^2 \text{ mineral*seconds}}\right] \cdot \mathcal{R}_m S_n \tag{27}$$

where $\bar{V}_m$ is the molar volume of mineral m (in cubic meters/mole). Surface roughness actually increases the rates of dissolution of undersaturated minerals as compared to the geometric surface areas, as accounted for in the parameter $\mathcal{R}_m$. The parameter S_m refers to the number of sides in a particular direction that the mineral grows. It is 2 if the mineral is growing on both sides in a particular direction, but is 1 if the mineral is attached and growing in one direction.

Initial data:

Porosity fraction =0.95 was calculated from the capsule's contents of 1.2 mL of a solution of 0.96 molal or 1 molar $NaHCO_3$ in the presence of 0.2 g forsterite cubic grains. For the secondary species, using the reactions written above, the equilibrium constants at 150 bar and 200 C the equilibrium constants are (calculated from data files supplied from Wolery) shown in Table 3. Initial concentrations of all species were chosen from a solution of a nonlinear system for equilibrium and charge balance.

Table 3. Equilibrium 'constants' at 150 bar and 200 C for reactions assumed to be in equilibrium

Aqueous Reaction Eq. # k	Associated Species	$\log_{10} \hat{K}_{s:k}$
(s1)	OH^-	11.22873
(s2)	$H_3SiO_4^-$	9.04259
(s3)	HCO_3^-	7.137615
(s4)	CO_3^2-	17.52631
(s5)	$MgCO_3(aq)$	13.01281
(s6)	$NaCO_3^-$	19.8290
(s7)	$MgHCO_3^+$	4.751825
(s8)	$MgOH^+$	7.8536
(s9)	$NaOH(aq)$	11.20482
(s10)	$NaHSiO_3(aq)$	7.643351
(s11)	$NaHCO_3(aq)$	8.4106

For $\hat{K}_{s:6}$, $\hat{K}_{s:8}$, and $\hat{K}_{s:11}$ only low pressure data was available.

For the minerals brucite, amorphous silica, talc, forsterite, chrysotile, and magnesite, respectively, using the reactions written abovem again at 150 bar and 200 C (fit from data files supplied from Wolery).

Table 4. Equilibrium 'constants' at 150 bar and 200 C for the mineral reactions

Mineral Reaction Eq. # m	Associated Mineral	$\log_{10} K_{min:m}$
(m1)	brucite	9.349423
(m2)	amorphous silica	1.791744
(m3)	talc	9.821108
(m4)	forsterite	14.24297
(m5)	chrysotile	16.59034
(m6)	magnesite	5.977282

The secondary minerals were assumed to precipitate at a characteristic grain spacing between 20 and 40 microns, similar to experimental observations. Kinetic data in Table 5 for the mineral reactions was taken from the USGS compilation by Palandri and Kharaka (2004) (cf. Eq 26).

Table 5. Kinetic data for the mineral reactions Format for kinetic data from USGS compilation by Palandri and Kharaka (2004). This format has number of mechanisms i to input (and sum over) followed by $log_{10}(k_{i:m}^{298.15K})$, $E_{act:i:m}$ (kJ/mol.), the number of catalytic or inhibitors n's to follow, n for H^+ or other catalytic or inhibiting species, then species referred to by n (e.g. H^+, other species, or blank if there is no such inhibiting or catalyzing species), then p & q. The notation USGS below refers to Palandri and Kharaka (2004) PK04 (cf. Eq 26). For chrysotile, we used serpentine.

Mineral	Min.#	PK04	Mech#	$log_{10}(k:298.15)$	E_{act}	cat/inhib#	exponent n	species	p	q
brucite	1	p. 41	mech1	-4.73	59.0	1	$n_1 = 0.5$	H+	1	1
			mech2	-8.24	42.	1	$n_2 = .0$		1	1
amor.silica	2	p. 15	mech1	-12.73	76.	1	$n_1 = .0$		1	1
talc	3	p. 40	mech1	-12.00	42.	1	$n_1 = .0$		1	1
forsterite	4	p. 35	mech1	-6.85	67.2	1	$n_1 = 0.47$	H+	1	1
			mech2	-10.64	79.0	1	$n_2 = 0.$		1	1
chrysotile	5	p. 40	mech1	-12.0	73.5	1	$n_1 = .0$		1	1
			mech2	-13.58	73.5	1	$n_2 = -0.23$	H+	1	1
magnesite	6	p. 42	mech1	-6.38	14.4	1	$n_1 = 1.$	H+	1	1
			mech2	-9.34	23.5	1	$n_2 = 0$	H+?**	1	1
			mech3	-5.22	62.8	1	$n_3 = 1.$	CO2(aq)	1	1

The carbonate mechanism has some notational inconsistencies between Palandri and Kharaka and the original publications they source. We also coded the forsterite dissolution kinetics from Hanchen, et al., (2006), of the form

$$k_{Fo} = -\left[854(mol/m^2/s)a_{H^+}^{0.46}\exp\left(\frac{-52900J}{RT(K)}\right)(1-(Q_{min:m}/K_{Fo}))\right] \tag{28}$$

with the deviation from equilibrium with respect to the mineral reaction put in the same form as Palandri and Kharaka (2004).

Some Recommendations for future experiments

Many of our experiments have had the solution compositions evolve more quickly than perhaps anticipated. From a modeling perspective, this is not desirable if comparisons are to be made between the data and simulations. Factors that make the solution composition be better resolved by the experiments include some combination of lower temperatures, larger grain sizes (in the case of experiments done on powders), as well as more closely space measurements near the beginning of the experiments. We still have to check the adequacy of the pH measurements, and to correct them to the experimental temperatures properly. Accurate characterization of actual surface areas used in a particular experiment is also important. Agitation of the fluid is recommended for the low temperature experiments.

Conclusions

Significant progress has been made in forward modeling of the carbonation experiments and the forsterite dissolution experiments for both single crystals and powders. We are also making progress comparing to experiments with higher pH initial conditions, but the agreement between model and experiment still

needs improvement. Modification of the KINFLOW database has been made for forsterite kinetics based on the inverse modeling at 100C. We anticipate additional accomplishments and experimental improvements during the coming year.

References

Bolton, E.W., A.C. Lasaga and D.M. Rye, (1996) A model for the kinetic control of quartz dissolution and precipitation in porous media flow with spatially variable permeability: Formulation and examples of thermal convection, Journal of Geophysical Research, 101, 22157-22187.

Garrels, R.M. and Christ, C.L., 1990 *Solutions, Minerals and Equilibria*, Jones & Bartlett Publ., Boston.

Hanchen, M., Prigiobbe, V., Storti, G., Seward, T.M., Mazzotti, M., 2006, Dissolution kinetics of fosteritic olivine at 90-150 degrees C including effects of the presence of CO2, Geochim. Cosmochim. Acta, 70, 4403-4416.

Helgeson, H.C., and Kirkham, D.H., 1974, Theoretical prediction of the thermodynamic behavior of aqueous electrolytes at high pressures and temperatures: II. Debye- Hückel parameters for activity coefficients and relative partial molal properties, American Journal Of Science, Vol. 274, 1199-1261.

Kirkner, D.J., and Reeves, H., 1988, Multicomponent mass transport with homogeneous and heterogeneous chemical reactions: Effect of chemistry on the choice of numerical algorithm, 1. Theory, *Water Resources Research*, **24**, 1719–1729.

Lictner, P.C., 1985, Continuum model for simultaneous chemical reactions and mass transport in hydrothermal systems, *Geochimica and Cosmochimica Acta*, **49**, 779–800.

Palandri, J.L., Kharaka, Y.K. (2004) A compilation of rate parameters of water-mineral interaction kinetics for application to geochemical modeling Open File Report 2004-1068, U.S. Geological Survey. [PK04]

Reed, M.H., 1982, Calculation of multicomponent chemical equilibria and reaction progress in systems involving minerals, gases and an aqueous phase, *Geochimica and Cosmochimica Acta*, **46**,

513–528.

Saldi, G.D., J. Schott, O.S. Pokrovsky, and E.H. Oelkers, (2010) An experimental study of magnesite dissolution rates at neutral to alkaline conditions and 150 and 200 deg C as a function of pH, total dissolved carbonate concentration, and chemical affinity, Geochimica et Cosmochimica Acta, Vol. 74, 63446356.

Saldi, G.D., J. Schott, O.S. Pokrovsky, Q. Gautier, and E.H. Oelkers, (2012) An experimental study of magnesite precipitation rates at neutral to alkaline conditions and 100200 deg C as a function of pH, aqueous solution composition and chemical affinity, Geochimica et Cosmochimica Acta, vol. 83, 93109.

Schott, J., O.S. Pokrovsky, and E.H. Oelkers (2009) The Link Between mineral Dissolution/Precipitation Kinetics and Solution Chemistry, Reviews in Mineralogy & Geochemistry Vol. 70 pp. 207-258.

Wolery, T.J., (1979) *Calculation of chemical equilibrium between aqueous solution and minerals: the EQ3/6 software package*, Lawrence Livermore Laboratory URCL-52658, 41 p.

Wolery T. J. (1992) *EQ6, A Computer Program for Reaction Path Modeling of Aqueous Geochemical Systems: Theoretical Manual, User's Guide, and Related Documentation.* UCRL-MA-110662 PT IV., Lawrence Livermore Laboratory, Livermore, CA.